UNIVERSITY OF SOUTHAMPTON

Virtual Testing of Composite Risers

by

Hossam Ali Ragheb

A thesis submitted for the degree of
Doctor of Philosophy

in the
Faculty of Engineering and Physical Sciences
Civil, Maritime and Environmental Engineering
Maritime Engineering Research Group

June 2023

UNIVERSITY OF SOUTHAMPTON

ABSTRACT

FACULTY OF ENGINEERING AND PHYSICAL SCIENCES
CIVIL, MARITIME AND ENVIRONMENTAL ENGINEERING
MARITIME ENGINEERING RESEARCH GROUP

Doctor of Philosophy

VIRTUAL TESTING OF COMPOSITE RISERS

by Hossam Ali Ragheb

Hydrocarbon reserves maintain high market demand for energy security reasons, while the world governments promote ramping up renewable energy production. Companies exploit deeper reservoirs as current reserves start to deplete. Composite risers, with their tailored high strength-to-weight ratio properties that reduce the effective tensions and bending moments, are lucrative options to transport hydrocarbons compared to conventional steel risers. However, there is a limited research into composite risers full-scale behaviour. The main topic, that is missing from the literature, is the combined effect of far-field loading and mechanical properties uncertainties on composite risers integrity. Offshore complaint risers are exposed to dynamic vessel motion, environmental stochastic conditions and high pressure high temperature operational conditions. These complex multi-axial loadings result in non-linear riser response. The combined responses to these conditions with composite material in-situ, in addition to the environmental and manufacturing uncertainties are not well understood. Composites uncertainties due to material properties degradation associated with in-situ conditions, such as water absorption and manufacturing imperfections like voids and statistical variations require further investigation.

This work aims to capture the far-field loading effects on composite risers, that contains imperfections that require full-scale testing and to develop a virtual testing multi-scale approach, that is lucrative to manufacturers to optimize the qualification testing processes. Three models are developed in a sequential multi-scale framework. A non-linear extensible algorithm is developed based on beam theory to capture the global riser response and to provide boundary conditions and loads to a meso scale composite FEA pipe model. The predicted principal strains, that are post-processed from the global riser response, are imposed to a microscopic peridynamics RVE model that incorporates the statistical void percentage and fibre distributions in the matrix. An integrity analysis is conducted using Monte Carlo method that reveals that mechanical properties variation due to moisture absorption reduces the riser reliability by two orders of magnitude. The increase in manufacturing voids percentage reduces the tensile and transverse strengths to less than half of its no-void values. Another integrity analysis is conducted to investigate the effect of manufacturing uncertainties using peridynamics. The predicted damages are benchmarked against Tsai-Wu failure criterion which is found to be matching the final failure conclusion. However, it is observed that the Tsai-Wu stress-based equality is invariant to the microscopic geometry imperfections such as, voids and fibre distribution and size. Although peridynamics micro modelling is a computationally expensive approach to composite risers failure predictions, however, it is a promising technique to investigate wider varieties of manufacturing uncertainties effect on the composite riser integrity when combined with far-field loading and harsh operational conditions. The methodology presented allows the composite riser manufacturers to optimize qualification tests to mimic full-scale testing and control the parameters that correlate with failure.

Contents

List of Figures

List of Tables

Declaration of Authorship

I, Hossam Ali Ragheb, declare that this thesis entitled Virtual Testing of Composite Risers and the work presented in it are my own and has been generated by me as the result of my own original research.

I confirm that:

1. This work was done wholly or mainly while in candidature for a research degree at this University;
2. Where any part of this thesis has previously been submitted for a degree or any other qualification at this University or any other institution, this has been clearly stated;
3. Where I have consulted the published work of others, this is always clearly attributed;
4. Where I have quoted from the work of others, the source is always given. With the exception of such quotations, this thesis is entirely my own work;
5. I have acknowledged all main sources of help;
6. Where the thesis is based on work done by myself jointly with others, I have made clear exactly what was done by others and what I have contributed myself;
7. Either none of this work has been published before submission, or parts of this work have been published as: Hossam A. Ragheb *et al.* 2022.

Signed:

Date:

Acknowledgements

The author acknowledge financial support from the EPSRC Centre for the Next Generation Computational Modelling, NGCM Doctoral Training grant EP/L015382/1

The author acknowledge the use of the IRIDIS High Performance Computing Facility, and associated support services at the University of Southampton, in the completion of this work.

Nomenclature

Δx	Mesh size
ϵ	Strain
γ_m	Composite risers material resistance factor
Φ	The angle between the tangent and the horizontal global axis
ρ	Seawater density
ρ_f	Riser fluid density
$\hat{\mathbf{n}}$	Transversal direction
$\hat{\mathbf{t}}$	Tangential direction
A	Vessel motion amplitude
c	Peridynamics 3D elastic constant
C_{dn}	Riser normal drag coefficient
C_{dt}	Riser tangential drag coefficient
CV_f	Fibre diameter coefficient of variation
d	Ocean water depth
d_i	Riser internal diameter
d_o	Riser outer diameter
E_1	Elastic modulus in the fibre direction
E_2	Elastic modulus in the transverse direction
E_f	Fibre elastic modulus
E_m	Matrix elastic modulus
EA	Riser axial stiffness
EI	Riser flexural stiffness
F_{den}	Fibre density

$F_{r\sigma}$ Fibre radius standard deviation

F_{rmean} Fibre mean radius

G_cF Fibre strain energy release rate

G_cint Matrix/Fibre strain energy release rate

G_cM Matrix strain energy release rate

G_{IC} Initiation fracture toughness

H_max Maximum wave height

Int_{den} Interface density

L RVE side length

m Riser mass in air empty

m_a Riser added mass

M_{den} Matrix density

P_f Probability of failure

P_i Internal pressure

S Total riser length

s_0 Peridynamic critical stretch length

S_n Shear force in the transversal direction

T Tension in riser

t Time

T_p Peak wave period

u Axial velocity

v Tangential velocity

V_f Fibre volume fraction

v_{nc} Current transversal particle velocity

v_{nr} Transversal relative velocities

v_{nw} Wave transversal particle velocity

$V_{r\mu}$ Spherical voids mean radius

$V_{r\sigma}$ Spherical voids standard deviation

V_{rmax} Spherical voids maximum radius

V_{rmin} Spherical voids minimum radius

v_{tc} Current tangential particle velocity

v_{tr} Tangential relative velocities

v_{tw} Wave tangential particle velocity

Vl_{ratio} Void length to width ratio

w_0 Riser apparent weight per meter

X_C Compressive strength

X_T Longitudinal tensile strength

X_{HO} Hang-off horizontal coordinate

Y_{HO} Hang-off vertical coordinate

Chapter 1

Introduction

1.1 Background

1.1.1 Oil and Gas Market

The rapid growth in the demand for energy increases the desire to access new hydrocarbon reserves below the ocean floor, especially gas reserves to act as a low carbon and medium term energy transition fuel. Approximately 12% of global conventional hydrocarbon reserves lie between 1,000 to 4,000 meters under water. This equates to a total reserve of approximately 300 billion barrels, which is estimated as 9 million barrels per day by 2035. To transport fluids from reservoirs, sub-sea riser systems are indispensable devices to deep-water fields. They are long conduits used in various functions related to hydrocarbon production, such as transporting fluids, injection, hydraulic control fluids and gas lift between the well-head at the seabed and a surface floater vessel. They are built with a level of compliance relying on variants of the catenary shape in the water column as shown in Figure 1.1. Most of these configurations are useful in shallow/mid-water depths where decoupling of the floater motion is essential to maintain the integrity of the riser cross-section at the touch-down zone, while for deep-water applications, the floater motion have minimal effect on the near seabed section of the riser, therefore, the simple catenary configuration is preferred for its simplicity and cost efficiency. Traditionally, these riser elements have been constructed from metal alloys, predominantly steel, which are susceptible to corrosion in the ocean environment and due to internal fluids composition, therefore, expensive non-corrosive metal-alloys are often required based on titanium, copper-nickel, duplex and super duplex stainless steel. These conventional materials have had great success in providing safe structures for depths up to 1500m however, the potential advantages of composite-based risers at greater depths are investigated [15, 16]. Catenary risers, are cheaper solutions and widely used by the industry for moderate and deep-water developments [1]. However, there is a potential for total project cost reduction over the risers life cycle due to operational and maintenance cost savings, if composite materials are used [17, 18]. Capital expenditure CAPEX, increases for deep-water applications with the use of steel due to the need for larger floating production vessels and high capacity top-side tensioners to support the heavy steel riser systems, which are often a few kilometres in length. In addition to the high CAPEX costs, a higher operational

expenditure OPEX is expected. Composite materials, such as carbon-epoxy and carbon-PEEK, have potential benefits for offshore applications due to a unique combination of their high specific strength, thermal conductivity and low maintenance requirements. Due to these benefits there have been a growing number of investigations into the use of these materials but the lack of research literature and short track record, in addition to the large coefficient of variation observed for composite laminates has resulted in large resistance safety factors, such as detailed in DNV-RP-F202 [12]. These large resistance factors demonstrate that these materials are not fully understood for use in these applications, and requiring further investigation. One important area highlighted by Pham et al [19], is the lack of available studies investigating the reliability of such systems.

Composite risers material resistance factor γ_m is given as a function of the coefficient of variation of the composite laminate properties as shown in Table 1.1. That is because the composite laminate properties varies according to types of polymer, carbon fibre yarn used, manufacturing and curing techniques. This makes the coefficient of variation of composite laminates properties higher than that of steel and requires higher safety factor to cover the range of possible varying properties that are available in the market. This fact is evident when comparing the material resistance factors given in Table 1.1 [12] to the value presented in [20] of 1.15 to use with steel risers. The high safety class with the highest COV recommends almost two times the material resistance factor given for steel. That is also apparent with the brittle target annual failure rate, which is for the highest safety class is 10^{-6} for composite risers as shown in Table 1.2, and 10^{-5} for steel risers that is order of magnitude lower than composite risers [12, 20].

TABLE 1.1: Material resistance factor γ_m for composite risers brittle fracture[12]

	COV of the strength		
Safety class	COV ¡10%	10%-12.5%	12.5%-15%
Low	1.22	1.33	1.49
Normal	1.34	1.53	1.83
High	1.47	1.75	2.29

TABLE 1.2: Target annual failure rate for composite risers as recommended by DNV [12, 13]

	Failure Consequence		
Failure Type	Low Safety Class	Normal Safety Class	High Safety Class
Ductile	$P_f = 10^{-3}$	$P_f = 10^{-4}$	$P_f = 10^{-5}$
Brittle	$P_f = 10^{-4}$	$P_f = 10^{-5}$	$P_f = 10^{-6}$

This is despite the fact that DNV [12] outlines a reliability-based design in their recommendations for composite risers which should meet the target safety levels, outlined in Table 1.2, which reflect the probability of structural failure due to normal variability in load and resistance. Further motivation comes from Skogdalen and Vinnem [21, 22] who describe the risks that can occur in offshore scenarios such as riser breakage which can have major consequences and who advocate a proactive risk-based approach to safety, requiring a greater quantitative understanding of new technologies. Composite products are growing within the hydrocarbons, renewable and hydrogen economies, with expectations up to £1,100 million by 2030 as shown in Figure 1.2. Thermoplastic Composite pipes are recently developed into sub-sea riser systems which is a promising applications for composites in the oil and gas.

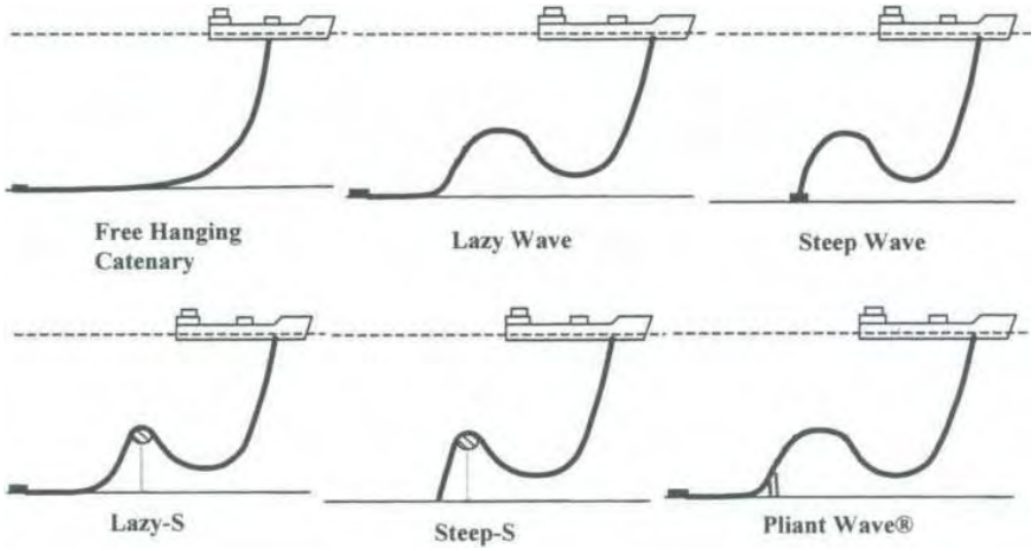

FIGURE 1.1: Riser system configurations [1]

FIGURE 1.2: UK Composites Market Study carried out by NCC [2]

1.1.2 Riser Types

Composite risers are categorised according to their cross-sectional design. For composites the cross-sectional layers are either bonded or un-bonded. Un-bonded risers are made from several laminated armour and pressure layers that are free to slip relative to each other. This allows a lower bending radius which is beneficial compared to the bonded layers. An example of an un-bonded composite riser is *Flexible Fibre Reinforced Pipe*, FFRP. Where it's cross-section consists of a concentric helical layers starting from a polymer liner and followed by pressure, hoop and tensile reinforcement layers, similar to a flexible steel riser structure. The majority of composite risers in the market are bonded. Bonded risers are simpler in structures with a steel or polymer inner liner surrounded with bonded angle ply laminates, where number of plies are optimised to withstand the loads on the pipe. An external sheath acts as a protective layer that decreases

the probability of water absorption. Figure 1.3 shows example of three products bonded and un-bonded composite pipes.

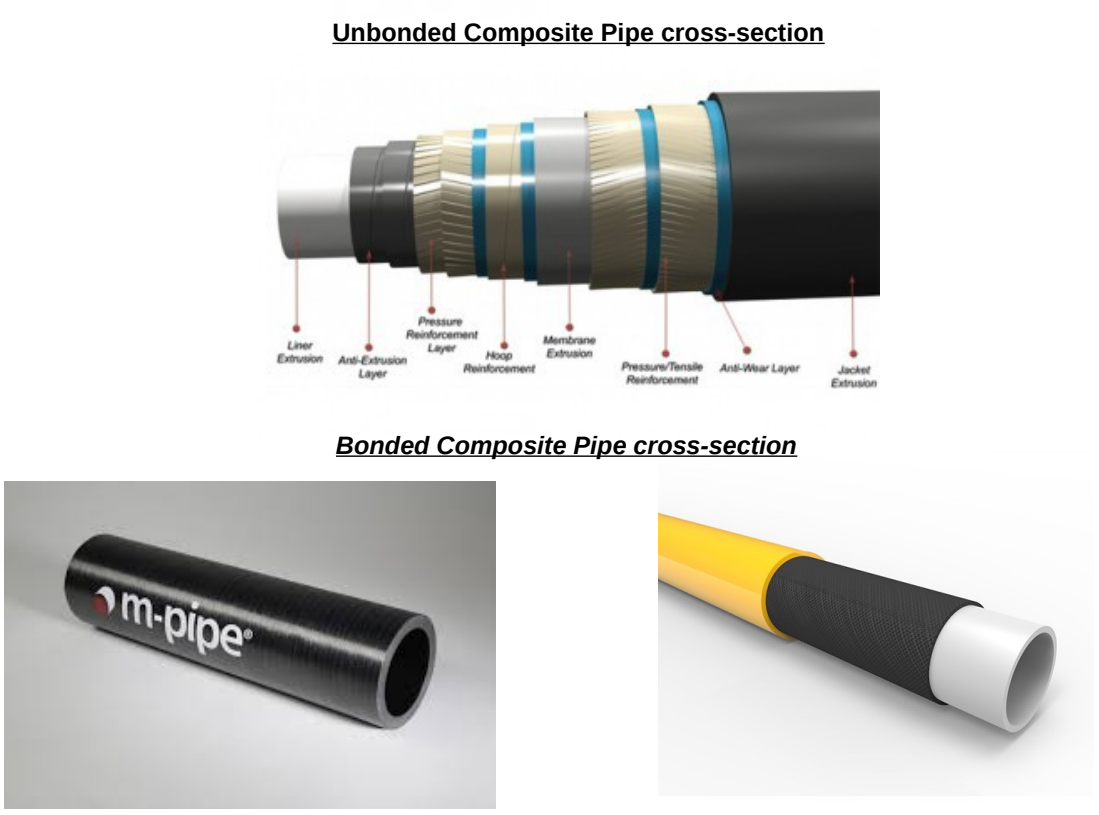

FIGURE 1.3: Bonded and un-bonded composite pipes cross-sections [3, 4, 5]

1.1.3 Riser Qualification

Composite risers are exposed to dynamic motion due to the floating vessel motion and wave loading. It's important to understand the effect of these multi-axial mechanical loadings alongside the inherit uncertainties caused by the manufacturing imperfections that promotes complex failure mechanisms. Fracture of composites initiates at the microscopic level that coalesce into micro-cracks that are triggered by structural loads, which leads to fracture and failure. Due to these complex loading and fracture mechanisms combined, which is less understood, conservative safety factors are adopted in composites design. DNV recommends values between 15 and 50 indicating lack of understanding of the problem [23, 24]. The current composites qualification approach used in industry is *make and test* to assure the reliability of structures, however testing slows the qualification process and increases expenses, additionally it becomes prohibitive to investigate complicated loading scenarios [25]. Standards such as ISO and ASTM require a large number of experiments to be performed to qualify new composite products to be used in the offshore environment. These requirements are due to the lack of composite risers performance records in deep water sub-sea environments and to ensure safe operations. Experiments have to capture all the operating conditions, increasing the number of test samples. Qualification costs are also expensive, in the order of tens of millions for each new composite product [26]. Often tests

at the coupon, laminate, pipe and full-scale model is required as per DNV [24]. However the full-scale testing is often impossible, especially with large structures such as riser systems, therefore the largest tested scale is limited by size. Therefore, to mitigate this challenge and achieve the desired capital savings, without compromising on safety, there is a need to optimize the selected tests to reflect critical scenarios that incorporates the large scale qualification processes by developing a Virtual Testing strategy.

The exponential growth in high performance computing capacity, with parallel computing and GPU processing coupled with recent advances in simulation and modelling techniques, creates an opportunity to optimize the industrial capital expenditure. The role of computational modelling in the product design and qualification, composite failure modelling techniques is limited to determining the initial sizing of the structures and in some limited scope of the qualification process. With growing computational power there is an opportunity to grow the role of computational modelling in the qualification process to reduce costs by exploiting the available resources. Integrated Computational Materials Engineering offers a promising solution to reduce qualification costs and time. Computational Materials Engineering and virtual testing of composite riser cross-section is expected to enable a deeper understanding of the failure mechanisms, safety factors, optimisation of composite riser cross-section design and a reduction in the qualification costs a better understanding of the required tests [27, 28].

1.1.4 Multiscale Testing

The Virtual Testing concept relies on utilising a multi-scale approach, using highly detailed numerical models to create a multi-scale digital twin of the offshore structure, linking the RVE scale up to full scale response. It's computationally impractical to model every atom in a long composite pipe, often a few kilometres long. Instead the multi-scale approach is the most suitable to model the problem where different models are used to capture, with appropriate fidelity and high computational efficiency, the dominant behaviour at each scale. Models are developed at the Macro Riser Scale, to provide the boundary loads to the Meso Pipe Scale. To model the structural failure, the Micro Laminate Scale model is used to determine the laminate damage. This approach facilitates optimization of testing strategies. Often closed form composite failure theories are relied upon, however with Virtual Testing models, it is possible to improve these failure and design methods, allowing evaluation and optimization of large scale structures such as composite dynamic risers which are exposed to multi-axial dynamic loading in offshore environment. Virtual testing models of composite dynamic risers allows high fidelity modelling that is not possible to achieve with conventional failure theories. The multi-scale pyramid approach is illustrated in Figure 1.4

1.2 Problem statement

As illustrated in Figure 1.5, composite risers are expected to lower the required operational expenditure compared to conventional steel risers, in addition to the potential to reduce the capital expenditure associated with deep water compared to steel. However, there are few obstacles that

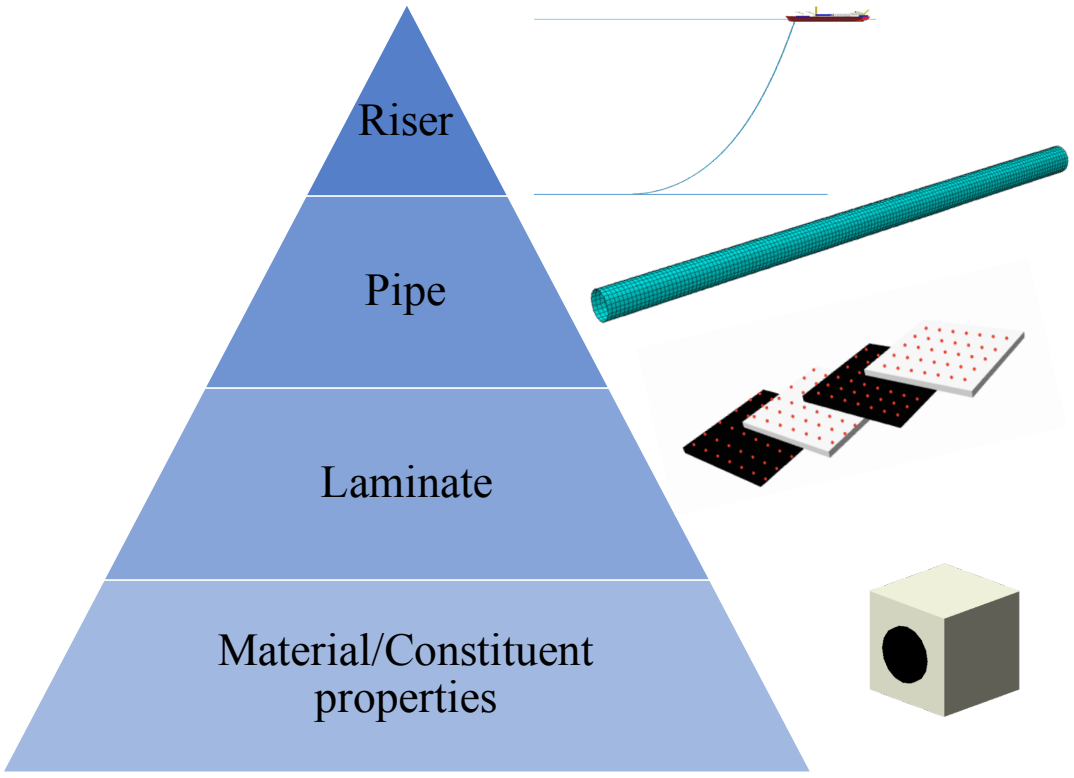

FIGURE 1.4: Virtual Testing Multi-scale Hierarchy Pyramid

requires the development of computationally efficient full-scale numerical models for virtual testing, of carbon fibre composite structures, accounting for uncertainties in the composite laminates properties, with the aim to asses composite structure integrity while operating in the offshore environment, to reduce the qualification costs and optimize material resistance factors.

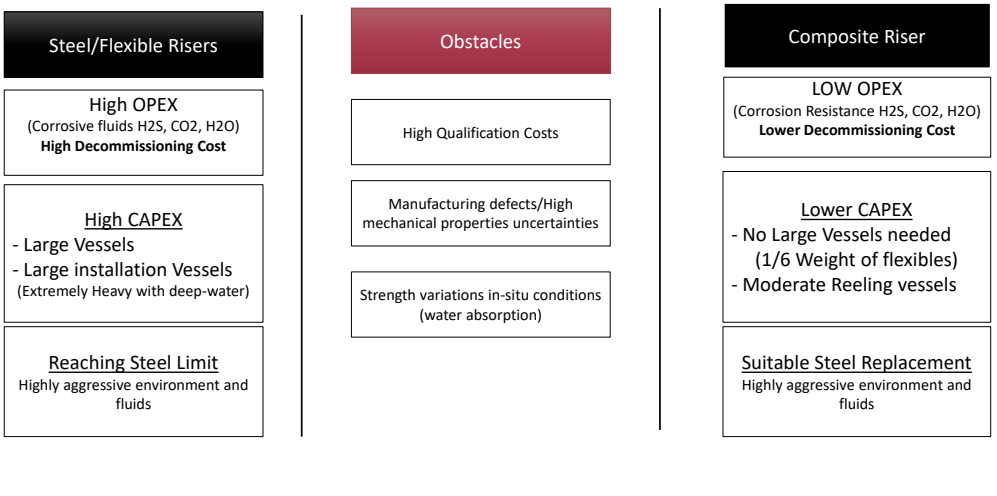

FIGURE 1.5: Motivation and problem statement

1.3 Research aim

The thesis aims to develop a multi-scale riser model that allows for virtual experiments. Aiming to expand the computational modelling scope in the qualification process to reduce costs and conservative safety factors used in composite riser design, due to the lack of knowledge about composite riser integrity that is exposed to harsh far-field loadings combined with composite mechanical properties uncertainness.

1.4 Research novelty

The novelty of this work is full-scale structural failure modelling of composites, incorporating material properties uncertainties and damage from the matrix and fibre. At these scales fracture and crack propagation models are incorporated. These will be coupled to higher structural level models to determine how these changes in properties combined with structural complex loading affect composite riser integrity. a multi-scale approach is the most suitable to model the problem where multiple models are used to capture, with appropriate fidelity and high computational efficiency the dominant behaviour at each length scale.

1.5 Research objectives

In order to reduce composite risers qualification costs, optimise highly conservative material resistance factors and increase confidence in in-situ composite riser integrity. two main objectives are targeted to achieve this aim, these objectives focus on the effects of far-field loadings, operational conditions effect on composites integrity given void percentage uncertainties and de-rated mechanical properties due to moisture absorption. To achieve these objectives, the approach requires a balanced multi-scale approach, where simplified physics is required to achieve computationally feasible predictions, starting from full riser model to capture the in-situ environmental loading to peridynamics RVE model to capture the laminate integrity as shown in the Figure 1.6.
The following objectives are planned to study the research question:

1. To survey the state-of-the-art literature on; riser global modelling, composite pipe models, composite fracture.
2. Development and verification of a numerical model capable of predicting the risers dynamic behaviour in the offshore environment.
3. Development and verification of a static and dynamic composite pipe model, including investigating various suitable element types.
4. Development and verification of numerical models capable of representing a range of composite damage modes and material imperfections.
5. Explore specific far-field loading and operational conditions on composite riser integrity and performing parametric studies to reduce conservative safety factors and enable for Virtual testing to reduce composite qualification costs.

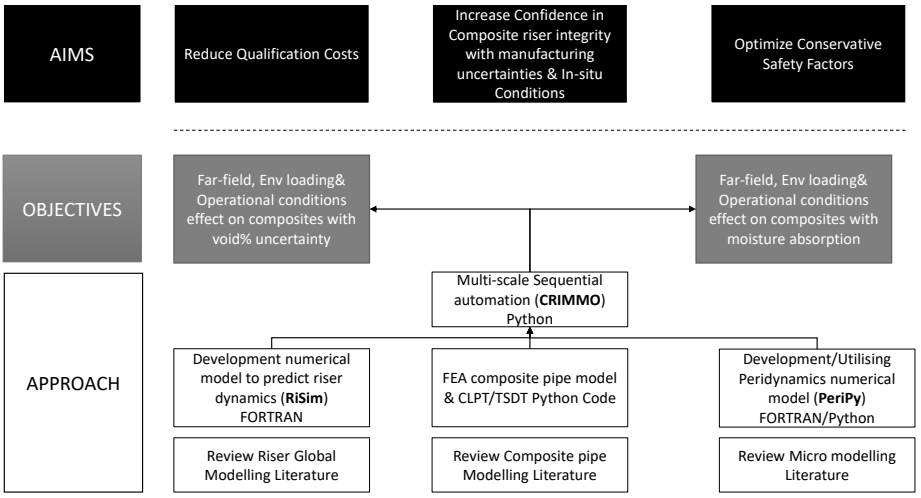

FIGURE 1.6: Aims, objectives and approach

1.6 Research scope

The scope of this project excludes:

1. Torsional loading is not part of the study, because riser systems are often exposed to negligible torsion during operations.
2. Experiments are not part of the scope, since the aim of the project it to develop computational model allowing for virtual testing.

1.7 Publications

1. Hossam Ragheb, Adam Sobey, "Effects of extensible modelling on composite riser mechanical responses", OceanEngineering,Volume 220, 2021, 108426, ISSN0029-8018, https://doi.org/10.1016/j.
2. H.A.Ragheb, M.Goodridge,D.C.Pham,A.J.Sobey, "Extreme response based reliability analysis of composite risers for applications in deepwater", Marine Structures,Volume 78, 2021, 103015, ISSN0951-8339, https://doi.org/10.1016/j.marstruc.2021.103015.
3. Hossam A., Ragheb, Przemyslaw A. Grudniewski, Adam J., Sobey. Composite risers design and optimisation using Multi-Level selection Genetic Algorithm, 2017, 20th International Conference on Composite Structures.
4. H.Ragheb, A.Sobey, "Far-field loading effects on carbon fibre composite pipes failure", Composite science and technology (in Progress)
5. H.Ragheb, A.Sobey, "Data Centric Digital Twins for: Offshore Dynamic Structures" , Data-centric Engineering Journal (in Progress)

1.8 Report structure

Chapter 2 is the literature review section, divided into four main review sections, Uncertainties in composite properties 2.1, structural 2.2, material 2.3, and multi-scale methods 2.4. Chapter 3 describes formulation and development of the riser beam and pipe models and applicability to composite dynamic risers. Chapter 4 investigates the effect of composite properties uncertainty due to water absorption on the reliability of composite risers. Chapter 5 includes the development of the micro-model based on bond-based peridynamics formulation, and the investigation of properties uncertainties due to voids and statistical variation of fibre diameter distribution. The model is used for RVE verification and analysis.

Chapter 2

Literature review

The literature review aims to investigate the effect of combined environmental and operational conditions on the composite riser integrity, given the uncertainties of the in-situ composite laminate mechanical properties. As shown in Table 2.1 the literature is scarce on this topic. A multi-scale approach is required, where a physical model at each spatial scale, while the mechanical properties uncertainties are considered at the material scale. The link between material properties and the structural scales are considered in the pipe model and global loads and structural response are considered at the riser scale. The review is divided into four main sections, uncertainties in composite properties 2.1, Structural modelling 2.2, Material modelling 2.3 and Multi-scale methods 2.4. The uncertainties in composite properties section 2.1 focuses on randomness in composites. The structural modelling section reviews modelling methods available in the literature to model the macro riser scale in subsection 2.2.1, and the meso pipe scale in subsection 2.2.2 to model composite pipe. The Material modelling section focuses on methods to model the micro laminate scale in subsection 2.3. The structural section is concerned with intact modelling techniques, while the multi-scale methods section 2.4 is concerned with surveying the literature for successful implementation of a multi-scale methods and framework to model material fracture and damage problem. Figure 2.1 provides a high-level summary of the approach to the research objectives and the reasoning behind the reviewed literature.

Table 2.1: Literature on modelling of composites

Riser	Composite pipe	Micro modelling	Composite imperfections effect on mechanical properties	Far-field effect and composite imperfections on global composite riser failure
[29],[30],[31], [40],[41],[42], [50],[51],[52], [61],[52],[62],	[32],[33],[34] [43],[44],[23] [44],[53],[54]	[32],[33],[34] [43],[44]	[35],[36],[37],[38],[39] [45],[46],[47],[48],[49] [55],[56],[57],[36],[58],[59],[60] [57],[63],[64], [65],[66],[39]	-

[67],[52],[68],
[69],[70],[71],
[72],[73],[74],
[75],[41],[76],
[77],[78]

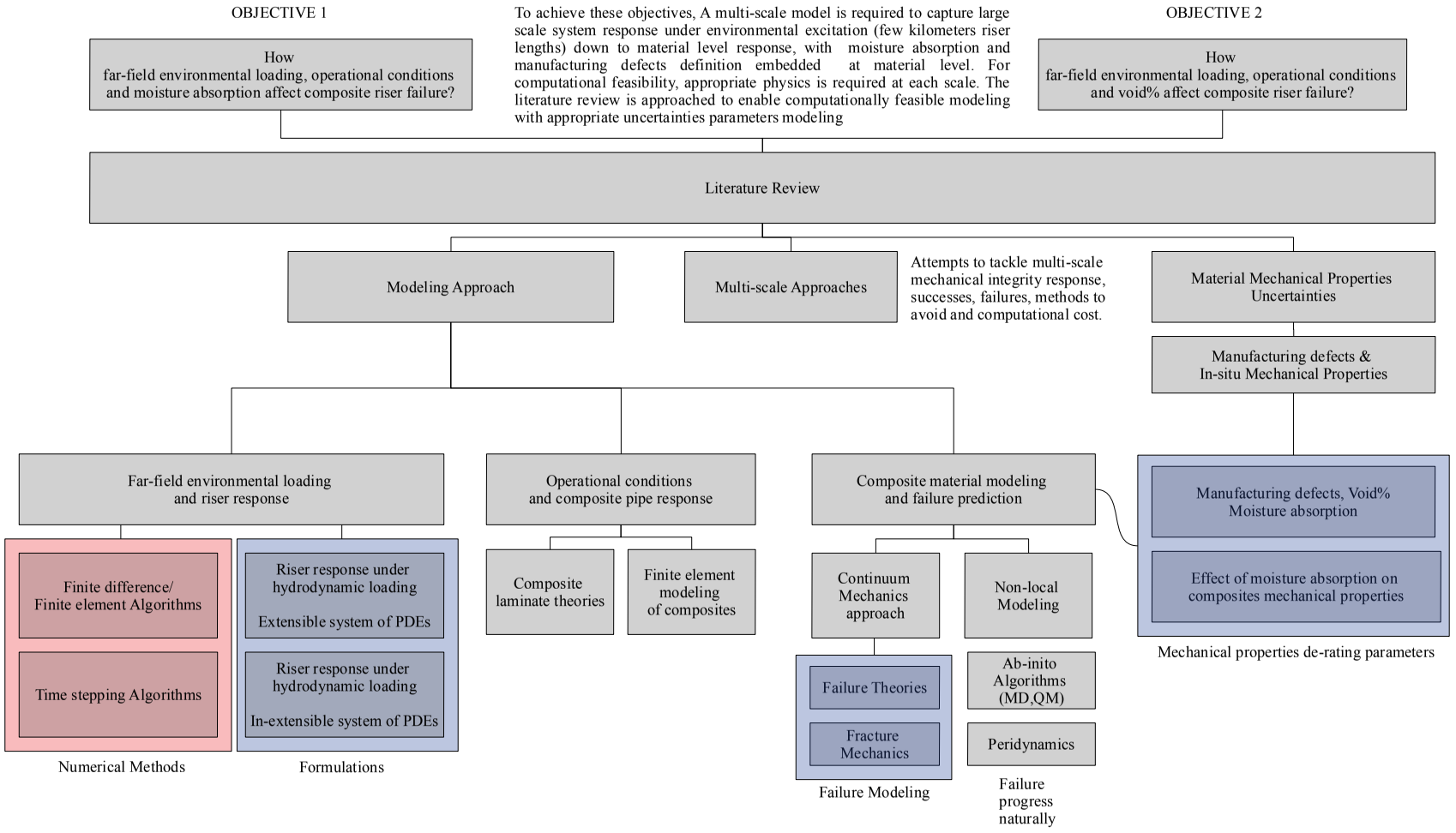

FIGURE 2.1: Literature review roadmap

2.1 Uncertainties in composite properties

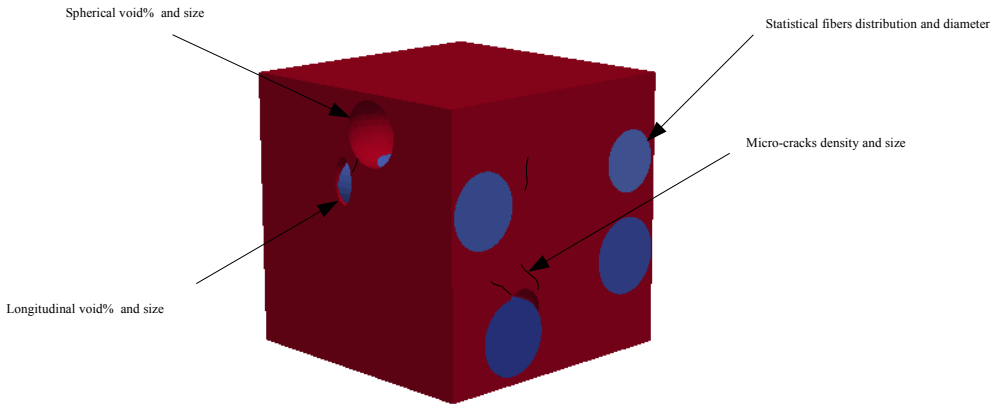

FIGURE 2.2: Uncertainties in Composites Mechanical Properties

2.1.1 Statistical variation in composites mechanical properties

A micro-mechanical model of a carbon-fibre composite laminate is central to investigate the effect of far-field loading and material micro-mechanical properties on the local composite failure. The stochastic nature of failure is evident in the literature that investigates their homogenised properties, deformation and damage processes. These probabilistic characteristics originates from multiple micro level sources of the composite material. Randomness inherited in one or more parameters due to the manufacturing and loading processes, as illustrated in figure 2.2, fibres distribution and its bonding strength to the matrix, micro-cracks density and void-defects are examples of these parameters [45, 46, 47]. The random distribution of these parameters affect the stress concentration and local deformations; leading to stochastic behaviour at the macro level. Although manufacturing processes aims to reduce irregularities in the material, however it is important to understand what type of irregularities affect the composite material response.

Any loading scenario on composite laminate directly results in complex interactions between the fibre, matrix, microcracks and voids. Therefore detailed micro model that is statistically representative of the material is highly desirable to understand the consequence to the structural damage and failure. An accurate micromechanical model depends on realistic representative volume element (RVE). To define the fibres distribution in the matrix multiple algorithms are developed in the literature such as nearest neighbour algorithm (NNA)[48]. Models that incorporate these irregularities is preferred over periodic micro-models. Periodic models are concluded in the literature to underestimate the onset of damage initiation and matrix cracks, moreover, don't correctly represent the microscopic stress state [49].

Voids are a common irregularity of composites, that is formed from coalesce of bubbles originated from entrapped air or volatile gases evolution during the curing process. Voids aspect ratio, which is the ratio between the width and length of the void is influenced by the void content. The

more entrapped bubbles, the higher the expected void content, which is directly proportional to the cure pressure. The void content and aspect ratio and fibre stacking sequence increases the probability that cracks emanates from voids, leading to a degraded mechanical properties. There is a direct correlation between crack initiating from voids and large void lengths, larger than $400\mu m$ and void content that exceeds 0.4% [55].

The fibres arrangement in the composite microstructure has a large effect on the composite failure properties for specific loading scenarios [48]. However, there is no correlation between void content, void aspect ratio and fibre break density. A skewed probability of fibre breakage is observed within proximity of voids, where its found that fibres are 5 times more likely to break within half a fibre diameter of an existing void [56].

Matrix cracking initiation and propagation is a phenomena that originates at micro level where micro-cracks coalescence occurs, forming a macro scale crack. Micro-cracks forms at micro level due to curing stresses and increases with thermal cycles [57, 36]. further micro-cracks forms once the laminate is exposed to the first load application [58]. The micro-cracks density increases due to thermal stresses, density of microcracks is reported to increase from 8.5 to 72 $crack/cm^3$, corresponding to temperature increase from 69 to 142 $\circ C$. Microcracks size is estimated to be of a similar size of carbon fibres between 5-10μm [59]. The orientation of these microcracks is an important factor in crack propagation at macro scale level. The coalescence of the micro cracks to form a long macro crack is expected to increase with higher microcracks density and lower level of microcrack randomness [60].

2.1.2 Moisture absorption effect on composites mechanical properties

The stochastic behaviour gets more complicated with diffusion of water in matrix, it increases the covariation coefficient of material fracture properties and causes internal stresses due laminate swelling. Diffusion of ocean waters is a slow process, compared to fresh water due to sodium chloride molecules. The variation in manufacturing properties and amount of voids and microcracks in the composite matrix directly influences the effect of water absorption on the composite mechanical properties and the long-term integrity of the structure while operational in the offshore environment. There is limited published evidence of stochastic analyses for composite risers, steel designs have been utilised for longer and methods are already available to investigate their reliability. Carrillo et al. [79] presents a methodology to analyse the structural reliability of the ultimate limit strength of a steel catenary riser (SCR) under conditions present in the Gulf of Mexico. The results indicate that the lowest probability of failure occurs at the contact point and submarine connection, with annual failure probabilities of 2.958 x 10-5 and 7.318 x 10-5, with the elements connected with the TLP and Catenary Transition areas experiencing failure rates of 1.731 x 10-14 and 1.133 x 10-11 respectively. Li and Low [80] performed a fatigue reliability analysis for steel risers utilising FORM on a response surface method generated from an Orcaflex model and outlines a number of other studies in this area demonstrating the importance of these studies. While reliability studies have been conducted on steel catenary risers, application of these to a large-scale composite riser still remains an important challenge, Pham et al. [19].Experiments confirms that composites' strength and fracture are affected by fluids penetrating composites along path of connected microcracks and delamination and eventually

leads to plasticisation and degradation of properties [57, 63], causing a reduction of glass temperature Tg. An increase in the initiation fracture toughness G_{IC} is reported while a reduction in the propagation G_{IC} [64]. The cyclic nature of the load is believed to trap the water and causes high pressure that deteriorate the composite mechanical properties [65]. Although, water absorption degrades the matrix dominated properties, however a sustained bending radius reduces the amount of absorbed water[66, 39]. Although, experimental sample edges are often exposed to sea-water which doesn't replicate manufactured sheathed risers, but still shows the effect of sea-water on the reliability of the in-situ composite structures is a concern. There is a clear gap in the literature to investigate the effect of manufacturing uncertainties and randomness combined with far-field loading on carbon/epoxy on composite pipes integrity in offshore environment. Therefore, to investigate the combined far-field loading multi-scale model is investigated where the most suitable global modelling method of the composite riser is chosen from the literature. To transfer the loads from the global scale to the micro model, the literature is reviewed to select suitable pipe scale modelling method that is able to capture the laminate stresses. The micro modelling methods in the literature are reviewed to chose a method able to capture stochastic elements of the composite laminate, with the ability to model cracks initiation and propagation.

2.2 Structural modelling

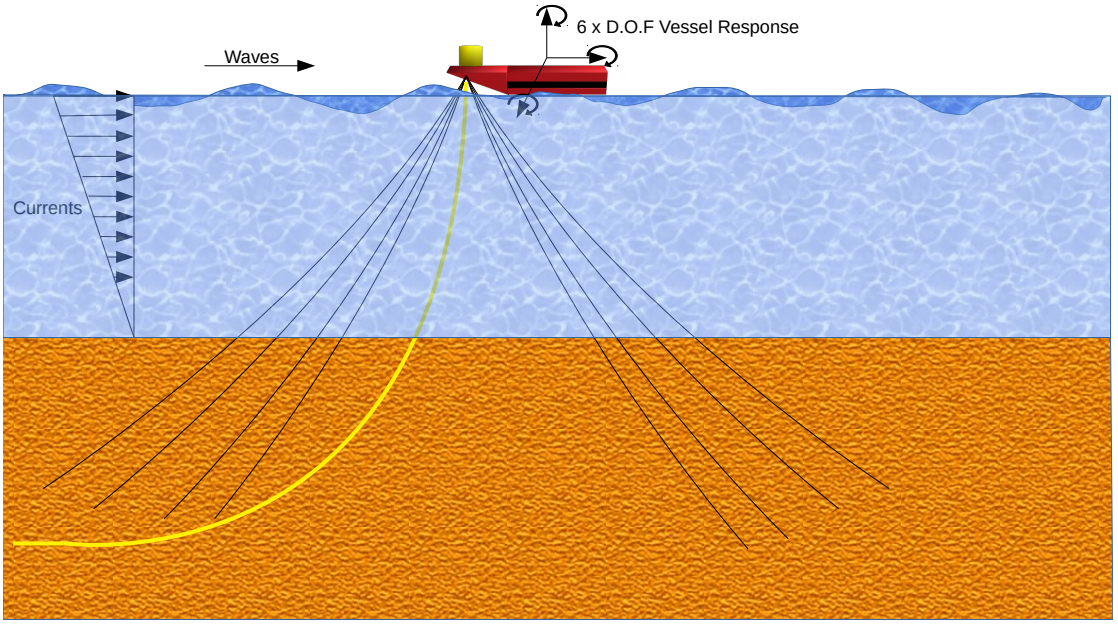

FIGURE 2.3: Typical composite catenary riser in deep-water environment

2.2.1 Macro model (Riser Global Response)

Production risers are vital subsea components for hydrocarbon production. However, the design process is complex as they are long, slender and exposed to dynamic multi-axial loading conditions. In addition, they are subjected to large temperature and pressure differentials through the thickness which are caused by the transfer of hot fluids between the surface platforms and

the subsea systems, as shown in figure **??**, sometimes in parts of the ocean where the ambient temperature is below $0°C$. Where temperature and pressure differentials leads to the seabed sections of a pipeline or SCR walking, which can lead to failure [81, 82, 83]. Steel is the most common material used in subsea applications. However, at large depths the technical challenges increase due to the large top-tensions, installation difficulties and long-term integrity issues related to corrosion. As the offshore industry expands their operations to greater depths, potentially beyond 4000 meters, these problems will only get worse. Gradually replacing steel with composite materials could reduce the operational and capital expenditure due to their higher specific strength to weight ratios, lack of corrosion and excellent vibrational damping properties [15, 16, 84]. However, these benefits do not come without challenges, for example, the lighter weight of the composite could lead to higher compression loads [85] that requires ballast weights or internal metallic liners and high initial costs that are dependent on the manufacturing and qualification processes. This is in part because of the lack of full-scale in-situ field data due to the short track record in the offshore environment, in addition to the complexity and lack of accuracy of the failure prediction tools [19]. A possible reduction in the qualification costs can be provided by sufficiently accurate and rapid numerical models developed to predict full-scale in-situ behaviour and failure during operation. However there is little published research on the suitability of the current riser numerical models to capture the composite riser's non-linear dynamic response at the global riser and pipe levels.

The analysis of riser systems has been conducted by various studies using a number of different techniques. DNV [12, 13] recommends a global-local procedure, where a global analysis is first conducted to extract effective tensions, bending moments, thermal loads and pressure loads, which act as boundary conditions for the subsequent local analysis. The local analysis then yields the local stresses and strains which are applied to a particular failure criteria to evaluate possible failure mechanisms of the riser elements. Tan et al. [8], Kang et al. [86] and Zhan [87] all conducted studies utilising static global catenary models to determine equilibrium positions, force extraction or the basis for a further dynamic study. Kang et al. [86] noted that the bending moments generated were larger than those calculated via other methodologies along with some discrepancy in the static position of the riser as compared to other models. However, Bridge [88] concludes that the use of the simple catenary equations is considered a good approximation. In a similar application Da Silva et al. [89] utilised this type of model to optimize a composite laminate structure for a riser system. An analytical catenary solver was used for the static global model due to the faster run times compared to FEA while also providing representative results.

Riser design is performed in two stages for computational efficiency. First the global response of the entire riser is modelled under the influence of environmental and vessel loads. The dynamic excitations are captured within the vessel's top excitation. This dynamic time domain analysis is required to identify the critical riser responses and sections for ultimate and fatigue limits states. The second step is to build a detailed model of the critical cross-section. This analysis is performed to predict the stresses and strains in the laminate to optimise the layup. Outputs from the global analysis, the tensions and rotations at both ends of the critical sections are applied as boundary conditions to the cross-section model.

The catenary equation is the simplest approach for modelling the global response of catenary shaped risers. However, the closed-form formulation limits its application. Solving dynamic riser simulations requires the solution of the full set of partial differential equations with time varying

boundary conditions and loads and can only be solved with a suitable numerical method such as finite elements or finite differencing. The riser's global dynamics can be formulated using two main approaches: extensible and in-extensible beams. Cables exhibit two main vibrating modes, 'elastic', where the axial waves propagate with a velocity proportional to the axial stiffness, and 'transverse', where they propagate as a function of the beam flexural stiffness. Flexible steel risers exhibit high axial stiffnesses due to their multi-layer cross-sectional design which are often five orders of magnitude higher than their flexural stiffness, due to their multi-layer cross-sectional design, while maintaining favourable low bending stiffnesses. Therefore, it is reasonable to approximate these flexible pipes response using an in-extensible beam model. Approaches that are specifically developed for flexible steel risers enforce these conditions to avoid the singularity that arises in the numerically ill-conditioned system matrix [52] and this is common in most design software. However, composite risers exhibit a lower axial stiffness that is likely to be only three orders of magnitude higher than the flexural stiffness. At these lower ratios the elastic waves could be excited and it may be necessary to model the composite riser as an extensible cable. The dynamic equilibrium system that governs the riser response consists of a number of non-linear coupled hyperbolic partial differential equations with boundary value constraints. The full-scale response of the riser can be adequately modelled using Bernoulli beam formulation as the length to thickness ratio is larger than the limit below which the Timoshenko-beam theory applies [90] .

To solve these partial differential equations the Lagrangian coordinate formulation makes up the largest portion of the open literature. Initially these models are solved with a numerical semi-implicit finite differencing scheme [68]. The method is conditionally stable if the time step is carefully calculated based on the arc length and the tension. However, this method is not practical for industrial applications as the stability parameters vary dynamically. Therefore, unconditionally stable time integration methods are favoured. To improve the accuracy and stability of the solution Galerkin's finite element formulation and first-order Adams-Moulton time integration algorithm is implemented [41]. However, the multi-step integration implemented in Adams-Moulton method is computationally expensive. A variational finite element approach and the Newton-Raphson algorithm improved the computational feasibility of this method [42]. A static finite element method is proposed, to improve the deformation dependency of the boundary conditions and load points. This includes a predictor-corrector multi-step scheme formulation based on non-linear vectorial equilibrium formulation is proposed however, the method is computationally expensive and its stability is not discussed in the literature [91].

The increase in flexible riser installations required new formulations to overcome the simulation difficulties attributed to the large axial stiffnesses. Therefore, a 2D Cartesian in-extensible hybrid beam-column formulation is proposed for un-bonded flexible risers implementing a convected coordinate scheme; where the hybrid beam formulation is used to solve the flexible riser ill-conditioned system stiffness matrix problem. In addition, a local coordinate system is fixed to each element, to decouple the rigid body motion and strains. This is connected to the global Cartesian coordinate system via rotation angles allowing for large deflections [62]. The hybrid-beam element formulation is used in which the axial deformation and in-extensibility conditions are satisfied. The method uses non-linear programming techniques to apply the Lagrangian constraint and imposes the in-extensibility condition allowing for large deformations with convected axes. This method is extended to a 3D analysis [67] and implemented in a

commercial riser three-dimensional non-linear finite element package Flexcom. The method uses Houbolt operator time integration which is shown to be suitable for the slow motion periods that flexible risers exhibit [52, 62]. Another time integration method is suggested, the Hilbert-Hughes-Taylor one step method which is unconditionally stable with linear systems and allows for variable time steps. The optimal time step is calculated automatically using the current step period parameter and after a few incremental steps the optimal value is chosen [92]. Recently a multi-scale element type for flexible risers is developed [93] which allows the stick/slip behaviour of flexible steel risers to be captured via a hybrid beam element user defined subroutine in Abaqus. However, this method mostly benefits un-bonded flexible riser analysis and doesn't provide additional information about the bonded cross-sections at the global riser scale since composite pipes are bonded and don't exhibit hysteresis like flexible risers.

The literature related to extensible formulations is sparse compared to the in-extensibility formulations. A non-linear cable formulation is successfully solved with the finite element technique and New-mark's time integration method [75]. However, this method causes large errors in predicting the cable natural frequencies [94] as the lumped mass technique is implemented [40]. A full 3D extensible cable is derived in [69, 70], which is solved with an implicit second order box finite difference method [71] resulting in an unconditionally stable method that is discretized and centred in space and time and second order accurate. However, the method is developed for negligible flexural stiffness cables and requires the inverse of the system matrix, which causes a singularity in slack conditions. The method is expanded to include cables with considerable flexural stiffness and solved with Newton-Raphson method [78, 95] and later solved with relaxation method [72, 73].

Although the literature is rich with multiple extensible and in-extensible dynamic analysis methods, it lacks a comparison between the two methods especially to quantify the effect of composite riser cross-section properties on the calculated tensions and curvatures.

2.2.2 Meso model (Pipe)

Composites laminates modelling is divided into four categories: smeared equivalent single layer theories (**ESL**), layer wise theories, Homogenisation and Microscopic models. Microscopic models are based on micro mechanics, where the fibres and matrix are modelled separately as homogeneous materials with a separate constitutive relation, such models allow micro failures such as fibre breakage, crack propagation in the matrix, fibre pull-out and de-lamination to be modelled explicitly. However, these models are computationally expensive and it is currently not feasible to model full composite structures using these methods. 3D elasticity and Layer wise formulations are based on use stacks of layers allowing for higher accuracy to describe the stresses across a relatively thick composite laminate. Layer wise where the accuracy is close to the 3D elasticity models and lower in computational cost. Equivalent single layer theories are simplified methods where the computational cost is lower than microscopic models.

Homogenisation method is useful for thick composites, where homogenised elastic constants are derived. Homogenised elastic constants provide added value to the predicted stresses and deformations with larger thickness and smaller radii, this is when the elastic constants become dependent on the stacking sequence. However with lower thickness or large diameter pipes, the

results obtained from the homogenisation method are identical to single layer theories [44]. 3D continuum elements are adopted in composite modelling, where the conventional elasticity theory is applied and the constitutive relation is not derived from shell theories. Layer-wise theories are developed for assessments where the through thickness deformation is important in the case of thick shells. The theory requires an explicit geometry of the shell thickness and enforce the first order shell assumptions via cross-thickness interpolation. The theory is based on assuming that the displacement field has C^0 continuity across the laminate thickness. This assumption allows for continuous inter-laminar stresses at the interfaces between plies. The Layer-wise model has computational advantage over 3D continuum models, it reduces the 3D problem to a stack of 2D equivalent single layers. The 3D finite element model is based on 3D elasticity theory and Navier's equations are the governing element shape function, while the layer-wise model, which is a 2D laminate theory is a semi-discretized Navier's equations, Thus the layer-wise theory approximates the 3D equations with the ability to adjust the discretized sections as needed. Reddy benchmarked number of operations needed to form the element stiffness matrix in both layer-wise and 3D models. The computational cost is lower in the case of the layer-wise theories [34].

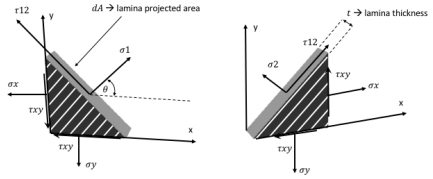

FIGURE 2.4: ESL laminate theory force balance

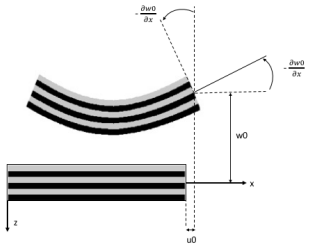

FIGURE 2.5: Illustration of CLPT theory

Equivalent single layer theories are developed based on classical elasticity theory, starting with force balance as shown in figure 2.4, with suitable polynomial that describes through thickness deformation. This assumption reduces the problem dimensionality to 2D representation of the laminate with an equivalent single layer. Classical laminated plate theory **CLPT** is the simplest equivalent single layer theory, based on the classical plate that satisfied *Kirchhoff* hypothesis. The shear across the laminate thickness is assumed to be constant [34, 32]. First order shear deformation theory **FSDT** is developed based on **CLPT** assumptions,as illustrated in figure 2.5, however allows additional degree of freedom, which is the linear transverse shear terms. The theory is based on the Reissner Mindlin model [33]. Third order shear deformation theory **TSDT** is a higher order theory that uses a cubic transverse shear across the thickness. The equivalent single layers are optimum to predict the global response of thin layer laminates. However to capture crack initiation and propagation in a laminate, the through thickness behaviour is important to be predicted with higher accuracy. The localised inter-laminar defects and cracks response is non-linear and therefore requires a higher fidelity theory [34]. The third order shear deformation theory is extended to provide a closed form solution [53] with pressure effects [54].

A pipe tends to behave like a thick shell if the ratio between its bending radius and thickness is small. However there is no clear separation in the literature between thin and thick shells for

cylindrical pipe applications. There are few attempts in the literature to evaluate the performance of each element type to model pipes that are exposed to bending and tension loadings. Shell and solid elements predict similar behaviour for metal pipes under uniform bending as long as the bending radius to thickness ratio is equal to 10 [96]. However solid continuum element becomes inaccurate and not feasible with ratios up to 25. The study is carried out with rigid beam multi-point constrain between a reference point and the pipe circumference. Composite pipes under tension, pressure and buckling loads using 3D solid element [97]. The study is performed constraining one displacement and applying pure tension on the other end for optimisation study. A homogenised solution compares the results to FE static solution, however boundary conditions used in the analysis are not addressed in the paper [44]. Composite pipes modelling is a gap in the literature, element based comparative study is required to provide confidence in the element types effect on predicting laminate stresses and composite riser behaviour.

2.3 Material modelling

2.3.1 Failure theories

There is no global consensus on a single representatives failure theory [25], the industry depends on *make and test* approach to assure composite structures and components reliability. However the need to quantify the accuracy of composite strength predictions motivated the *World Wide Failure Exercise* WWFE to assess complex performance of composite structures under general loading conditions , benchmarking more than 17 composite failure theories against experiments. The main conclusion is that 50% of current failure theories are mature to predict fibre failure, however the remaining theories miss-predicted the fibre failure. All theories were over conservative and poorly predicted leakage in pressurised pipes and did not account for non-linear stress/strain behaviour of composites. Progressive damage predictions are not mature enough to be implemented and further development is required. All theories fail to predict residual thermal stresses and in-situ lamina properties. The final conclusion vetted five leading failure theories,that are theoretically and experimentally the most reliable among other theories, which are chosen to develop comprehensive guidelines and recommendations, to develop a framework for composite design. These theories are; Tsai-wu that assumes linear elastic properties of the material and depends on reduced stiffness of the matrix after initial failure, Puck theory, that is based on three dimensional non-linear progressive failure approach. Cuntze theory, that is based on a similar approach to Puck theory but includes some dependency between failure modes based on probabilistic effects. Bogetti theory that is based on maximum strain failure criterion, progressive failure analysis and non-linear lamina stress-strain relation. It's important to note that Puck and Cuntze theories provide the closest predictions, with ten percent mean error, to experimental values [98]. The top five theories, can't predict leakage, high strains effect on stress-strain behaviour of the laminate. Therefore, deeper exploration of the initial failure and progressive damage, shear non-linearity and crack multiplication is required. Some of the failure theories numerical codes can not be easily obtained or integrated into FE packages. WWFE study recommends the following modelling problems to reduce the gap between test results and the composite failure predictions: Thermal Residual Stress, in-situ strength, matrix failure progression and large deformation behaviour. More improvement to the theoretical understanding

of: initial failure, progressive damage, crack multiplication, de-lamination. Therefore, relying only on these theories to optimize experimental work needed for qualifying new composite products or '*Virtual Testing*', is ruled out as an option. The definition of composite failure is currently application dependent, however experimental studies provide evidences that laminated composite failure is the result of progressive damage process ending up with a complete failure[99], that requires detailed micro modelling approaches, with special focus on theories that are based on the non-local properties of the material and fracture mechanics to predict laminate failure initiation and propagation.

2.3.2 Micro model (Laminate)

Finite element based micro models are based on continuum mechanics. A Representative volume element, RVE approximates microscopic heterogeneous material, such as carbon fibre composites. Multilevel FE^2 method relies on defining the constitutive relations at the element integration points with numerical homogenisation of suitable RVE at one or multiple levels [100, 101]. Although the method can be combined with the aid of cohesive elements to model fracture, however, this requires Ex-scale High Performance Computational simulations to capture fracture with FE^2 method. This computational intensity is demonstrated where over 390K cores which are required for realistic detailed simulations, allowing for virtual testing of materials [102]. Due to the high computational burden, few load cases are feasible. Therefore, it is not efficient enough to assess reliability or design load cases, that often require large numbers of load cases. A Voroni Cell FE based method is developed to solve elastic-plastic problems with heterogeneous materials under small deformation, however the method is not applied to fracture problems [103, 104], the method also requires high computational costs to micro FE sub-model, which is required for each integration point. It's essential with finite element micro models to combine continuum mechanics with damage mechanics, fracture mechanics and cohesive elements to capture fracture across the laminate. However, continuum mechanics approaches combined with cohesive elements or fracture mechanics are computationally expensive, and limited by defined crack paths. A core continuum mechanics assumption is material continuity and the continuum mechanics equations of motion are formulated in differential equation form. The derivative term, in these equations, is the source for a major and critical problem when a crack is formed in the material. The onset of crack formation, by definition is a discontinuity in the material, that causes a singularity at the crack-tip. That is because the strain energy grows exponentially at the crack-tip, which is concentrated into a single point. The classical formulation can't describe this complicated phenomena such as crack initiation and propagation, and requires a reformulation that depends on the stress intensity around the crack-tip area. That leads to the development of fracture mechanics, to fill in the gap within the continuum mechanics theory. Fracture and damage mechanics are able to predict few failure modes, however it's mathematically and numerically cumbersome. Implementing fracture mechanics in the finite element framework, requires adaptive meshing, which is computationally expensive. Therefore, the XFEM is developed to avoid the mesh refinement, however it involves higher computational cost compared to traditional FEM. Crack initiation is also an uncertain since it originates at the material atomic level, and multiple crack becomes computationally infeasible to model. Also crack path prediction is problematic and needs further research [43]

The shortcomings within continuum mechanics, makes non-local micro modelling lucrative to investigate, that is because the atomic bonds within the material are non-local. Each atom bonds neighbouring atoms that are within its vicinity, through intermolecular pair potential. Therefore, coarse-graining methods that resemble molecular dynamics, is expected to overcome the limitation of continuum mechanics in a computationally feasible manner. A double scale non-local asymptotic homogenisation is developed for brittle composite heterogeneous materials. The method is based on a closed form damage expression to relate overall strain, local fields to damage as an attempt to overcome the inherited difficulty to predict damage in continuum mechanics [105]. Peridynamics models are regarded as upscaling of molecular dynamics, the **MD** solution can be recovered from Peridynamics simulations [106]. Peridynamics was successfully used to model crack growth patterns in **CFRP** laminates with a pre-existing crack, naturally capturing de-lamination and fibre breakage [43]. A non-local *bond based* Peridynamics theory is formulated, based on a newton equation of motion, using a pair wise interaction between material points [107], however, the theory is restricted to Poisson's ratio of 1/4, due to an assumption that each two material points contributes to equal and opposite peridynamics force. The generalised *state-based* Peridynamics theory developed further to relax the bond-based assumption, allowing for material points to contribute with non-equal peridynamics force, however, maintaining the direction limitation that both material points peridynamics forces acts inline. This provides means to implement a conventional constitutive model of solid mechanics within a Peridynamics model, allowing for plastic incompressibility conditions [108]. A *non-ordinary state-based* Peridynamics formulation followed to relax the direction limitation, allowing for material points peridynamics forces to act in an arbitrary direction with non-equal magnitudes. This is useful for transient three-dimensional dynamic problem, allowing the theory to make more realistic predictions and large scale models that can be related to first Piola-Kirchhoff stress tensor, **P** [109]. It is possible to implement Peridynamics within finite element formulation, utilising lumped mass truss elements that represents bonds between Peridynamics material points [110]. Molecular dynamics can also be coupled to Peridynamics simulation allowing for variable material properties to account for thermal, in-situ, plasticity properties and other constitutive properties with a multi-scale model coupling **MD** *multi-scale micromorphic molecular dynamics* **MMMD** theory. Splitting the problem into two scales, Peridynamics is the macro scale and **MD** is the micro-scale, and linked via Cauchy-Born rule based stress evaluation turning it to a state-based Peridynamics formulation. The method allows the Peridynamics formulation to be enriched with molecular information. This method also supports the reversed approach where each traction is applied to the material, the optimum molecular state can be recovered based on Parinello-Rahman method allowing inhomogeneous and finite sized problem to be solved where the material represented by **RVE** [111]. The examples were limited to one and two dimensions, the **MD** caused wave propagation problems [112, 113].

Although, the prospect of initiating the Peridynamics material properties at the Ab-initio level is interesting with powerful supercomputing capabilities. However, one of the main problems with the Ab-initio molecular dynamics models is to select a suitable intermolecular empirical pair potential. In some non-standard cases, such as composite matrix, the empirical pair potential isn't easy to approximate. In such cases the empirical relation can be replaced with **DFT** or **TB** quantum calculations to describe molecular potentials that doesn't fit within standard potential theories [114, 115]. The Car-Parinello method is an example of concurrent multi-scale modelling

where the atomic potential is calculated *on the fly* via **DFT** calculations [116]. Although modern orbital-free DFT method and Tight-Binding TB theories simplifies the quantum mechanics equation to increase number of atoms that are possible to simulate, which is often used in material science [75, 117, 118, 119], the simulations requires large number of cores, and usually limited to few thousands of atoms for a time span of **fs** to **ns** and are suitable for modelling very few number of load cases [120, 121]. Therefore, using quantum mechanics based theories to approximate the intermolecular pair potential for molecular dynamics is not a feasible option. There are few attempts to develop accelerated **MD** techniques to stretch simulation scales limit. *Monte Carlo Molecular Dynamics* **MCMD** is a techniques used in statistical mechanics [120], the technique is used to capture thermodynamic properties such as equilibrium, energy, temperature and pressure based on the statistical distribution of the property. Further development in the area of **MC** simulation is promising to expand the limitation of **MD** simulations such as meta-dynamics, hyper-dynamics, umbrella sampling allowing to extend the molecular dynamics simulated time scale by more than two order of magnitudes[122, 123, 114].These methods aims at rare events probability to speed up the simulation process, however at the current state of such theories are not mature.

Although coupling quantum mechanics with molecular dynamics and Peridynamics provides an accurate representation of the inter atomic potential, the allowed spatial and temporal scales are still computationally expensive. Scales of such simulation usually don't exceed nano meters/second, these are not sufficient to model material related failures such as crack propagation, on large spatial or temporal scales for industrial applications, and it is more suited, for the time being, to investigate microscopic material properties or investigating new type of materials behaviour. In addition to the wave propagation problem that originates at the molecular dynamics and Quantum mechanics scales is problematic for large scale simulations on structural level. Therefore, the use of these Ab-initio methods to approximate the Peridynamics bonds is ruled out and the bond-based peridynamics theory, with fracture properties derived from experimental data, is the most suitable method for scope of this thesis.

2.4 Multi-scale methods

Engineers often face two main categories of problems, the first category where macro-scale behaviour is the main focus, then its assumed that the micro behaviour can be substituted by a predefined and simplified constitutive relation. The second category where the main focus of the problem is micro-scale, in this case its often assumed that a micromodel is sufficient to describe the problem. Most engineering problems could be solved using the single scale approach [124]. The selection of a multi-scale method is divided into three general steps. **Step 1** is to define what is the most efficient way to exchange information between scales. This is mainly dependent on the number of missing parameters that requires variables from a micro scale model solution. **Step 2** is to define which kind of problem is the focus of our study. Do we want a micro model across the whole domain or around a localised singularity or defect. **Step 3** It's important to select a multi-scale frame work to handle calculations and information exchange between scales. That is classified according to information flow between scales. Either to pre-calculate the missing parameters prior to performing the macro model analysis (sequential) or calculate it on the fly (concurrent).

There are many attempts available in the literature to develop a multi-scale approach to assess structural integrity, therefore, it is important to review these trials and understand the difficulties, advantages and disadvantages, challenges and computational cost of all these methods, in order to select an appropriate methods that bridge the gap between physics that occurs at large structural scale and slow temporal responses, down to microscopic size phenomena that occurs at the speed of sound, which is fracture. *Sequential multi-scale coupling*, also known as *hierarchical, serial, parameter passing,pre-computing,microscopically-informed modelling* is used for limited problem types, where small number of missing parameters in the macro scale model that depends on few microscopic variables. Pre-computing of these parameters based on a micro scale model is feasible in this case. The micro scale computed parameters, which are often stored as lookup tables, are passed to the macro scale to complete the model. If any missing data were not pre-computed, then linear interpolation is required to obtain the values between the pre-calculated parameters. An example of sequential coupling is a well known composite mechanics problem where a *representative volume element* **RVE** is chosen to statistically represent a heterogeneous material such as carbon fibre composite. The elasticity tensor is calculated using **RVE** method with suitable averaging technique, and used in the macro model to describe stress and strain relation in the material. Any problem that requires many parameters to be evaluated that depends on larger number of variables is deemed not feasible with sequential coupling. As a rule of thumb if the number of missing parameters in the macro model are lower than the problem dimensions the sequential method is feasible.[125] *Concurrent multi-scale coupling* is often referred to as *on the fly* computation. It is used when the number of missing parameters is high and function of multiple variables. Often multi-scale modelling concept is related to this type of coupling where the information is exchanged on the fly between scales. An example of sequential coupling is *Car-Parrinello molecular dynamics method* **CPMD**. This type of simulation is not feasible using a sequential approach. It's not simple to exchange information *on the fly* between scales, often boundary conditions is problematic and requires the researcher to be careful in selecting boundary conditions [126]. In summary the number of calculations required for the concurrent coupling method are $\mathcal{O}(\Delta x^{-d})$ where Δx is the mesh size and d is the problem dimensions required to calculate the missing data. For the sequential coupling the number of calculations are roughly $\mathcal{O}(h^{-m})$ where **h** is the uniform grid size and **m** is the number of variables needed to calculate the missing parameter.

A modern approach to classify multi-scale methods is according to the problem types. Type A of problems deals with localised events such as singularities, dislocations, local defects, boundary layer problems, and shocks. The assumption that the macro scale model can describe the most of the domain, however fails to do so around the local defects and a micro model is used to only around this region. Few modelling techniques are examples of problem A: **Macroscopic, Atomistic, AB Initio Dynamics MAAD**, in which coupling of finite element model to statistical molecular dynamics and down to quantum mechanics through semi-empirical tight binding approach. The algorithm is applied to model rapid silicon slab brittle fracture, with a micro-crack defect, where uniaxial tension is applied to the slab [6, 127]. **Non-local Quasi-continuum Methods** are limited to cracks, dislocations and local defects in crystalline structures. The continuum scale is based on non-linear elasticity finite element. The method makes use of the adaptive mesh refinement algorithm at the local defects, reducing the size of the mesh to the atomic scale where a molecular dynamics simulation is modelled around the defect. The method suffers from phonon's reflections at the boundaries between the *MD* and FE regions, this is

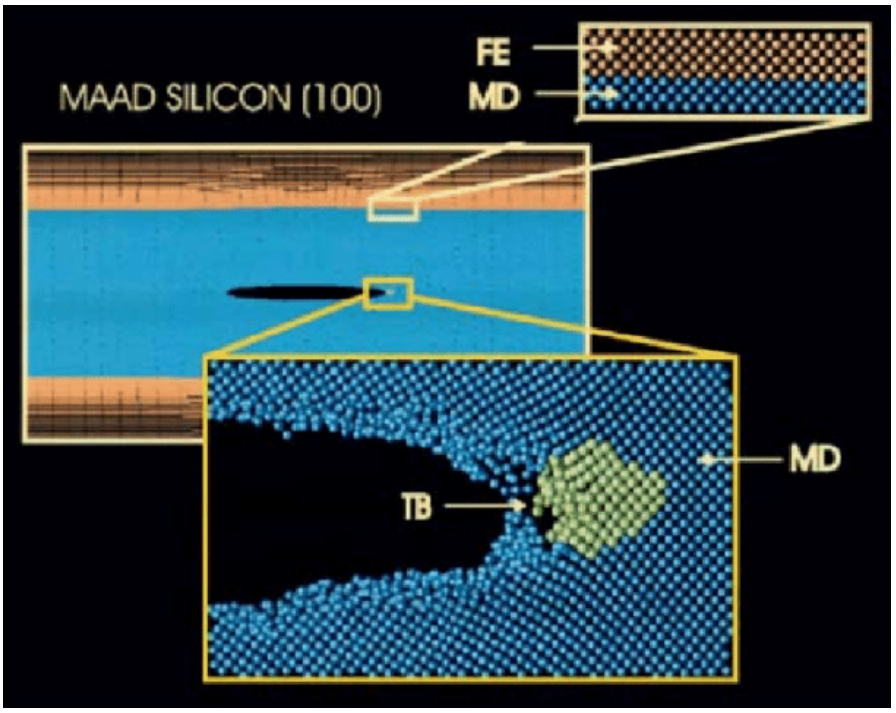

FIGURE 2.6: Illustration of the MAAD multi-scale method [6]

mainly due to the periodic nature of the molecular dynamics boundary conditions. This problem can cause some simulation to over heat and melt the crystal which doesn't happen in reality [128, 129, 130, 131, 132, 133, 134, 135, 124, 136, 137]. **Coarse-Grained Molecular Dynamics CGMD**, which is a method similar to peridynamics but smaller in scale down to molecular level. The method was initially developed to simulate micron scale systems providing a seamless coupling between the atomic micro and macro scales with the ability to simulate finite temperatures. The method is based on formulating constitutive equation at each scale that is compatible with micro atomic scale at local region. Statistical coarse grained region facilitates the coupling to the FE domain away from the localised defect [138].

Problem B is where the micro model constitutive properties is not known across the whole domain, either to enrich the macro model or to replace some missing parameters. A typical plasticity problem where the atomic locations are used to define the stress strain behaviour of the material[139], utilising the **Multilevel FE^2 Method** [100, 101]. **Local Quasi-continuum Method** The local quasi-continuum theory formulates the material constitutive relation based on Cauchy-born rule and molecular dynamics simulation, however the method is limited to crystalline structures [128, 129, 130, 131]. **Gap-Tooth scheme-Equation-free method** An example of this scheme is the *Equation-free method*. The method is a general form of the concept used in the local QC method, where the model is initiated with macroscopic prediction, and micro model is solved for few domain patches as short carefully chosen burst of appropriately initiated micro models, where the solution is averaged in these domains and by interpolation ,the macro solution is calculated, the domain patches communicates with each other while the solution progresses to maintain macroscopic connections and boundary conditions[140]. Mathematical homogenisation and averaging methods are used where effective properties of the model is the main focus. A periodic represented volume is selected and the properties of the composite structure is averaged over the domain [141, 142, 143]. The multi-grid method [144, 145], fast

multipole method **FMM** [146, 147], domain decomposition method, adaptive mesh refinement method [124]. Multi-resolution representation method [148], has been successfully applied to composite materials. However, these all based on local continuum mechanics, and requires fracture mechanics to model cracks, making it computationally expensive.

2.5 Conclusion

The literature review in this section excluded some of the advanced methods, such as Molecular Dynamics and Tight Binding methods due to it's computational feasibility required for the scope of this thesis. Table 2.2 narrows down few of the computationally feasible methods that are required to establish a multi-scale model of the composite riser system to achieve the research objectives in section 1.5.

TABLE 2.2: Computationally Feasible Theories and Methods Summary

Method	Type	Application	Feature
		Macro riser model	
Small angle Bernoulli beam	Finite element	Beams with small deflection	Computationally efficient but not suitable for large deflections that riser experience
Large angle Bernoulli beam	Finite element	Flexible risers and cables	Suitable for riser problem,computationally expensive
Lagrangian formulation	Finite difference	Flexible risers and cables	Simpler implementation, computationally less expensive than FE
		Meso pipe model	
CLPT	Equivalent single layer	Thin Composite laminate	Constant transverse shear
FSDT	Equivalent single layer	Moderate thickness Composite laminate	Linear transverse shear, shear locking
TSDT	Equivalent single layer	Thin/Thick Composite laminate	Quadratic transverse shear
LWT	Layerwise theory	Thin/Thick Composite laminate	Moderate and Thick laminates

3D Conintuum	Theory of elasticity	Composite laminate modelling	Computationally expensive without additional benefit at pipe level
		Micro laminate model	
VCCT	Fracture Mechanics	De-lamination	Computationally expensive, can simulate crack path, multiple cracks of pre-cracked model
Gradual Degradation Method	Damage Mechanics	Laminate macro failure	Computationally feasible, can predict Final failure with good accuracy
Cohesive Elements	Fracture/Damage Mechanics	De-lamination	Requires a predefined crack path
Peridynamics	Non-local theory	Intact/Damage	Realistic prediction of crack initiation, propagation, Computationally expensive

Chapter 3

Effects of extensible modelling on composite riser mechanical responses

3.1 Mathematical formulation

RiSim, a non-linear extensible, time-domain implicit Keller-box finite difference code is developed in FORTRAN based on the formulation derived in [71, 78]. The non-linear system of equations is solved with a modified Powell hybrid method. The method is suitable for calculating the local minima of complex functions without the need to calculate its derivatives [149]. RiSim is used to investigate the composite riser response and compared to a finite element in-extensible hybrid formulation implemented in the riser simulation package, Flexcom, which is based on the method developed in[92, 62, 67] to determine the accuracy of these models with the reduced axial stiffness exhibited by composite risers.

Riser design is performed in two stages for computational efficiency reasons. First the response of the entire riser is modelled under the influence of environmental and vessel loads. The effect of the maximum mean and low frequency vessel responses are modelled as a static step with an offset to the initial position of the vessel, while the high frequency dynamic excitations are captured within the vessel's RAOs. This dynamic time domain analysis is required to identify the critical riser responses and sections for ultimate and fatigue limits states. The second step is to build a detailed model of the critical cross-section. This analysis is performed to predict the stresses and strains in the laminate to optimise the layup. Outputs from the global analysis, the tensions and rotations at both ends of the critical sections are applied as boundary conditions to the cross-section model.

In this analysis the inline linear waves and sinusoidal hang-off excitation are applied to the riser system. The riser motion is assumed to occur in a 2D plan for simplicity. The governing dynamic equilibrium system is presented as a series of partial differential equations in 3.1 to 3.6. The derivation is based on the extensible non-linear Lagrangian partial differential equations

representing the 2D riser boundary-value problem. Variables u and v are the velocities in the tangential and transversal directions $\hat{\mathbf{t}}$ and $\hat{\mathbf{n}}$, T is the tension, S_n is the shear force in the transverse direction and G_b is the curvature about the bi-normal direction $\hat{\mathbf{n}}$. Φ is the angle between the tangent and the horizontal. m and ma are the mass in air and the added mass per meter, w_0 is the apparent weight of the riser per meter. d_o is the outer diameter of the riser. EA and EI are the axial and bending stiffnesses. s is the Lagrangian, un-stretched coordinate, v_{tr} and v_{nr} are the tangential and transversal relative velocities, C_{dt} and C_{dn} are the tangential and transversal drag coefficients, t is the time and ρ is the sea water density, v_{tc} ,v_{nc}, v_{tw} and v_{nw} are the current and wave tangential and transversal particle velocities.

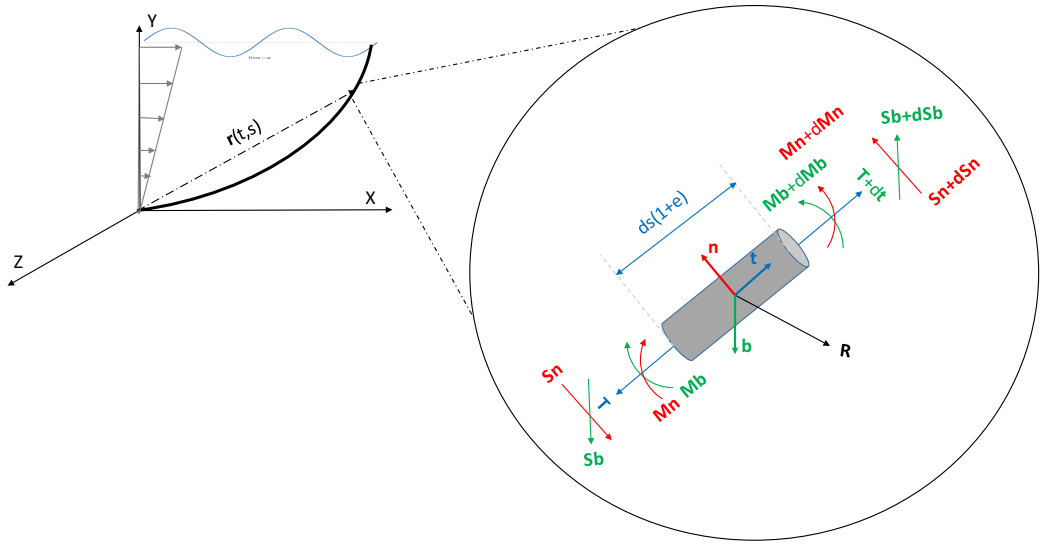

FIGURE 3.1: Riser element loads equilibrium diagram

The relationship between the rate of change of the velocities frame angle Φ with respect to time at each node as a function of tension variation and the total force balance along the riser in the tangential $\hat{\mathbf{t}}$ direction described in equation 3.1,

$$\begin{aligned} & m\left(\frac{\partial u}{\partial t} - v\frac{\partial \Phi}{\partial t}\right) - \frac{\partial T}{\partial s} + S_n\Omega_b + w_0 sin\Phi \\ & + \frac{1}{2}\pi\rho d_o C_{dt} v_{tr}|v_{tr}|\sqrt{1+(\frac{T}{EA})} = 0. \end{aligned} \tag{3.1}$$

and in transversal direction $\hat{\mathbf{n}}$ in 3.2,

$$\begin{aligned} & m(\frac{\partial v}{\partial t} + u\frac{\Phi}{\partial t}) + m_a\frac{\partial v_{nr}}{\partial t} - \frac{\partial S_n}{\partial s} - \Omega_b T + w_0 cos\Phi \\ & + \frac{1}{2}\rho d_o C_{dn} v_{nr}|v_{nr}|\sqrt{1+(\frac{T}{EA})} = 0. \end{aligned} \tag{3.2}$$

The governing relationship between the temporal rate of change of the tension, as a function of axial stiffness, nodal velocities and curvatures, is described in equation 3.3,

$$\frac{\partial T}{\partial t} - EA(\frac{\partial u}{\partial s} - \Omega_b v) = 0, \tag{3.3}$$

and the reference frame angle is shown in equation 3.4,

$$(1 + (\frac{T}{EA}))\frac{\partial \Phi}{\partial t} - \frac{\partial v}{\partial s} - u\Omega_b = 0, \tag{3.4}$$

The coupled relationship between the axial and bending strains are provided in equation 3.5,

$$EI\frac{\partial \Omega_b}{\partial s} + S_n(1 + (\frac{T}{EA}))^3 = 0, \tag{3.5}$$

While the definition for the curvature as a function of the reference frame angle along the riser is provided in equation 3.6,

$$\frac{\partial \Phi}{\partial s} - \Omega_b = 0, \tag{3.6}$$

The tangential and transverse relative velocities, when the wave and current are applied, are given by equations 3.7 and 3.8,

$$v_{tr} = u - v_{tc} - v_{tw}, \tag{3.7}$$

$$v_{nr} = v - v_{nc} - v_{nw}. \tag{3.8}$$

3.2 Boundary conditions

The 2D riser behaviour is governed by six, first order partial differential equations. The finite difference discretisation leads to $n-1$ equations and the missing 6 equations to solve the system are given by the equal number of boundary conditions given by equations 3.9- 3.11.

At the touch-down point the boundary conditions are given by equation 3.9,

$$G_b{}^0 = 0, u^0 = 0, v^0 = 0, \tag{3.9}$$

and the boundary conditions in the case of wave loading and pinned hang-off node are defined in equation 3.10,

$$G_b{}^{N-1} = 0, u^{N-1} = 0, v^{N-1} = 0. \tag{3.10}$$

Assuming a sinusoidal excitation at the hang-off node, the boundary conditions are given by equation 3.11,

$$G_b{}^{N-1} = 0, u^{N-1} = 0, v^{N-1} = A\sin(\omega t). \tag{3.11}$$

Where A is the amplitude of the sinusoidal excitation.

3.3 The Keller-box method

The Keller-box numerical scheme is an implicit method, designed to solve first order parabolic partial differential equations in time and space [150]. The solution is second order accurate and simple to implement for large numbers of coupled PDEs. The method requires all the PDEs to be reformulated in first order form before discretisation.

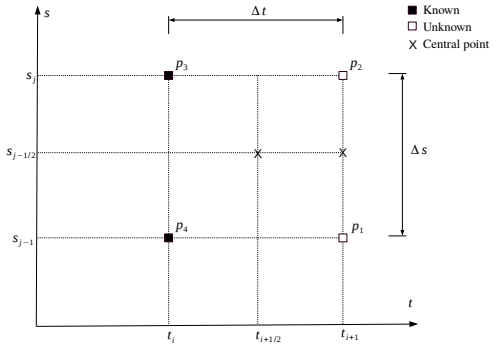

FIGURE 3.2: Keller-box method finite difference grid

The algorithm requires discretisation in space and time that is chosen at the central point $\left(t_{i+1/2}, s_{j-1/2}\right)$, where i and j represent the current time and spatial node. The discretization is performed between the points P_1, P_2, P_3 and P_4 as shown in figure 3.2. These points represents the function evaluation at either the previous time, the next time or spatial step. Let Y be the unknown variable and then the central differencing of the temporal derivative at the centre point is determined by fixing the spatial coordinate while the temporal derivative is replaced by equation 3.12,

$$\begin{aligned}\frac{\partial Y}{\partial t} =& \frac{Y^{i+1}_{j-1/2} - Y^{i}_{j-1/2}}{\Delta t_i} + \mathcal{O}(h^2) \\ =& \frac{Y^{i+1}_{j} + Y^{i+1}_{j-1} - Y^{i}_{j} - Y^{i}_{j-1}}{\Delta t_i} + \mathcal{O}(h^2).\end{aligned} \tag{3.12}$$

Similarly, the spatial derivative is replaced by equation 3.13,

$$\begin{aligned}\frac{\partial Y}{\partial s} =& \frac{Y_j^{i+1/2} - Y_{j-1}^{i+1/2}}{\Delta s_i} + \mathcal{O}(h^2) \\ =& \frac{Y_j^{i+1} + Y_j^i - Y_{j-1}^{i+1} - Y_{j-1}^i}{\Delta s_i} + \mathcal{O}(h^2).\end{aligned} \tag{3.13}$$

By neglecting the higher order terms and expanding equations 3.12- 3.13 the central point is given by the expressions in equation 3.14,

$$t_{i+1/2} = \frac{1}{2}\left(t_{i+1} + t_i\right), s_{j-1/2} = \frac{1}{2}\left(s_j + s_{j-1}\right). \tag{3.14}$$

3.4 Riser model benchmarking

The static and dynamic responses of the riser are benchmarked using the in-house developed algorithm RiSim and FE commercial package Flexcom. An 11 inch composite catenary riser is investigated with a comparison of when it is unpressurised and with a 200 bar internal pressure. The riser properties and environmental data are listed in table 3.1, including the maximum wave height, H_{max}, and corresponding peak wave period, T_p. A wave train that originates at a location above the global axes origin, on the seabed, that is located at the mid-water line propagates in the positive horizontal axes direction.The seabed is intentionally not modelled in this study to isolate the effects of extensibility on the riser response. The structural damping depends on the type of structure and the material; this is made more complex when considering composite materials as they exhibit variable damping properties which are dependent on the natural frequency of each vibration mode. Damping tests are required to quantify these variable damping values, as assuming variable damping can be misleading. Therefore, riser analysis is performed without structural damping as a base case [151, 152].

TABLE 3.1: Properties for the benchmarked riser

Parameter	Value
Water depth (d) $[m]$	400.00
Total riser length (S) $[m]$	487.43
Bending stiffness (EI) $[Nm^2]$	49.52E+06
Axial stiffness (EA) $[N]$	37.23E+09
Mass in air empty (m) $[kg/m]$	163.85
Internal fluid density (ρ_f)$[kg/m^3]$	1025.0
Tangential drag coefficient (C_{Dt})	0.05
Normal drag coefficient (C_{Dn})	1.2
Outer diameter (d_o) $[m]$	0.324
Internal diameter (d_i) $[m]$	0.28
Maximum wave height (H_{max}) $[m]$	18.6
Wave period (T_p) $[s]$	14.9
Hang-off horizontal coordinate (X_{HO}) $[m]$	224.7
Hang-off vertical coordinate (Y_{HO}) $[m]$	400.00
Internal Pressure (P_i)[bar]	0/200
Sinusoidal Excitation Amplitude (A) $[m/s]$	5

3.4.1 Static comparison of extensible and in-extensible methods

A comparison between the tensions and bending moments predicted by the extensible and in-extensible formulations are shown in figure 3.3 for the tension and figure 3.4 for the resultant bending moment. A visual check of the figures 3.3- 3.4 infers that both methods predict tension and bending moments that are indistinguishable from each other. That is because the static tension and bending moments demonstrate a negligible percentage differences of less than 0.02% for the maximum static tension, while the maximum bending moment demonstrates a 0.09% difference which shows that both methods are predicting similar static solution.

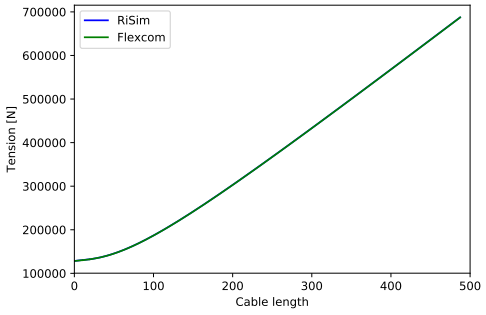

FIGURE 3.3: Effective tension along riser length

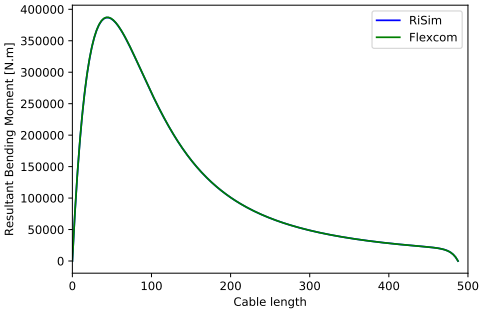

FIGURE 3.4: Resultant bending moment along riser length

3.4.2 Dynamic comparison of extensible and in-extensible methods

3.4.2.1 Comparison in regular waves

Dynamic riser analysis is performed by applying regular waves to the riser system. This test is used to verify the regular wave algorithm used in RiSim before applying the top-side excitation. The wave data is chosen based on the extreme conditions from a 100 year return period that typically occur at the west of the Shetlands. A good match is reported between the two methods as documented in table 3.2 for an extreme wave height and table 3.3 for a moderate wave height. When applying an extreme wave that has 34.5 meters wave height and a 17.5 seconds wave period, the maximum percentage difference between the two methods along the length of the risers is at the minimum tension with a value of 0.65%, as shown in table 3.2. However, the maximum percentage difference reduces to 0.06% when a moderate wave is applied with a 18.6 meter wave height and 14.9 seconds wave period, table 3.3. Showing that when an extreme wave condition with a 100-year return period is applied, the differences between the two models are negligible with less than 1% maximum error. This gives confidence in the regular wave algorithm implemented in the RiSim code.

TABLE 3.2: 100 year extreme wave conditions-pinned model

	Hmax=34.5m Tp=17.5s		
Parameter	Flexcom	RiSim	D%
Max Tension $[kN]$	709.25	709.83	0.08%
Min Tension $[kN]$	671.92	667.52	-0.65%
Max Curvature $\left[m^{-1}\right]$	0.0086	0.0086	0.0%

TABLE 3.3: 100 year moderate wave conditions-pinned model

	Hmax=18.6 Tp=14.9		
Parameter	Flexcom	RiSim	D%
Max Tension $[kN]$	694.37	694.84	0.07%
Min Tension $[kN]$	680.4	679.99	-0.06%
Max Curvature $\left[m^{-1}\right]$	0.0084	0.0084	0.0%

Despite the similarity in results, the FE in-extensible solution experiences some numerical instabilities during the first wave period and a number of smaller numerical instabilities are exhibited. However, while the extensible finite difference solution converges immediately to the final response and doesn't experience high frequency spurious numerical oscillations. Looking beyond the first wave period, the comparison between the two methods is shown in figure 3.5 which shows the time-trace of the hang-off node tension performed in both Flexcom and RiSim with 3 meter element lengths. Figure 3.5 shows that elastic waves are excited in addition to the transverse waves, and these are only captured by the extensible riser formulation. For typical composite risers, which are likely to have axial and flexural stiffnesses separated by only three orders of magnitude, elastic waves can be excited and the behaviour can be captured using the extensible formulation implemented in RiSim.

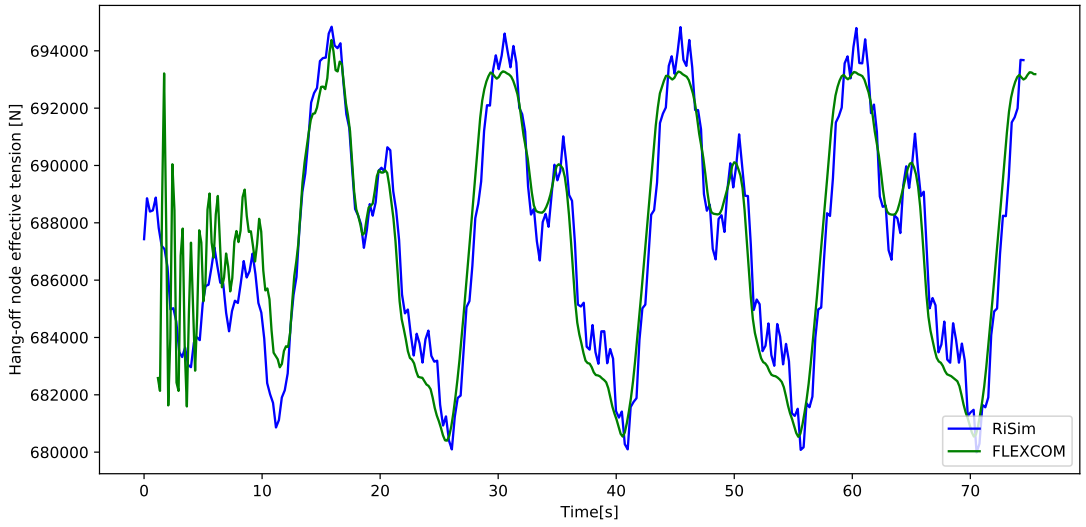

FIGURE 3.5: Hang-off effective tension

3.4.2.2 Regular waves with top-side excitation

Two types of sinusoidal excitations are applied to replicate a general range of top-side excitations in the surge direction: an excitation with angular frequency that is in phase with the wave train and another 180 degrees out of phase. The excitation is applied to the hang-off node of a 200 bar pressurised and unpressurised riser in the transverse direction in addition to the regular waves. Using equation 3.11 a sinusoidal velocity is applied in the normal direction $\vec{n}$ to the hang-off node. The corresponding Cartesian time traces of the horizontal and vertical coordinates are extracted and applied to the FEA in-extensible model as a displacement boundary condition applied to the hang-off node.

Both methodologies match well for the in-phase wave with the top-side excitations using the hang-off tension time-trace. A maximum difference of less than 0.5% is observed after the inextensible method has stabilised beyond the first wave period. The results from the 180 degree phase shift also exhibits a close behaviour with a maximum 1% percentage difference after the FE solution converges to the steady state solution after three wave periods, this is shown in figure 3.6. Although the variation between both methods is within the maximum documented percentage difference between dynamic analysis methods in the literature [153], figure 3.6 illustrates this difference for the pressurised riser. It is observed, for both the pressurised and unpressurised cases, that the RiSim Finite Differencing algorithm converges immediately to the final steady state system response while the finite element solution experiences higher order oscillations that are sensitive to the solutions convergence tolerance.

The in-extensible method experiences 3 times the number of cycles for the tension ranges up to $20kN$ compared to the extensible formulation, figure 3.7. The number of cycles reduces to 2 times larger if the first 3 wave periods are ignored from the in-extensible analysis. This implies that often the first 3 wave periods should be avoided when using in-extensible methods and a longer simulation period is required for reliable results. It is not likely that the high order oscillations have a large effect on the total fatigue life of the riser, however either human or automated filtering process is required to avoid these numerical instabilities. This problem is not experienced with the extensible formulation.

The hybrid element formulation is a probable cause for such instabilities. It is implemented in the in-extensible software where the in-extensibility condition is enforced artificially, in which the axial strain is decoupled and interpolated separately. This type of mixed field variable formulation is reported to cause spurious numerical errors if the interpolation function used with the axial force is not the same

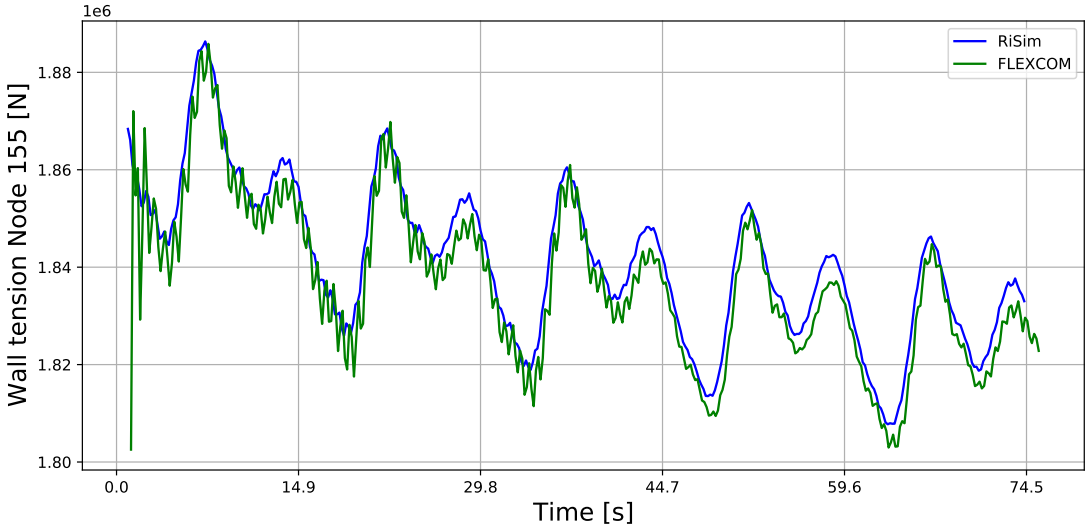

FIGURE 3.6: Hotspot wall tension time-trace

order as the strain, ϵ. This can cause a second kind errors in the solution even for arbitrarily small meshes [62]. The extensible method solved with Keller-box scheme finite difference is demonstrated to be stable and converges in fewer time steps to the final system steady state response while remaining consistent to the results from the in-extensible model.

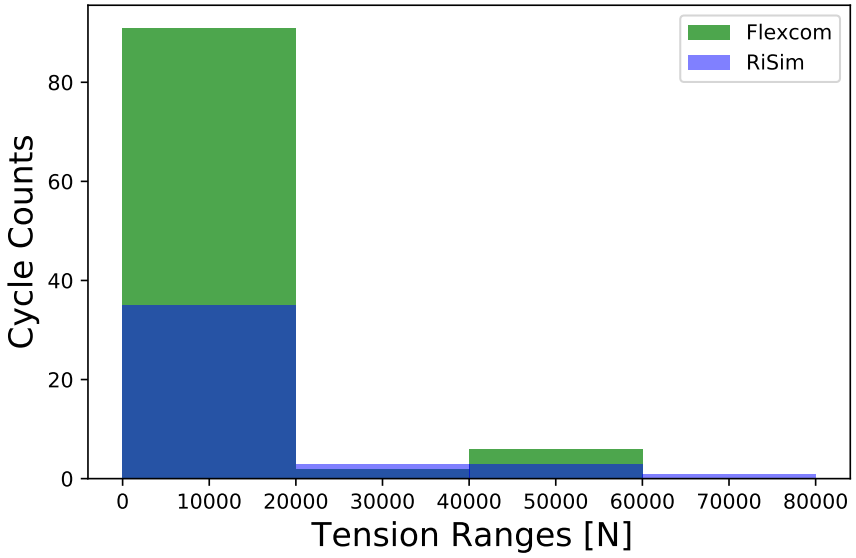

FIGURE 3.7: Tension range Vs Cycle count

To investigate the phenomena further, the tension time-traces high frequency cycles are counted using the rain-flow method applied to the extensible and in-extensible results. It is found that for the riser system analysed the ratio of the observed high frequency oscillations average amplitude to the top tension high frequency cycle amplitude is close to 1.5%, therefore cycle counting is performed at 1.5% of the top tension range. The oscillations are calculated using rain-flow counting algorithm to investigate this phenomena.

To assess the effect of the riser cross-section design on the top tension high frequency cycles. A non-dimensional parameter λ is introduced, defined in equation 3.15. The parameter is suitable for

investigating the relationship between the in-extensible formulation and the high frequency oscillations that are observed, since it is used to investigate the cross-over phenomena of the cable elastic and transverse natural frequencies [154]. Four riser cross-sections are assessed, where the internal diameter of the riser is kept constant while increasing the outer diameter. The corresponding cross-sectional properties are estimated as shown in table 3.4 and used in the analysis. The analysis performed in section 3.4.2.2 is repeated with four cross-sections and the results are is shown in figure 3.8.

TABLE 3.4: Riser Load Cases

Parameters	LC1	LC2	LC3	LC4
Internal diameter $[m]$	0.28	0.28	0.28	0.28
Outer diameter $[m]$	0.35	0.42	0.49	0.55
Thickness $[m]$	0.03	0.07	0.10	0.14
Bending Stiffness (EI) $[Nm^2]$	3.87e+07	9.27e+07	1.78e+08	3.06e+08
Axial Stiffness (EA) $[N]$	3.12e+09	5.90e+09	9.07e+09	1.27e+10
Mass in air $[kg/m]$	116.70	216.22	329.79	460.02
λ [-]	16.33π	18.46π	20.19π	17.19π

Figure 3.8 demonstrates the relationship between the parameter λ, varied as multiples of π, in comparison to the number of cycles from the rain-flow counting of the high frequency tension cycles with amplitude 1.5% of the average tension. A curve is fitted to the data points to demonstrate the trend. It is found that both extensible and in-extensible formulations follow a closely related trend with respect to λ, however the effect of the high order oscillations observed in the in-extensible commercial code is demonstrated in figure 3.8 where the average number of cycles is between 2 to 8 times higher than predicted by the extensible code.

The low amplitude, high frequency, spurious oscillations are only observed in the in-extensible tension time-traces and don't appear in the curvature time-trace. This suggests that the behaviour is related to the interpolation function implemented in the hybrid element formulation and so the extensible formulation is favoured for composite cross-sections,

$$\lambda = \sqrt{\frac{(w_0 S)^2 E A_0}{T_{horz}^3} \cos \Phi_a}. \tag{3.15}$$

A further investigation of the phenomena strengthen the deduction about the in-extensibility as the cause of these spurious oscillations observed in Flexcom. Figure 3.9 shows a positive trend, where a direct increase of the number of oscillations is observed with the increase in the axial stiffness.

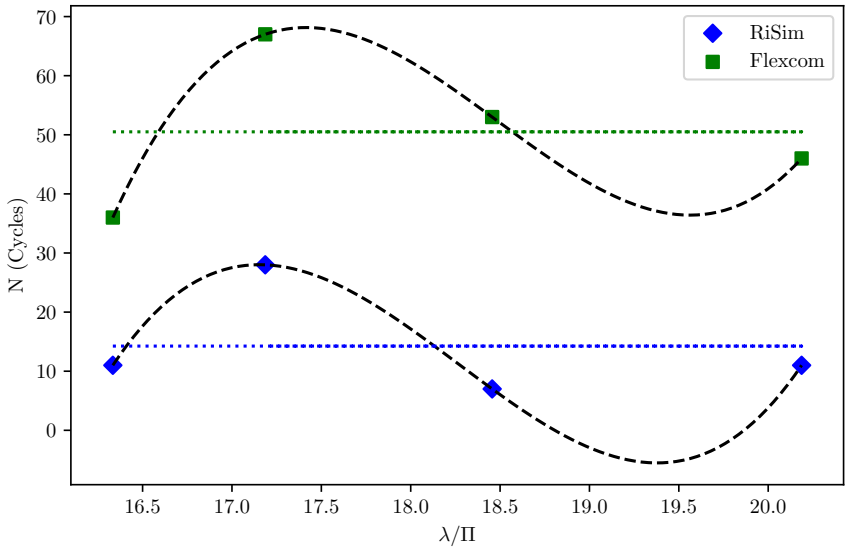

FIGURE 3.8: Number of Cycles N at ΔT=1.5% static tension at hot-spot

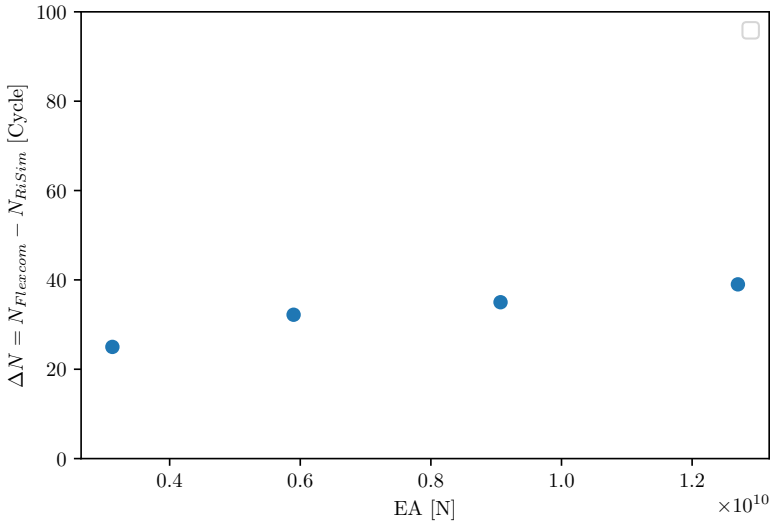

FIGURE 3.9: Increase in number of oscillations predicted by Flexcom Vs RiSim as a function of axial stiffness

3.5 Composite pipe numerical model

Global riser analysis is required to estimate the critical section of the riser, the 'hot-spot'. The tension and curvatures time-traces are then imposed as boundary conditions to the composite pipe model. However, there is a gap in the composite pipe modelling literature for offshore applications where it is not clear what elements can be used to accurately model the laminate stresses. Therefore further studies are required to provide higher confidence levels in the modelling methods.

Various element types are developed to model composites: equivalent single layer shells, layer-wise continuum shell and 3D continuum solid elements [34]. The suitability of these element depends on the pipe thickness to bending radius ratio. A pipe tends to behave like a thick shell if the ratio between its

bending radius and thickness is lower than a specific threshold. However, there is no clear separation in the literature between thin and thick shells for cylindrical pipe applications. Metallic pipes under uniform bending are considered thick and modelled with brick elements as long as the bending radius to thickness ratio is below a factor of 10, while solid continuum elements become inaccurate with larger ratios i.e ratios beyond 25 [96]. 3D solid elements are used for the laminate layup and thickness optimisation by constraining one displacement and applying pure tension on the other end, however the study is limited to laminates under tension load [97]. Homogenisation is used to reduce the computational burden, especially for thick composites, where homogenised elastic constants are derived based on an asymptomatic expansion. The homogenised elastic constants is beneficial when it depends on the stacking sequence, that is often the case with larger thicknesses and small radii. The results obtained from homogenisation methods of thin composites are often identical to single layer theories [44].

To assess the suitability and computational efficiency of shell, continuum shell and solid elements for composite riser modelling, the loads that are predicted by the global model are imposed as boundary conditions to a composite pipe model which is built in ABAQUS finite element packages. A comparison is made between the following elements: quadratic composite shell *S8R*, continuum composite shell *SC8R*, linear solid composite *C3D8R* and quadratic solid composite *C3D20R*. The results are compared to the homogenization and FE methods that are reported in [44].

3.5.1 FEA model definition

A 22-layer carbon/epoxy composite riser is chosen based on the geometry tabulated in [44]. The composite riser consists of (from inner to outer layers), a titanium internal liner, composite layers with a layup $[0/90/45/-45]_5$ and a polymer outer sheath. The cross-section design and stacking sequence are illustrated in figure 3.10. The pipe bonded cross-section dimensions and lay-up are listed in table 3.5, where contact is not explicitly considered. The titanium liner, composite plies and outer sheath material properties used in the study are in table 3.6.

Table 3.5: Composite riser cross-sectional data

Parameters	Value
Internal diameter $[m]$	0.28
Outer diameter $[m]$	0.31432
Pipe length $[m]$	10.0
Liner thickness $[m]$	0.005
Outer sheath thickness $[m]$	0.002
Composite layers thickness $[m]$	0.01016

Where E_1 and E_2 are the Young's moduli along the fibre and in the transverse direction respectively; ν_{12}, ν_{23}, ν_{13} are the Poisson's ratios; G_{12} and G_{13} are the in-plane shear moduli and G_{23} is the transverse shear modulus. For failure prediction: X_T and X_C are the longitudinal tensile and compressive strengths; Y_T and Y_C are the transverse tensile and compressive strengths and S is the in-plane shear strength.

The boundary conditions and reference points are illustrated in figure 3.11. Both ends of the pipe are constrained using *multi-point constraint* to reference points that lie on the pipe neutral axis. The reference points are designated RP1 and RP2 and are located in the plane perpendicular to the pipe ends. The boundary conditions and reference points are illustrated in figure 3.11. Reference points RP1 and RP2 are allowed to rotate freely but RP1 is constrained in the translational X, Y and Z directions. RP2 is free to move in the longitudinal Z direction. Boundary conditions and loads are applied to the reference points and transferred via the multi-point constraint to the circumference, to assure even distribution of loads. The boundary conditions and reference points are illustrated in figure 3.11.

TABLE 3.6: Composite riser material properties

Liner (Titanium)	Composite ply	Outer sheath (Polymer)
$E = 120.0$	$E_1 = 135.0$	E=3.0
$\nu = 0.33$	$E_2 = 8.0$	$\nu = 0.40$
	$E_3 = 8.0$	
	$G_{23} = 2.7$	
	$G_{13} = 3.8$	
	$G_{12} = 3.8$	
	$\nu_{23} = 0.49$	
	$\nu_{13} = 0.27$	
	$\nu_{12} = 0.27$	
	$X_T = 2.45$	
	$X_C = 1.57$	
	$Y_T = 0.07$	
	$Y_C = 0.133$	
	$S = 0.098$	

[1] All moduli are in GPa

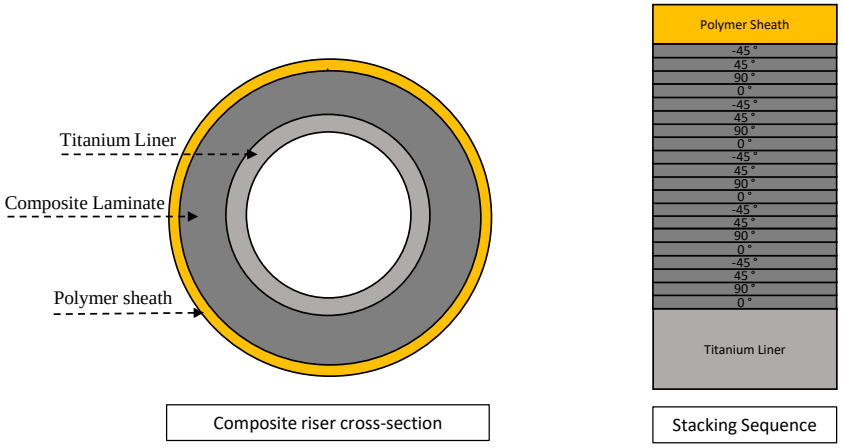

FIGURE 3.10: Composite riser cross-section design and stacking sequence

3.6 Composite pipe benchmarking

The benchmarking cases are chosen to assess the suitability and computational efficiency of shell, continuum shell and solid elements for composite riser modelling. Stress distributions across the laminate thickness are investigated, under axial and bending moment loading conditions. Four models are developed and the results are compared to the homogenization and FE methods that are reported in [44]. Figures 3.12- 3.13 shows the longitudinal and hoop stresses σ_z resulting from axial force of 1kN and bending moment load of 1kN.m. The model results obtained from the static FE analysis are found to match the stresses obtained by the homogenization method in [44]. All the elements are reported to predict the stress distribution for the tension and bending cases within a 5% difference. It's found that layers with fibre angles of 90° and ±45° experience higher hoop stresses, compared to the Titanium liner, outer polymer sheath and 0° fibre plies. Maximum axial stresses appear in the Titanium liner and 0° composite plies as shown in figure 3.12 and 3.13.

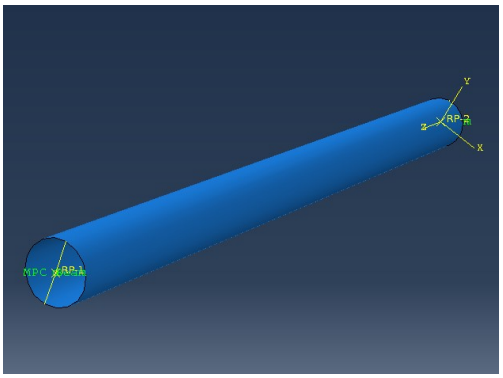

FIGURE 3.11: Pipe model MPC constrain

TABLE 3.7: FEA element type comparison

Element type	nodes	elements	D.O.F	CPU time[s]
C3D20R	168240	24000	506172	705.27
C3D8R	48098	24000	144876	260.37
SC8R	48098	24000	144876	43.95
S8R	66090	22000	396540	83.85
S4R	22046	22000	132276	27.51

A 10 meter pipe with the properties shown in tables 3.5 and 3.6 is loaded with a combined 1kN axial force and a 1kN.m moment at both reference points RP1 and RP2. The solid quadratic brick element *C3D20R* is taken as a reference in this study to quantify the relative percentage difference of each element type. Table 3.7 provides the total number of nodes, elements, degrees of freedom and CPU time required for this analysis.

Figures 3.12- 3.13 show the maximum percentage differences in stress of 4%, which are exhibited by the linear and quadratic shell *S4R* and *S8R* elements. Lower percentage differences are observed for the *SC8R* continuum shells and the linear *C3D8R* brick element which shows the lowest difference. However, the *SC8R* predicts hoop stresses closer to the quadratic solid *C3D20R* than the *C3D8R* brick element. In general the *SC8R* elements provide an acceptable prediction accuracy compared to it's computational cost which is demonstrated in table 3.7. Therefore, the continuum shell element *SC8R* is recommended to model composite risers as it provides the optimum computational cost to accuracy followed by *S8R* element.

3.7 Riser-pipe coupled dynamic analysis

The coupled responses between the global and local responses are compared when using the extensible and in-extensible formulations. First the dynamic global analysis results that are described in section 3.4.2.2 are used to identify the hot-spot. Then, a finite element model of the pipe is built for this critical

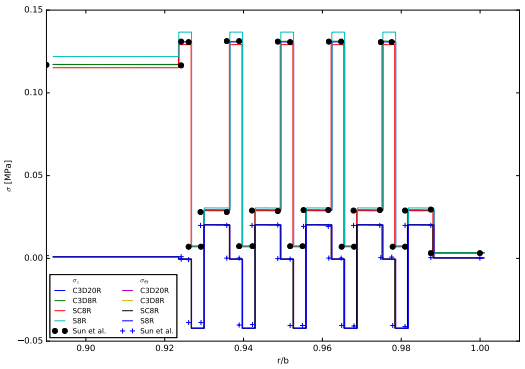

FIGURE 3.12: Stress distributions under axial force

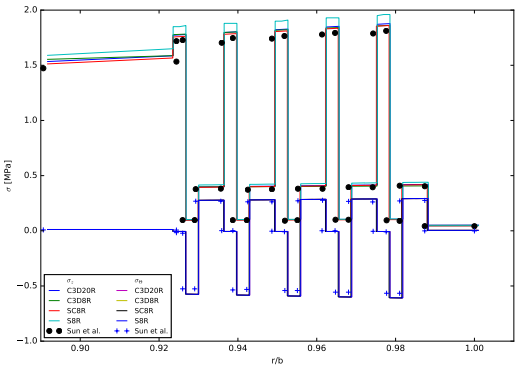

FIGURE 3.13: Stress distributions under bending moment

section to investigate the effect of the global loading time-traces predicted by the global models on the composite laminate stresses. The extensible and in-extensible models are used to predict the global riser behaviour, where a top-side sinusoidal motion is applied in the surge direction and the environmental loads are modelled using linear waves according to the methodology described in section 3.4.2.2, in addition to the parameters in table 3.1. The rotations and tension time-traces are extracted from the global models and used as boundary conditions for the finite element continuum shell, composite pipe model. The finite element implicit time domain analysis is performed using the continuum shell elements, *SC8R*. The simulation is five wave periods long with a total time for the simulation of 74.5 seconds. The hot-spot is identified based on the highest tension and curvature standard deviations. Tensions and curvatures time-traces are the output of the riser analysis, which are applied to the composite pipe model.

A failure criteria is required, in order to quantify the effect of the global methods on the failure of the composite riser at the pipe level. The Tsai-Wu failure criterion is selected, which is a commonly used criterion to predict the first-ply failure and it is recommended as one of the more robust failure theories by the World Wide Failure Exercise. The first-ply is predicted to fail if the left-hand side of equation 3.16 is equal to, or higher than, unity. Where the terms σ_1, σ_2 and τ_{12} are the fibre longitudinal stress, the stress in the normal to fibre direction and shear stress in the ply; X_t and Y_t are the longitudinal and transverse tensile strengths; while X_c and Y_c are the compressive strengths and; S_{12} is the in-plane shear strength. F_1 is a failure coefficient that is given by equation 3.17. Composite risers are designed with large safety factors and therefore failure is not expected with the riser properties used in this study. However, the criteria is used here to quantify the effect of both the extensible and in-extensible global models on the Tsai-Wu failure index at the hot-spot location.

$$\left(\frac{\sigma_1}{X_t X_C}\right)^2+\left(\frac{\sigma_2}{Y_t Y_C}\right)^2+\left(\frac{1}{X_T}-\frac{1}{X_C}\right)\sigma_1+\left(\frac{1}{Y_T}-\frac{1}{Y_C}\right)\sigma_2+\left(\frac{2F_1 2\sigma_1\sigma_2}{\sqrt{X_T X_C Y_T Y_C}}\right)+\left(\frac{\tau_{12}}{S_{12}}\right)^2=1 \quad (3.16)$$

$$F1=\frac{1}{X_t}-\frac{1}{X_c} \quad (3.17)$$

The boundary conditions are described in section 3.2. The tension time-traces are extracted from the riser beam model simulation and applied to node RP2 as a point force via the amplitude module in ABAQUS while the rotation angle time-traces are applied to both RP1 and RP2 reference points as boundary conditions.

3.7.1 Dynamic results

The results shows that the maximum Tsai-Wu failure index is found to be 15% higher for the inextensible formulation in comparison with the extensible simulation, for the unpressurised riser. However, when the pressure in the riser increases to 200 bar then the percentage difference between RiSim and Flexcom decreases to 2.3% as shown in table 3.8. Although the percentage difference is attributed to higher oscillations observed with the in-extensible formulation as explained in section 3.4.2.2. The Tsai-Wu failure indices are therefore similar and the formulations don't have a large effect on the composite failure index in strength conditions. The percentage difference is noticed to decrease with higher internal pressure as shown in table 3.8. Based on the presented results a reliability analysis or dynamic fatigue simulation is expected to predict marginally higher probabilities of failure if the in-extensible method is used compared to the extensible model. However, these differences are currently captured within the recommended high safety factors that are used in the composite riser design. The finite element analysis running time is 6.8 minutes to simulate 74.5 seconds of real time on an *Intel(R) Core(TM) i7-6700 CPU @ 3.40GHz* with 31 GB RAM computer.

Table 3.8: Tsai-Wu failure index

Global model	Tsai-Wu failure index	
	Unpressurised	Pressurised
RiSim	0.014	0.101
Flexcom	0.016	0.103

RiSim is developed based on an extensible formulation and compared to an in-extensible FE riser commercial package Flexcom. Both methods predict similar maximum tensions and curvatures with less than 1% difference. However, for the environmental loading conditions listed in table 3.3 and sinusoidal top-side excitation following equation 3.11, the riser tension predicted by the in-extensible formulation experiences spurious high frequency oscillations, although these reduce after the first three wave periods. The source of such oscillations is expected to originate from the in-extensibility condition applied to risers that exhibit lower axial stiffness than flexible steel risers, therefore user care is required during the post-processing stage. The extensible solution doesn't suffer from spurious oscillations and requires minimal user intervention, and is therefore more suitable for efficient automation and digital-twinning applications, especially those involving supervised learning where these oscillations could affect the machine learning. Composite elements are compared where continuum shell, SC8R, and quadratic shell, S8R, elements are found to be the most suitable to model composite pipe cross-sections. The cross-sectional stresses predicted by the pipe FE model coupled with the in-extensible formulation predicts a Tsai-Wu failure index that is marginally higher than predicted with the extensible formulation. These higher stresses do not have a large effect on the strength response of the composite pipe.

Chapter 4

Far-field loading and in-situ conditions effect on composite riser integrity

4.1 Requirement for composite risers

To help address the gap in the literature on the composite riser integrity under the influence of far-field loading combined with variation of material properties and properties variation due to water absorption this section performs an analysis of composite risers to determine failure at maximum loads and compares the trends in behaviour to those of steel catenary risers. A static global catenary analysis is performed with the addition of Classical Laminate Theory which is shown to be accurate to FEA within 10% and its performance is empirically adjusted to further reduce this error. A strength-based assessment is selected to provide an initial understanding of risers at larger depths and it is also rare for fatigue failures to occur in composite materials where first-ply failure is a common mode of analysis. In addition, this analysis is extended to investigate the effect of moisture absorption on the composite properties between wet and dry conditions as all current riser analysis addresses only the intact condition. The effect of moisture absorption on the composite extreme failure based on the Tsai-Wu failure criterion is incorporated.

4.2 Monte-Carlo simulation of a riser

Tensions and moments are predicted by the the global catenary analysis and used as an input to the Classical Laminate Theory (CLT) algorithm to conduct a local analysis of critical sections of the riser and to extract the stresses and strains acting on a segment of the riser. The resulting stresses from the Classical Laminate Theory were then assessed by the Tsai-Wu criterion to determine possible failure. The local model is utilised as the basis for the reliability analysis with the addition of the von Mises failure criterion when metallic risers are considered. To perform the reliability analysis a Monte Carlo simulation was employed, shown in figure 4.1, to analyse variations in mechanical and manufacturing properties of laminate materials, as well as environmental loads, following a similar procedure to Sobey et al. [155]. The Monte Carlo simulation generates a large number of random values for the stochastic variables (Xi), which are then inserted into the limit state function G(X) to determine if the structure

will fail. The method allows for the calculation of the probability of failure over the entire domain of load inputs. In addition to its simplicity and accuracy, the Monte Carlo simulation is also robust in its applicability to various situations. However, in cases of small probabilities of failure, the required number of simulations increases significantly, resulting in additional computational time.

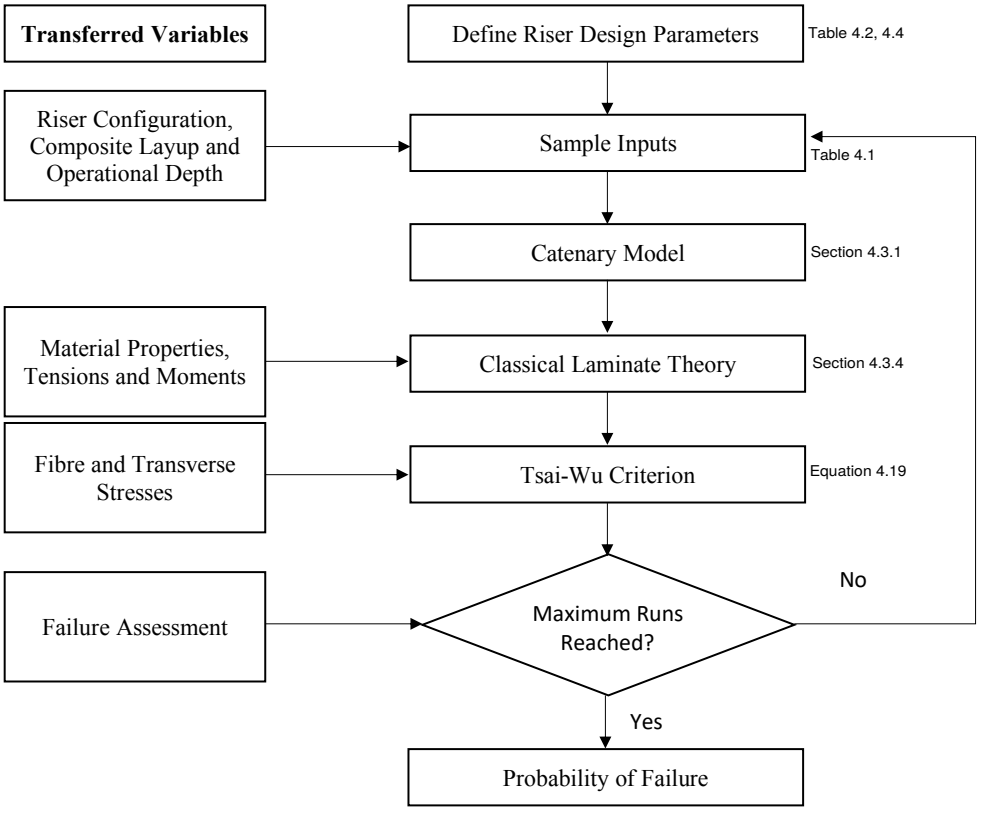

FIGURE 4.1: Monte Carlo simulation methodology

The material properties for the riser are based on Carbon/Epoxy T700/X4201 manufactured by Torayca in Japan with statistical distributions taken from Philippidis et al. [156]. Properties for steel are taken from Xia et al.[157], which alongside the mechanical properties, are given in table 4.1 , where Xt and Xc are the carbon fibre tensile strength in tension and compression in the fibre direction; similarly Yt and Yc are the strengths in the transverse direction; S is the shear strength; Ex and Ey are the elasticity modulus in the fibre and transverse directions; G is the shear modulus and ν is the Poisson's ratio. It is expected that composite material parameters exhibit co-variation between these properties, however, the available in the literature doesn't account for this co-variation, and therefore, it is assumed that the material properties are statistically independent.

Two different types of risers, from Tan et al. [8] and from Wei [7], are assessed with the topology and layup for each riser given in table 4.2 and illustrated in figure 4.2. The steel riser was developed to have the same thickness as the larger composite riser found in Wei [7] with a corresponding unit mass of 115 kg/m. The risers were subjected to a horizontal tension of 1.3×10^5 N and were assumed to have an internal fluid density of $700 kg/m^3$. The riser designs are selected to determine trends in behaviour, not as direct comparisons between each other.

TABLE 4.1: Statistical variations and material properties for carbon/epoxy and steel.

	Composite		Steel		Distribution
	Mean Wei z [7]	CoV Philippidis et al. [156]	Mean Xia et al. [157]	CoV Xia et al. [157]	
Xt (MPa)	2450	5%	N/A	N/A	Normal
Xc (MPa)	1570	16%	N/A	N/A	Normal
Yt (MPa)	70	18%	N/A	N/A	Normal
Yc (MPa)	133	16%	N/A	N/A	Normal
S (MPa)	98	11%	N/A	N/A	Normal
Yield Strength (MPa)	N/A	N/A	550	6%	Normal
Ex (MPa)	125	10%	197.5	2%	Normal
Ey (MPa)	9.588	16%	197.5	2%	Normal
G (MPa)	5.4	20%	78	3%	Normal
ν (MPa)	0.35	11%	0.3	1%	Normal

TABLE 4.2: Layup structure and Global properties of each composite pipe under study

Pipe structure	Steel	Tan et al. [8]	Wei [7]
Number of Laminae	N/A	20-ply	56-ply
Layup	N/A	[45/-45/15/80]s	[90/15/-15/90/45/-45/45/-45/45/-45]5 +[45/-45]3
Number of Laminae	18.3	5	7
Number of Laminae	0.1834	0.2796	0.1836
Number of Laminae	0.22	0.31667	0.22
Number of Laminae	N/A	0.675	0.075
Number of Laminae	N/A	13.5	11.2
Number of Laminae	91	57	46
Number of Laminae	11.9	27.5	8.83
Number of Laminae	2319.19	2500.96	1756.65

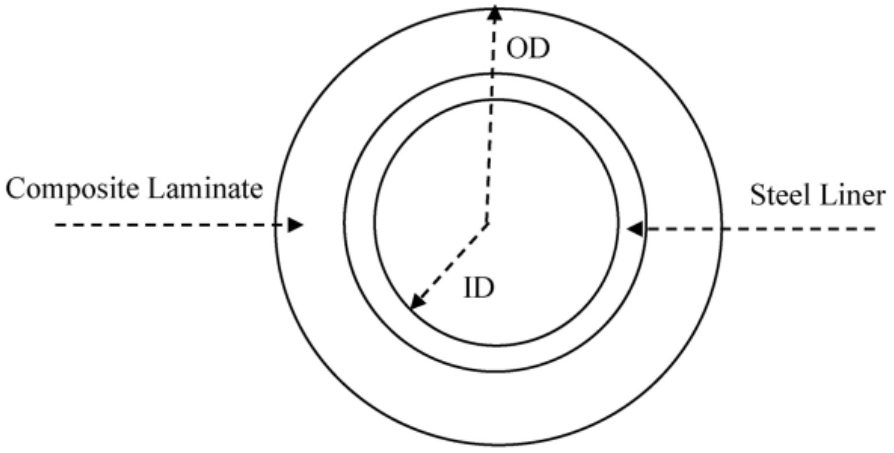

FIGURE 4.2: Composite riser cross-section design

4.3 Global response model

The static catenary model is modelled using an analytical approach based on the work of Faltinsen [158], describing the behaviour of catenary mooring lines and is chosen for computational efficiency.

4.3.1 Catenary model

The global model used to determine the static equilibrium position of the riser was derived from the steel catenary riser models employed in a number of other analyses including Duan et al. [159], Bridge [88] and Kang et al. [86]. The catenary model allows a simple representation of the risers including the specification of the geometry of the system as well as the extraction of axial tensions. While bending stiffness is inherently neglected in this approach, bending moments can be extracted by including material

properties and curvature at each point. The governing mathematical equations for the catenary shape assume neglected bending stiffness, in-extensible cable, infinite axial stiffness, and no hydrodynamic forces. The equation requires the following inputs: w, submerged weight per unit length of the cable; T_H, horizontal tension; ρ_l, density of constituent laminate structure; ρ_i, density of internal fluids; ρ_f, density of external medium; h, operational depth and the geometry of the cylindrical pipe to evaluate the second order differential equation, equation 4.1,

$$y''(x) = \frac{1}{\alpha}\sqrt{1 + (y'(x))^2}, \tag{4.1}$$

where α is the catenary parameter, $\frac{T_H}{w}$The boundary conditions are imposed such that equations 4.2- 4.4 are valid:

$$y(0) = 0, \tag{4.2}$$

$$y'(0) = 0, \tag{4.3}$$

$$\tan\theta_0 = 0, \tag{4.4}$$

where θ_0 , is the angle of the seabed at the touchdown point. Assuming the angle of the seabed is 0 leads to equation 4.5,

$$y(x) = \frac{T_H}{w}[\cosh(\frac{w}{T_H}x) - 1] - h, \tag{4.5}$$

which is a catenary curve with a departure point at y = 0, sea level and a touchdown point at a depth of h metres below the sea surface. The length of the catenary section, s, based on the horizontal, x, distance from touch-down point can be determined using equation 4.6,

$$y(x) = \frac{T_H}{w}\sinh(\frac{w}{T_H}x), \tag{4.6}$$

Forces acting on the riser include tension, both vertical and horizontal, as well as the bending moments, which were estimated using equations 4.7 and 4.8,

$$T_v(x) = w.s(x), \tag{4.7}$$

$$T(x) = \sqrt{(T_v^2(x) + T_H^2)}, \tag{4.8}$$

where $T_v(x)$ is the distribution of the vertical component of tension along the length of the riser. In addition, the bending moments acting on a segment of the riser can be estimated by multiplying the curvature by the bending stiffness inherent to the material and the geometry, which is shown in equation 4.9,

$$M(x) = EI.\kappa(x) = EI\frac{w}{T_H\cos h^2(\frac{w}{T_H}x)}, \tag{4.9}$$

This model does not consider any environmental factors, and represents the static position as a free hanging chain which excludes sea current and wave effects. These factors were then included via statistical distributions based on the findings of DNV [12]; Chu [14] and Zhan [87] where the forces related to undersea currents are modelled as additions to the constant T_H, while wave and current variability is modelled as additions to the sea depth using the Weibull probability density function shown in equation 4.10, where the parameters α_H and β are the scale and shape parameters of the Weibull distribution as shown in table 4.3. The forces related to current flow were applied using the following simplified assumptions: 1. Tangential current velocity is neglected; this is recommended by DNV [12]; as it is an insignificant consideration for riser applications. 2. Normal current velocity is constant in the Y, vertical direction or depth. This simplifies the application of an ocean current, without losing generality. 3. Acceleration of ocean currents is excluded. It is assumed that the normal velocity of the ocean currents remain constant which eliminates inertial loading effects as predicted by Morison's Formula.

TABLE 4.3: Characteristics of ocean current velocity and wave height, DNV [12] and Chur[14]

	Distribution	Suggested Parameters
Wave Height	Weibull	$\alpha_H = 0.681, \beta = 2.126$
Current Velocity	Weibull	$\alpha_H = 0.3, \beta = 2$

$$p(wp) = \frac{\beta}{\alpha_H}\left(\frac{wp}{\alpha_H}^{\beta-1}\right)\exp\left[-\left(\frac{wp}{\alpha_H}\right)^{\beta}\right], \tag{4.10}$$

The Weibull shape parameter β is equal to the slope of the probability plot where $\beta > 1$ indicates that the value is close to the mean wave height and slightly positively skewed with a tail to right of the distribution curve, while the scale parameter α_H shrink or squeeze the density function and affect if the function is narrow or wide banded. Therefore, the force acting on the riser per unit length for constant current is equivalent to the drag term of the Morison formula in equation 4.12. Where v_rel is the riser velocity relative to the water particle velocity, accounting for wave, v_{wave} , and current velocities, $v_{current}$ as given by equation 4.11,

$$v_{rel} = v_{riser} - v_{current} - v_{wave}, \tag{4.11}$$

As this study is based on the static catenary model, the riser velocity, v_{riser} is equal to zero in equation 4.11. The dynamic effect of the wave and the hang-off excitation is accounted for in the Dynamic Amplification Factor, which is equal to unity for wave conditions that are described in section 4.3.2 and are the basis of this study.

$$F_n = \frac{1}{2}\rho C_D D v_{rel}|v_{rel}|. \tag{4.12}$$

where F_n is the force per unit length, ρ is the density of surrounding fluids, C_D is the normal drag coefficient, D is the diameter and v is the current velocity. The C_D for the purpose of this analysis a value of 1.25 was chosen.

4.3.2 Verification of riser model

The outputs of the developed model using the properties listed in Table 4.4 are shown in Figures 4.4 and 4.5 in comparison to the FEA model utilised in Zhan [87]. Both models reflect similar results for the static geometric profile and characteristic forces acting on the riser. Maximum tensions and bending moments as well as their distribution along the length of the riser are similar and almost identical between the models. A sensitivity study is carried out using FLEXCOM software to quantify the maximum dynamic amplification factor due to waves and the FPSO motion. A 270 m FPSO is chosen and exposed to a range of sea states with wave periods close to its heave heave natural frequency, of 15.7 s, and water depths, of 1500, 2000, 3000 and 4000 m, to replicate the worst-case scenario. This is performed using the thicker, 56-ply riser configuration proposed for the later studies, documented in Figure 4.6, and top-tensions in Table 4.5. The sensitivity results in Figure 4.3 show that the dynamic model using regular waves can be approximated by the simple static approach for regions which are dominant by waves of up to 4 m wave height, at which the dynamic amplification factor is close to unity. This approximation is acceptable for regions, such as Gulf of Guinea, where the short-term environmental conditions matches the criteria of the 4 m maximum wave height. In such cases the variations between the simple static analytical approach and the FEA approach are less than 1%. The effects of wave height are not included in the final model as they are found to increase the computational expense but with a limited increase in accuracy, while current effects are still included.

4.3.3 Investigation into riser response

A simple comparison between the steel and composite risers, shown in Table 4.5, gives an indication for the differences between the maximum bending moments that are observed at the touch-down zone and maximum tensions at the hang-off point. Water depths of 1500 m are chosen to represent current deep-water applications with incremental increases to 4000 m, indicating the maximum depth for which future riser applications are likely to be aiming.

Composite catenary risers exhibit greater horizontal displacements than the traditional steel catenary risers with similar operating depths as a result of the lower density and transverse stiffness of composite systems as shown in Figure 4.6. This also has the consequence of increasing the necessary length of composite systems compared to steel catenary risers to reach the surface elevation starting from the same touch-down point, due to lighter apparent weight of composites. This is most evident for the 20-ply composite system which has the lowest density, and requires a total length of 2079 m to reach its operating depth of 1500 m. It is observed that the maximum bending moments remain constant for those models with the same materials, and is thus independent of operating depth, as opposed to tensions which are weight, and hence depth, dependant. As a result, steel catenary risers incur significantly larger bending moments, which peak at the touchdown point.

Table 4.4: SCR Verification Study Properties

Parameter	Value
Outer diameter (m)	0.273
Wall thickness (m)	0.0127
Weight in air (kg/m)	125
Internal fluid density (kg/m^3))	700
Length (m)	2240
Water depth (m)	1000
Hang-off to point of no motion (Horizontal distance)(m)	1500
Modulus of elasticity (GPa)	207
Boundary condition	Pinned-Pinned
Analysis type	Static

Table 4.5: Maximum bending moments and tensions related to global models

Water Depth (m)	Arc-Length (m)	Max. Tension (N)	Max. Bending Moment (Nm)
56-ply composite Wei [7]			
1500	1957	485914	28049
2000	2471	613628	27526
3000	3490	866054	28019
4000	4498	1116779	28049
20-ply composite Tan et al. [8]			
1500	2079	392603.7	66068
2000	2601	491228.6	66893
3000	3625	684859	66922
4000	4642	876417	66068
Steel			
1500	1659	1323057	79672
2000	2160	1723999	80664
3000	3176	2522527	79863
4000	4181	3323526	79672

4.3.4 Pipe model

Global loads are obtained from the catenary equation but because the method is based on a one-dimensional beam formulation, that only represents the centre line of the riser, there is missing information for the remaining two spatial dimensions of the pipe cross-section. Two interface equations are

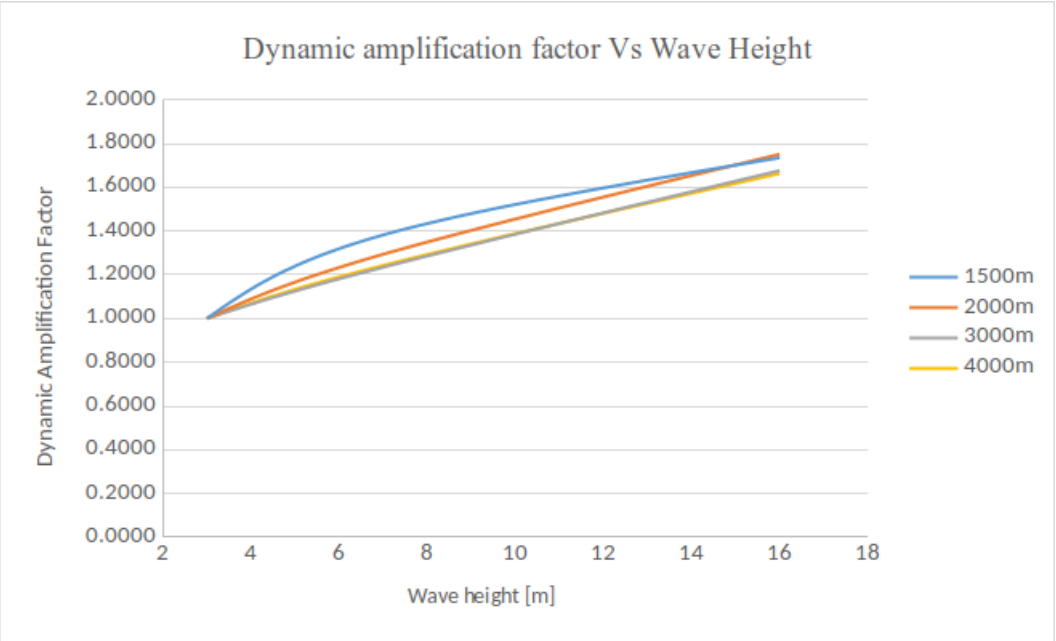

FIGURE 4.3: Amplification factor sensitivity between the static analysis and a dynamic case

needed to recover this information for the cross-sectional local analysis and to calculate the equivalent in-plane force, N, and the equivalent induced moment, M. If an infinitesimal section of the composite pipe wall is considered at the maximum curvature location, then the in-plane forces at this location is due to the tension in the beam and the tension induced by the curvature at the location of the outer ply.

The tension, T, and the bending moment, M,are calculated from the catenary equation. The equivalent in-plane force, N, is the equivalent force that is applied to the laminate x direction and causes the same stress at the outer ply that results from the tension force and bending moment. The calculations are based on equation 4.13,

$$N = T + Feq_{outerply}, \tag{4.13}$$

which is dependant on $Feq_{outerply}$, the equivalent force at the outer ply, defined in equation,

$$Feq_{outerply} = \frac{M_{global} * r_{outerply} * A_C}{I}, \tag{4.14}$$

where r is distance from the pipe neutral axis to the outer ply centre, Ac is the cross-sectional area and I is the second moment of area of the pipe.

The difference between the stress at the outer ply and the mid-plane of the composite laminate generates a rectifying moment about the y axis of the laminate that is located at the neutral axis of the laminate section as shown in Figure 4.7. Therefore, the equivalent moment is calculated using equation 4.15,

$$M = \frac{t * (Feq_{outerply} - Feq_{mid-plane})}{2}, \tag{4.15}$$

where t is the thickness of the riser. The equivalent force at the mid-plane, $Feq_{mid-plane}$, can be found by replacing $r_{outerply}$ with $r_{midplane}$ in equation 4.14. The principal stresses obtained by this analytical method are verified against a finite element model constructed using continuum shell elements, where

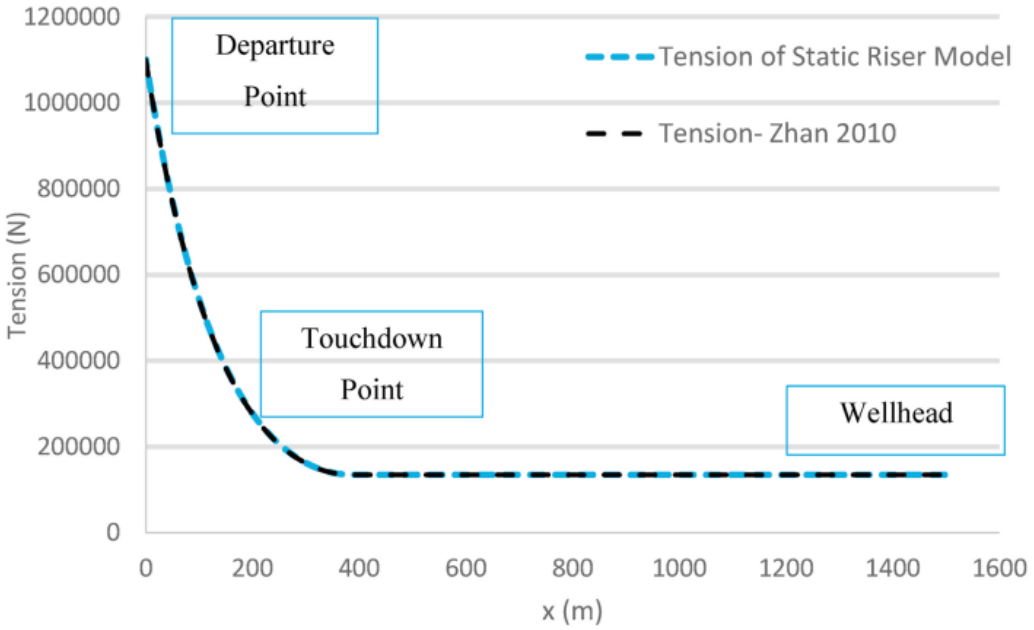

FIGURE 4.4: Tension forces from static global model in comparison to Zhan

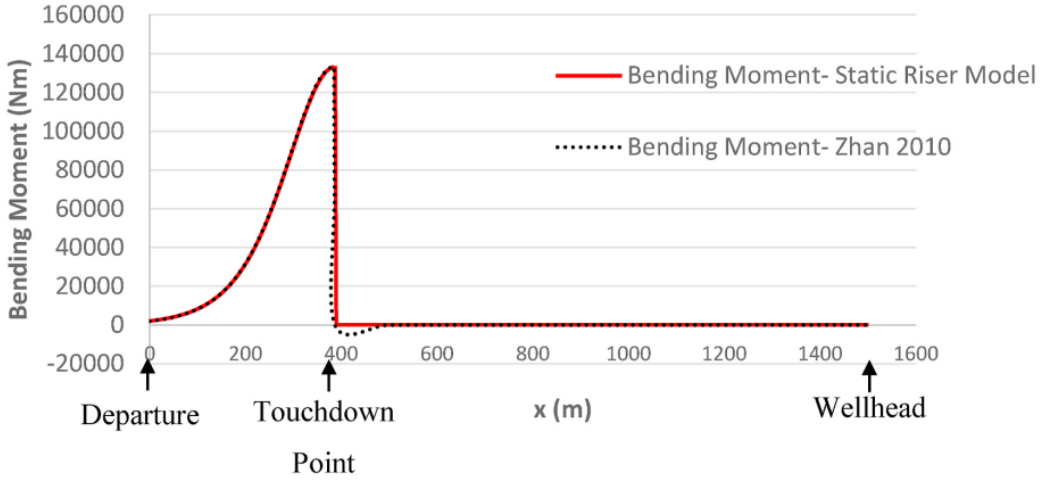

FIGURE 4.5: Bending moments from static global model in comparison to Zhan

the load from the static model is applied and the end of the pipe are constrained using a multi-point constraint which are tied to a point on the neutral axis. The highest principal component stress at the outer ply is found to be 10% higher than the analytical values, and therefore a multiplier of 1.1 is applied to the analytical model to adjust for this difference. The pipe analysis is conducted to determine the stresses and strains acting on the laminate structure of the riser. This is performed using Classical Laminate Theory (CLT), defined in equation 4.16, using the notation from Nijhof [160];

$$\begin{pmatrix} N \\ M \end{pmatrix} = \begin{bmatrix} A & B \\ B & D \end{bmatrix} \begin{Bmatrix} \epsilon^0 \\ \kappa \end{Bmatrix} \tag{4.16}$$

where A is the extension stiffness matrix; B is the bending-extension coupling effects between in plane stresses and curvatures and between bending and twisting moments and in plane strains; D is the stiffness of the laminate in the perpendicular direction under the influence of bending and twisting moments;

ϵ^0 is the vector of strain at a particular point in the laminate; κ is the vector of curvatures induced in the laminate by the external forces; N represents the in-plane forces acting on the segment of the composite pipe and M representing the corresponding induced moments about the laminate mid-plane. The in-plane strain vector $\{\epsilon\}\kappa$ for the kth lamina is given by equation 4.17,

$$\{\epsilon\}_k = [Q']_k\{\epsilon^0\} + z_k[Q']\{\kappa\}, \tag{4.17}$$

The stress-strain relationship can be determined for the kth lamina by employing equation 4.18,

$$\{\sigma\}_k = \{\epsilon^0\} + z_k\{\kappa\}. \tag{4.18}$$

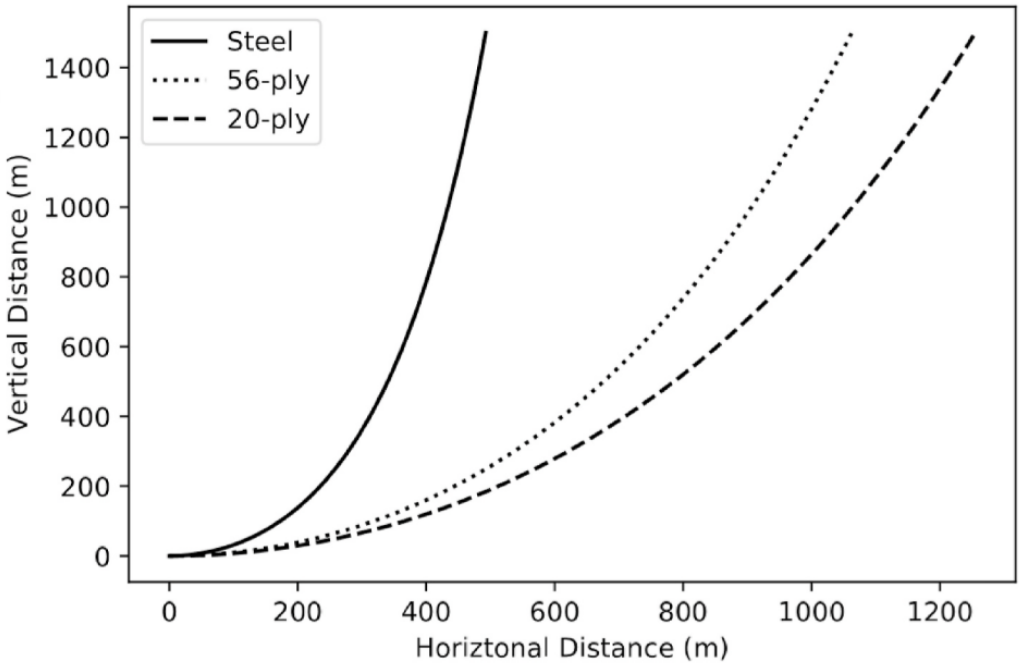

FIGURE 4.6: Comparison of configurations for risers manufactured using different material properties

where z_k is the distance from the mid-plane of the laminate in the thickness direction, Q' is the transformed reduced stiffness matrix for each lamina, dependent on the lamina's angle relative to the principle direction of the laminate, and $\epsilon = \{\epsilon_x, \epsilon_y, \epsilon_{xy}\}$ is a vector of in-plane strains experienced by the laminate. The stress components of $\{\sigma\}_k$ are evaluated by the Tsai-Wu failure criterion, in equation 4.19, and is used to determine the reliability.

$$(\frac{\sigma_1}{X_T X_C})^2 + (\frac{\sigma_2}{Y_T Y_C})^2 + (\frac{1}{X_T} - \frac{1}{X_C})\sigma_1 + (\frac{1}{Y_T} - \frac{1}{Y_C})\sigma_2 + (\frac{2F_1 2\sigma_1\sigma_2}{\sqrt{X_T X_C Y_T Y_C}}) + (\frac{\tau_{12}}{S_{12}})^2 = 1 \tag{4.19}$$

The Tsai-Wu criterion is chosen as a good predictor of first-ply failure, and it is assumed that after this initial failure that the riser is unsafe and that the failure will propagate. The left-hand side of the equation is evaluated, at each node along the riser length, and the utilisation factor can take values between 0 and 1, where 1 indicates first ply failure. The highest Tsai-Wu value for each riser is found near the touchdown point (x = 0) or departure point which agrees with the findings of Wang et al. [161] and Buberg [162]; where bending moments and tension forces are maximized respectively. As the operational depth increases the Tsai-Wu value closest to the departure point fails, until by 4000 m, the

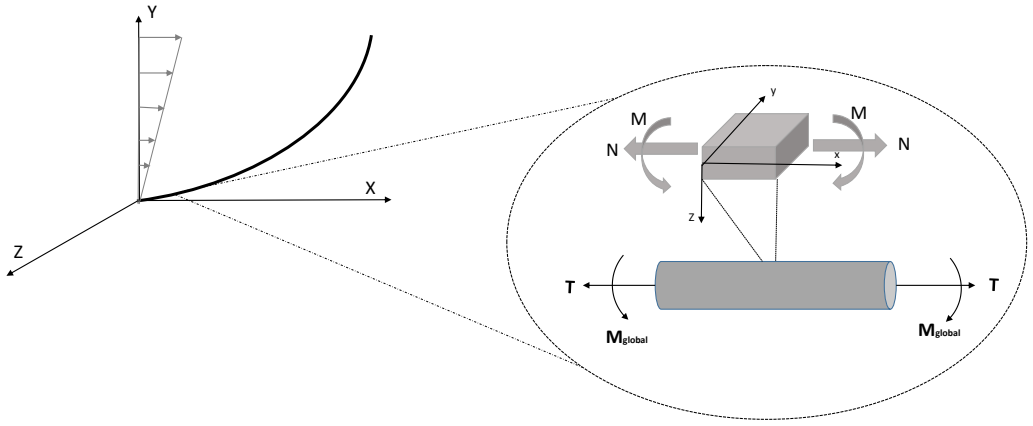

FIGURE 4.7: Schematic of the global loads applied to the local cross-section

Tsai-Wu value is lowest at the departure point. This analysis is selected to provide initial guidance on the probability of failure for composite risers, which are unlikely to fail in the same manner as steel, and to ascertain the importance of water saturation. The steel analysis forms a point of reference and in reality extreme bending moments are an unlikely reason for failure in steel catenary risers that are in service because the riser configuration is often designed to avoid low bending radii and that the most likely form of failure is due to fatigue at the touch-down zone.

The integral equation required to evaluate the probability of failure over the total number of Monte-Carlo simulations are given by the weighted sum of failed runs over N total number of total runs as per equation 4.20:

$$p_f = E[I(\mathbf{X})] \approx \frac{\sum_{i=1}^{N} I(\mathbf{x}_{(i)})}{N} \tag{4.20}$$

4.4 Reliability of risers

An analysis is performed to compare the trends in reliability between conventional steel risers with composite alternatives across different configurations. This analysis is also extended to investigate the change in reliability estimation of FRP composite risers in wet and dry conditions. The number of runs used for each simulation is 10^8 with values below this probability judged to be due to numerical phenomena rather than an accurate estimate of the reliability. The probability of failure $P_f$is calculated as the ratio between the number of failures predicted by Tsai-Wu criteria divided by the total number of runs, which is equal to 10^8. The analysis predicting the probability of failure due to extreme wave loading conditions and not due to fatigue. The probability of encountering a specific extreme current velocity, wave height and waver period is given by equation 4.10 and distribution parameters listed in Table 4.3. Each Monte-Carlo simulation run draws a sample of the wave height, period and current velocities. These environmental loads are used as an input to the global riser model. The global riser model, given these environmental loads, predicts tensions and moments along the riser length. These tensions and moments are sequentially transferred to the composite laminate theory model, that predicts strains and stresses across the laminate. These stresses and strains are used to evaluate the Tsai-Wu

failure criteria in equation 4.19. At the onset where the evaluation of the Tsai-Wu failure index is higher than unity, a failure is register for that specific run. This process is repeated for 10^8 runs for each water depth, for two cross-sections, 56-ply and 20-ply and for three material properties; dry laminate, Malmstein and Zafar with properties de-rated due to water absorption.

4.4.1 Sensitivity to dynamic effects

One challenge when combining a dynamic FEA analysis and Monte-Carlo simulation, is the computational expense which makes the approach infeasible. However, a dynamic amplification factor study, shown in Figure 4.3, predicts values close to unity for significant wave height conditions that are lower than 4 m. To verify this assumption the following steps are followed and the results compared to the quasi-static approach for dry and wet conditions:

1. A load case matrix is constructed covering 1–6 m wave heights and wave periods ranging between 12 and 22 s. A Flexcom finite element riser model, that is used in the dynamic amplification study in Fig. 3, is utilised to perform the detailed analysis of the load matrix cases. The dynamic amplification factors are estimated for maximum tension and curvature using regular waves. The dynamic amplification factors are estimated as the ratio between the maximum tension or curvature along the riser length divided by the static value for each load case; these values are listed in Tables 1 and 2 in section 5.
2. For conservatism, extreme short-term omni-directional wave conditions are assumed. The annual waves distribution is predicted by Weibull distribution in equation (10) and parameters listed in Table 4. This distribution is found to represent the short-term wave height in the Gulf of Guinea region. The maximum short-term significant wave height is found to be 2.67 m, Akinsanya [163]. The environmental directions are assumed to be in the far and near directions for conservatism. In-line waves, currents and offset directions are considered to capture both extreme cases of maximum top-tensions and curvatures.
3. The drag force is calculated using a quasi-static approach by summing the constant velocity current and the maximum wave particle velocities along the riser length.
4. The 2nd Order FPSO response is captured by varying the offset as a function of the wave height as shown in equation 4.21, the bottom tension is re-calculated for each run with new configurations after adding the offset and the corresponding top tension is estimated. The load case offset, offset LC, is given by the following equation 4.21,

$$offset_{LC} = offset_{max} * (\frac{H_{LC}^2}{H_{max}^2}), \tag{4.21}$$

   where the maximum offset, $offset_{max}$, is defined as 0.9% of the depth.
5. The maximum axial force that propagates along the riser, due to the FPSO pitch and heave motions, is approximated using the tension dynamic amplification factor.
6. The maximum curvature that occurs due to the transverse waves propagating along the riser length, due to the FPSO motion, is approximated using the curvature dynamic amplification factor.
7. Two distinctive dynamic amplification factors are used, one for the tension and another for curvature to capture the difference in peak dynamic amplification factor noticed around different wave periods. For environmental conditions that lies between the pre- simulated dynamic amplification factors provided in section 5, Tables 1 and 2 a linear interpolation is incorporated.

   The reliability analysis results, shown in Figure 4.12, are the probability of failures calculated using the quasi-static approach, compared to the detailed dynamic amplification factor predicted by the

FEA analysis. A slight increase of the probability of failure is observed, however, the figure shows that the quasi-static approach remains a reasonable approximation for the short-term extreme environmental conditions in the Gulf of Guinea region.

4.4.2 Steel catenary risers vs composite risers

The reliability of two Steel Catenary Risers, one at 1500 m and another at 4000 m, are analysed and compared to the results of a composite-based riser system to establish a benchmark for comparison. The results show negligible probability of failure and justifies why such risers are in widespread use for offshore hydrocarbon extraction. Further simulations are not performed as the results demonstrate that the probability of failure is low and simulations where failures only occur deep in the tails of the distributions may not be significant from a practical perspective. The reliability of these simulations is similar to the dynamic results from Carrillo et al. [79]; which is assessed to be $1.33x10^{-11}$ in the catenary transition zone and $1.73x10^{-14}$ at the connection to the tension leg platform for a riser of unknown length, but who quote a reliability on the order of 10^{-5} at the weakest points near the Touchdown Zone which are not exhibited in this model. The simulation of the Steel Catenary Riser operating in ocean depths of 4000 m reveals a significantly higher top tension much larger than that of the of the Steel Catenary Riser operating at 1500 m. However, the probability of failure for these risers is still lower than composites.

To determine the probability of failure, a convergence study is performed to select the appropriate number of runs required for the Monte-Carlo simulation, illustrated in Figures 4.8 and 4.9. In comparison, Figure 4.8 reveals the rate of failures for the 56-ply composite layup operating at 1,500 m. These simulations provide a probability of failure of $4.4x10^{-7}$ which is higher than the steel catenary riser operating at 1500 m which recorded no failures. However, this is still determined to be a safe value according to the DNV rules, Table 1.2. This increases to $1.6x10^{-5}$ for depths of 4000 m which is still safe, but more importantly shows only a small increase in probability of failure but where the rate in change of failure for the steel catenary is unknown as no failures have occurred.

Figure 4.9 shows that the probability of failure for the 20-ply riser, [8]; has not converged but reaches a value of $6.0x10^{-8}$. However, this can be considered to be a numerical anomaly as they are occurring in the tails in the normal distribution and unlikely to represent real properties as they are unrealistically far from the mean value. Therefore, the simulations are stopped at this point and assumed to be a very low value. This demonstrates a similar probability of failure to that of a steel catenary riser with similar thickness and operating depth. For the 20-ply case the probability of failure increases to $1.2x10^{-7}$ at 4000 m demonstrating convergence and a similar low probability of failure.

Table 4.6 compares the different systems with respect to the unit weight and the total weight of the entire riser system. Steel catenary risers show smaller deflections than the composite risers and the low stiffness exhibited by composite materials increases the overall length of the composite system. A larger thickness for the riser might improve the performance of the riser system but will also require higher tension loads and the results in this analysis demonstrate the opposite effect, thin and light risers are less likely to fail. The Marginal Reliability, the improvement in probability of failure for each kilogram of additional material, of Carbon/Epoxy improves reliability by $9.07x10^{-13}$ and $1.53x10^{-13}$ for the 56-ply and 20-ply composite riser respectively and at 4000 m this increased to $1.43x10^{-11}$ and $1.37x10^{-13}$. The probability of failure per kilogram, Pf/kg is a normalized failure probability that is a parameter to allow easier comparison of the cross-sectional design by addition or reduction of riser material to indicate the change in the probability of failure.

Both composite layups fulfil DNV's lower safety class recommendation, $P_f = 10 - 5$ DNV [12]; at depths of 1500 m and 4000 m. This builds confidence in the ability of composite risers to be utilised

in deep-water conditions and the potential to benefits from lower weight, and therefore reduced installation costs. However, the analysis shows limited benefits, in terms of reliability, over steel under extreme conditions. The steel catenary riser provides a higher level of reliability than the design using a composite material statically. However, the two composite riser and steel catenary riser designs are chosen arbitrarily and the analysis shows that thinner thicknesses of pipe provide a safer design but that the steel benefits from a higher stiffness. This analysis therefore needs to be extended with an analysis performed on optimally designed pipes for each distance, supported by the findings from the parametric study performed in this section, and a dynamic analysis.

4.4.3 The impact of moisture absorption on riser reliability

Whilst the results of the previous study indicate the potential for composites for deep-water applications, it is unlikely that these materials will perform for extended periods with the performance of testing in dry conditions. To account for this, the riser properties are degraded to represent the wet state according to experiments from the open literature. Malmstein et al. [164] provide data for glass/epoxy composites in conditions lasting up to 6 weeks in distilled water. The material properties of the degraded material are shown to be more dependent on the composite matrix resin material, so findings related to the degradation percentage of glass provides can be extrapolated to carbon, due to the small quantity of data available in the open literature. The findings of these experiments show that the riser flexural strength is reduced by 50% and the weight is increased by 2%; the flexural modulus is also reduced by 1.6% but this reduction is ignored. The degradation of composites in distilled water is often higher than in salt water and the results are also for flexure, rather than tension, and so this degradation factor is considered as a worst-case scenario. Experiments are also performed on carbon/epoxy specimens by Zafar et al. [165] who found an increase in weight of 2.12% in conditions lasting up to 300 days in salt water. The corresponding loss of tensile strength was 20% and Young's modulus was 10%. These values are therefore included into the model where Zafar et al. [165] represents more realistic values for risers due to the similar materials and tensile properties alongside experiments conducted in salt water. The reliability analysis for different depths is reported in Figure 4.10 where the probability of failure is shown in logarithmic scale, for the 56-ply case, and similarly, Figure 4.11, for the 20-ply case. The results are assumed to have converged as the probability of failure for the wet simulations should be higher than those in the dry condition, requiring fewer runs to converge and therefore the same number of simulations are performed.

These results imply that, as expected, there is a negative relationship between water retention and reliability. The reduction in ultimate tensile strength and Young's Modulus combined with the increased weight per unit leads to a combined effect of increasing the tension while reducing the materials resistance to external loadings. This explains why the probability of failure is higher for the moisture absorbed riser systems. Comparing the two types of moisture absorption the Zafar et al. [165] case reports higher probability of failures for all of the risers in comparison to the dry properties; at lower depths this increase is mild however at the larger depths it is more significant. This trend also occurs for the less realistic properties from Malmstein et al. [164] but the probability of failure is higher.

The results for the wet composites, summarised in Table 4.7, are more indicative of the number of failures to be expected as the system matures over time, and may be used to establish the upper limits for the operating lifetime for FRP riser systems. Even in the worst-case material degradation scenario, the Malmstein et al. [164] ageing and the thicker 56 ply case, the probability of failure for the 1,500 m is still $7.56x10^{-6}$ and is only predicted to pass the lower safety limit at 4,000 m with a probability of failure of $3.05x10^{-3}$, which could be reduced with enhanced cross-sectional design.

The increase in probability of failure due to the hygrothermal ageing is higher for the thicker composite, where the values increase by a factor of 62–746 over the intact riser for the extreme case of Malmstein et al. [164] and by 1–6 for the more realistic ageing case of Zafar et al. [165]; than for the thinner riser, with an increase by a factor of 17–190 for the extreme ageing case of Malmstein et al.[164] and 1.18–1.98 for the more realistic ageing case of Zafar et al. [165]; where these values are highest at the higher depths. This underscores the need for effective and robust waterproof layering to protect the laminate from direct contact with the surrounding saline environment as suggested by Tan et al. [8] for their composite system. This system will extend the operating lifetime of the pipeline, and potentially reduce maintenance and operational expenses in the long run by reducing moisture contact with the laminate. However, it is unlikely that it will be totally able to remove the moisture from the environment and determining the levels of absorption over time appears to be a critical characteristic in reducing safety factors for composite risers in deep-water conditions, where even the more realistic water uptake estimates give an increase in probability of failure of 6 for the thicker riser and 1.98 for the thinner riser.

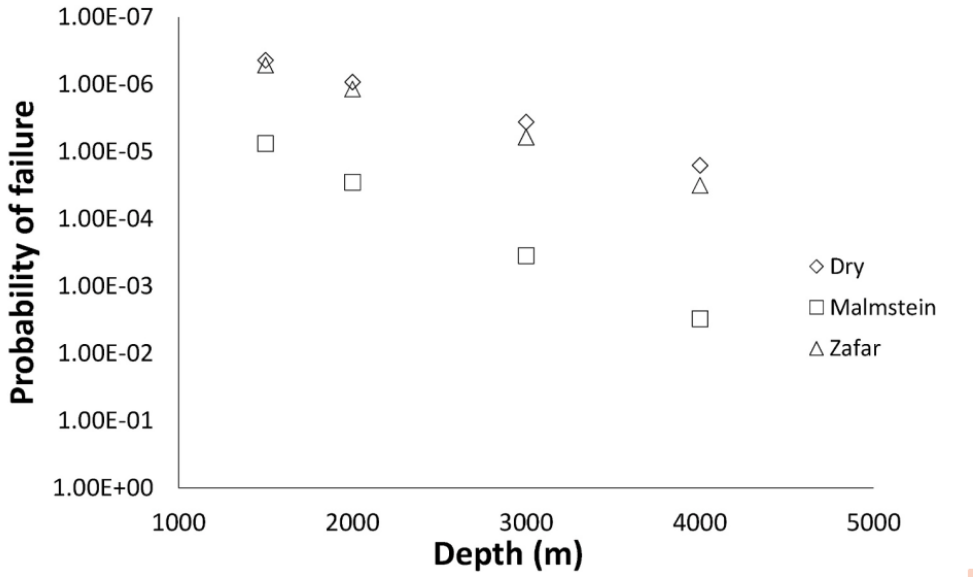

FIGURE 4.8: Probability of failure for the 56-ply composite, Wei [7];operating at 1500 m.

TABLE 4.6: Comparison of weight and probability of failure for steel catenary and composite risers.

	1500 m			**4000 m**		
	Steel	56-ply	20-ply	Steel	56-ply	20-ply
Submerged Weight Full of Product (N/m)	794	248	189	794	248	189
Arc-Length (m)	1659	1957	2079	4181	4498	4642
Total Weight (kg)	1.3E+06	4.9E+05	3.9E+05	3.3E+06	1.1E+06	8.8E+05
P_f (MPa)	¡1.0E-8	4.4E-07	6.0E-08	¡1.0E-8	1.6E-05	1.2E-07
P_f/kg	¡1.0E-13	9.1E-13	1.5E-13	¡1.0E-13	1.4E-11	1.4E-13

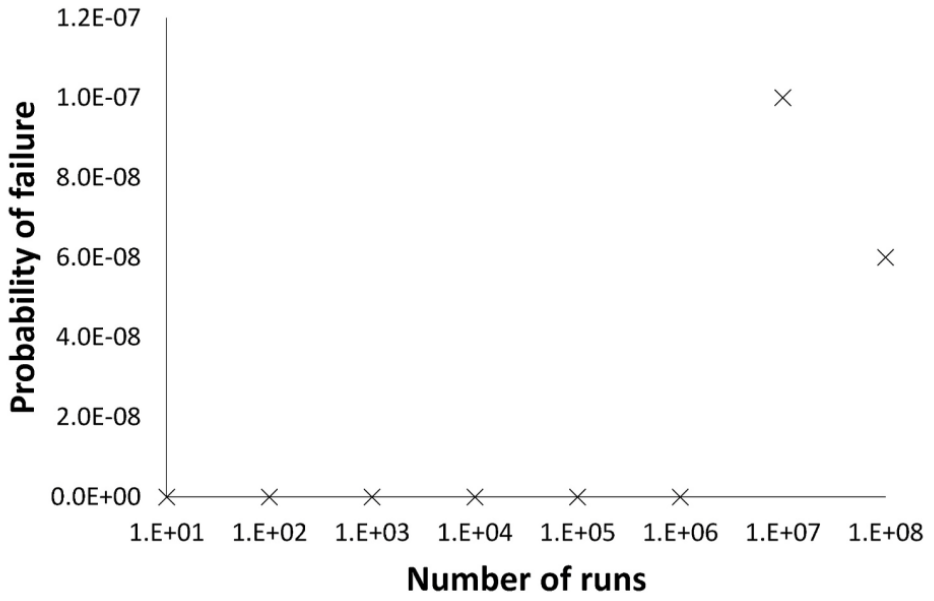

FIGURE 4.9: Probability of failure for the 20-ply composite, Tan et al. [8];operating at 1500 m.

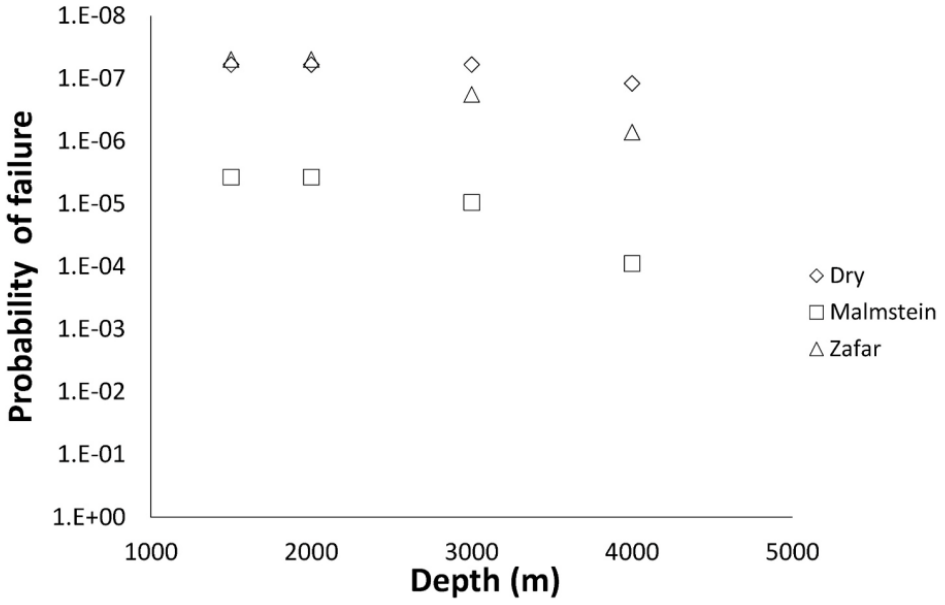

FIGURE 4.10: Probability of failure for the 56-ply composite, Wei [7]; after water absorption ageing at increasing water depths.

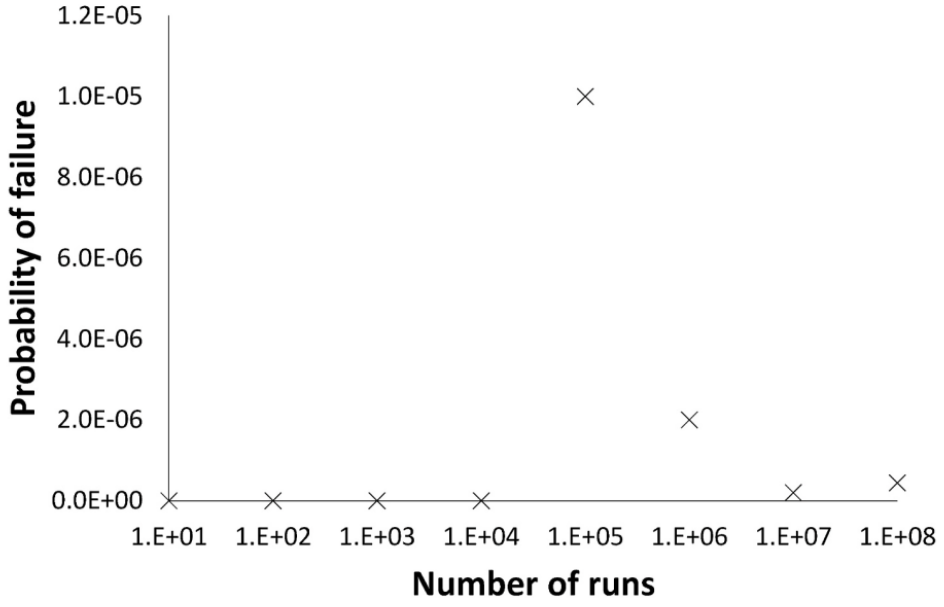

FIGURE 4.11: Probability of failure for the 20-ply composite, Tan et al. [8];after water absorption ageing at increasing water depths.

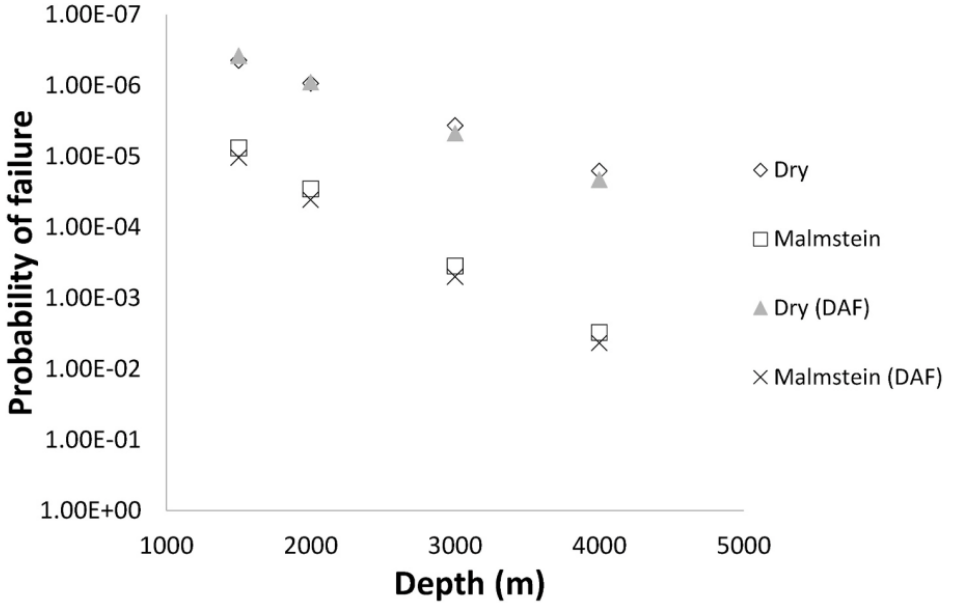

FIGURE 4.12: Probability of failure for the 56-ply composite riser using a quasi-static analysis and dynamic analysis, for dry and after water absorption ageing at increasing water depths.

TABLE 4.7: Probabilities of failure for composite risers with moisture absorption.

	56-ply			**20-ply**		
	Dry	Malmstein et al.[164]	Zafar et al.[165]	Dry	Malmstein et al.[164]	Zafar et al.[165]
1500 m						
P_f	4.40E-07	7.56E-06	5.20E-07	6.00E-08	3.74E-06	5.00E-08
Weight (kg)	4.85E+05	4.89E+05	4.89E+05	3.92E+05	3.99E+05	3.99E+05
P_f/kg	9.07E-13	1.55E-11	1.06E-12	1.53E-13	9.37E-12	1.25E-13
2000 m						
P_f	9.30E-07	2.87E-05	1.18E-06	6.00E-08	3.75E-06	5.00E-08
Weight (kg)	6.13E+05	6.18E+05	6.18E+05	4.91E+05	4.99E+05	4.99E+05
P_f/kg	1.52E-12	4.65E-11	1.91E-12	1.22E-13	7.51E-12	1.00E-13
3000 m						
P_f	3.64E-06	3.52E-04	6.08E-06	6.00E-08	9.50E-06	1.80E-07
Weight (kg)	8.65E+05	8.72E+05	8.72E+05	6.84E+05	6.97E+05	6.97E+05
P_f/kg	4.21E-12	4.04E-10	6.97E-12	8.77E-14	1.36E-11	2.58E-13
4000 m						
P_f	1.60E-05	3.05E-03	3.18E-05	1.20E-07	8.95E-05	7.20E-07
Weight (kg)	1.12E+06	1.12E+06	1.12E+06	8.76E+05	8.92E+05	8.93E+05
P_f/kg	1.43E-11	2.71E-09	2.82E-11	1.37E-13	1.00E-10	8.06E-13

Chapter 5

Far-field loading and laminate mechanical properties manufacturing uncertainties effect on composite riser integrity

5.1 Peridynamics micro modelling

As established in section 4, a higher failure probability of the composite risers are expected due to mechanical properties uncertainties, that are caused by water absorption combined with far-field dynamic riser loadings. As shown in the literature review in section 2.1, other sources of the mechanical properties uncertainties are the variations of void content, in addition to its statistical arrangement within the laminate. To investigate these variational effects, a micro model is based on peridynamics non-local theory as summarised in the literature review. That is because it is required to simulate fracture initiation and propagation to determine the ultimate strength of the RVE under the influence of these micro model variations. In this section peridynamics RVE is modelled to investigate the void content effect on RVE properties. A representative 25 years environmental data of the north sea are used to simulate full-scale model under stochastic wave conditions. The full scale model utilise *RiSim* algorithm developed in section 3 to predict tension and curvatures along the riser length, *CRIMMO* algorithm in section 5 extract the boundary conditions at two hot-spot locations, the hang-off and touch-down zones and creates Abaqus dynamic shell element composite model, the maximum strain element is identified and peridynamics model is created using *PeriPy* algorithm. The Tsai-wu failure criterion is used and compared to the damage predicted with peridynamics to benchmark the peridynamics failure predictions and highlight the advantage of peridynamics model to capture cross-sectional defects.

5.1.1 Bond-based peridynamics formulation

Peridynamics is a continuum form of molecular dynamics, the equation of motion is formulated in [107]. The domain is discretized into material points, each material point acceleration $\ddot{u}$, that is located at coordinate $\boldsymbol{x}$ in the un-deformed configuration, at time instance t is given by,

$$\rho\ddot{\mathbf{u}}(\mathbf{x},t) = \int_{H_x} f(\mathbf{u}(\mathbf{x}',t) - \mathbf{u}(\mathbf{x},\mathbf{t}), \mathbf{x}' - \mathbf{x}) dV_{x'} + \mathbf{b}(\mathbf{x},\mathbf{t}), \tag{5.1}$$

where ρ is the mass density, $\mathbf{u}$ is the displacement vector field, $\mathbf{x}$ is the point coordinate vector,$\mathbf{f}$,is the *pairwise force function* between points $\mathbf{x}$ and $\mathbf{x}'$ and is influenced by material points in the neighbourhood, H_x, and limited by the horizon radius δ and $\mathbf{b}$ is the body force density field. The relative position vector between material points $\mathbf{x}$ and $\mathbf{x}'$ in the deformed configuration is given by $\eta + \zeta$, where ζ is the relative position vector, given by equation 5.2 and η is the relative displacement, which is given by equation 5.3. The *bond* between material points $\mathbf{x}$ and $\mathbf{x}'$ is the attraction force that is exchanged between the particles and extends beyond the adjacent particles to the horizon limit. The concept of a *bond* between particles that are within a specific horizon necessitate that the force at each material point is the vector sum of each neighbour particle contribution that lies within the horizon. This *non-local* property is the main fundamental difference between classical continuum mechanics theory and peridynamics.

$$\zeta = \mathbf{x}' - \mathbf{x} \tag{5.2}$$

$$\eta = \mathbf{u}(\mathbf{x}',t) - \mathbf{u}(\mathbf{x},t) \tag{5.3}$$

The *bond* force, between material points is a scalar quantity and given by

$$f(\eta,\zeta) = \frac{\zeta+\eta}{|\zeta+\eta|} f(y(t),\zeta,t) \quad \forall\zeta,\eta, \tag{5.4}$$

$$y = |\eta + \zeta| \tag{5.5}$$

By substituting the scalar bond force equation 5.4 to the peridynamics equation of motion 5.1, the perdynamics equation can be discretized. The quantity s, described as scalar bond stretch is developed to formulate the constitutive properties of the material and can be utilised to define bond breakage, given by equation 5.6,

$$s = \frac{|\zeta+\eta| - \zeta}{\zeta} \tag{5.6}$$

$$s_0 = \sqrt{\frac{5G_0}{9\kappa\delta}} \tag{5.7}$$

The key equation that describes the material microscopic properties is the scalar function f. The composite matrix and fibres behaviour can be approximated with brittle microelastic material properties as follows,

$$f(s,t,\zeta) = \mu(t,\zeta) = \mu(t,\zeta)cs \tag{5.8}$$

where c is the elastic constant, which is a function of the material bulk modulus κ and μ is the damage function, that takes a value of 0 for a broken bond or 1 for an active bond, the bond is considered broken if the stretch s exceeds a specific critical stretch s_0. For brittle materials, the linear elastic critical stretch is a material related property that can by related to the critical energy release rate, G_0. It is formulated so the energy release rate should be equal to the work required to break all bonds per unit area as given by equation 5.7. The damage at each point is an accumulative function, where damage is defined as the ratio between the sum of all broken bonds connected to a material point to the total number of bonds and given by equation 5.10,

$$\mu(t,\zeta) = \begin{cases} 1 & if\ s(t',\zeta) < s_0 \quad \forall 0 \leq t' \leq t \\ 0 & \text{otherwise} \end{cases} \tag{5.9}$$

$$\phi(\mathbf{x},t) = \frac{1 - \int_{H_x} \mu(\mathbf{x},t,\zeta) dV_\zeta}{\int_{H_x} dV_\zeta}. \tag{5.10}$$

Equation 5.9 represent the peridynamics bond damage function, and the accumulative damage is given by equation 5.10. The 3D elastic constant c is given by equation 5.11,

$$c = \frac{18\kappa}{\pi\delta^4}. \tag{5.11}$$

5.2 Model verification

5.2.1 RVE geometry

PeriPy code is utilised [166] to simulate the peridynamics equation of motion. An RVE with $50\mu m$ cube length, contains carbon fibres in an epoxy matrix is modelled. RVE fibres diameter are randomly generated, with a fibre mean radius F_{rmean} and coefficient of variation CV_f. Voids are explicitly modelled in the RVE as spherical voids according to a specific void ratio. Voids are randomly created, following a normal distribution with size between V_{rmin} and V_{rmax}, and void length to width ratio Vl_{ratio} for longitudinal voids. Table 5.1 is a summary of the properties used to build the RVE model, shown in Figure 5.1.

The distribution of the voids and fibres sizes follows the Gaussian distribution probability density function as shown in equation 5.12, using the mean and standard deviation values listed in Table 5.1.

$$p(x) = \frac{1}{\sqrt{2\pi\sigma^2}} e^{\frac{-(x-\mu)^2}{2\sigma^2}} \tag{5.12}$$

TABLE 5.1: RVE Properties [9]

Property	Description	Value
CV_f	Fibre diameter coefficient of variation	0.17
Vl_{ratio}	Void length to width ratio	20
L	RVE side length (μm)	20
V_f	Fibre volume fraction(%)	60
F_{rmean}	Fibre mean radius(μm)	5.0
$F_{r\sigma}$	Fibre radius standard deviation(μm)	0.5
V_{rmin}	Spherical voids minimum radius (μm)	2.5
V_{rmax}	Spherical voids maximum radius (μm)	5.0
$V_{r\mu}$	Spherical voids mean radius (μm)	3.75
$V_{r\sigma}$	Spherical voids standard deviation (μm)	1.25
F_{den}	Fibre density (kg/m^3)	2000.0
M_{den}	Matrix density (kg/m^3)	1400.0
E_f	Fibre elastic modulus (GPa)	230
E_m	Matrix elastic modulus (GPa)	3.2
Int_{den}	Interface density (kg/m^3)	1600.0
G_cM	Matrix strain energy release rate (J/m^2)	78
G_cF	Fibre strain energy release rate (J/m^2)	100
G_cint	Matrix/Fibre strain energy release rate (J/m^2)	100

The units utilised are according to the consistent units as listed in Table 5.2. All RVE dimensions are in μm. The geometry is created in *gmsh* [167] python API to create stochastic RVE with specific void ratio. A special code is written for this thesis to create the RVE is attached in section 5. The *.msh* file created by the algorithm is passed to the code to analyse the stress/strain response of the RVE.

TABLE 5.2: Consistent Units

Description	SI Unit	Consistent Unit
Mass	M	kg
Length	L	μm
Time	T	s
Force	-	μN
Energy	-	pJ
Stress	-	MPa
Density	-	$10^{-18} kg/m^3$
Damping	-	$kg/\mu m^3$

The peridynamics code is able to simulate multiple material bonds, however, a special function is required to identify the bond type for each material point to calculate the peridynamics force. The python code that creates the RVE, in section 5, returns a list of material points that are in the fibre and matrix domains. This enables the peridynamics code to compare each material point to a predefined list for each fibres and matrix and use the suitable bond stiffness and stretch. The following code snippet is used with the peridynamics code to to identify matrix and fibre bond types and density.

```
class bonding:
  """
  Returns bond density given two points in the material
  """
  def __init__(self, fibres_data):
    self.fibres_data = fibres_data
  def is_fibre(self,X):
    in_chk = [(X[0] - key[0])**2 + (X[1] - key[1])**2 - self.fibres_data[key]**2
    for key in self.fibres_data.keys()]
```

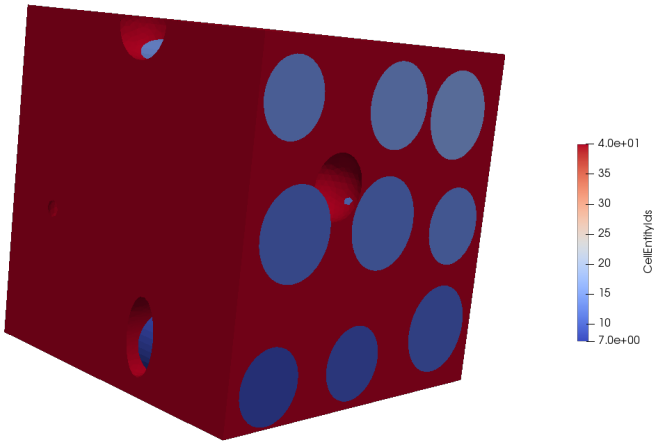

FIGURE 5.1: Stochastic RVE Geometry

```
    if any(chk<= 0 for chk in in_chk):
      return True
    else:
      return False
  def bond(self,x,y):
    output = 0
    p1 = self.is_fibre(x)
    p2 = self.is_fibre(y)
    if matrix == 1:
      output = 2 # index of matrix
    elif p1 and p2:
      output = 0 # index of fiber
    elif p1 != p2:
      output = 1 # index of interface
    else:
      output = 2 # index of matrix
    return output

class density:
  """
  Returns bond type given two points in the material
  """
  def __init__(self, fibres_data,Fden,Mden,intden):
    self.fibres_data = fibres_data
  def is_fibre(self,X):
    in_chk = [(X[0] - key[0])**2 + (X[1] - key[1])**2 - self.fibres_data[key]**2
    for key in self.fibres_data.keys()]
    if any(chk<= 0 for chk in in_chk):
      return True
    else:
      return False
  def dens(self,x):
    matrix = 0
    output = Mden
    p1 = self.is_fibre(x)
```

```
43      if matrix == 1:
44        output = Mden # index of matrix
45      elif p1:
46        output = Fden # index of fiber
47      elif not p1:
48        output = Mden # index of interface
49      else:
50        output = Mden # index of matrix
51      return output
```

5.2.2 Transverse tensile strength

The transverse stress/strain response of the RVE is assessed in this section, assuming no voids in the matrix, and the maximum transverse strength is verified against published FEA model that is using cohesive elements modelling for a similar size RVE, with no voids [9]. The FEA model is selected to verify the peridynamics model, since the FEA model doesn't incorporate voids, before incorporating the voids in the peridynamics model. As shown in Figure 5.3 the maximum FEA transverse stress is observed to be 40 MPa, this is confirmed by the peridynamics virtual experiment shown in Figure 5.2. Both figures shows that the maximum stress is reached at 2% strain after which the RVE damage accumulates and strength is lost down to 25 MPa at 3% strain. Although, the main aim of this verification is to benchmark the maximum transverse strength of the RVE, which is successfully demonstrated in this figures 5.2 and 5.3. An investigation of the transverse elastic modulus predicted by both FEA and peridynamics is carried out. The FEA model elastic modulus of 7.0 GPa is calculated from figure 5.3. However, it is observed that the peridynamics RVE exhibits lower transverse elastic modulus at 0.2% strain, which is 3.5GPa. There are multiple factors that contributes to this difference, such as damage accumulating in peridynamics model can occur at any material point, while the FEA model is limited to damage at pre-defined cohesive zones, but one of the largest contributing factors is the limitation on the bond-based peridynamics formulation, which limits Poisson's ratio to $\frac{1}{4}$. This limitation leads to a restriction on the material point force vector direction and magnitude, imposing a specific limitation on the elastic properties. It is noted in the literature that the material stiffness predicted by peridynamics with Poisson's ratio of 0.45 can lead to error percentage up to 56% [168].

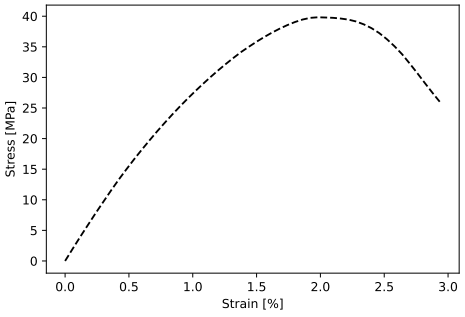

FIGURE 5.2: Peridynamics predicted Transverse stress/strain Response

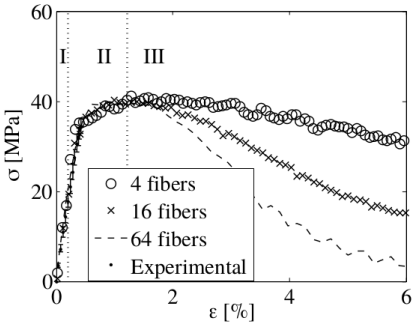

FIGURE 5.3: Verification Transverse stress/strain Response [9]

It is shown that bond-based peridynamics predicts the transverse stress-strain relation and RVE damage with less than 5% error, but results in less stiffer matrix response.

5.2.3 Axial tensile strength

To verify the axial response of the RVE, the closest carbon fibre composite material with T300 carbon fibres is used here to verify the model ability to model the axial tensile stress-strain response and strength [10]. Maximum CFRP stress is observed to reach 550 MPa at 1.8% strain as shown in the peridynamics predicted response in Figure 5.4, this is a 10% higher maximum stress compared to the experimental value shown in Figure 5.5. The experimental data shows that the maximum CFRP stress reaches 500 MPa at 1.5% strain. It is observed that the axial stiffness correlates much closer to the experimental values, that is because the carbon fibre Poisson's ratio is close to 0.25, which is the bond-based peridynamics limit.

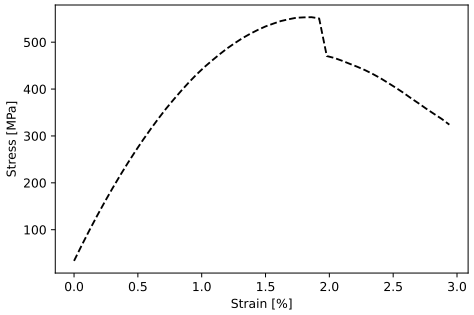

FIGURE 5.4: Peridynamics Predicted Axial Tensile Strength

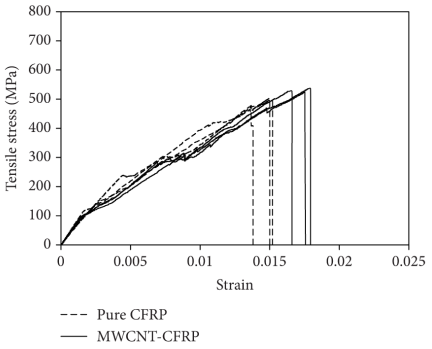

FIGURE 5.5: Verification Axial stress/strain Response [10]

5.2.4 Void content effect on RVE strength

After verifying the peridynamcis code, to investigate the effect of void content uncertainty on the RVE integrity an RVE with voids is created. It is shown the literature that voids larger than 0.4% negatively affect the mechanical properties of composites [55]. Therefore, the RVE is built, as explained in section 5.2.1 with stochastic spherical and longitudinal voids to simulate the entrapped bubbles in the epoxy mixture, these bubbles coalesce into larger spherical and longitudinal voids. The introduction of bubbles in the model allows to study the effect of void ratio on mechanical properties.

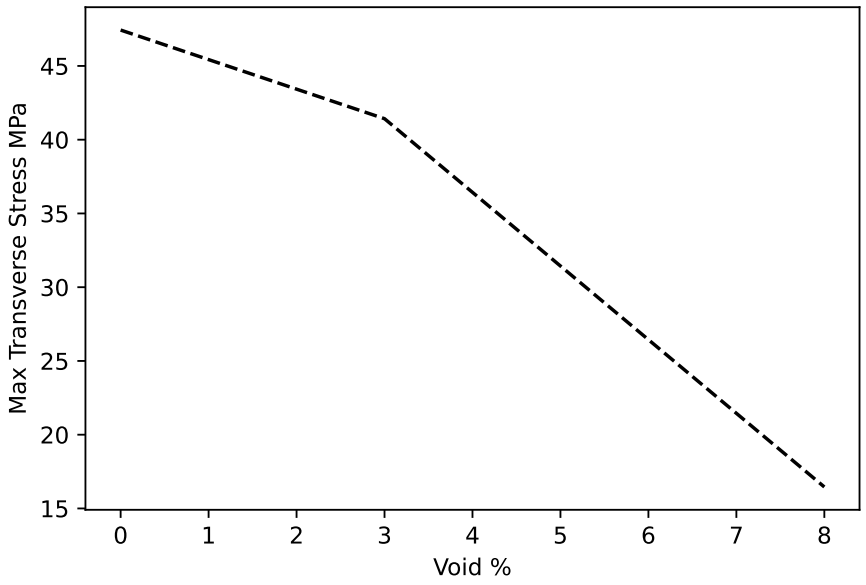

FIGURE 5.6: Void content % effect on Transverse Tensile Strength

The transverse stress is investigated against a range of void ratios that are simulated between no voids and up to 10% void content. A fixed random seed is used to create the RVE geometry, including voids and fibre diameters and locations. The seed is chosen to be fixed at the seed producing the mean ultimate tensile strength. Figure 5.6 shows the results of maximum stress observed for each void percentage simulated. There is a clear reduction observed in the maximum stress of the RVE with void content. A rapid reduction in the mechanical properties of the RVE is observed at 8% void content, with a maximum stress reduction of 65%.

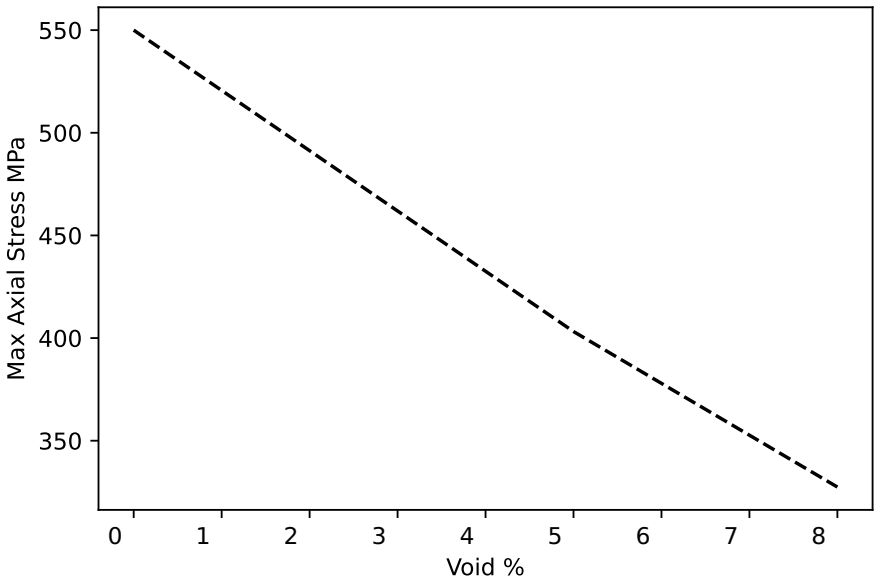

FIGURE 5.7: Void content % effect on Axial Tensile Strength

The axial tensile strength is also investigated as shown in figure 5.7. It is observed that the maximum reduction at 8% void content with a reduction of 40% of the maximum tensile strength with no void. It is also observed that the reduction is linear in contrary to the transverse strength.

5.2.5 Mechanical properties statistical distribution

To investigate the effect of void, fibre diameters and distributions on the mechanical properties variations, the statistical distribution of the composite RVE mechanical properties is sampled, with 5% void ratio is investigated. 300 peridynamics simulation are carried out to create the histogram shown in figures 5.8-5.9. The coefficient of variation for the axial tensile strength distribution is found to be 45% while 70% for transverse tensile strength the [156]. Although a large number of samples is required to quantify the stationary statistical distribution of the mechanical properties, an attempt is made to investigate the distribution function suitable to describe the variation in properties.

Various probability distribution functions are iterated, using Scipy python package [169], to fit the statistical simulated data shown in the histogram figures 5.8- 5.9, these distributions are compared to the data and the sum of square errors, **SSE**, is used to select the best fitting distributions. It is found that both the axial tensile strength and the transverse tensile strengths follows a Johnson SB distribution match better the transverse tensile strength simulated samples with 0.0001 **SSE**.

The coefficient of variation is shown to higher with the transverse tensile properties, compared to the axial properties. That is because the transverse strength is relying on the matrix strength and the random distribution of the voids in the matrix has higher variational effect on the strength of the composite in that direction, while for axial loading the fibres are dominating the strength of the laminate.

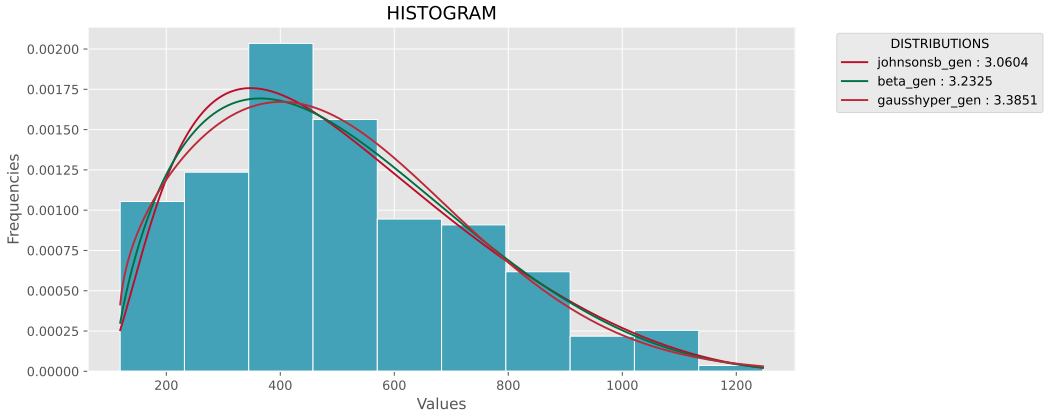

FIGURE 5.8: Axial Tensile Strength Properties Distribution (MPa)

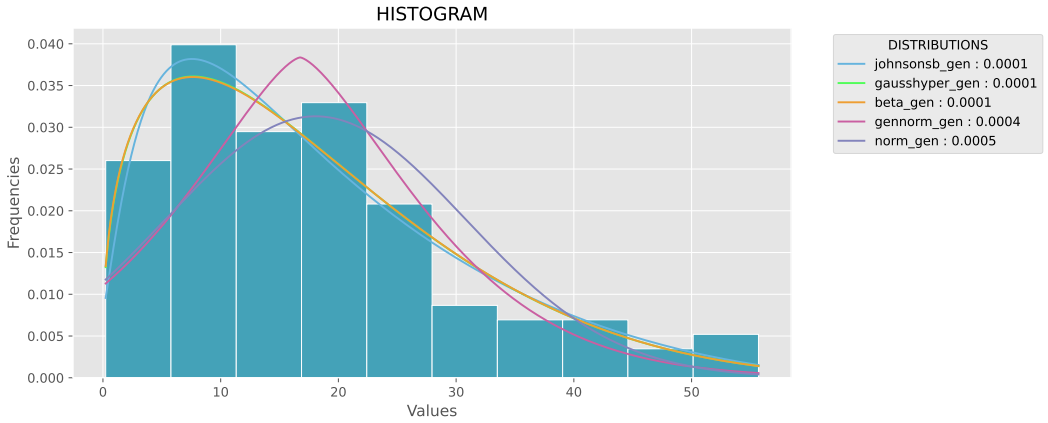

FIGURE 5.9: Transverse Tensile Strength Properties Distribution (MPa)

5.2.6 Integrity of risers exposed to stochastic waves

This section aims to investigate the full-scale riser response, using the full multi-scale algorithm developed in this thesis. The riser geometrical properties in table 3.1 and cross-sectional properties listed in tables 3.5 and 3.6 are used in this section to create a multi-scale model. The scatter diagram shown in table 5.4 is the long-term met-ocean wave data for the north of Shetland region. The scatter diagram provides information about the expected wave heights and the associated peak wave periods and it's occurrence over 25 years period. Wave heights and periods are divided into bins, in which waves that fits the bins wave height and period criteria fall into it and the number of occurrences are predicted. The analysis performed in this section is not a reliability study, therefore it doesn't aim to predict the probability of failure of the composite riser in real environment, however the main aim of this analysis is to predict the failure of a specific riser configuration that is exposed to realistic environmental loading of a typical sea states in the north sea region, using the full multi-scale approach developed in this thesis, including peridynamics. The peridynamics failure predictions are benchmarked against Tsai-Wu failure criterion predictions.

TABLE 5.3: Operational Conditions

Description	Value	Units
Internal Pressure	200	*bar*
Temperature	80	C°

RiSim code is used to simulate the wave bins using stochastic sea-states. Each wave bin is simulated using 3 hours JONSWAP spectrum. The riser is assumed to be connected to the FPSO, which is under dynamic motion due to wave conditions and exposed to harsh operational conditions as shown in table 5.3. This is simulated using FLEXCOM software and the dynamic motion of the riser hang-off point is extracted for each wave bin and is used as a boundary condition to RiSim code. RiSim simulates the dynamic motion of the riser and predicts tension and angle at each node along the riser length. The multi-scale algorithm, CRIMMO shown in the appendix 5, is a multi-scale python code created for this analysis and is used to extract tensions, angles at two hot-spot locations, the touch-down zone and hang-off zone. The algorithm extracts wall tensions and rotation angles for a length that covers the hot-spot region. The nodes at which the tensions and rotation angles are extracted is determined based on the tension and curvature values that is lower than 10% of the hot-spot values. This is to minimize the boundary conditions effects on the hotspot response in the composite pipe FEA model. It is found that failure predicted for few of the wave bin cases are due to buckling at the composite pipe scale, this is only captured by combining the far-field loading with the pipe and laminate scale models. The temperature, pressure effects combined with the dynamic motion of the riser initiates a buckling effect that leads to the composite riser failure due to extreme strain that initiates failure at a microscopic level.

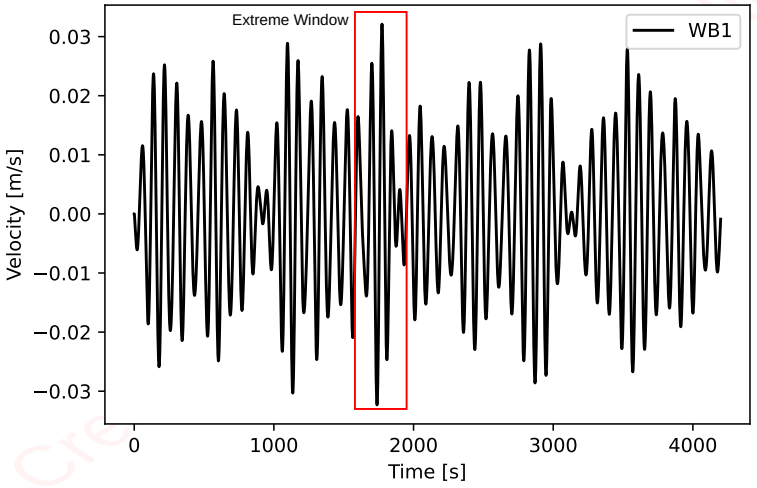

FIGURE 5.10: Stochastic node velocity (m/s)

The multi-scale frame-work and the information flow diagram between the scales are shown in figure 5.12. A dynamic analysis of the composite riser us performed, using stochastic waves. The extreme wave conditions, which is typical to the north sea region, are used in the analysis. The global analysis is performed using RiSim, simulating 3 hours of stochastic waves simulation for each wave bin. The composite riser is modelled using beam formulation, where the tensions and rotation angles are extracted for an extreme response window. A shorter simulation window is selected, based on the global simulation results, extending 100 seconds around the maximum tension and curvature onset as shown in figure 5.10. The multi-scale algorithm creates approximately 12 m length of the composite pipe model around the hot-spot region. The length of the section is selected to maintain the tension and curvature at 10% of the hot-spot predicted values, to reduce the boundary effects in the composite pipe FEA model. The boundary conditions that are post-processed from the RiSim analysis results are rotation angles at both end nodes of the selected section and wall tension time-traces. The Abaqus model is post-processed for the maximum principle logarithmic strain along the composite pipe length. The strain values are used as an input to the peridynamics model and simulates, in a quasi-static model, the

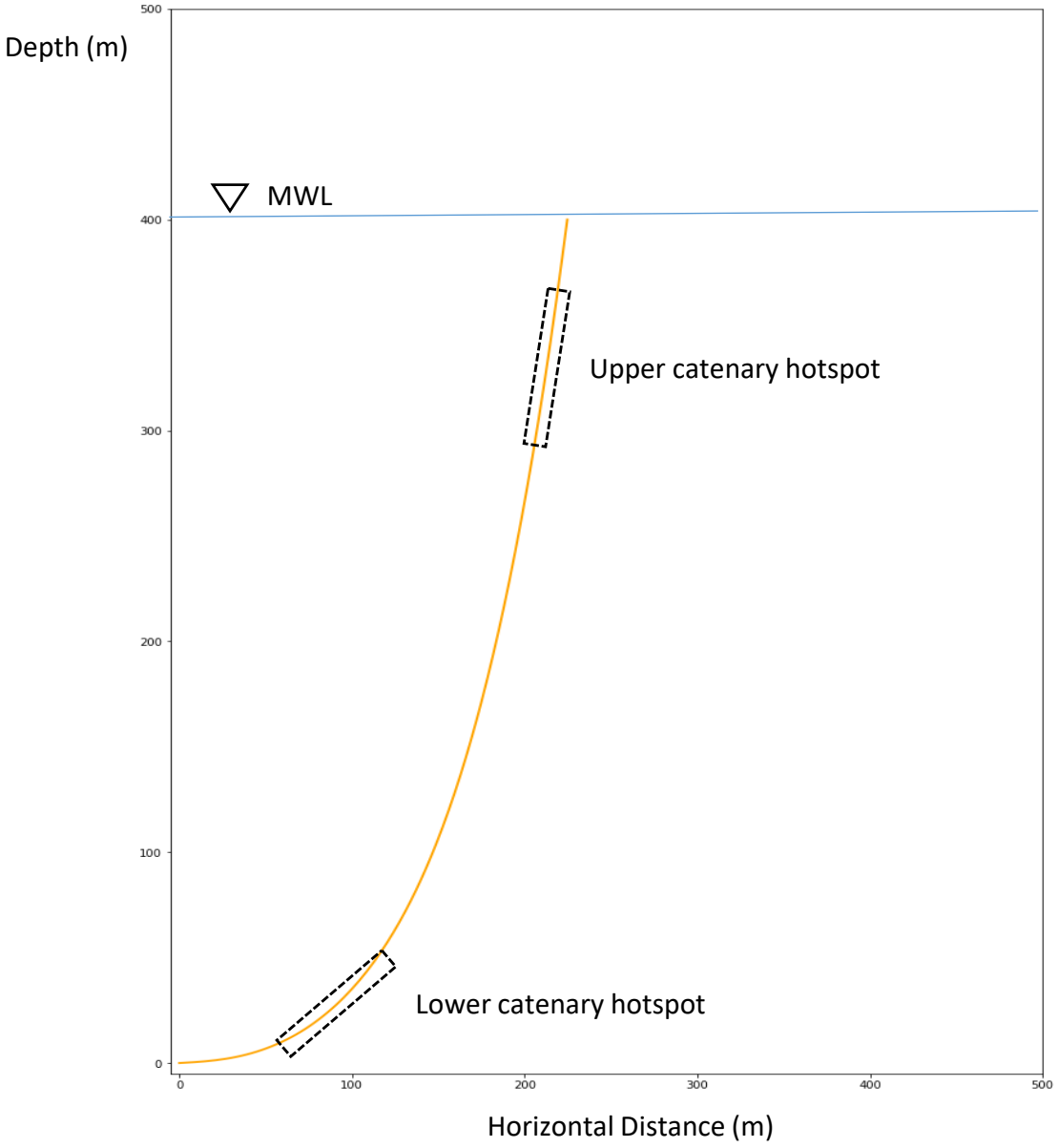

FIGURE 5.11: Composite Riser Hotspots

predicted damage for each wave bin in the RVE as shown in figure 5.14.The damage predicted with the peridynamics micro-model, assuming 5% void content is compared to the Tsai-Wu failure criterion, that is evaluated with equation 3.16. Th Tsai-Wu failure criterion is calculated based on the axial, transverse and shear stresses that are post-processed directly from the composite pipe FEA Abaqus model, using the composite laminate post-processed results at the outer-ply.

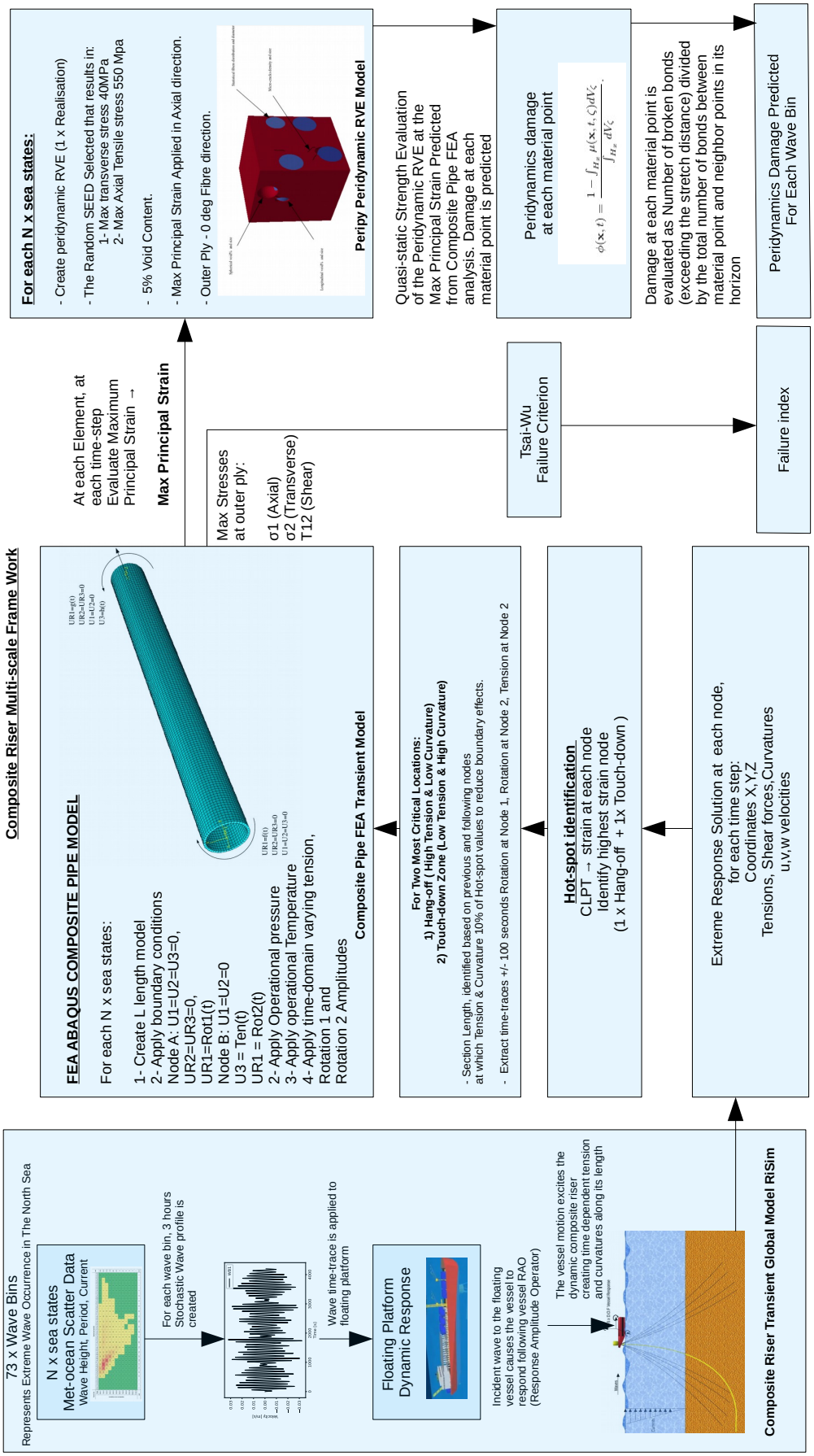

FIGURE 5.12: Multi-scale Framework Flow Diagram

The onset of failure is assessed using both Tsai-Wu criterion and peridynamics elastic bond damage model. Tsai-Wu failure criterion, is a quadratic, stress-based criterion that predicts ply failure, if any of the three principal stresses exceeds the ultimate strength value, by evaluating the equality shown in equation 5.13. The maximum stresses are post-processed of the FEA composite pipe analysis in the axial and transverse directions in addition to shear stress. The criterion assumes no interaction between stress components, moreover it doesn't account for micro-level variations of laminate properties such as fibre diameter and distribution, voids size and distribution.

$$\left(\frac{\sigma_1}{X_t X_C}\right)^2+\left(\frac{\sigma_2}{Y_t Y_C}\right)^2+\left(\frac{1}{X_T}-\frac{1}{X_C}\right)\sigma_1+\left(\frac{1}{Y_T}-\frac{1}{Y_C}\right)\sigma_2+\left(\frac{2F_1 2\sigma_1\sigma_2}{\sqrt{X_T X_C Y_T Y_C}}\right)+\left(\frac{\tau_{12}}{S_{12}}\right)^2=1 \quad (5.13)$$

$$F1=\frac{1}{X_t}-\frac{1}{X_c} \quad (5.14)$$

The peridynamics damage concept is a micro modelling approach, The bond damage model is a strain based non-local failure model, which is applied at the fibre and matrix micro levels. The peridynamics model accounts for the fibre and void diameter variation and distribution, which are directly modelled. Both two failure prediction methods used in this analysis can't be directly compared, since peridynamics models encapsulates the details of the microscopic geometrical properties of the RVE, while Tsai-Wu is applied at the ply level and relies on ply stresses. The aim is to compare both methods final predicted failure, as a benchmark, while investigating the opportunities that comes with peridynamics non-local modelling capabilities.

The peridynamics damage is given by equation 5.18, where the damage at each material point, which is at microscopic scale, is given by the sum of damaged bonds, divided by the total bonds (of all damaged material points) within the horizon volume of that material point. The total damage in the RVE is the total number damaged bonds among all damaged material points to the total number of bonds for all damaged material points. A damaged bond in peridynamics is given by equation **??** where the bond is considered either intact or damaged. Damaged bonds are those that are stretched beyond a critical stretch value at microscopic level. The critical stretch is given by equation 5.16 which is a function of the strain energy release rate of the material, and is determined experimentally. The damage in peridynamics initiates when the first bond is broken at a specific material point, due to exceeding the critical stretch limit, after which the force interaction between this point and the other points within it's horizon are re-distributed between the remaining intact bonds. This force redistribution increases the force per bond share, leading to higher stretching of these bonds and eventually the crack propagates until final failure. This process occurs at independent sites in the RVE, depending on the geometry, loading axes and force distribution within the RVE.

$$\mu(t,\zeta)=\begin{cases}1 & if\ s(t',\zeta)<s_0 \quad \forall 0\le t'\le t\\ 0 & \text{otherwise}\end{cases} \quad (5.15)$$

$$s_0=\sqrt{\frac{5G_0}{9\kappa\delta}} \quad (5.16)$$

The bond model used in this analysis is given by equations 5.15 and 5.16 is based on binary state of the elastic bonds failure. Which is used for linear elastic brittle materials, similar to carbon fibre and the matrix which are common for composite pipe failures. This bond model definition results in an abrupt failure of the bond, which is dominating the sudden failure observed as shown in figure 5.14.

There are alternative bond models that can be implemented to provide progressive failure damage and material properties degradation to substitute the model used in this analysis. As the example shown in equation 5.17 and figure 5.13, which is bond model developed for cohesive quasi brittle materials [11]. Multiple other models are possible depending on the material behaviour. However the current analysis focuses on ultimate strength of the composite pipe under extreme loading conditions in offshore low temperature environment,where the outer ply is expected to be exposed to temperature down to 4 deg C, therefore the classical bond model is chosen to be suitable to predict the brittle sudden failure under extreme loading.

$$\mu(t,\zeta) = \begin{cases} cs & , s < s_0 \\ cs_0 \left(\exp^{-k\frac{s-s_0}{s_0}} + \alpha\frac{s-s_0}{s} \right) & , s > s_0 \end{cases} \tag{5.17}$$

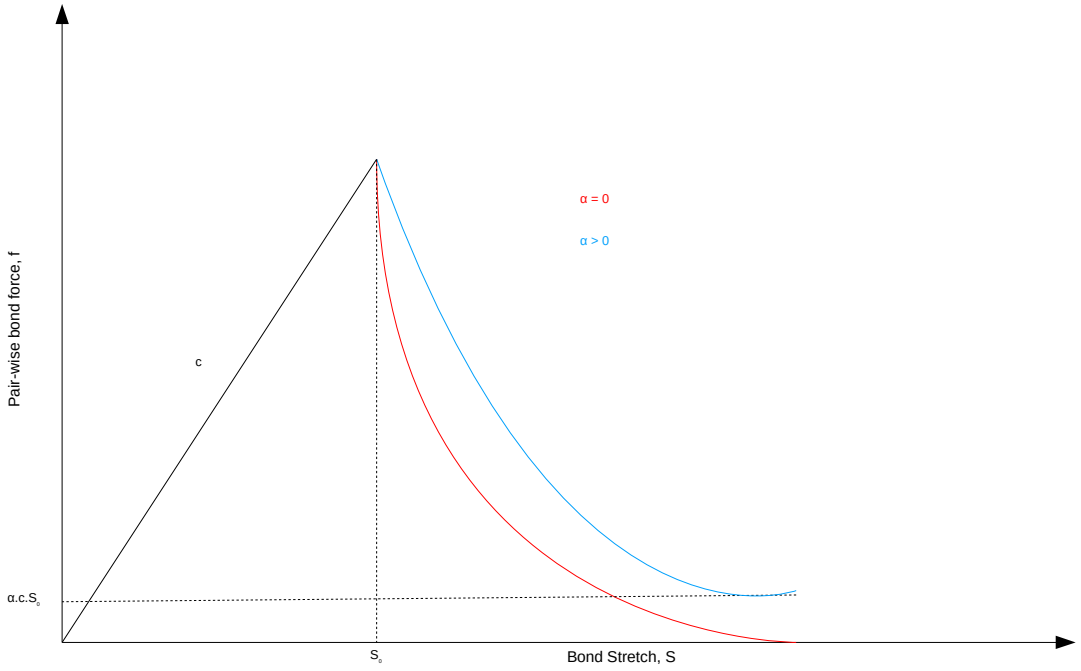

FIGURE 5.13: Cohesive Quasi-brittle bond damage model [11]

Tsai-Wu failure criterion and peridynamics damage can not be linearly correlated beyond failure index equal to unity, since both predictions are focusing on different parameters of failure. The Tsai-Wu failure criterion is a quadratic approximation of the yield ellipsoidal surface which cannot be open-ended, with the use of strength tensors. Any Tsai-Wu failure index exceeding unity means that the stress vector $\sigma_1, \vec{\sigma_2}, \tau_{12}$ reaches the failure ellipsoid surface defined by the equality shown in equation 5.13. There is no meaningful interpretation or information in the literature about the failure index higher than unity and the relation between the Tsai-Wu failure index that exceeds unity and peridynamics damage, moreover, there are multiple limits imposed by the stability conditions in the formulation. Therefore, no correlation against the damage predicted by peridynamics is expected, other than the final failure conclusion [170]. Further research in this area is required. Therefore, The index value is only interpreted in this work to indicate failure, without speculating on the physical interpretation of index values that exceeds unity. Peridynamics bond damage captures micro cracks initiation as a damage at a specific material point, in such case peridynamics predicts a damage percentage at each material point and globally ratio of the total damage. The damage in peridynamics can occur at multiple material points and the damage parameter keeps track of the failure initiation and progression or history of the damage. However, Tsai-Wu failure criterion is based on evaluating failure in composite ply based on principal stress components. Tsai-Wu have been successfully used to predict composite failures, but peridynamics shows promising

technique to predict micro cracks and evolution of fracture, given specific manufacturing defects, such as voids, opening the door for more deeper understanding of the microstructure effect on failure.

$$\phi(\mathbf{x}, t) = \frac{1 - \int_{H_x} \mu(\mathbf{x}, t, \zeta) dV_\zeta}{\int_{H_x} dV_\zeta}. \tag{5.18}$$

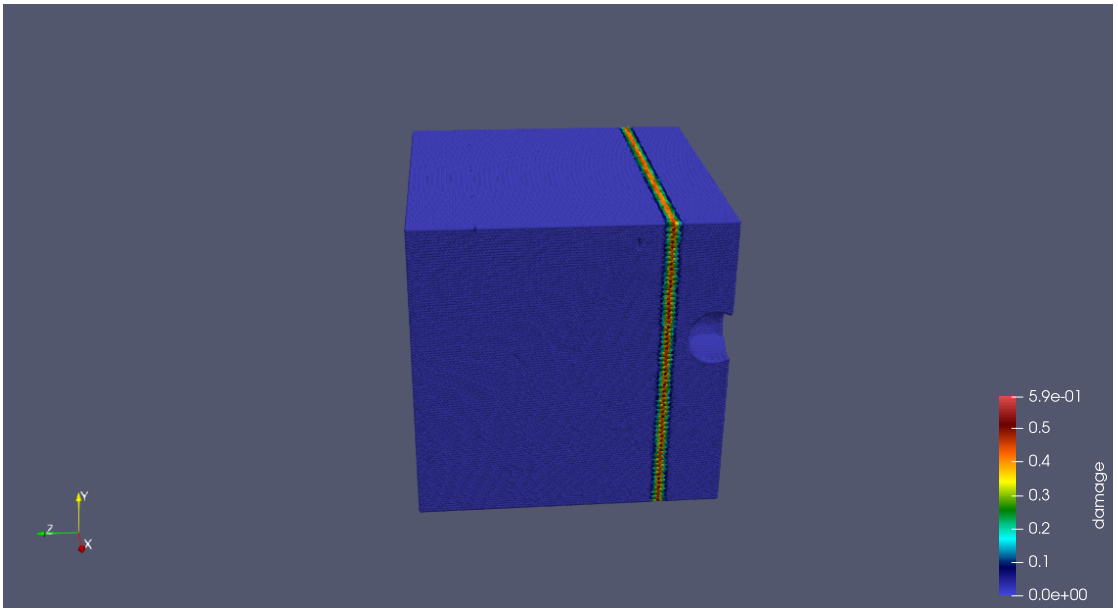

FIGURE 5.14: RVE damage

The analysis results shows similar final failure predictions for both peridynamics and Tsai-Wu criterion. The Tsai-Wu failure index results are plotted on figure 5.15, which shows that for all wave bins, both touch-down and hang-off zones first ply failure is predicted with failure index larger than unity. It is observed that the for the majority of wave blocks a large failure index is observe.

Comparing the Tsai-Wu failure index shown in figure 5.15 to the peridynamics predicted total damage of the damaged material points bonds, it is shown in figure 5.16 that for the majority of wave blocks 100% bonds failure is not reached. However,for all wave bins the damaged material points have a damage higher than 50%. It is difficult to draw a line to what is considered as a total failure. The total damaged material points damage is shown to be on average 80% of the cross-sectional total bonds that are broken for most of the wave blocks, although it is not 100% bonds failure, however in reality that means the crack initiated and propagating and that will be considered as failure. the Tsai-Wu failure index and peridynamics damage results are shown in table 5.4, highlighting that for all wave bins both theories predict outer-ply failure. The peridynamics RVE is created with 5% void content, however the Tsai-Wu criterion doesn't account for voids in the material. Although, as a final conclusion both theories predicts failure. Peridynamics total damage, although it doesn't predict 100% cross-sectional material points failure, but a complete crack surface is formed and also considered as failure.

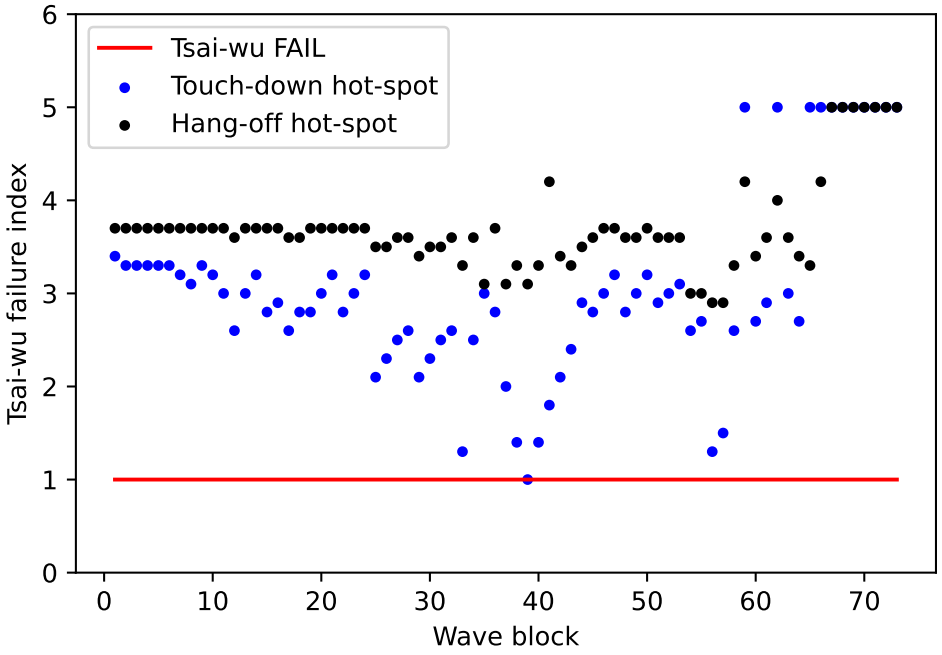

FIGURE 5.15: Wave blocks Tsai-Wu failure index

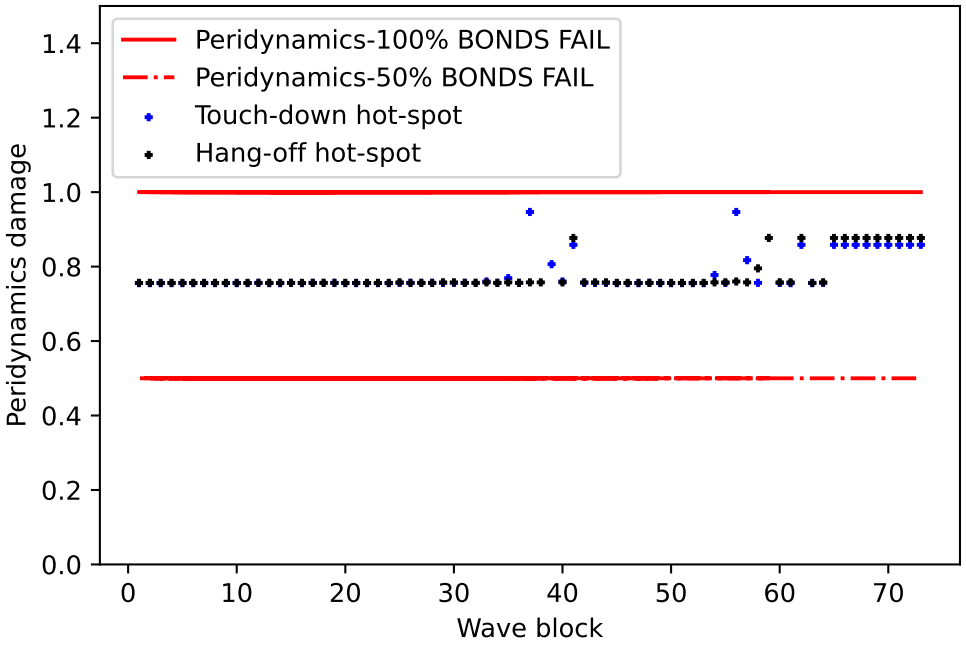

FIGURE 5.16: Wave blocks peridynamics damage

Table 5.4: Wave scatter diagram failure assessment - Touch-down Zone

Wave Block	Wave Height, H (m)	Wave Period, Tp (s)	TDZ Tsai-Wu	Status	TDZ Peri	Status
1	1	5.8	3.36	FAIL	0.76	FAIL
2	3	6.4	3.34	FAIL	0.76	FAIL
3	5	6.7	3.27	FAIL	0.76	FAIL
4	7	7	3.34	FAIL	0.76	FAIL
5	1	8.9	3.34	FAIL	0.76	FAIL
6	2	9	3.29	FAIL	0.76	FAIL
7	3	9	3.24	FAIL	0.76	FAIL
8	7	8.5	3.15	FAIL	0.76	FAIL
9	1	10.9	3.29	FAIL	0.76	FAIL
10	2	10.9	3.16	FAIL	0.76	FAIL
11	3	10.9	3.01	FAIL	0.76	FAIL
12	7	10.4	2.58	FAIL	0.76	FAIL
13	5	9.5	3.02	FAIL	0.76	FAIL
14	4	9.5	3.2	FAIL	0.76	FAIL
15	5	10.5	2.82	FAIL	0.76	FAIL
16	4	10.5	2.93	FAIL	0.76	FAIL
17	5	11.5	2.62	FAIL	0.76	FAIL
18	4	11.5	2.77	FAIL	0.76	FAIL
19	3	12.5	2.82	FAIL	0.76	FAIL
20	2	12.5	3.02	FAIL	0.76	FAIL
21	1	12.5	3.24	FAIL	0.76	FAIL
22	3	13.5	2.82	FAIL	0.76	FAIL
23	2	13.5	2.97	FAIL	0.76	FAIL
24	1	13.5	3.23	FAIL	0.76	FAIL
25	7	12.5	2.07	FAIL	0.76	FAIL
26	6	12.5	2.28	FAIL	0.76	FAIL
27	5	12.5	2.47	FAIL	0.76	FAIL
28	4	12.5	2.64	FAIL	0.76	FAIL
29	7	13.5	2.1	FAIL	0.76	FAIL
30	6	13.5	2.29	FAIL	0.76	FAIL
31	5	13.5	2.47	FAIL	0.77	FAIL
32	4	13.5	2.63	FAIL	0.76	FAIL
33	12	12.5	1.29	FAIL	0.76	FAIL
34	7	10.7	2.5	FAIL	0.76	FAIL
35	12	14.8	3	FAIL	0.76	FAIL
36	12	9.2	2.81	FAIL	0.76	FAIL
37	14	13	2	FAIL	0.76	FAIL
38	18	14.9	1.37	FAIL	0.76	FAIL
39	16	12.3	0.98	FAIL	0.76	FAIL
40	18	12.6	1.37	FAIL	0.86	FAIL
41	23	13	1.76	FAIL	0.76	FAIL
42	7	14.9	2.12	FAIL	0.76	FAIL
43	7	17	2.38	FAIL	0.76	FAIL
44	7	22.9	2.88	FAIL	0.76	FAIL
45	3	14.5	2.78	FAIL	0.76	FAIL
46	2	14.5	3.03	FAIL	0.76	FAIL
47	1	14.5	3.22	FAIL	0.76	FAIL
48	3	15.5	2.8	FAIL	0.76	FAIL
49	2	15.5	2.99	FAIL	0.76	FAIL
50	1	15.5	3.23	FAIL	0.76	FAIL
51	3	17.1	2.94	FAIL	0.76	FAIL
52	3	20	2.97	FAIL	0.78	FAIL
53	3	23	3.08	FAIL	0.76	FAIL
54	12	17	2.55	FAIL	0.95	FAIL
55	12	19.9	2.69	FAIL	0.82	FAIL
56	14	14.9	1.3	FAIL	0.76	FAIL
57	14	17	1.55	FAIL	0.76	FAIL
58	18	16.9	2.56	FAIL	0.76	FAIL
59	23	14.9	5	FAIL	0.76	FAIL
60	7	20	2.71	FAIL	0.86	FAIL
61	7	26	2.95	FAIL	0.76	FAIL
62	21.8	17.6	5	FAIL	0.76	FAIL
63	6	30.27	3.04	FAIL	0.86	FAIL
64	12	22.98	2.7	FAIL	0.86	FAIL
65	18	19.73	5	FAIL	0.86	FAIL
66	23	18.69	5	FAIL	0.86	FAIL
67	23	10.46	5	FAIL	0.86	FAIL
68	23	16.79	5	FAIL	0.86	FAIL
69	27	12.14	5	FAIL	0.86	FAIL
70	27	14.44	5	FAIL	0.86	FAIL
71	27	16.92	5	FAIL	0.86	FAIL
72	32	16.9	5	FAIL	0.86	FAIL
73	34	14.3	5	FAIL	0.86	FAIL

TABLE 5.5: Wave scatter diagram failure assessment - Hang-off Zone

Wave Block	Wave Height, H (m)	Wave Period, Tp (s)	HO Tsai-Wu	Status	HO Peri	Status
1	1	5.8	3.75	FAIL	0.76	FAIL
2	3	6.4	3.74	FAIL	0.76	FAIL
3	5	6.7	3.74	FAIL	0.76	FAIL
4	7	7	3.74	FAIL	0.76	FAIL
5	1	8.9	3.74	FAIL	0.76	FAIL
6	2	9	3.73	FAIL	0.76	FAIL
7	3	9	3.72	FAIL	0.76	FAIL
8	7	8.5	3.7	FAIL	0.76	FAIL
9	1	10.9	3.72	FAIL	0.76	FAIL
10	2	10.9	3.7	FAIL	0.76	FAIL
11	3	10.9	3.68	FAIL	0.76	FAIL
12	7	10.4	3.63	FAIL	0.76	FAIL
13	5	9.5	3.69	FAIL	0.76	FAIL
14	4	9.5	3.7	FAIL	0.76	FAIL
15	5	10.5	3.65	FAIL	0.76	FAIL
16	4	10.5	3.67	FAIL	0.76	FAIL
17	5	11.5	3.63	FAIL	0.76	FAIL
18	4	11.5	3.65	FAIL	0.76	FAIL
19	3	12.5	3.65	FAIL	0.76	FAIL
20	2	12.5	3.69	FAIL	0.76	FAIL
21	1	12.5	3.72	FAIL	0.76	FAIL
22	3	13.5	3.65	FAIL	0.76	FAIL
23	2	13.5	3.66	FAIL	0.76	FAIL
24	1	13.5	3.71	FAIL	0.76	FAIL
25	7	12.5	3.5	FAIL	0.76	FAIL
26	6	12.5	3.54	FAIL	0.76	FAIL
27	5	12.5	3.59	FAIL	0.76	FAIL
28	4	12.5	3.62	FAIL	0.76	FAIL
29	7	13.5	3.42	FAIL	0.76	FAIL
30	6	13.5	3.47	FAIL	0.76	FAIL
31	5	13.5	3.52	FAIL	0.76	FAIL
32	4	13.5	3.57	FAIL	0.76	FAIL
33	12	12.5	3.27	FAIL	0.76	FAIL
34	7	10.7	3.61	FAIL	0.76	FAIL
35	12	14.8	3.09	FAIL	0.76	FAIL
36	12	9.2	3.69	FAIL	0.76	FAIL
37	14	13	3.05	FAIL	0.76	FAIL
38	18	14.9	3.3	FAIL	0.88	FAIL
39	16	12.3	3.1	FAIL	0.76	FAIL
40	18	12.6	3.3	FAIL	0.76	FAIL
41	23	13	4.22	FAIL	0.76	FAIL
42	7	14.9	3.36	FAIL	0.76	FAIL
43	7	17	3.35	FAIL	0.76	FAIL
44	7	22.9	3.54	FAIL	0.76	FAIL
45	3	14.5	3.6	FAIL	0.76	FAIL
46	2	14.5	3.65	FAIL	0.76	FAIL
47	1	14.5	3.7	FAIL	0.76	FAIL
48	3	15.5	3.6	FAIL	0.76	FAIL
49	2	15.5	3.65	FAIL	0.76	FAIL
50	1	15.5	3.7	FAIL	0.76	FAIL
51	3	17.1	3.59	FAIL	0.76	FAIL
52	3	20	3.63	FAIL	0.76	FAIL
53	3	23	3.64	FAIL	0.76	FAIL
54	12	17	2.99	FAIL	0.76	FAIL
55	12	19.9	3.02	FAIL	0.76	FAIL
56	14	14.9	2.85	FAIL	0.8	FAIL
57	14	17	2.86	FAIL	0.88	FAIL
58	18	16.9	3.3	FAIL	0.76	FAIL
59	23	14.9	4.22	FAIL	0.76	FAIL
60	7	20	3.45	FAIL	0.76	FAIL
61	7	26	3.56	FAIL	0.88	FAIL
62	21.8	17.6	4	FAIL	0.76	FAIL
63	6	30.27	3.58	FAIL	0.76	FAIL
64	12	22.98	3.38	FAIL	0.88	FAIL
65	18	19.73	3.3	FAIL	0.88	FAIL
66	23	18.69	4.22	FAIL	0.88	FAIL
67	23	10.46	5	FAIL	0.88	FAIL
68	23	16.79	5	FAIL	0.88	FAIL
69	27	12.14	5	FAIL	0.88	FAIL
70	27	14.44	5	FAIL	0.88	FAIL
71	27	16.92	5	FAIL	0.88	FAIL
72	32	16.9	5	FAIL	0.88	FAIL
73	34	14.3	5	FAIL	0.88	FAIL

Chapter 6

Conclusion and recommendations

6.1 Conclusion

The effect of far-field loading on composite risers, combined with uncertainties in the laminate mechanical properties is investigated. A multi-scale modelling framework is utilised, with three numerical models. The riser model is finite difference Fortran code that is developed based on beam theory formulation, RiSim. Beam theory is a simplified approach to reduce the complexity and the total number of degrees of freedom required to model the total riser length, which can be longer than 500m. The response of the riser under harsh environmental conditions and vessel excitation is captured using wave theories and Morisons equation. The composite pipe model, which uses the risers model tensions and curvatures predictions as boundary conditions, is created in finite element package Abaqus. A python multi-scale framework is developed to automate the loads post-processing produced with RiSim and creates a composite pipe length to predict the response through the pipe cross-section. Shell elements are used and the maximum principal strain among all elements is post-processed. A peridynamics RVE model is developed and used to predict fracture at the element that exhibits the highest maximum principal strain, at the outer ply, using the parallelised python package PeriPy. The analysis is performed utilising the high performance computing facility , Iridis 5.

All developed algorithms are benchmarked against commercial software packages or published literature as shown in sections 3, 5. Loads and material uncertainties are investigated in this study at multiple levels, which propagates from the far-field loadings, that are due to the response of the floating vessel and the riser to the temporal variation of the environmental conditions, coupled with the effect of these loading regimes on the composite riser response, given the inherited uncertainties in the composite laminates mechanical properties. Finally all research components are combined together to investigate the effect of far-field stochastic environmental conditions on the integrity of composite risers, which is susceptible to mechanical properties uncertainties due to void entrapment, fibre diameter variation and variation in its distribution. The analysis of the full-scale system is carried out simulate the riser response that is exposed to stochastic environmental conditions. A wave scatter diagram representative of the north of Shetland area, UK is used. Utilising the RiSim composite riser macro model, FEA composite pipe meso model and finally the micro peridynamics RVE model. The damage predicted for each wave bin is calculated with both peridynamics and Tsai-Wu failure criterion.

The findings of this work are summarised as follows:

1. RiSim, the finite difference extensible beam modelling algorithm that is developed as part of this thesis, is able to capture the composite riser response with less than 1% percentage difference wen benchmarked against commercial packages. The riser top tension predicted with in-extensible formulation experiences high frequency oscillations in harsh weather conditions, compared to the extensible formulation as shown in section 3.
2. Reliability of Epoxy based deep-water composite risers is lower in comparison to steel equivalents in-situ, due to moisture absorption. The reliability becomes more pronounced at depths exceeding 2000m. The probability of failure at 1500m, for the riser configuration investigated in this thesis, is 1,700% the dry conditions. While, the probability of failure, for the same riser properties, increases with depth to 19,000% the dry conditions.The variation of composite riser mechanical properties due to water absorption are investigated in section 4
3. Peridynamics has few limitations such as computational capacity. The amount of computational capacity required to model highly detailed peridynamics model requires high performance computational capabilities to solve compared to same problem solved with continuum mechanics FE model.
4. Bond-based peridynamics, which is based on the limitation on material points interaction magnitude and direction is only suitable for materials that are brittle and exhibits a Poisson's ratio close to $\frac{1}{4}$. This is prominent when comparing the predictions of the elastic modulus that are predicted by peridynamics composite RVE model to finite element or experimental methods.
5. Transverse and axial strengths of Carbon-fibre/Epoxy RVE are found to follow Johnson SB distribution, which is observed over three hundred random samples that are created with random voids distribution and fibres diameters following a normal distribution with mean values as shown in table 5.1. The analysis in section 5.2.5 shows that the properties have a mean value corresponds to the experimental average properties values. The effect of voids percentage in the composite matrix as shown in section 5.2.4, the axial and transverse tensile strength reduces between 40% and 70% of the no-void predicted values. This highlights the importance of accurate micro modelling to capture the variation in composite riser properties.
6. Failure prediction, using strain-based bond damage criteria using Peridynamics microscopic RVE model is benchmarked against Tsai-Wu stress-based failure criterion. Both methods predicts same final conclusion for the wave bins analysed in section 5.2.6.
7. Both Tsai-wu and peridynamics predict failure for this composite riser cross section,that is due to the harsh environmental conditions. Peridynamics bond damage is evaluated as shown in section 5.2.6 for wave bins that are representative of harsh weather conditions in the north sea. The damage predicted, on average, among all wave bins analysed is 80% of the fracture surface bonds. Which is failure of the outer ply and the composite riser integrity is compromised.
8. Altough Tsai-Wu failure criterion is successfully used to predict failure, as shown in section 5.2.6 and the criterion is suitable as a rapid design tool. It is found that non-local peridynamics modelling is a promising modelling approach to predict composite failure given specific composite material uncertainties, manufacturing quality and imperfections such as voids. The virtual testing method detailed in this thesis enables to investigate and isolate the manufacturing and environmentally induced imperfections and its effect on the final fracture due to far-field harsh loadings. The method allows manufacturers to optimize the qualification processes and tests required to capture the effect of the composite riser mechanical properties uncertainties on composites failure.

6.2 Recommendations and Future Work

The work presented in this thesis demonstrates that far-field modelling of composite risers using a multi-scale approach to model the far-field loading and the composite pipe response. That includes a non-local micro modelling peridynamics approach, which is demonstrated to be a promising technique that allows to capture complex fracture initiation and propagation responses that occurs in dynamic composite riser, in-situ and exhibits multiple manufacturing defects within its laminate.

The following recommendations and future research that are required to complete the virtual testing framework and add value to composites manufacturers, these recommendations are summarised in the following points:

1. A reliability study is suggested as future research to be performed similar to the study presented in section 4, using the full multi-scale frame work that is developed in the analysis and presented in section 5.2.6. In such analysis it is recommended to perform initial study to predict the suitable number of RVE samples that produces stationary statistical material strength properties distribution.
2. Fatigue analysis is recommended to be analysed in future work using the multi-scale frame work presented in section 5.2.6. A modification of the failure bond model is recommended, following a suitable bond failure model that incorporates progressive damage behaviour similar to the model presented in [11].
3. Moisture absorption is found to negatively affect the mechanical properties of composite risers. It is recommended to investigate in future work the moisture absorption phenomena that affect the composite matrix. There are two physical processes that governs the composite properties uncertainties in such case. Water absorption through micro cracks and moisture accumulation in voids is short term phenomena, in such case the void percentage and operational temperatures will have a large effect on the mechanical properties degradation, usually through the vapour/fluid pressure entrapped in these voids. The second process is through plasticisation which occurs at the molecular level. This process will requires a non-ordinary state-based peridynamics formulation and possibly utilising molecular-dynamics to initiate the constitutive equation of the matrix.
4. Peridynamics calibration using Digital Volume/Image Correlation can be used successfully to calibrate the peridynamics bonds using the strain energy density parameter. In addition to characterizing matrix micro-cracks and voids percentage that has a direct effect on fracture. This shall done using Inverse Bayesian approach where multi-level Markov Chain Monte Carlo simulation is used to calibrate the uncertainty in the modelling and experimental biases.The research is promising and has a great potential to create a truly digital twin at the material level that could be able to replicate experiments and failure process.
5. Markov Chain Monte Carlo simulations are suggested to be implemented with peridynamics virtual testing framework to capture the effect of each of the environmental and material uncertainties on composite riser integrity, enhancing partial safety factors of the load and material resistance factors used in the codes and standards.

References

[1] Yong Bai, , and Qiang Bai. Ocean engineeringseries. In *Subsea Pipelines and Risers*. Elsevier Science Ltd, Oxford, 2005. ISBN 978-0-08-044566-3. doi: https://doi.org/10.1016/B978-008044566-3.50045-2. URL http://www.sciencedirect.com/science/article/pii/B9780080445663500452.

[2] Composite Leadership Forum. The 2016 uk composite strategy. Technical report, 2016.

[3] Deepflex. URL http://www.deepflex.com/.

[4] Magma global. URL https://www.magmaglobal.com/.

[5] Airborne oil and gas. URL https://airborneoilandgas.com.

[6] R.E. Rudd and J.Q. Broughton. Concurrent coupling of length scales in solid state systems. *physica status solidi (b)*, 217(1):251–291, 2000. ISSN 1521-3951. doi: 10.1002/(SICI)1521-3951(200001)217:1⟨251::AID-PSSB251⟩3.0.CO;2-A. URL http://dx.doi.org/10.1002/(SICI)1521-3951(200001)217:1<251::AID-PSSB251>3.0.CO;2-A.

[7] Wei Z. Mechanical and fatigue test of cfrp risers, 2015.

[8] L.B. Tan, Y. Chen, Rajeev K. Jaiman, X. Sun, V.B.C. Tan, and T.E. Tay. Coupled fluid–structure simulations for evaluating a performance of full-scale deepwater composite riser. *Ocean Engineering*, 94:19–35, 2015. ISSN 0029-8018. doi: https://doi.org/10.1016/j.oceaneng.2014.11.007. URL https://www.sciencedirect.com/science/article/pii/S0029801814004193.

[9] L. Wu, D. Tjahjanto, G. Becker, A. Makradi, A. Jérusalem, and L. Noels. A micro–meso-model of intra-laminar fracture in fiber-reinforced composites based on a discontinuous galerkin/cohesive zone method. *Engineering Fracture Mechanics*, 104:162–183, 2013. ISSN 0013-7944. doi: https://doi.org/10.1016/j.engfracmech.2013.03.018. URL https://www.sciencedirect.com/science/article/pii/S0013794413001252.

[10] Hai Van Choi Kyoung-Kyu Truong, Gia Toai Tran. Tensile behavior of carbon fiber-reinforced polymer composites incorporating nanomaterials after exposure to elevated temperature. *Journal of Nanomaterials*, 2019, 2019. ISSN 1687-4110. doi: https://doi.org/10.1155/2019/4139208.

[11] Yue Tong, Wanqing Shen, Jianfu Shao, and Jueliang Chen. A new bond model in peridynamics theory for progressive failure in cohesive brittle materials. *Engineering Fracture Mechanics*, 223:106767, January 2020. doi: 10.1016/j.engfracmech.2019.106767. URL https://hal.science/hal-02500691.

[12] Det Norske Veritas. Dynamic risers. 2010. URL https://rules.dnv.com/docs/pdf/dnvpm/codes/docs/2010-10/RP-F201.pdf.

[13] Det Norske Veritas. Dnv-rp-c205 composite risers. 2010. URL https://rules.dnv.com/docs/pdf/dnvpm/codes/docs/2010-10/RP-F202.pdf.

[14] Peter C Chu. Weibull distribution for the global surface current speeds obtained from satellite altimetry. In *IGARSS 2008-2008 IEEE International Geoscience and Remote Sensing Symposium*, volume 3, pages III–59. IEEE, 2008.

[15] Yu. M. Tarnopol'skii, V. L. Kulakov, and D. D. Mungalov. Composites in offshore technology in the next century. *Mechanics of Composite Materials*, 35(5):365–372, 1999. ISSN 0191-5665. doi: 10.1007/BF02329321.

[16] Ozden O. Ochoa and Mamdouh M. Salama. Offshore composites: Transition barriers to an enabling technology. *Composites Science and Technology*, 65:2588–2596, 2005. ISSN 02663538. doi: 10.1016/j.compscitech.2005.05.019.

[17] Turid Stothaug Brian Spencer Mamdouh M. Salama, Gisle Stjern and Andreas Echtermeyer. The First Offshore Field Installation for a Composite Riser Joint. 2002.

[18] F.J.Fischer. Composite production risers for deepwater offshore structures. *Oil and Gas Science and Technology*, pages 35 – 43, 1995. doi: DOI:10.2516/ogst:1995003. URL https://www.researchgate.net/publication/239385596_Composite_Production_Risers_for_Deepwater_Offshore_Structures.

[19] Dinh-Chi Pham, N. Sridhar, Xudong Qian, Adam J. Sobey, Mithila Achintha, and Ajit Shenoi. A review on design, manufacture and mechanics of composite risers. *Ocean Engineering*, 112:82–96, 2016. ISSN 00298018. doi: 10.1016/j.oceaneng.2015.12.004.

[20] Det Norske Veritas. Recommended practice composite risers. 2010. URL https://rules.dnv.com/docs/pdf/dnvpm/codes/docs/2010-10/RP-F202.pdf.

[21] Jon Espen Skogdalen and Jan Erik Vinnem. Quantitative risk analysis offshore—human and organizational factors. *Reliability Engineering and System Safety*, 96(4):468–479, 2011. ISSN 0951-8320. doi: https://doi.org/10.1016/j.ress.2010.12.013. URL https://www.sciencedirect.com/science/article/pii/S0951832010002693.

[22] Jon Espen Skogdalen and Jan Erik Vinnem. Quantitative risk analysis of oil and gas drilling, using deepwater horizon as case study. *Reliability Engineering and System Safety*, 100:58–66, 2012. ISSN 0951-8320. doi: https://doi.org/10.1016/j.ress.2011.12.002. URL https://www.sciencedirect.com/science/article/pii/S0951832011002651.

[23] Dinh-Chi Pham, N. Sridhar, Xudong Qian, Adam J. Sobey, Mithila Achintha, and Ajit Shenoi. A review on design, manufacture and mechanics of composite risers. *Ocean Engineering*, 112: 82 – 96, 2016. ISSN 0029-8018. doi: http://dx.doi.org/10.1016/j.oceaneng.2015.12.004. URL http://www.sciencedirect.com/science/article/pii/S0029801815006587.

[24] DNV Det Norske Veritas. Recommended practice, composite risers, dnv-rp-f202. 2010. URL http://rules.dnvgl.com/docs/pdf/DNV/codes/docs/2010-10/RP-F202.pdf.

[25] M.J Hinton and P.D Soden. Predicting failure in composite laminates: the background to the exercise. *Composites Science and Technology*, 58(7):1001 – 1010, 1998. ISSN 0266-3538.

[26] P. A. M. Dirac. New dnv gl projects have potential to save 10m. *Oil and gas people*, 2015. URL http://www.oilandgaspeople.com/news/4888/new-dnv-gl-projects-have-potential-to-save-10m/.

[27] J. LLorca, C. González, J. M. Molina-Aldareguía, J. Segurado, R. Seltzer, F. Sket, M. Rodríguez, S. Sádaba, R. Muñoz, and L. P. Canal. Multiscale modeling of composite materials: a roadmap towards virtual testing. *Advanced Materials*, 23(44):5130–5147, 2011. ISSN 1521-4095. doi: 10.1002/adma.201101683. URL http://dx.doi.org/10.1002/adma.201101683.

[28] A. G. Gibson. The cost effective use of fibre reinforced composites offshore. 2003. URL http://www.hse.gov.uk/research/rrpdf/rr039.pdf.

[29] Alain H Peyrot and Alain M Goulois. Analysis of flexible transmission lines. *Journal of the Structural Division*, 104(5):763–779, 1978.

[30] A.H. Pevrot and A.M. Goulois. Analysis of cable structures. *Computers and Structures*, 10(5): 805 – 813, 1979. ISSN 0045-7949. doi: http://dx.doi.org/10.1016/0045-7949(79)90044-0. URL http://www.sciencedirect.com/science/article/pii/0045794979900440.

[31] F.B. Seyed and M.H. Patel. Mathematics of flexible risers including pressure and internal flow effects. *Marine Structures*, 5(2):121 – 150, 1992. ISSN 0951-8339.

[32] a. T. Nettles. Basic Mechanics of Laminated Composite Plates. (October):107, 1994. URL http://www.ntrs.nasa.gov/archive/nasa/casi.ntrs.nasa.gov/19950009349{_}1995109349.pdf.

[33] S. Srinivas and A.K. Rao. A three-dimensional solution for plates and laminates. *Journal of the Franklin Institute*, 291(6):469 – 481, 1971. ISSN 0016-0032. doi: http://dx.doi.org/10.1016/0016-0032(71)90004-4. URL http://www.sciencedirect.com/science/article/pii/0016003271900044.

[34] J.N.Reddy. *Mechanics of Laminated Composite Plates and Shells*. 2 edition, 2003. ISBN 0-8493-1592-1. doi: https://doi.org/10.1201/b12409.

[35] Branca F. Oliveira and Guillermo J. Creus. An analytical–numerical framework for the study of ageing in fibre reinforced polymer composites. *Composite Structures*, 65(3):443 – 457, 2004. ISSN 0263-8223. doi: https://doi.org/10.1016/j.compstruct.2003.12.006. URL http://www.sciencedirect.com/science/article/pii/S0263822303003647.

[36] Chao Zhang, Wieslaw K. Binienda, Gregory N. Morscher, Richard E. Martin, and Lee W. Kohlman. Experimental and FEM study of thermal cycling induced microcracking in carbon/epoxy triaxial braided composites. *Composites Part A: Applied Science and Manufacturing*, 46(1):34–44, 2013. ISSN 1359835X. doi: 10.1016/j.compositesa.2012.10.006. URL http://dx.doi.org/10.1016/j.compositesa.2012.10.006.

[37] M. Meng, M. J. Rizvi, S. M. Grove, and H. R. Le. Effects of hygrothermal stress on the failure of CFRP composites. *Composite Structures*, 133:1024–1035, 2015. ISSN 02638223. doi: 10.1016/j.compstruct.2015.08.016.

[38] M. Meng, M. J. Rizvi, H. R. Le, and S. M. Grove. Multi-scale modelling of moisture diffusion coupled with stress distribution in CFRP laminated composites. *Composite Structures*, 138:295–304, 2016. ISSN 02638223. doi: 10.1016/j.compstruct.2015.11.028.

[39] Xiaopeng Shi, Shulin Li, Fei Chang, and Dongliang Bian. Postbuckling and failure analysis of stiffened composite panels subjected to hydro/thermal/mechanical coupled environment under axial compression. *Composite Structures*, 118(1):600–606, 2014. ISSN 02638223. doi: 10.1016/j.compstruct.2014.08.022. URL http://dx.doi.org/10.1016/j.compstruct.2014.08.022.

[40] Pal G. Bergan, Egil Mollestad, and Nils Sandsmark. Nonlinear static and dynamic response analysis for floating offshore structures. *Engineering Computations*, 2(1):13–20, 1985. doi: 10.1108/eb023596.

[41] D. L. Garrett. Dynamic analysis of slender rods. *Journal of Energy Resources Technology*, 104, 1982. doi: 10.1115/1.3230419.

[42] T. Huang and S. Chucheepsakul. Large displacement analysis of a marine riser. *Journal of Energy Resources Technology, Transactions of the ASME*, 107(1):54–59, 1985. ISSN 15288994.

[43] Erkan Oterkus and Erdogan Madenci. Peridynamic analysis of fiber-reinforced composite materials erkan oterkus and erdogan madenci. *Journal of Mechanics of Materials and Structures*, 7(1):45–84, 2012. ISSN 1559-3959. doi: 10.2140/jomms.2012.7.45.

[44] X. S. Sun, Y. Chen, V. B. C. Tan, R. K. Jaiman, and T. E. Tay. Homogenization and Stress Analysis of Multilayered Composite Offshore Production Risers. *Journal of Applied Mechanics*, 81(3):031003, 2013. ISSN 0021-8936. doi: 10.1115/1.4024695.

[45] R. TALREJA. Damage analysis for structural integrity and durability of composite materials. *Fatigue & Fracture of Engineering Materials & Structures*, 29(7):481–506, 2006. doi: 10.1111/j.1460-2695.2006.00974.x. URL https://onlinelibrary.wiley.com/doi/abs/10.1111/j.1460-2695.2006.00974.x.

[46] Kl Reifsnider and Scott W Case. Damage tolerance and durability of material systems. *Damage Tolerance and Durability of Material Systems, by Kenneth L. Reifsnider, Scott W. Case, pp. 435. ISBN 0-471-15299-4. Wiley-VCH , April 2002.*, -1, 03 2002.

[47] Pierre Ladeveze, Gilles Lubineau, David Violeau, and David Marsal. A computational damage micromodel for laminate composites. *Solid Mechanics and its Applications*, 135:1–12, 01 2006. doi: 10.1007/1-4020-4566-2_1.

[48] T.J. Vaughan and C.T. McCarthy. A combined experimental–numerical approach for generating statistically equivalent fibre distributions for high strength laminated composite materials. *Composites Science and Technology*, 70(2):291 – 297, 2010. ISSN 0266-3538. doi: https://doi.org/10.1016/j.compscitech.2009.10.020. URL http://www.sciencedirect.com/science/article/pii/S0266353809003832.

[49] Masaki Hojo, Masaaki Mizuno, Thomas Hobbiebrunken, Taiji Adachi, Mototsugu Tanaka, and Sung ha. Effect of fiber array irregularities on microscopic interfacial normal stress states of transversely loaded ud-cfrp from viewpoint of failure initiation. *Composites Science and Technology*, 69, 09 2009. doi: 10.1016/j.compscitech.2008.08.032.

[50] M. Bernitsas John E. Kokarakis Asjhar Imron Michael. Large deformation three-dimensional static analysis of deep water marine risers. *Applied Ocean Research*, 7, 1985. doi: 10.1016/0141-1187(85)90024-0.

[51] K M Mathisen and P G Bergan. Nonlinear static analysis of flexible risers. 1986. URL https://trid.trb.org/view.aspx?id=429265.

[52] M.H. Patel and F.B. Seyed. Review of flexible riser modelling and analysis techniques. *Engineering Structures*, 17(4):293 – 304, 1995. ISSN 0141-0296. doi: http://dx.doi.org/10.1016/0141-0296(95)00027-5.

[53] M. Xia, H. Takayanagi, and K. Kemmochi. Analysis of multi-layered filament-wound composite pipes under internal pressure. *Composite Structures*, 53(4):483 – 491, 2001. ISSN 0263-8223. doi: https://doi.org/10.1016/S0263-8223(01)00061-7. URL http://www.sciencedirect.com/science/article/pii/S0263822301000617.

[54] Hamid Reza Eipakchi. THIRD-ORDER SHEAR DEFORMATION THEORY FOR STRESS ANALYSIS OF A THICK CONICAL SHELL UNDER PRESSURE. *Journal of Applied Mechanics and Structures*, 2010.

[55] Hongyan Zhu, Baochang Wu, Dihong Li, Dongxing Zhang, and Yuyong Chen. Influence of Voids on the Tensile Performance of Carbon/epoxy Fabric Laminates. *Journal of Materials Science and Technology*, 27(1):69–73, 2011. ISSN 10050302. doi: 10.1016/S1005-0302(11)60028-5. URL http://dx.doi.org/10.1016/S1005-0302(11)60028-5.

[56] A. E. Scott, I. Sinclair, S. M. Spearing, M. N. Mavrogordato, and W. Hepples. Influence of voids on damage mechanisms in carbon/epoxy composites determined via high resolution computed tomography. *Composites Science and Technology*, 90:147–153, 2014. ISSN 02663538. doi: 10.1016/j.compscitech.2013.11.004. URL http://dx.doi.org/10.1016/j.compscitech.2013.11.004.

[57] Anders Sjögren. *Matrix and Interface Effects on Microcracking in Polymer Composites*. PhD thesis, 1997.

[58] R Talreja. A conceptual framework for studies of durability in composite materials. In *Fatigue of Textile Composites*, pages 3–27. 2015. ISBN 9781782422938. doi: 10.1016/B978-1-78242-281-5.00001-8.

[59] Pierre Jacques Liotier, Vautrin Alain, and Delisée Christine. Characterization of 3D morphology and microcracks in composites reinforced by multi-axial multi-ply stitched preforms. *Composites Part A: Applied Science and Manufacturing*, 41(5):653–662, 2010. ISSN 1359835X. doi: 10.1016/j.compositesa.2010.01.015. URL http://dx.doi.org/10.1016/j.compositesa.2010.01.015.

[60] T. Li and W. Yang. Expected coalescing length of displacement loading collinear microcracks. *Theoretical and Applied Fracture Mechanics*, 36(1):17–21, 2001. ISSN 01678442. doi: 10.1016/S0167-8442(01)00052-0.

[61] A. Engseth, A. Bech and C M Larsen. Efficient method for analysis of flexible risers. 1988. URL https://trid.trb.org/view.aspx?id=433272.

[62] J. F. McNamara, P. J. O'Brien, and S. G. Gilroy. Nonlinear Analysis of Flexible Risers Using Hybrid Finite Elements. *Journal of Offshore Mechanics and Arctic Engineering*, 110(3):197–204, 08 1988. ISSN 0892-7219. doi: 10.1115/1.3257051.

[63] S.K. Rege and S.C. Lakkad. Effect of salt water on mechanical properties of fibre reinforced plastics. *Fibre Science and Technology*, 19(4):317 – 324, 1983. ISSN 0015-0568. doi: http://dx.doi.org/10.1016/0015-0568(83)90017-9. URL http://www.sciencedirect.com/science/article/pii/0015056883900179.

[64] Yucheng Zhong and Sunil Chandrakant Joshi. Impact behavior and damage characteristics of hygrothermally conditioned carbon epoxy composite laminates. *Materials and Design (1980-2015)*, 65:254 – 264, 2015. ISSN 0261-3069. doi: https://doi.org/10.1016/j.matdes.2014.09.030. URL http://www.sciencedirect.com/science/article/pii/S0261306914007316.

[65] Akawut Siriruk and Dayakar Penumadu. Degradation in fatigue behavior of carbon fiber–vinyl ester based composites due to sea environment. *Composites Part B: Engineering*, 61:94 – 98, 2014. ISSN 1359-8368. doi: https://doi.org/10.1016/j.compositesb.2014.01.030. URL http://www.sciencedirect.com/science/article/pii/S1359836814000407.

[66] Innocent Kafodya, Guijun Xian, and Hui Li. Durability study of pultruded CFRP plates immersed in water and seawater under sustained bending: Water uptake and effects on the mechanical properties. *Composites Part B: Engineering*, 70:138–148, 2015. ISSN 13598368. doi: 10.1016/j.compositesb.2014.10.034. URL http://dx.doi.org/10.1016/j.compositesb.2014.10.034.

[67] P. J. O'Brien and J. F. McNamara. Analysis of Flexible Riser Systems Subject to Three-Dimensional Seastate Loading. *Int. Conf. on Behaviour of Offshore Structures (BOSS '88)*, pages 1373–1388, 1988.

[68] R. P. Nordgren. On computation of the motion of elastic rods. *Journal of Applied Mechanics*, 41, 1974. doi: 10.1115/1.3423387.

[69] MJ Casarella and M Parsons. Cable systems under hydrodynamic loading. *Marine Technology Society Journal*, 4(4):27–44, 1970. ISSN 00253324.

[70] Mario J. Choc, Young-Il; Casarella. Configuration of a towline attached to a vehicle moving in a circular path. *Journal of Hydronautics*, 6, 01 1972. doi: 10.2514/3.62894.

[71] C.M. Ablow and S. Schechter. Numerical simulation of undersea cable dynamics. *Ocean Engineering*, 10(6):443 – 457, 1983. ISSN 0029-8018. doi: http://dx.doi.org/10.1016/0029-8018(83)90046-X.

[72] Ioannis K. Chatjigeorgiou. A finite differences formulation for the linear and nonlinear dynamics of 2d catenary risers. *Ocean Engineering*, 35(7):616 – 636, 2008. ISSN 0029-8018. doi: https://doi.org/10.1016/j.oceaneng.2008.01.006.

[73] Spyros A. Chatjigeorgiou, Ioannis K.and Mavrakos. *Cable Dynamics for Marine Applications*, pages 875–906. Springer International Publishing, Cham, 2016. ISBN 978-3-319-16649-0. doi: 10.1007/978-3-319-16649-0_38.

[74] Qiao, Hongdong, Ruan, Weidong, Shang, Zhaohui, and Bai, Yong. Non-linear static analysis of offshore steep wave riser. *MATEC Web of Conferences*, 65:01009, 2016. doi: 10.1051/matecconf/20166501009. URL https://doi.org/10.1051/matecconf/20166501009.

[75] Isaac Fried. Large deformation static and dynamic finite element analysis of extensible cables. *Computers and Structures*, 15(3):315 – 319, 1982. ISSN 0045-7949. doi: http://dx.doi.org/10.1016/0045-7949(82)90022-0.

[76] M.H. Patel; A.S. Jesudasen. Theory and model tests for the dynamic response of free hanging risers. *Journal of Sound and Vibration*, 112, 1987. doi: 10.1016/s0022-460x(87)80099-8.

[77] R.P. Cowan, R.; Andris. Total pipelaying system dynamics. doi: 10.4043/2914-MS.

[78] F. S. Hover, M. A. Grosenbaugh, and M. S. Triantafyllou. Calculation of dynamic motions and tensions in towed underwater cables. *IEEE Journal of Oceanic Engineering*, 19(3):449–457, Jul 1994. ISSN 0364-9059.

[79] Castelazo Carrillo, Barranco Sicilia, and Francisco Casanova-del Angel. Structural reliability in catenary upstream pipelines. *El Portulano de la Ciencia*, III:907–914, 02 2011.

[80] Feng Zi Li and Ying Min Low. Fatigue reliability analysis of a steel catenary riser at the touchdown point incorporating soil model uncertainties. *Applied Ocean Research*, 38:100–110, 2012. ISSN 0141-1187. doi: https://doi.org/10.1016/j.apor.2012.07.005. URL https://www.sciencedirect.com/science/article/pii/S0141118712000661.

[81] Forbes; Bruton David A.S. Carr, Malcolm; Sinclair. Pipeline walking understanding the field layout challenges and analytical solutions developed for the safebuck jip. *SPE Projects Facilities and Construction*, 3, 2008. doi: safebuckJIP. URL https://www.onepetro.org/journal-paper/SPE-120022-PA.

[82] Ahmed Reda, Ibrahim A. Sultan, Ian M. Howard, Gareth L. Forbes, and Kristoffer K. McKee. Pipeline walking and anchoring considerations in the presence of riser motion and inclined seabed. *International Journal of Pressure Vessels and Piping*, 162:71 – 85, 2018. ISSN 0308-0161. doi: https://doi.org/10.1016/j.ijpvp.2018.01.003. URL http://www.sciencedirect.com/science/article/pii/S0308016117303824.

[83] Ahmed Reda, Kristoffer K. McKee, Ian M. Howard, and Ibrahim A. Sultan. When is a subsea anchor required for a short pipeline/scr system? *International Journal of Pressure Vessels and Piping*, 171:278 – 298, 2019. ISSN 0308-0161. doi: https://doi.org/10.1016/j.ijpvp.2019.02.009. URL http://www.sciencedirect.com/science/article/pii/S0308016118304204.

[84] A. I. Beyle, C. G. Gustafson, V. L. Kulakov, and Yu M. Tarnopol'skii. Composite risers for deep-water offshore technology: Problems and prospects. 1. Metal-composite riser. *Mechanics of Composite Materials*, 33(5):403–414, 1997. ISSN 01915665. doi: 10.1007/BF02256894.

[85] Ahmed M. Reda, Gareth L. Forbes, Faisal Al-Mahmoud, Ian M. Howard, Kristoffer K. McKee, and Ibrahim A. Sultan. Compression limit state of hvac submarine cables. *Applied Ocean Research*, 56:12 – 34, 2016. ISSN 0141-1187. doi: https://doi.org/10.1016/j.apor.2016.01.002. URL http://www.sciencedirect.com/science/article/pii/S0141118716000031.

[86] Zhuang Kang, Li Zhang, and Xiang Zhang. Analysis on j lay of scr based on catenary and large deflection beam theory. *Ocean Engineering*, 104:276–282, 2015. ISSN 0029-8018. doi: https://doi.org/10.1016/j.oceaneng.2015.05.017. URL https://www.sciencedirect.com/science/article/pii/S0029801815001936.

[87] Jin Ping Zhan. Review and verification of marine riser analysis programs. Master's thesis, Norges teknisk-naturvitenskapelige universitet, Fakultet for . . . , 2010.

[88] Christopher Bridge. *Effects of seabed interaction on steel catenary risers*. University of Surrey (United Kingdom), 2005.

[89] Rafael Fernandes da Silva, Fábio Anderson Fonteles Teófilo, Evandro Parente, Antônio Macário Cartaxo de Melo, and Áurea Silva de Holanda. Optimization of composite catenary risers. *Marine Structures*, 33:1–20, 2013. ISSN 0951-8339. doi: https://doi.org/10.1016/j.marstruc.2013.04.002. URL https://www.sciencedirect.com/science/article/pii/S0951833913000294.

[90] S Timoshenko, D H Young, and W Weaver. *Vibration Problems in Engineering*, volume 208. 1990. ISBN 0471632287. doi: 10.1038/208964b0.

[91] Michael M. Bernitsas and John E. Kokarakis. Importance of nonlinearities in static riser analysis. *Applied Ocean Research*, 10(1):2 – 9, 1988. ISSN 0141-1187. doi: https://doi.org/10.1016/S0141-1187(88)80019-1.

[92] P.J. O'Brien and J.F. McNamara. Significant characteristics of three-dimensional flexible riser analysis. *Engineering Structures*, 11(4):223 – 233, 1989. ISSN 0141-0296. doi: https://doi.org/10.1016/0141-0296(89)90041-2.

[93] B. D. Edmans, D. C. Pham, Z.-Q. Zhang, T. F. Guo, N. Sridhar, and G. Stewart. An Effective Multiscale Methodology for the Analysis of Marine Flexible Risers. *Journal of Marine Science and Engineering*, 7(10):340, 2019. ISSN 2077-1312. doi: 10.3390/jmse7100340. URL https://www.mdpi.com/2077-1312/7/10/340.

[94] F. A. Leckie and G.M. Lindberg. The effect of lumped parameters on beam frequencies. *Aeronautical Quarterly*, 14(3):224–240, 1963. doi: 10.1017/S0001925900002791.

[95] M. S. Triantafyllou. The dynamics of taut inclined cables. *The Quarterly Journal of Mechanics and Applied Mathematics*, 37(3):421–440, 1984. doi: 10.1093/qjmam/37.3.421.

[96] Adam J. Sadowski and J. Michael Rotter. Solid or shell finite elements to model thick cylindrical tubes and shells under global bending. *International Journal of Mechanical Sciences*, 74:143 – 153, 2013. ISSN 0020-7403. doi: https://doi.org/10.1016/j.ijmecsci.2013.05.008.

[97] Chunguang Wang, Krishnakumar Shankar, and Evgeny V. Morozov. Tailored local design of deep sea frp composite risers. *Advanced Composite Materials*, 24(4):375–397, 2015. doi: 10.1080/09243046.2014.898438.

[98] M.J. Hinton, P.D. Soden, and A.S. Kaddour. Failure criteria in fibre-reinforced-polymer composites. In M.J. Hinton, A.S. Kaddour, and P.D. Soden, editors, *Failure Criteria in Fibre-Reinforced-Polymer Composites*. Elsevier, Oxford, 2004. ISBN 978-0-08-044475-8.

[99] Matthews FL. Camanho PP, Bowron S. Failure mechanisms in bolted cfrp. *Journal of Reinforced Plastics and Composites*, 1998. 17:205-33.

[100] Frédéric Feyel. Multiscale {FE2} elastoviscoplastic analysis of composite structures. *Computational Materials Science*, 16(1–4):344 – 354, 1999. ISSN 0927-0256. doi: https://doi.org/10.1016/S0927-0256(99)00077-4. URL http://www.sciencedirect.com/science/article/pii/S0927025699000774.

[101] Frédéric Feyel and Jean-Louis Chaboche. {FE2} multiscale approach for modelling the elastoviscoplastic behaviour of long fibre sic/ti composite materials. *Computer Methods in Applied Mechanics and Engineering*, 183(3–4):309 – 330, 2000. ISSN 0045-7825. doi: https://doi.org/10.1016/S0045-7825(99)00224-8. URL http://www.sciencedirect.com/science/article/pii/S0045782599002248.

[102] Matthew Mosby and Karel Matouš. Computational homogenization at extreme scales. *Extreme Mechanics Letters*, 6:68 – 74, 2016. ISSN 2352-4316. doi: https://doi.org/10.1016/j.eml.2015.12.009. URL http://www.sciencedirect.com/science/article/pii/S2352431615300134.

[103] Somnath Ghosh and Suresh Moorthy. Elastic-plastic analysis of arbitrary heterogeneous materials with the voronoi cell finite element method. *Computer Methods in Applied Mechanics and Engineering*, 121(1):373 – 409, 1995. ISSN 0045-7825. doi: https://doi.org/10.1016/0045-7825(94)00687-I. URL http://www.sciencedirect.com/science/article/pii/004578259400687I.

[104] Somnath Ghosh, Zdzislaw Nowak, and Kyunghoon Lee. Quantitative characterization and modeling of composite microstructures by voronoi cells. *Acta Materialia*, 45(6):2215 – 2234, 1997. ISSN 1359-6454. doi: https://doi.org/10.1016/S1359-6454(96)00365-5. URL http://www.sciencedirect.com/science/article/pii/S1359645496003655.

[105] Jacob Fish, Qing Yu, and Kamlun Shek. Computational damage mechanics for composite materials based on mathematical homogenization. *International Journal for Numerical Methods in Engineering*, 45(11):1657–1679. doi: 10.1002/(SICI)1097-0207(19990820)45:11⟨1657::AID-NME648⟩3.0.CO;2-H.

[106] Pablo Seleson, Michael L. Parks, Max Gunzburger, and Richard B. Lehoucq. Peridynamics as an upscaling of molecular dynamics. *Multiscale Modeling and Simulation*, 8:204–227, 2009.

[107] S.A. Silling. Reformulation of elasticity theory for discontinuities and long-range forces. *Journal of the Mechanics and Physics of Solids*, 48(1):175 – 209, 2000. ISSN 0022-5096. doi: http://dx.doi.org/10.1016/S0022-5096(99)00029-0. URL http://www.sciencedirect.com/science/article/pii/S0022509699000290.

[108] S. A. Silling, M. Epton, O. Weckner, J. Xu, and E. Askari. Peridynamic states and constitutive modeling. *Journal of Elasticity*, 88(2):151–184, 2007. ISSN 1573-2681. doi: 10.1007/s10659-007-9125-1. URL http://dx.doi.org/10.1007/s10659-007-9125-1.

[109] Thomas L. Warren, Stewart A. Silling, Abe Askari, Olaf Weckner, Michael A. Epton, and Jifeng Xu. A non-ordinary state-based peridynamic method to model solid material deformation and fracture. *International Journal of Solids and Structures*, 46(5):1186 – 1195, 2009. ISSN 0020-7683. doi: http://dx.doi.org/10.1016/j.ijsolstr.2008.10.029. URL http://www.sciencedirect.com/science/article/pii/S0020768308004496.

[110] Richard W. Macek and Stewart A. Silling. Peridynamics via finite element analysis. *Finite Elements in Analysis and Design*, 43(15):1169 – 1178, 2007. ISSN 0168-874X. doi: http://dx.doi.org/10.1016/j.finel.2007.08.012. URL http://www.sciencedirect.com/science/article/pii/S0168874X07001035.

[111] Q. Tong and S. Li. A multiscale molecular dynamics allowing macroscale mechanical loads. *EPL*, 110(6), 2015. doi: 10.1209/0295-5075/110/60005. cited By 0.

[112] Qi Tong and Shaofan Li. Multiscale coupling of molecular dynamics and peridynamics. *Journal of the Mechanics and Physics of Solids*, 95:169 – 187, 2016. ISSN 0022-5096. doi: http://dx.doi.org/10.1016/j.jmps.2016.05.032. URL http://www.sciencedirect.com/science/article/pii/S0022509615303422.

[113] Shaofan Li and Shingo Urata. An atomistic-to-continuum molecular dynamics: Theory, algorithm, and applications. *Computer Methods in Applied Mechanics and Engineering*, 306: 452 – 478, 2016. ISSN 0045-7825. doi: http://dx.doi.org/10.1016/j.cma.2016.03.048. URL http://www.sciencedirect.com/science/article/pii/S0045782516301359.

[114] J.A.Elliott. Novel approaches to multiscale modelling in materials science. 2011. URL http://people.ds.cam.ac.uk/jae1001/CUS/research/Elliott_IMR_2011_corrected_proof.pdf.

[115] N Bernstein, J R Kermode, and G Csányi. Hybrid atomistic simulation methods for materials systems. *Reports on Progress in Physics*, 72(2):026501, 2009. URL http://stacks.iop.org/0034-4885/72/i=2/a=026501.

[116] R. Car and M. Parrinello. Unified approach for molecular dynamics and density-functional theory. *Phys. Rev. Lett.*, 55:2471–2474, Nov 1985. doi: 10.1103/PhysRevLett.55.2471. URL https://link.aps.org/doi/10.1103/PhysRevLett.55.2471.

[117] W. Kohn and L. J. Sham. Self-consistent equations including exchange and correlation effects. *Phys. Rev.*, 140:A1133–A1138, Nov 1965. doi: 10.1103/PhysRev.140.A1133. URL https://link.aps.org/doi/10.1103/PhysRev.140.A1133.

[118] P. Hohenberg and W. Kohn. Inhomogeneous electron gas. *Phys. Rev.*, 136:B864–B871, Nov 1964. doi: 10.1103/PhysRev.136.B864. URL https://link.aps.org/doi/10.1103/PhysRev.136.B864.

[119] J. C. Slater and G. F. Koster. Simplified lcao method for the periodic potential problem. *Phys. Rev.*, 94:1498–1524, Jun 1954. doi: 10.1103/PhysRev.94.1498. URL https://link.aps.org/doi/10.1103/PhysRev.94.1498.

[120] B. J. Alder and T. E. Wainwright. Studies in molecular dynamics. i. general method. *The Journal of Chemical Physics*, 31(2):459–466, 1959. doi: 10.1063/1.1730376. URL http://dx.doi.org/10.1063/1.1730376.

[121] P. Hohenberg and W. Kohn. *Phys. Rev.*, 136:B864–B871, Nov 1964. doi: 10.1103/PhysRev.136.B864. URL https://link.aps.org/doi/10.1103/PhysRev.136.B864.

[122] Alessandro Laio and Michele Parrinello. Escaping free-energy minima. *Proceedings of the National Academy of Sciences*, 99(20):12562–12566, 2002. doi: 10.1073/pnas.202427399. URL http://www.pnas.org/content/99/20/12562.abstract.

[123] Arthur F. Voter. Hyperdynamics: Accelerated molecular dynamics of infrequent events. *Phys. Rev. Lett.*, 78:3908–3911, May 1997. doi: 10.1103/PhysRevLett.78.3908. URL https://link.aps.org/doi/10.1103/PhysRevLett.78.3908.

[124] E. Weinan, Xiantao Li, and Eric Vanden-Eijnden. *Some Recent Progress in Multiscale Modeling*, pages 3–21. Springer Berlin Heidelberg, Berlin, Heidelberg, 2004. ISBN 978-3-642-18756-8. doi: 10.1007/978-3-642-18756-8_1. URL http://dx.doi.org/10.1007/978-3-642-18756-8_1.

[125] Weinan E. *Principles of Multiscale Modeling*. 2011. URL http://www.cambridge.org/gb/academic/subjects/mathematics/mathematical-modelling-and-methods/principles-multiscale-modeling?format=HB&isbn=9781107096547.

[126] M. Buehler. *Atomistic Modeling of Materials Failure*. Springer US, 2008. ISBN 9780387764252. URL https://books.google.co.uk/books?id=z5m0NAEACAAJ.

[127] F. F. Abraham, J. Q. Broughton, N. Bernstein, and E. Kaxiras. Spanning the continuum to quantum length scales in a dynamic simulation of brittle fracture. *EPL (Europhysics Letters)*, 44 (6):783, 1998. URL http://stacks.iop.org/0295-5075/44/i=6/a=783.

[128] E. B. Tadmor, M. Ortiz, and R. Phillips. Quasicontinuum analysis of defects in solids. *Philosophical Magazine A*, 73(6):1529–1563, 1996. doi: 10.1080/01418619608243000. URL http://dx.doi.org/10.1080/01418619608243000.

[129] R. Miller, M. Ortiz, R. Phillips, V. Shenoy, and E.B. Tadmor. Quasicontinuum models of fracture and plasticity. *Engineering Fracture Mechanics*, 61(3–4):427 – 444, 1998. ISSN 0013-7944. doi: https://doi.org/10.1016/S0013-7944(98)00047-2. URL http://www.sciencedirect.com/science/article/pii/S0013794498000472.

[130] J. Knap and M. Ortiz. An analysis of the quasicontinuum method. *Journal of the Mechanics and Physics of Solids*, 49(9):1899 – 1923, 2001. ISSN 0022-5096. doi: http://dx.doi.org/10.1016/S0022-5096(01)00034-5. URL http://www.sciencedirect.com/science/article/pii/S0022509601000345. The JW Hutchinson and JR Rice 60th Anniversary Issue.

[131] V.B. Shenoy, R. Miller, E.b. Tadmor, D. Rodney, R. Phillips, and M. Ortiz. An adaptive finite element approach to atomic-scale mechanics—the quasicontinuum method. *Journal of the Mechanics and Physics of Solids*, 47(3):611 – 642, 1999. ISSN 0022-5096. doi: https://doi.org/10.1016/S0022-5096(98)00051-9. URL http://www.sciencedirect.com/science/article/pii/S0022509698000519.

[132] Weinan E and Zhongyi Huang. A dynamic atomistic–continuum method for the simulation of crystalline materials. *Journal of Computational Physics*, 182(1):234 – 261, 2002. ISSN 0021-9991. doi: http://dx.doi.org/10.1006/jcph.2002.7164. URL http://www.sciencedirect.com/science/article/pii/S0021999102971640.

[133] Weinan E and Zhongyi Huang. Matching conditions in atomistic-continuum modeling of materials. *Phys. Rev. Lett.*, 87:135501, Sep 2001. doi: 10.1103/PhysRevLett.87.135501. URL https://link.aps.org/doi/10.1103/PhysRevLett.87.135501.

[134] Gregory J. Wagner and Wing Kam Liu. Coupling of atomistic and continuum simulations using a bridging scale decomposition. *Journal of Computational Physics*, 190(1):249 – 274, 2003. ISSN 0021-9991. doi: http://dx.doi.org/10.1016/S0021-9991(03)00273-0. URL http://www.sciencedirect.com/science/article/pii/S0021999103002730.

[135] Harold S. Park, Eduard G. Karpov, Patrick A. Klein, and Wing Kam Liu. Three-dimensional bridging scale analysis of dynamic fracture. *Journal of Computational Physics*, 207(2):588 – 609, 2005. ISSN 0021-9991. doi: http://dx.doi.org/10.1016/j.jcp.2005.01.028. URL http://www.sciencedirect.com/science/article/pii/S0021999105000422.

[136] Assyr Abdulle and Achim Nonnenmacher. A short and versatile finite element multiscale code for homogenization problems. *Computer Methods in Applied Mechanics and Engineering*, 198 (37–40):2839 – 2859, 2009. ISSN 0045-7825. doi: https://doi.org/10.1016/j.cma.2009.03.019. URL http://www.sciencedirect.com/science/article/pii/S0045782509001273.

[137] Patrick Henning and Mario Ohlberger. The heterogeneous multiscale finite element method for elliptic homogenization problems in perforated domains. *Numerische Mathematik*, 113(4):601–629, 2009. ISSN 0945-3245. doi: 10.1007/s00211-009-0244-4. URL http://dx.doi.org/10.1007/s00211-009-0244-4.

[138] Robert E. Rudd. The atomic limit of finite element modeling in mems: Coupling of length scales. *Analog Integrated Circuits and Signal Processing*, 29(1):17–26, 2001. ISSN 1573-1979. doi: 10.1023/A:1011217927309. URL http://dx.doi.org/10.1023/A:1011217927309.

[139] D. Arnold S. Ziaei-Rad T. Rabczuk M. Silani, H. Talebi. On the Coupling of a Commercial Finite Element Package with LAMMPS for Multiscale Modeling of Materials. 2011.

[140] Ioannis G. Kevrekidis, C. William Gear, James M. Hyman, Panagiotis G Kevrekidid, Olof Runborg, and Constantinos Theodoropoulos. Equation-free, coarse-grained multiscale computation: Enabling mocroscopic simulators to perform system-level analysis. *Commun. Math. Sci.*, 1(4): 715–762, 12 2003. URL http://projecteuclid.org/euclid.cms/1119655353.

[141] Jacob Fish, Kamlun Shek, Muralidharan Pandheeradi, and Mark S. Shephard. Computational plasticity for composite structures based on mathematical homogenization: Theory and practice. *Computer Methods in Applied Mechanics and Engineering*, 148(1):53 – 73, 1997. ISSN 0045-7825. doi: http://dx.doi.org/10.1016/S0045-7825(97)00030-3. URL http://www.sciencedirect.com/science/article/pii/S0045782597000303.

[142] Dominique Leguillon. Comparison of matched asymptotics, multiple scalings and averages in homogenization of periodic structures. *Mathematical Models and Methods in Applied Sciences*, 07 (05):663–680, 1997. doi: 10.1142/S0218202597000359. URL http://www.worldscientific.com/doi/abs/10.1142/S0218202597000359.

[143] T.M. Edmunds and J.R. Willis. Matched asymptotic expansions in nonlinear fracture mechanics—ii. longitudinal shear of an elastic work-hardening plastic specimen. *Journal of the Mechanics and Physics of Solids*, 24(4):225 – 237, 1976. ISSN 0022-5096. doi: http://dx.doi.org/10.1016/0022-5096(76)90004-1. URL http://www.sciencedirect.com/science/article/pii/0022509676900041.

[144] Jacob Fish and Vladimir Belsky. Multigrid method for periodic heterogeneous media part 1: Convergence studies for one-dimensional case. *Computer Methods in Applied Mechanics and Engineering*, 126(1):1 – 16, 1995. ISSN 0045-7825. doi: http://dx.doi.org/10.1016/0045-7825(95)00811-E. URL http://www.sciencedirect.com/science/article/pii/004578259500811E.

[145] Jacob Fish and Vladimir Belsky. Multi-grid method for periodic heterogeneous media part 2: Multiscale modeling and quality control in multidimensional case. *Computer Methods in Applied Mechanics and Engineering*, 126(1):17 – 38, 1995. ISSN 0045-7825. doi: http://dx.doi.org/10.1016/0045-7825(95)00812-F. URL http://www.sciencedirect.com/science/article/pii/004578259500812F.

[146] J. Carrier, L. Greengard, and V. Rokhlin. A fast adaptive multipole algorithm for particle simulations. *SIAM Journal on Scientific and Statistical Computing*, 9(4):669–686, 1988. doi: 10.1137/0909044. URL https://doi.org/10.1137/0909044.

[147] L. Greengard and V. Rokhlin. A fast algorithm for particle simulations. *Journal of Computational Physics*, 73(2):325–348, 1987. ISSN 0021-9991. doi: 10.1016/0021-9991(87)90140-9.

[148] Cahal McVeigh, Franck Vernerey, Wing Kam Liu, and L. Cate Brinson. Multiresolution analysis for material design. *Computer Methods in Applied Mechanics and Engineering*, 195(37):5053 – 5076, 2006. ISSN 0045-7825. doi: http://dx.doi.org/10.1016/j.cma.2005.07.027. URL http://www.sciencedirect.com/science/article/pii/S0045782505005372. John H. Argyris Memorial Issue. Part I.

[149] M. J. D. Powell. An efficient method for finding the minimum of a function of several variables without calculating derivatives. *The Computer Journal*, 7(2):155–162, 01 1964. ISSN 0010-4620. doi: 10.1093/comjnl/7.2.155.

[150] K. V. Prasad K. Vajravelu. *Keller-Box method and Its Application*. Berlin, Boston: De Gruyter, 2014. ISBN 978-7-04-038891-6. URL https://www.degruyter.com/view/product/180086.

[151] S.; Dalton C. Rakshit, T.; Atluri. Viv of a composite riser at moderate reynolds number using cfd. *Journal of Offshore Mechanics and Arctic Engineering*, 130, 2008. doi: 10.1115/1.2783849.

[152] Wood (2018). *Flexcom Theory Manual*. Wood.

[153] Carl M. Larsen. Flexible riser analysis comparison of results from computer programs. *Marine Structures*, 5(2):103–119, 1992. ISSN 0951-8339. doi: https://doi.org/10.1016/0951-8339(92)90024-J. URL http://www.sciencedirect.com/science/article/pii/095183399290024J.

[154] J.J. Burgess and M.S. Triantafyllou. The elastic frequencies of cables. *Journal of Sound and Vibration*, 120(1):153 – 165, 1988. ISSN 0022-460X. doi: https://doi.org/10.1016/0022-460X(88)90340-9.

[155] A.J. Sobey, J.I.R. Blake, and R.A. Shenoi. Monte carlo reliability analysis of tophat stiffened composite plate structures under out of plane loading. *Reliability Engineering and System Safety*, 110:41–49, 2013. ISSN 0951-8320. doi: https://doi.org/10.1016/j.ress.2012.08.011. URL https://www.sciencedirect.com/science/article/pii/S0951832012001718.

[156] T.P. Philippidis, D.J. Lekou, and D.G. Aggelis. Mechanical property distribution of cfrp filament wound composites. *Composite Structures*, 45(1):41–50, 1999. ISSN 0263-8223. doi: https://doi.org/10.1016/S0263-8223(99)00012-4. URL https://www.sciencedirect.com/science/article/pii/S0263822399000124.

[157] Jie Xia, Purnendu K. Das, and Daniel Karunakaran. A parametric design study for a semi/scr system in northern north sea. *Ocean Engineering*, 35(17):1686–1699, 2008. ISSN 0029-8018. doi: https://doi.org/10.1016/j.oceaneng.2008.09.007. URL https://www.sciencedirect.com/science/article/pii/S0029801808002023.

[158] Odd Faltinsen. *Sea loads on ships and offshore structures*, volume 1. Cambridge university press, 1993.

[159] Menglan Duan, Jinghao Chen, and Zhigang Li. Mechanics of deepwater steel catenary riser. *Numerical Analysis-Theory and Application*, 2011.

[160] AH Nijhof. Analysis of laminated composites. 1993.

[161] Yanbin Wang, Deli Gao, and Jun Fang. Static analysis of deep-water marine riser subjected to both axial and lateral forces in its installation. *Journal of Natural Gas Science and Engineering*, 19:84–90, 2014. ISSN 1875-5100. doi: https://doi.org/10.1016/j.jngse.2014.04.019. URL https://www.sciencedirect.com/science/article/pii/S1875510014001048.

[162] Thomas Buberg. Design and analysis of steel catenary riser systems for deep waters. Master's thesis, Institutt for marin teknikk, 2014.

[163] Akinyemi Olugbenga Akinsanya, Ove Tobias Gudmestad, and Jasper Agbakwuru. Swell description for bonga offshore nigeria location. *Ocean Systems Engineering*, 7:345–369, 2017. ISSN 2093-6702. doi: 10.12989/ose.2017.7.4.345.

[164] M. Malmstein, A.R. Chambers, and J.I.R. Blake. Hygrothermal ageing of plant oil based marine composites. *Composite Structures*, 101:138–143, 2013. ISSN 0263-8223. doi: https://doi.org/10.1016/j.compstruct.2013.02.003. URL https://www.sciencedirect.com/science/article/pii/S0263822313000822.

[165] A. Zafar, F. Bertocco, J. Schjødt-Thomsen, and J.C. Rauhe. Investigation of the long term effects of moisture on carbon fibre and epoxy matrix composites. *Composites Science and Technology*, 72 (6):656–666, 2012. ISSN 0266-3538. doi: https://doi.org/10.1016/j.compscitech.2012.01.010. URL https://www.sciencedirect.com/science/article/pii/S0266353812000206.

[166] B. Boys, T.J. Dodwell, M. Hobbs, and M. Girolami. Peripy - a high performance opencl peridynamics package. *Computer Methods in Applied Mechanics and Engineering*, 386:114085, 2021. ISSN 0045-7825. doi: https://doi.org/10.1016/j.cma.2021.114085. URL https://www.sciencedirect.com/science/article/pii/S0045782521004163.

[167] Geuzaine, Christophe and Remacle, Jean-Francois. Gmsh. URL http://http://gmsh.info/.

[168] Naveen Prakash. Calibrating bond-based peridynamic parameters using a novel least squares approach. 10 2018.

[169] Pauli Virtanen, Ralf Gommers, Travis E. Oliphant, Matt Haberland, Tyler Reddy, David Cournapeau, Evgeni Burovski, Pearu Peterson, Warren Weckesser, Jonathan Bright, Stéfan J. van der Walt, Matthew Brett, Joshua Wilson, K. Jarrod Millman, Nikolay Mayorov, Andrew R. J. Nelson, Eric Jones, Robert Kern, Eric Larson, C J Carey, İlhan Polat, Yu Feng, Eric W. Moore, Jake VanderPlas, Denis Laxalde, Josef Perktold, Robert Cimrman, Ian Henriksen, E. A. Quintero, Charles R. Harris, Anne M. Archibald, Antônio H. Ribeiro, Fabian Pedregosa, Paul van Mulbregt, and SciPy 1.0 Contributors. SciPy 1.0: Fundamental Algorithms for Scientific Computing in Python. *Nature Methods*, 17:261–272, 2020. doi: 10.1038/s41592-019-0686-2.

[170] Stephen W. Tsai and Edward M. Wu. A general theory of strength for anisotropic materials. *Journal of Composite Materials*, 5(1):58–80, jan 1971. doi: 10.1177/002199837100500106. URL https://doi.org/10.1177%2F002199837100500106.

[171] Beckry Abdel-Magid, Saeed Ziaee, Katrina Gass, and Marcus Schneider. The combined effects of load, moisture and temperature on the properties of E-glass/epoxy composites. *Composite Structures*, 71(3-4):320–326, 2005. ISSN 02638223. doi: 10.1016/j.compstruct.2005.09.022.

[172] E. Barjasteh and S. R. Nutt. Moisture absorption of unidirectional hybrid composites. *Composites Part A: Applied Science and Manufacturing*, 43(1):158–164, 2012. ISSN 1359835X. doi: 10.1016/j.compositesa.2011.10.003. URL http://dx.doi.org/10.1016/j.compositesa.2011.10.003.

[173] a.J. Cervenka, D.J. Bannister, and R.J. Young. Moisture absorption and interfacial failure in aramid/epoxy composites. *Composites Part A: Applied Science and Manufacturing*, 29:1137–1144, 1998. ISSN 1359835X. doi: 10.1016/S1359-835X(98)00012-8.

[174] J. R M D'Almeida, R. C. de Almeida, and W. R. de Lima. Effect of water absorption of the mechanical behavior of fiberglass pipes used for offshore service waters. *Composite Structures*, 83 (2):221–225, 2008. ISSN 02638223. doi: 10.1016/j.compstruct.2007.04.020.

[175] J. S. Earl and R. A. Shenoi. Hygrothermal ageing effects on FRP laminate and structural foam materials. *Composites Part A: Applied Science and Manufacturing*, 35(11):1237–1247, 2004. ISSN 1359835X. doi: 10.1016/j.compositesa.2004.04.007.

[176] Man Hee Han and John A. Nairn. Hygrothermal aging of polyimide matrix composite laminates. *Composites Part A: Applied Science and Manufacturing*, 34(10):979–986, 2003. ISSN 1359835X. doi: 10.1016/S1359-835X(03)00154-4.

[177] J. Jedidi, F. Jacquemin, and A. Vautrin. Accelerated hygrothermal cyclical tests for carbon/epoxy laminates. *Composites Part A: Applied Science and Manufacturing*, 37(4):636–645, 2006. ISSN 1359835X. doi: 10.1016/j.compositesa.2005.05.007.

[178] Branca F. Oliveira and Guillermo J. Creus. An analytical-numerical framework for the study of ageing in fibre reinforced polymer composites. *Composite Structures*, 65(3-4):443–457, 2004. ISSN 02638223. doi: 10.1016/j.compstruct.2003.12.006.

[179] Narayanan Ramanujam, Pavankiran Vaddadi, Toshio Nakamura, and Raman P. Singh. Interlaminar fatigue crack growth of cross-ply composites under thermal cycles. *Composite Structures*, 85 (2):175–187, 2008. ISSN 02638223. doi: 10.1016/j.compstruct.2007.10.018.

[180] J. Rivera and V. M. Karbhari. Cold-temperature and simultaneous aqueous environment related degradation of carbon/vinylester composites. *Composites Part B:Engineering*, 33(1):17–24, 2002. ISSN 13598368. doi: 10.1016/S1359-8368(01)00058-0.

[181] Mechanical properties and failure behaviour of carbon fibre-reinforced polymer composites under the influence of moisture. *Composites Part A: Applied Science and Manufacturing*, 28(6):595–604, 1997. ISSN 1359835X. doi: 10.1016/S1359-835X(96)00154-6.

[182] A. Simar, M. Gigliotti, J. C. Grandidier, and I. Ammar-Khodja. Evidence of thermo-oxidation phenomena occurring during hygrothermal aging of thermosetting resins for RTM composite applications. *Composites Part A: Applied Science and Manufacturing*, 66:175–182, 2014. ISSN 1359835X. doi: 10.1016/j.compositesa.2014.07.007. URL http://dx.doi.org/10.1016/j.compositesa.2014.07.007.

[183] Jonathon D. Tanks, Stephen R. Sharp, and Devin K. Harris. Kinetics of in-plane shear degradation in carbon/epoxy rods from exposure to alkaline and saline environments. *Composites Part B: Engineering*, 110:204–212, 2017. ISSN 13598368. doi: 10.1016/j.compositesb.2016.10.092. URL http://dx.doi.org/10.1016/j.compositesb.2016.10.092.

[184] A. Zafar, F. Bertocco, J. Schjødt-Thomsen, and J. C. Rauhe. Investigation of the long term effects of moisture on carbon fibre and epoxy matrix composites. *Composites Science and Technology*, 72(6):656–666, 2012. ISSN 02663538. doi: 10.1016/j.compscitech.2012.01.010. URL http://dx.doi.org/10.1016/j.compscitech.2012.01.010.

[185] Shaofan Li and Qi Tong. A concurrent multiscale micromorphic molecular dynamics. *Journal of Applied Physics*, 117(15):154303, 2015. doi: 10.1063/1.4916702. URL https://doi.org/10.1063/1.4916702.

[186] A. Zafar, F. Bertocco, J. Schjødt-Thomsen, and J.C. Rauhe. Investigation of the long term effects of moisture on carbon fibre and epoxy matrix composites. *Composites Science and Technology*, 72(6):656 – 666, 2012. ISSN 0266-3538. doi: https://doi.org/10.1016/j.compscitech.2012.01.010. URL http://www.sciencedirect.com/science/article/pii/S0266353812000206.

[187] M. Meng, M.J. Rizvi, S.M. Grove, and H.R. Le. Effects of hygrothermal stress on the failure of cfrp composites. *Composite Structures*, 133(Supplement C):1024 – 1035, 2015. ISSN 0263-8223. doi: https://doi.org/10.1016/j.compstruct.2015.08.016. URL http://www.sciencedirect.com/science/article/pii/S0263822315006935.

[188] Mario J. Choc, Young-Il; Casarella. Configuration of a towline attached to a vehicle moving in a circular path. *Journal of Hydronautics*, 6, 01 1972. doi: 10.2514/3.62894.

[189] P. A. M. Dirac. Quantum mechanics of many-electron systems. *Proceedings of the Royal Society of London A: Mathematical, Physical and Engineering Sciences*, 123(792):714–733, 1929. ISSN 0950-1207. doi: 10.1098/rspa.1929.0094. URL http://rspa.royalsocietypublishing.org/content/123/792/714.

[190] G. R. Irwin. Analysis of Stresses and Strains Near the End of a Crack Traversing a Plate. *J. Appl. Mech.*, 1957.

[191] C.F. Shih. Relationships between the j-integral and the crack opening displacement for stationary and extending cracks. *Journal of the Mechanics and Physics of Solids*, 29(4):305 – 326, 1981. ISSN 0022-5096. doi: http://dx.doi.org/10.1016/0022-5096(81)90003-X. URL http://www.sciencedirect.com/science/article/pii/002250968190003X.

[192] J.W. Hutchinson. Plastic stress and strain fields at a crack tip. *Journal of the Mechanics and Physics of Solids*, 16(5):337 – 342, 1968. ISSN 0022-5096. doi: http://dx.doi.org/10.1016/0022-5096(68)90021-5. URL http://www.sciencedirect.com/science/article/pii/0022509668900215.

[193] ASTM International. Standard Test Method for J Ic , a Measure of Fracture Toughness. *ASTM International, West Conshohocken, PA*, 1981.

[194] J. R. Rice. A Path Independent Integral and the Approximate Analysis of Strain Concentration by Notches and Cracks. *Journal of Applied Mechanics*, 35:379, 1968. doi: 10.1115/1.3601206.

[195] Reeder J. R. An evaluation of mixed-mode delamination failure criteria. Technical report, 1992.

[196] S. Zheng and C.T. Sun. A double-plate finite-element model for the impact-induced delamination problem. *Composites Science and Technology*, 53(1):111 – 118, 1995. ISSN 0266-3538. doi: http://dx.doi.org/10.1016/0266-3538(94)00079-4. URL http://www.sciencedirect.com/science/article/pii/0266353894000794.

[197] Nicolas Moës, John Dolbow, and Ted Belytschko. A finite element method for crack growth without remeshing. *International Journal for Numerical Methods in Engineering*, 46(1):131–150, 1999. ISSN 1097-0207. doi: 10.1002/(SICI)1097-0207(19990910)46:1⟨131::AID-NME726⟩3.0.CO;2-J. URL http://dx.doi.org/10.1002/(SICI)1097-0207(19990910)46:1<131::AID-NME726>3.0.CO;2-J.

[198] Toshio Nagashima, Youhei Omoto, and Shuichi Tani. Stress intensity factor analysis of interface cracks using x-fem. *International Journal for Numerical Methods in Engineering*, 56(8):1151–1173, 2003. ISSN 1097-0207. doi: 10.1002/nme.604. URL http://dx.doi.org/10.1002/nme.604.

[199] D. J. Chen, W. S. Chan, and B. P. Wang. An efficient method to simulate one-and two-dimensional delamination growth in composite laminates. *Journal of Reinforced Plastics and Composites*, 15(9):944–957, 1996. doi: 10.1177/073168449601500905. URL http://dx.doi.org/10.1177/073168449601500905.

[200] M.L. Benzeggagh and M. Kenane. Measurement of mixed-mode delamination fracture toughness of unidirectional glass/epoxy composites with mixed-mode bending apparatus. *Composites Science and Technology*, 56(4):439 – 449, 1996. ISSN 0266-3538. doi: http://dx.doi.org/10.1016/0266-3538(96)00005-X. URL http://www.sciencedirect.com/science/article/pii/026635389600005X.

[201] A.A Wells. *Unstable Crack Propagation in Metals: Cleavage and Fast Fracture*, volume 1. 1961.

[202] G. R. Irwin. Plastic Zone Near a Crack and Fracture Toughness. *Sagamore Research Conference Proceedings*, 1961.

[203] H. M. Westergaard. *Bearing pressures and cracks*, pages 18–22. 1997.

[204] T. L. Anderson. *Fracture Mechanics: Fundamentals and Applications, Third Edition*. Taylor & Francis, New York, NY, 2005.

[205] Comparative evaluation of failure analysis methods for composite laminates. 1996. URL http://www.tc.faa.gov/its/worldpac/techrpt/ar95-109.pdf.

[206] G.R. Irwin. Onset of fast crack propagation in high strength steel and aluminum alloys. May 1956.

[207] A. A. Griffith. The phenomena of rupture and flow in solids. *Philosophical Transactions of the Royal Society of London A: Mathematical, Physical and Engineering Sciences*, 221 (582-593):163–198, 1921. ISSN 0264-3952. doi: 10.1098/rsta.1921.0006. URL http://rsta.royalsocietypublishing.org/content/221/582-593/163.

[208] D. Garcia-Gonzalez, R. Zaera, and A. Arias. A hyperelastic-thermoviscoplastic constitutive model for semi-crystalline polymers: Application to peek under dynamic loading conditions. *International Journal of Plasticity*, 88:27 – 52, 2017. ISSN 0749-6419. doi: https://doi.org/10.1016/j.ijplas.2016.09.011. URL http://www.sciencedirect.com/science/article/pii/S0749641916301760.

[209] S.A. Silling and E. Askari. A meshfree method based on the peridynamic model of solid mechanics. *Computers and Structures*, 83(17):1526 – 1535, 2005. ISSN 0045-7949. doi: https://doi.org/10.1016/j.compstruc.2004.11.026. URL http://www.sciencedirect.com/science/article/pii/S0045794905000805. Advances in Meshfree Methods.

[210] J. R. Morison, J. W. Johnson, and S. A. Schaaf. The force exerted by surface waves on piles. 1950. doi: 10.2118/950149-G.

[211] Gisle; Storhaug Turid; Spencer-Brian; Echtermeyer Andreas Salama, Mamdouh M.; Stjern. [offshore technology conference offshore technology conference - houston, texas (2002-05-06)] offshore technology conference - the first offshore field installation for a composite riser joint. doi: 10.4043/14018-MS.

[212] F.-K. Chang and K.-Y. Chang. A Progressive Damage Model for Laminated Composites Containing Stress Concentrations. *Journal of Composite Materials*, 21:834–855, January 1987. doi: 10.1177/002199838702100904.

[213] G.I. Barenblatt. *[Advances in Applied Mechanics] Advances in Applied Mechanics Volume 7 Volume 7 —— The Mathematical Theory of Equilibrium Cracks in Brittle Fracture*. 1962. ISBN 9780120020072. doi: 10.1016/S0065-2156(08)70121-2. URL http://gen.lib.rus.ec/scimag/index.php?s=10.1016/S0065-2156(08)70121-2.

[214] E. J. Barbero, J. N. Reddy, and Jan Teply. An accurate determination of stresses in thick laminates using a generalized plate theory. *International Journal for Numerical Methods in Engineering*, 29 (1):1–14, 1990. ISSN 1097-0207. doi: 10.1002/nme.1620290103. URL http://dx.doi.org/10.1002/nme.1620290103.

[215] E.J. Barbero and J.N. Reddy. Modeling of delamination in composite laminates using a layer-wise plate theory. *International Journal of Solids and Structures*, 28(3):373 – 388, 1991. ISSN 0020-7683. doi: http://dx.doi.org/10.1016/0020-7683(91)90200-Y. URL http://www.sciencedirect.com/science/article/pii/002076839190200Y.

[216] E. Fermi and J. Pasta. Studies of nonlinear problems. i. page 22, 1955. URL https://www.osti.gov/accomplishments/documents/fullText/ACC0041.pdf.

[217] Adri C. T. van Duin, Siddharth Dasgupta, Francois Lorant, and William A. Goddard. Reaxff a reactive force field for hydrocarbons. *The Journal of Physical Chemistry A*, 105(41):9396–9409, 2001. doi: 10.1021/jp004368u. URL http://dx.doi.org/10.1021/jp004368u.

[218] B. J. Alder and T. E. Wainwright. Studies in molecular dynamics. i. general method. *The Journal of Chemical Physics*, 31(2):459–466, 1959. doi: 10.1063/1.1730376. URL http://dx.doi.org/10.1063/1.1730376.

[219] Erkan Oterkus, Erdogan Madenci, Olaf Weckner, Stewart Silling, Philip Bogert, and Alexander Tessler. Combined finite element and peridynamic analyses for predicting failure in a stiffened composite curved panel with a central slot. *Composite Structures*, 94(3):839 – 850, 2012. ISSN 0263-8223. doi: http://dx.doi.org/10.1016/j.compstruct.2011.07.019. URL http://www.sciencedirect.com/science/article/pii/S0263822311002741.

[220] C. Diyaroglu, E. Oterkus, E. Madenci, T. Rabczuk, and A. Siddiq. Peridynamic modeling of composite laminates under explosive loading. *Composite Structures*, 144:14 – 23, 2016. ISSN 0263-8223. doi: https://doi.org/10.1016/j.compstruct.2016.02.018. URL http://www.sciencedirect.com/science/article/pii/S0263822316300381.

[221] Erkan Oterkus and Erdogan Madenci. Peridynamic theory for damage initiation and growth in composite laminate. In *Advances in Fracture and Damage Mechanics X*, volume 488 of *Key Engineering Materials*, pages 355–358. Trans Tech Publications, 1 2012. doi: 10.4028/www.scientific.net/KEM.488-489.355.

[222] Y. Hu, E. Madenci, and N. Phan. Peridynamics for predicting damage and its growth in composites. *Fatigue & Fracture of Engineering Materials & Structures*, 40(8):1214–1226. doi: 10.1111/ffe.12618. URL https://onlinelibrary.wiley.com/doi/abs/10.1111/ffe.12618.

[223] A. Rahman. Correlations in the motion of atoms in liquid argon. *Phys. Rev.*, 136:A405–A411, Oct 1964. doi: 10.1103/PhysRev.136.A405. URL https://link.aps.org/doi/10.1103/PhysRev.136.A405.

[224] Charlotte Froese Fischer. General hartree-fock program. *Computer Physics Communications*, 43 (3):355 – 365, 1987. ISSN 0010-4655. doi: http://dx.doi.org/10.1016/0010-4655(87)90053-1. URL http://www.sciencedirect.com/science/article/pii/0010465587900531.

[225] Mark F. Horstemeyer(auth.). *Integrated Computational Materials Engineering (ICME) for Metals Using Multiscale Modeling to Invigorate Engineering Design with Science*. 2012. ISBN 9781118022528,9781118342664. URL http://eu.wiley.com/WileyCDA/WileyTitle/productCd-1118022521.html.

[226] Douglas-Westwood. World Deepwater Market Report 2010-2014. 2010.

[227] P.D Soden, A.S Kaddour, and M.J Hinton. Recommendations for designers and researchers resulting from the world-wide failure exercise. *Composites Science and Technology*, 64(3–4):589 – 604, 2004. ISSN 0266-3538. doi: http://dx.doi.org/10.1016/S0266-3538(03)00228-8. URL http://www.sciencedirect.com/science/article/pii/S0266353803002288. Failure criteria in

fibre reinforced polymer composites Part C: Additional theories conclusions and recommendations.

[228] M.J Hinton; P.D Soden. Predicting failure in composite laminates: the background to the exercise. *Composites Science and Technology*, 58, 1998. doi: 10.1016/s0266-3538(98)00074-8.

[229] C.P. Sparks. Fundamental of Marine Riser Mechanics. 2007.

[230] K.J. Bathe. Finite element procedures. Prentice Hall, 2006. ISBN 9780979004902. URL https://books.google.co.uk/books?id=rWvefGICfO8C.

[231] N.D.P. Barltrop and A.J. Adams. 6 - waves and wave loading. In N.D.P. Barltrop, , and A.J. Adams, editors, *Dynamics of Fixed Marine Structures (Third Edition)*, pages 249 – 344. Butterworth-Heinemann, third edition edition, 1991. ISBN 978-0-7506-1046-9. doi: http://dx.doi.org/10.1016/B978-0-7506-1046-9.50012-2. URL http://www.sciencedirect.com/science/article/pii/B9780750610469500122.

[232] Daryl L. Logan. A First Course in the Finite Element Method. 2006.

[233] D. V. Griffiths I.M.Smith and L.Margetts. Programming the Finite Element Method. 2014.

[234] J. F. O'Brien, P. J. McNamara and F. P. E. Dunne. Three dimensional nonlinear motions of risers and offshore loading towers. 1988.

[235] Alain H. Peyrot. Large deflection analysis of beams, pipes, or poles. *Engineering Structures*, 4 (1):11 – 16, 1982. ISSN 0141-0296. doi: http://dx.doi.org/10.1016/0141-0296(82)90018-9. URL http://www.sciencedirect.com/science/article/pii/0141029682900189.

[236] SymPy Development Team. *SymPy: Python library for symbolic mathematics*, 2016. URL http://www.sympy.org.

[237] Conrad Sanderson and Ryan Curtin. *Armadillo: a template-based C++ library for linear algebra.*

Appendix A - Published papers

Ocean Engineering 220 (2021) 108426

Contents lists available at ScienceDirect

Ocean Engineering

journal homepage: www.elsevier.com/locate/oceaneng

Effects of extensible modelling on composite riser mechanical responses

Hossam Ragheb [a,*], Adam Sobey [a,b]

[a] Maritime Engineering Group, University of Southampton, Bolderwood Innovation Campus, Southampton, SO16 7QF, UK
[b] Marine and Maritime Group, Data-centric Engineering Programme, The Alan Turing Institute, The British Library, London, NW1 2DB, UK

ARTICLE INFO

Keywords:
Composite risers
Cable dynamics
Time domain
Benchmarking

ABSTRACT

The change from steel risers to composites comes with uncertainties that led to large safety factors. One area of uncertainty is the predicted response and stresses derived from commercial packages that are based on formulations that assume in-extensible riser. However, composite pipes exhibit a lower axial stiffness and therefore the velocity of the axial waves will change with a corresponding change in dynamic response. To determine the effect of this assumption, this paper assesses the effect of extensibility on the time-domain response. It is found that the in-extensible model predicts 3 times the number of high frequency tension cycles in the 20 kN tension range. To determine the impact of this change on the stress, the accuracy of available composite pipe models is benchmarked using shell, continuum-shell and solid elements. The quadratic and continuum-shell elements provide a maximum percentage difference of 4% compared to solid elements but the continuum-shell is selected as it has a lower computational cost. The response from the extensible and in-extensible models are input into the pipe model, they provide similar Tsai-Wu failure factors, alleviating concerns when modelling the strength. However, the change in dynamics remains a concern for other applications such as machine-learning or digital-twins.

1. The importance of composite risers

Production risers are vital subsea components for hydrocarbon production. However, the design process is complex as they are long, slender and exposed to dynamic multi-axial loading conditions. In addition, they are subjected to large temperature and pressure differentials through the thickness which are caused by the transfer of hot fluids between the surface platforms and the subsea systems, sometimes in parts of the ocean where the ambient temperature is below 0°*C*. Where temperature and pressure differentials leads to the seabed sections of a pipeline or SCR walking, which can lead to failure (Carr and Sinclair, 2008; Reda et al., 2018; Reda et al., 2019). Steel is the most common material used in subsea applications. However, at large depths the technical challenges increase due to the large top-tensions, installation difficulties and long-term integrity issues related to corrosion. As the offshore industry expands their operations to greater depths, potentially beyond 4000 m, these problems will only get worse. Gradually replacing steel with composite materials could reduce the operational and capital expenditure due to their higher specific strength to weight ratios, lack of corrosion and excellent vibrational damping properties (Tarnopol'skii et al., 1999; Ochoa and Salama, 2005; Beyle et al., 1997). However, these benefits do not come without challenges, for example, the lighter weight of the composite could lead to higher compression loads (Reda et al., 2016) that requires ballast weights or internal metallic liners and high initial costs that are dependent on the manufacturing and qualification processes. This is in part because of the lack of full-scale in-situ field data due to the short track record in the offshore environment, in addition to the complexity and lack of accuracy of the failure prediction tools (Pham et al., 2016). A possible reduction in the qualification costs can be provided by sufficiently accurate and rapid numerical models developed to predict full-scale in-situ behaviour and failure during operation. However there is little published research on the suitability of the current riser numerical models to capture the composite riser's non-linear dynamic response at the global riser and pipe levels.

This paper therefore aims to determine the effect that extensibility has on global riser and pipe levels, in an effort to improve confidence in modelling composite risers. First, the effect of the extensible and in-extensible beam formulations on the composite riser global response is investigated, to determine if the change in axial stiffness in composite pipes changes the behaviour and requires a different formulation than is currently used for flexible risers. Then, the suitability of different

* Corresponding author.
E-mail address: har1g15@soton.ac.uk (H. Ragheb).

https://doi.org/10.1016/j.oceaneng.2020.108426
Received 13 July 2020; Received in revised form 25 November 2020; Accepted 26 November 2020
Available online 22 December 2020

element types for predicting the composite pipe response is investigated, due to the lack of available benchmarks in the open literature. The investigation shows which of these different methods can accurately, and efficiently, capture the stresses within the laminate. Finally these two elements are combined to show how the choice of extensible or in-extensible methods affects the stress predictions at the laminate scale.

2. Catenary riser numerical model

2.1. Review of methods for modelling the global response

Riser design is performed in two stages for computational efficiency. First the global response of the entire riser is modelled under the influence of environmental and vessel loads. The dynamic excitations are captured within the vessel's top excitation. This dynamic time domain analysis is required to identify the critical riser responses and sections for ultimate and fatigue limits states. The second step is to build a detailed model of the critical cross-section. This analysis is performed to predict the stresses and strains in the laminate to optimise the layup. Outputs from the global analysis, the tensions and rotations at both ends of the critical sections are applied as boundary conditions to the cross-section model.

The catenary equation is the simplest approach for modelling the global response of catenary shaped risers. However, the closed-form formulation limits its application. Solving dynamic riser simulations requires the solution of the full set of partial differential equations with time varying boundary conditions and loads and can only be solved with a suitable numerical method such as finite elements or finite differencing. The riser's global dynamics can be formulated using two main approaches: extensible and in-extensible beams. Cables exhibit two main vibrating modes, 'elastic', where the axial waves propagate with a velocity proportional to the axial stiffness, and 'transverse', where they propagate as a function of the beam flexural stiffness. Flexible steel risers exhibit high axial stiffnesses due to their multi-layer cross-sectional design which are often five orders of magnitude higher than their flexural stiffness, due to their multi-layer cross-sectional design, while maintaining favourable low bending stiffnesses. Therefore, it is reasonable to approximate these flexible pipes response using an in-extensible beam model. Approaches that are specifically developed for flexible steel risers enforce these conditions to avoid the singularity that arises in the numerically ill-conditioned system matrix (Patel and Seyed, 1995) and this is common in most design software. However, composite risers exhibit a lower axial stiffness that is likely to be only three orders of magnitude higher than the flexural stiffness. At these lower ratios the elastic waves could be excited and it may be necessary to model the composite riser as an extensible cable.

The dynamic equilibrium system that governs the riser response consists of a number of non-linear coupled hyperbolic partial differential equations with boundary value constraints. The full-scale response of the riser can be adequately modelled using Bernoulli beam formulation as the length to thickness ratio is larger than the limit below which the Timoshenko-beam theory applies (Timoshenko et al., 1990).

To solve these partial differential equations the Lagrangian coordinate formulation makes up the largest portion of the open literature. Initially these models are solved with a numerical semi-implicit finite differencing scheme (Nordgren, 1974). The method is conditionally stable if the time step is carefully calculated based on the arc length and the tension. However, this method is not practical for industrial applications as the stability parameters vary dynamically. Therefore, unconditionally stable time integration methods are favoured. To improve the accuracy and stability of the solution Galerkin's finite element formulation and first-order Adams-Moulton time integration algorithm is implemented (Garrett, 1982). However, the multi-step integration implemented in Adams-Moulton method is computationally expensive. A variational finite element approach and the Newton-Raphson algorithm improved the computational feasibility of this method (Huang and Chucheepsakul, 1985). A static finite element method is proposed, to improve the deformation dependency of the boundary conditions and load points. This includes a predictor-corrector multi-step scheme formulation based on non-linear vectorial equilibrium formulation is proposed however, the method is computationally expensive and its stability is not discussed in the literature (Bernitsas and Kokarakis, 1988).

The increase in flexible riser installations required new formulations to overcome the simulation difficulties attributed to the large axial stiffnesses. Therefore, a 2D Cartesian in-extensible hybrid beam-column formulation is proposed for un-bonded flexible risers implementing a convected coordinate scheme; where the hybrid beam formulation is used to solve the flexible riser ill-conditioned system stiffness matrix problem. In addition, a local coordinate system is fixed to each element, to decouple the rigid body motion and strains. This is connected to the global Cartesian coordinate system via rotation angles allowing for large deflections (McNamara et al., 1988). The hybrid-beam element formulation is used in which the axial deformation and in-extensibility conditions are satisfied. The method uses non-linear programming techniques to apply the Lagrangian constraint and imposes the in-extensibility condition allowing for large deformations with convected axes. This method is extended to a 3D analysis (O'Brien and McNamara, 1988) and implemented in a commercial riser three-dimensional non-linear finite element package Flexcom. The method uses Houbolt operator time integration which is shown to be suitable for the slow motion periods that flexible risers exhibit (Patel and Seyed, 1995; McNamara et al., 1988). Another time integration method is suggested, the Hilbert-Hughes-Taylor one step method which is unconditionally stable with linear systems and allows for variable time steps. The optimal time step is calculated automatically using the current step period parameter and after a few incremental steps the optimal value is chosen (O'Brien and McNamara, 1989). Recently a multi-scale element type for flexible risers is developed (Edmans et al., 2019) which allows the stick/slip behaviour of flexible steel risers to be captured via a hybrid beam element user defined subroutine in Abaqus. However, this method mostly benefits un-bonded flexible riser analysis and doesn't provide additional information about the bonded cross-sections at the global riser scale since composite pipes are bonded and don't exhibit hysteresis like flexible risers.

The literature related to extensible formulations is sparse compared to the in-extensibility formulations. A non-linear cable formulation is successfully solved with the finite element technique and New-mark's time integration method (Fried, 1982). However, this method causes large errors in predicting the cable natural frequencies (Leckie and Lindberg, 1963) as the lumped mass technique is implemented (Bergan et al., 1985). A full 3D extensible cable is derived in (Casarella and Parsons, 1970; Choc and Young-IlCasarella, 1972), which is solved with an implicit second order box finite difference method (Ablow and Schechter, 1983) resulting in an unconditionally stable method that is discretized and centred in space and time and second order accurate. However, the method is developed for negligible flexural stiffness cables and requires the inverse of the system matrix, which causes a singularity in slack conditions. The method is expanded to include cables with considerable flexural stiffness and solved with Newton-Raphson method (Hover et al., 1994; Triantafyllou, 1984) and later solved with relaxation method (Chatjigeorgiou, 2008; ChatjigeorgiouIoannis and Mavrakos, 2016).

Although the literature is rich with multiple extensible and in-extensible dynamic analysis methods, it lacks a comparison between the two methods especially to quantify the effect of composite riser cross-section on the calculated tensions and curvatures.

2.2. Mathematical formulation

RiSim, a non-linear extensible, time-domain implicit Keller-box finite difference code is developed in FORTRAN based on the

formulation derived in (Ablow and Schechter, 1983; Hover et al., 1994). The non-linear system of equations is solved with a modified Powell hybrid method. The method is suitable for calculating the local minima of complex functions without the need to calculate its derivatives (Powell, 1964). RiSim is used to investigate the composite riser response and compared to a finite element in-extensible hybrid formulation implemented in the riser simulation package, Flexcom, which is based on the method developed in (O'Brien and McNamara, 1988, 1989; McNamara et al., 1988) to determine the accuracy of these models with the reduced axial stiffness exhibited by composite risers.

Riser design is performed in two stages for computational efficiency reasons. First the response of the entire riser is modelled under the influence of environmental and vessel loads. The effect of the maximum mean and low frequency vessel responses are modelled as a static step with an offset to the initial position of the vessel, while the high frequency dynamic excitations are captured within the vessel's RAOs. This dynamic time domain analysis is required to identify the critical riser responses and sections for ultimate and fatigue limits states. The second step is to build a detailed model of the critical cross-section. This analysis is performed to predict the stresses and strains in the laminate to optimise the layup. Outputs from the global analysis, the tensions and rotations at both ends of the critical sections are applied as boundary conditions to the cross-section model.

In this analysis the inline linear waves and sinusoidal hang-off excitation are applied to the riser system. The riser motion is assumed to occur in a 2D plan for simplicity. The governing dynamic equilibrium system is presented as a series of partial differential equations in 1–6. The derivation is based on the extensible non-linear Lagrangian partial differential equations representing the 2D riser boundary-value problem (see Fig. 1). Variables u and v are the velocities in the tangential and transversal directions $\hat{\mathbf{t}}$ and $\hat{\mathbf{n}}$, T is the tension, S_n is the shear force in the transverse direction and G_b is the curvature about the bi-normal direction $\hat{\mathbf{n}}$. Φ is the angle between the tangent and the horizontal. m and ma are the mass in air and the added mass per meter, w_0 is the apparent weight of the riser per meter. d_o is the outer diameter of the riser. EA and EI are the axial and bending stiffnesses. s is the Lagrangian, un-stretched coordinate, v_{tr} and v_{nr} are the tangential and transversal relative velocities, C_{dt} and C_{dn} are the tangential and transversal drag coefficients, t is the time and ρ is the sea water density, v_{tc} ,v_{nc}, v_{tw} and v_{nw} are the current and wave tangential and transversal particle velocities.

The relationship between the rate of change of the velocities frame angle Φ with respect to time at each node as a function of tension variation and the total force balance along the riser in the tangential $\hat{\mathbf{t}}$ direction described in equation 1,

$$m\left(\frac{\partial u}{\partial t}-v\frac{\partial \Phi}{\partial t}\right)-\frac{\partial T}{\partial s}+S_n\Omega_b+w_0 sin\Phi +\frac{1}{2}\pi\rho d_o C_{dt} v_{tr}|v_{tr}|\sqrt{1+\left(\frac{T}{EA}\right)}=0. \tag{1}$$

and in transversal direction $\hat{\mathbf{n}}$ in equation 2,

$$m\left(\frac{\partial v}{\partial t}+u\frac{\Phi}{\partial t}\right)+m_a\frac{\partial v_{nr}}{\partial t}-\frac{\partial S_n}{\partial s}-\Omega_b T+w_0 cos\Phi +\frac{1}{2}\rho d_o C_{dn} v_{nr}|v_{nr}|\sqrt{1+\left(\frac{T}{EA}\right)}=0. \tag{2}$$

The governing relationship between the temporal rate of change of the tension, as a function of axial stiffness, nodal velocities and curvatures, is described in equation 3,

$$\frac{\partial T}{\partial t}-EA\left(\frac{\partial u}{\partial s}-\Omega_b v\right)=0. \tag{3}$$

and the reference frame angle is shown in equation 4,

$$\left(1+\left(\frac{T}{EA}\right)\right)\frac{\partial \Phi}{\partial t}-\frac{\partial v}{\partial s}-u\Omega_b=0. \tag{4}$$

The coupled relationship between the axial and bending strains are provided in equation 5,

$$EI\frac{\partial \Omega_b}{\partial s}+S_n\left(1+\left(\frac{T}{EA}\right)\right)^3=0. \tag{5}$$

While the definition for the curvature as a function of the reference frame angle along the riser is provided in equation 6,

$$\frac{\partial \Phi}{\partial s}-\Omega_b=0. \tag{6}$$

The tangential and transverse relative velocities, when the wave and current are applied, are given by equations 7 and 8,

$$v_{tr}=u-v_{tc}-v_{tw}, \tag{7}$$

$$v_{nr}=v-v_{nc}-v_{nw}. \tag{8}$$

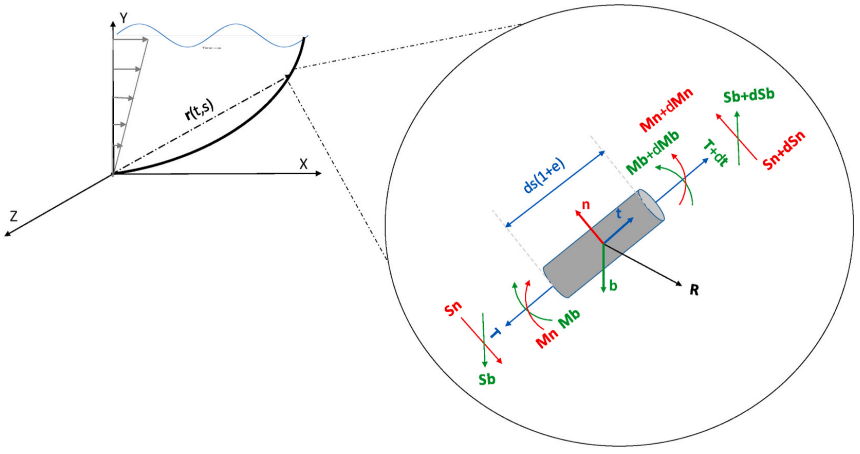

Fig. 1. Riser element loads equilibrium diagram.

2.3. Boundary conditions

The 2D riser behaviour is governed by six, first order partial differential equations. The finite difference discretisation leads to $n-1$ equations and the missing 6 equations to solve the system are given by the equal number of boundary conditions given by equations 9- 11.

At the touch-down point the boundary conditions are given by equation 9,

$$G_b^0 = 0, u^0 = 0, v^0 = 0, \tag{9}$$

and the boundary conditions in the case of wave loading and pinned hang-off node are defined in equation 10,

$$G_b^{N-1} = 0, u^{N-1} = 0, v^{N-1} = 0. \tag{10}$$

Assuming a sinusoidal excitation at the hang-off node, the boundary conditions are given by equation 11,

$$G_b^{N-1} = 0, u^{N-1} = 0, v^{N-1} = 5.0\sin(\omega t). \tag{11}$$

2.4. The Keller-box method

The Keller-box numerical scheme is an implicit method, designed to solve first order parabolic partial differential equations in time and space (Vajravelu, 2014). The solution is second order accurate and simple to implement for large numbers of coupled PDEs. The method requires all the PDEs to be reformulated in first order form before discretisation.

The algorithm requires discretisation in space and time that is chosen at the central point $(t_{i+1/2}, s_{j-1/2})$, where i and j represent the current time and spatial node. The discretisation is performed between the points P_1, P_2,P_3 and P_4 as shown in Fig. 2. These points represents the function evaluation at either the previous time, the next time or spatial step. Let Y be the unknown variable and then the central differencing of the temporal derivative at the centre point is determined by, fixing the spatial coordinate while the temporal derivative is replaced by equation 12,

$$\begin{aligned} &\frac{\partial Y}{\partial t} = \frac{Y_{j-1/2}^{i+1} - Y_{j-1/2}^{i}}{\Delta t_i} + \mathscr{O}\left(h^2\right) \\ &= \frac{Y_j^{i+1} + Y_{j-1}^{i+1} - Y_j^i - Y_{j-1}^i}{\Delta t_i} + \mathscr{O}\left(h^2\right). \end{aligned} \tag{12}$$

Similarly, the spatial derivative is replaced by equation 13,

$$\begin{aligned} &\frac{\partial Y}{\partial s} = \frac{Y_j^{i+1/2} - Y_{j-1}^{i+1/2}}{\Delta s_i} + \mathscr{O}\left(h^2\right) \\ &= \frac{Y_j^{i+1} + Y_j^i - Y_{j-1}^{i+1} - Y_{j-1}^i}{\Delta s_i} + \mathscr{O}\left(h^2\right). \end{aligned} \tag{13}$$

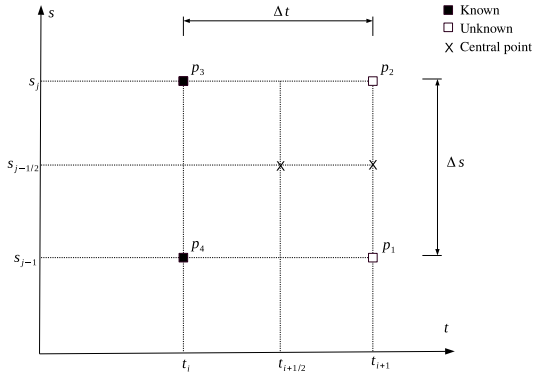

Fig. 2. Keller-box method finite difference grid.

By neglecting the higher order terms and expanding equations 12–13 the central point is given by the expressions in equation 14,

$$t_{i+1/2} = \frac{1}{2}(t_{i+1} + t_i), s_{j-1/2} = \frac{1}{2}\left(s_j + s_{j-1}\right). \tag{14}$$

3. Riser model benchmarking

The static and dynamic responses of the riser are benchmarked using the in-house developed algorithm RiSim and FE commercial package Flexcom. An 11 inch composite catenary riser is investigated with a comparison of when it is unpressurised and with a 200 bar internal pressure. The riser properties and environmental data are listed in Table 1, including the maximum wave height H_{max} and corresponding peak wave period T_p. A wave train that originates at a location above the global axes origin, on the seabed, that is located at the mid-water line propagates in the positive horizontal axes direction.The seabed is intentionally not modelled in this study to isolate the effects of extensibility on the riser response. The structural damping depends on the type of structure and the material; this is made more complex when considering composite materials as they exhibit variable damping properties which are dependent on the natural frequency of each vibration mode. Damping tests are required to quantify these variable damping values, as assuming variable damping can be misleading. Therefore, riser analysis is performed without structural damping as a base case (Rakshit and Atluri, 2008; Wood, 2018).

3.1. Static comparison of extensible and in-extensible methods

A comparison between the tensions and bending moments predicted by the extensible and in-extensible formulations are shown in Fig. 3 for the tension and Fig. 4 for the resultant bending moment. A visual check of the Figs. 3 and 4 infers that both methods predict tension and bending moments that are indistinguishable from each other. That is because the static tension and bending moments demonstrate a negligible percentage differences of less than 0.02% for the maximum static tension, while the maximum bending moment demonstrates a 0.09% difference which shows that both methods are predicting similar static solution.

3.2. Dynamic comparison of extensible and in-extensible methods

3.2.1. Comparison in regular waves

Dynamic riser analysis is performed by applying regular waves to the riser system. This test is used to verify the regular wave algorithm used in RiSim before applying the top-side excitation. The waves data are chosen based on the extreme conditions from a 100 year return period

Table 1
Properties for the benchmarked riser.

Parameter	Value
Water depth (d) [m]	400.00
Total riser length (S) [m]	487.43
Bending stiffness (EI) [Nm^2]	49.52E+06
Axial stiffness (EA) [N]	37.23E+09
Mass in air empty (m) [kg/m]	163.85
Internal fluid density (ρ_f) [kg/m^3]	1025.0
Tangential drag coefficient (C_{Dt})	0.05
Normal drag coefficient (C_{Dn})	1.2
Outer diameter (d_o) [m]	0.324
Internal diameter (d_i) [m]	0.28
Maximum wave height (H_{max}) [m]	18.6
Wave period (T_p) [s]	14.9
Hang-off horizontal coordinate (X_{HO}) [m]	224.7
Hang-off vertical coordinate (Y_{HO}) [m]	400.00
Internal Pressure [bar]	0/200

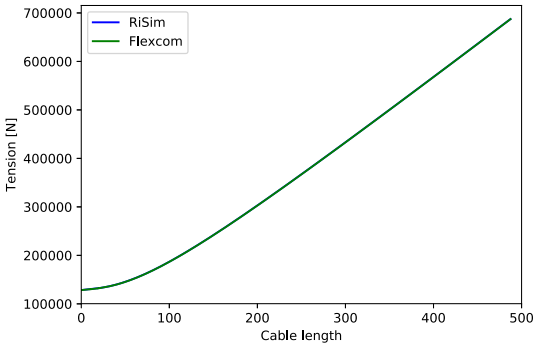

Fig. 3. Effective tension along riser length.

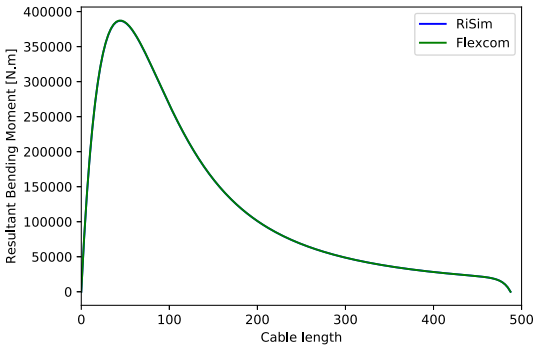

Fig. 4. Resultant bending moment along riser length.

extreme conditions that typically occurs at west of the Shetlands. A good match is reported between the two methods as documented in Table 2 for an extreme wave height and Table 3 for a moderate wave height. When applying an extreme wave that has 34.5 m wave height and a 17.5 s wave period, the maximum percentage difference between the two methods along the length of the risers is at the minimum tension with a value of 0.65%, as shown in Table 2. However, the maximum percentage difference reduces to 0.06% when a moderate wave is applied with 18.6 m wave height and 14.9 s wave period, Table 3. Showing that when an extreme wave condition with a 100-year return period is applied, the differences between the two models are negligible with less than 1% maximum error. This gives confidence in the regular wave algorithm implemented in the RiSim code.

Despite the similarity in results, the FE in-extensible solution experiences some numerical instabilities during the first wave period and a number of smaller numerical instabilities are exhibited. However, while the extensible finite difference solution converges immediately to the final response and doesn't experience high frequency spurious

Table 2
100 year extreme wave conditions-pinned model.

	Hmax = 34.5m		
	Tp = 17.5s		
Parameter	Flexcom	FD	D%
Max Tension $[kN]$	709.25	709.83	0.08%
Min Tension $[kN]$	671.92	667.52	−0.65%
Max Curvature $[m^{-1}]$	0.0086	0.0086	0.0%

Table 3
100 year moderate wave conditions-pinned model.

	Hmax = 18.6		
	Tp = 14.9		
Parameter	Flexcom	FD	D%
Max Tension $[kN]$	694.37	694.84	0.07%
Min Tension $[kN]$	680.4	679.99	−0.06%
Max Curvature$[m^{-1}]$	0.0084	0.0084	0.0%

numerical oscillations. Looking beyond the first wave period, the comparison between the two methods is shown in Fig. 5 which shows the time-trace of the hang-off node tension performed in both Flexcom and RiSim with 3 m element lengths. Fig. 5 shows that elastic waves are excited in addition to the transverse waves, and these are only captured by the extensible riser formulation. For typical composite risers, which are likely to have axial and flexural stiffnesses separated by only three orders of magnitude, elastic waves can be excited and the behaviour can be captured using the extensible formulation implemented in RiSim.

3.2.2. *Regular waves with top-side excitation*

Two types of sinusoidal excitations are applied to replicate a general range of top-side excitations in the surge direction: an excitation with angular frequency that is in phase with the wave train and another 180° out of phase. The excitation is applied to the hang-off node of a 200 bar pressurised and unpressurised riser in the transverse direction in addition to the regular waves. Using equation 11 a sinusoidal velocity is applied in the normal direction $\vec{n}$ to the hang-off node. The corresponding Cartesian time traces of the horizontal and vertical coordinates are extracted and applied to the FEA in-extensible model as a displacement boundary condition applied to the hang-off node.

Both methodologies match well for the in-phase wave with the top-side excitations using the hang-off tension time-trace. A maximum difference of less than 0.5% is observed after the inextensible method has stabilised beyond the first wave period. The results from the 180° phase shift also exhibits a close behaviour with a maximum 1% percentage difference after the FE solution converges to the steady state solution after three wave periods, this is shown in Fig. 6. Although the variation between both methods is within the maximum documented percentage difference between dynamic analysis methods in the literature (Larsen, 1992), Fig. 6 illustrates this difference for the pressurised riser. It is observed, for both the pressurised and unpressurised cases, that the RiSim Finite Differencing algorithm converges immediately to the final steady state system response while the finite element solution experiences higher order oscillations that are sensitive to the solutions convergence tolerance.

The in-extensible method experiences 3 times the number of cycles for the tension ranges up to 20kN compared to the extensible formulation, Fig. 7. The number of cycles reduces to 2 times larger if the first 3 wave periods are ignored from the in-extensible analysis. This implies that often the first 3 wave periods should be avoided when using in-extensible methods and a longer simulation period is required for reliable results. It is not likely that the high order oscillations have a large effect on the total fatigue life of the riser, however either human or automated filtering process is required to avoid these numerical instabilities. This problem is not experienced with the extensible formulation.

The hybrid element formulation is a probable cause for such instabilities. It is implemented in the in-extensible software where the in-extensibility condition is enforced artificially, in which the axial strain is decoupled and interpolated separately. This type of mixed field variable formulation is reported to cause spurious numerical errors if the interpolation function used with the axial force is not the same order as the strain ε. This can cause a second kind errors in the solution even for arbitrarily small meshes (McNamara et al., 1988). The extensible

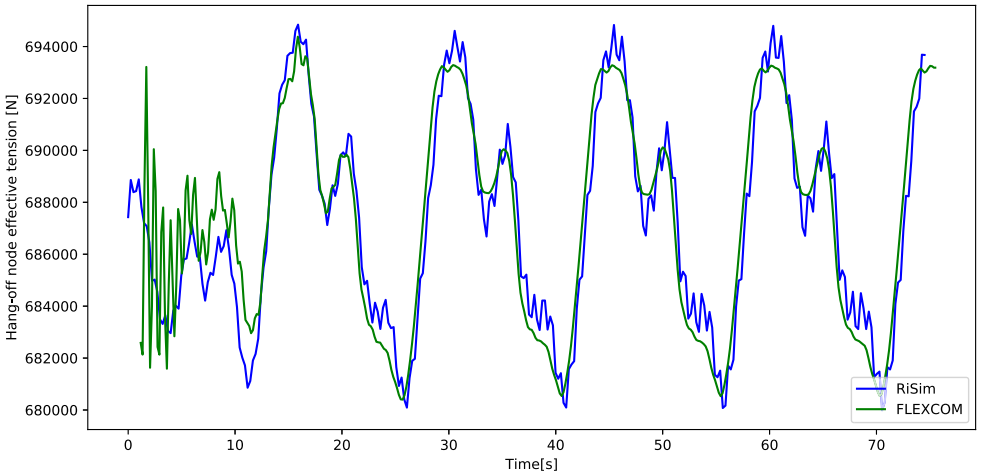

Fig. 5. Hang-off effective tension.

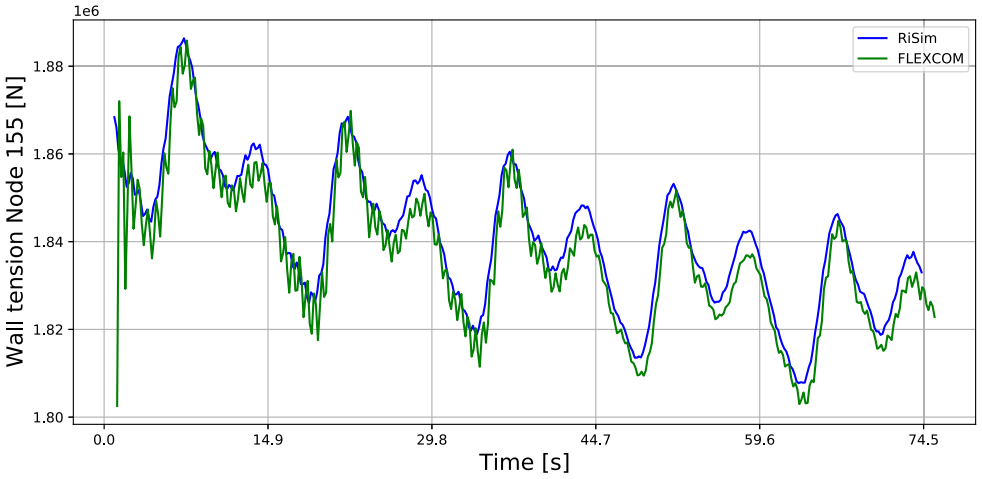

Fig. 6. Hot-spot wall tension time-trace.

method solved with Keller-box scheme finite difference is demonstrated to be stable and converges in fewer time steps to the final system steady state response while remaining consistent to the results from the in-extensible model.

To investigate the phenomena further, the tension time-traces high frequency cycles are counted using the rain-flow method applied to the extensible and in-extensible results. It is found that for the riser system analysed the ratio of the observed high frequency oscillations average amplitude to the top tension high frequency cycle amplitude is close to 1.5%, therefore cycle counting is performed at 1.5% of the top tension range. The oscillations are calculated using rain-flow counting algorithm to investigate this phenomena.

To assess the effect of riser cross-section design on the top tension high frequency cycles. A non-dimensional parameter λ is introduced, defined in equation 15. The parameter is suitable for investigating the relationship between the in-extensible formulation and the high frequency oscillations that are observed, since it is used to investigate the cross-over phenomena of the cable elastic and transverse natural frequencies in (Burgess and Triantafyllou, 1988). Four riser cross-sections are assessed, where the internal diameter of the riser is kept constant while increasing the outer diameter. The corresponding cross-sectional properties are estimated as shown in Table 4 and used in the analysis. The analysis performed in section 3.2.2 is repeated with the cross-sections and the results are is shown in Fig. 8.

Fig. 8 demonstrates the relationship between the parameter λ, varied as multiples of π, in comparison to the number of cycles from the rain-flow counting of the high frequency tension cycles with amplitude 1.5% of the average tension. A curve is fitted to the data points to demonstrate the trend. It is found that both extensible and in-extensible formulations follow a closely related trend with respect to λ, however the effect of the high order oscillations observed in the in-extensible commercial code is demonstrated in Fig. 8 where the average number of cycles is between 2 and 8 times higher than predicted by the extensible code.

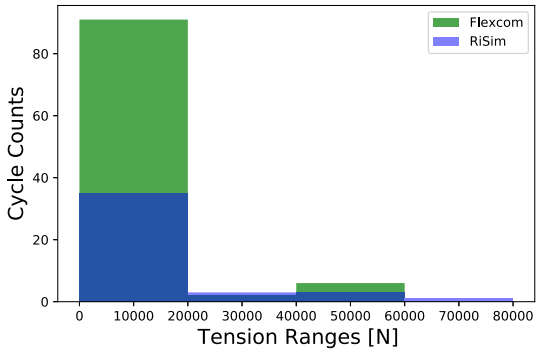

Fig. 7. Tension range Vs Cycle count.

Table 4
Riser load cases.

Parameters	LC1	LC2	LC3	LC4
Internal diameter [m]	0.28	0.28	0.28	0.28
Outer diameter [m]	0.35	0.42	0.49	0.55
Thickness [m]	0.03	0.07	0.10	0.14
Bending Stiffness (EI) [Nm^2]	3.87e+07	9.27e+07	1.78e+08	3.06e+08
Axial Stiffness (EA) [N]	3.12e+09	5.90e+09	9.07e+09	1.27e+10
Mass in air [$kg/\ m$]	116.70	216.22	329.79	460.02
λ [-]	16.33π	18.46π	20.19π	17.19π

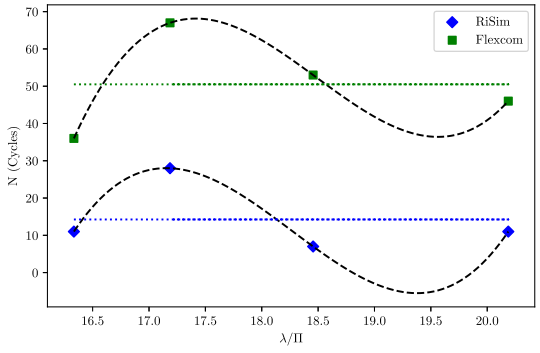

Fig. 8. Number of Cycles N at ΔT = 1.5% static tension at hot-spot.

The low amplitude, high frequency, spurious oscillations are only observed in the in-extensible tension time-traces and don't appear in the curvature time-trace. This suggests that the behaviour is related to the interpolation function implemented in the hybrid element formulation and so the extensible formulation is favoured for composite cross-sections.

$$\lambda = \sqrt{\frac{(w_0 S)^2 EA_0}{T_{horz}^3}\cos\Phi_a} \tag{15}$$

4. Composite pipe numerical model

Global riser analysis is required to estimate the critical section of the riser, the 'hot-spot'. The tension and curvatures time-traces are then imposed as boundary conditions to the composite pipe model. However, there is a gap in the composite pipe modelling literature for offshore applications where it is not clear what elements can be used to accurately model the laminate stresses. Therefore further studies are required to provide higher confidence level in the modelling methods.

Various element types are developed to model composites: equivalent single layer shells, layer-wise continuum shell and 3D continuum solid elements (Reddy, 2003). The suitability of these element depends on the pipe thickness to bending radius ratio. A pipe tends to behave like a thick shell if the ratio between its bending radius and thickness is lower than a specific threshold. However, there is no clear separation in the literature between thin and thick shells for cylindrical pipe applications. Metallic pipes under uniform bending are considered thick and modelled with brick elements as long as the bending radius to thickness ratio is below a factor of 10, while solid continuum elements become inaccurate with larger ratios i.e ratios beyond 25 (Sadowski and Rotter, 2013). 3D solid elements are used for the laminate layup and thickness optimisation by constraining one displacement and applying pure tension on the other end, however the study is limited to laminates under tension load (Wang et al., 2015). Homogenization is used to reduce the computational burden, especially for thick composites, where homogenised elastic constants are derived based on an asymptomatic expansion. The homogenised elastic constants is beneficial when it depends on the stacking sequence, that is often the case with larger thicknesses and small radii. The results obtained from homogenization methods of thin composites are often identical to single layer theories (Sun et al., 2013).

To assess the suitability and computational efficiency of shell, continuum shell and solid elements for composite riser modelling, the loads that are predicted by the global model are imposed as boundary conditions to a composite pipe model which is built in ABAQUS finite element packages. A comparison is made between the following elements: quadratic composite shell *S8R*, continuum composite shell *SC8R*, linear solid composite *C3D8R* and quadratic solid composite *C3D20R*. The results are compared to the homogenization and FE methods that are reported in (Sun et al., 2013).

4.1. FEA model definition

A 22-layer carbon/epoxy composite riser is chosen based on the geometry tabulated in (Sun et al., 2013). The composite riser consists of (from inner to outer layers), a titanium internal liner, composite layers with a layup $[0/90/45/-45]_5$ and a polymer outer sheath. The cross-section design and stacking sequence are illustrated in Fig. 9. The pipe bonded cross-section dimensions and lay-up are listed in Table 5, where contact is not explicitly considered. The titanium liner, composite plies and outer sheath material properties used in the study are in Table 6.

Where E_1 and E_2 are the Young's moduli along the fibre and in the transverse direction respectively; ν_{12}, ν_{23}, ν_{13} are the Poisson's ratios; G_{12} and G_{13} are the in-plane shear moduli and G_{23} is the transverse shear modulus. For failure prediction: X_T and X_C are the longitudinal tensile and compressive strengths; Y_T and Y_C are the transverse tensile and compressive strengths and S is the in-plane shear strength.

The boundary conditions and reference points are illustrated in Fig. 10. Both ends of the pipe are constrained using *multi-point constraint* to reference points that lie on the pipe neutral axis. The reference points are designated RP1 and RP2 and are located in the plane perpendicular to the pipe ends. The boundary conditions and reference points are illustrated in Fig. 10. Reference points RP1 and RP2 are allowed to rotate freely but RP1 is constrained in the translational X, Y and Z directions. RP2 is free to move in the longitudinal Z direction. Boundary conditions and loads are applied to the reference points and transferred via the multi-point constraint to the circumference, to assure even distribution of loads. The boundary conditions and reference points are illustrated in Fig. 10.

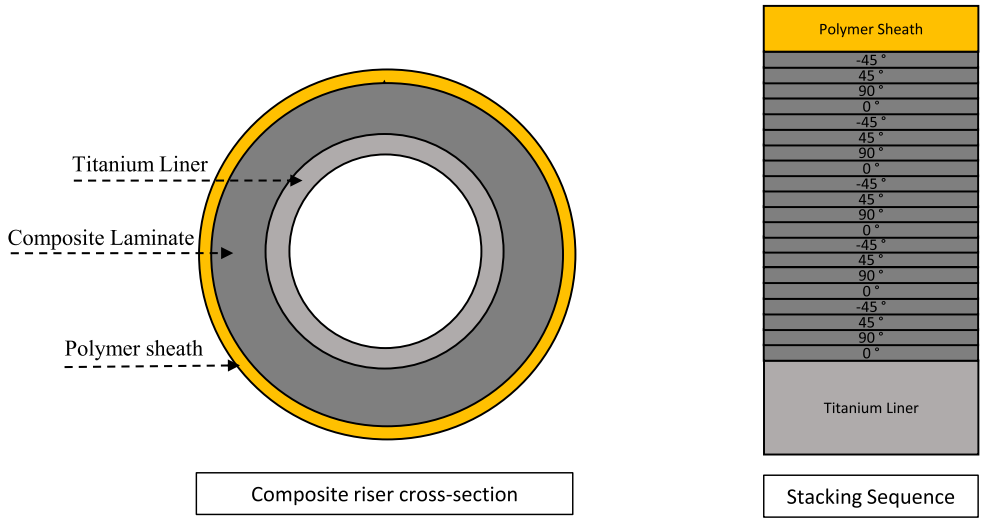

Fig. 9. Composite riser cross-section design and stacking sequence.

Table 5
Composite riser cross-sectional data.

Parameters	Value
Internal diameter [m]	0.28
Outer diameter [m]	0.31432
Pipe length [m]	10.0
Liner thickness [m]	0.005
Outer sheath thickness [m]	0.002
Composite layers thickness [m]	0.01016

Table 6
Composite riser material properties.

Liner (Titanium)	Composite ply	Outer sheath (Polymer)
$E = 120.0$	$E_1 = 135.0$	E = 3.0
$\nu = 0.33$	$E_2 = 8.0$	$\nu = 0.40$
	$E_3 = 8.0$	
	$G_{23} = 2.7$	
	$G_{13} = 3.8$	
	$G_{12} = 3.8$	
	$\nu_{23} = 0.49$	
	$\nu_{13} = 0.27$	
	$\nu_{12} = 0.27$	
	$X_T = 2.45$	
	$X_C = 1.57$	
	$Y_T = 0.07$	
	$Y_C = 0.133$	
	$S = 0.098$	

All moduli are in GPa.

5. Composite pipe benchmarking

The benchmarking cases are chosen to assess the suitability and computational efficiency of shell, continuum shell and solid elements for composite riser modelling. Stress distributions across the laminate thickness are investigated, under axial and bending moment loading conditions. Four models are developed and the results are compared to the homogenization and FE methods that are reported in (Sun et al., 2013). Figs. 11 and 12 shows the longitudinal and hoop stresses σ_z resulting from axial force of 1 kN and bending moment load of 1 kN m. The model results obtained from the static FE analysis are found to match the stresses obtained by the homogenization method in (Sun et al., 2013). All the elements are reported to predict the stress distribution for the tension and bending cases within a 5% difference. It's found that layers with fibre angles of 90° and ±45° experience higher hoop stresses, compared to the Titanium liner, outer polymer sheath and 0° fibre plies. Maximum axial stresses appear in the Titanium liner and 0° composite plies as shown in Figs. 11 and 12.

A 10 m pipe with the properties shown in Tables 5 and 6 is loaded with a combined 1 kN axial force and a 1 kN m moment at both reference points RP1 and RP2. The solid quadratic brick element *C3D20R* is taken as a reference in this study to quantify the relative percentage difference of each element type. Table 7 provides the total number of nodes, elements, degrees of freedom and CPU time required for this analysis.

Figs. 11 and 12 show the maximum percentage differences in stress of 4%, which are exhibited by the linear and quadratic shell *S4R* and *S8R* elements. Lower percentage differences are observed for the *SC8R* continuum shells and the linear *C3D8R* brick element which shows the lowest difference. However, the *SC8R* predicts hoop stresses closer to the quadratic solid *C3D20R* than the *C3D8R* brick element. In general the *SC8R* elements provide an acceptable prediction accuracy compared to it's computational cost which is demonstrated in Table 7. Therefore, the continuum shell element *SC8R* is recommended to model composite risers as it provides the optimum computational cost to accuracy followed by *S8R* element.

6. Riser-pipe coupled dynamic analysis

The coupled responses between the global and local responses are compared when using the extensible and in-extensible formulations. First the dynamic global analysis results that are described in section 3.2.2 are used to identify the hot-spot. Then, a finite element model of the pipe is built for this critical section to investigate the effect of the global loading time-traces predicted by the global models on the composite laminate stresses. The extensible and in-extensible models are used to predict the global riser behaviour, where a top-side sinusoidal motion is applied in the surge direction and the environmental loads are

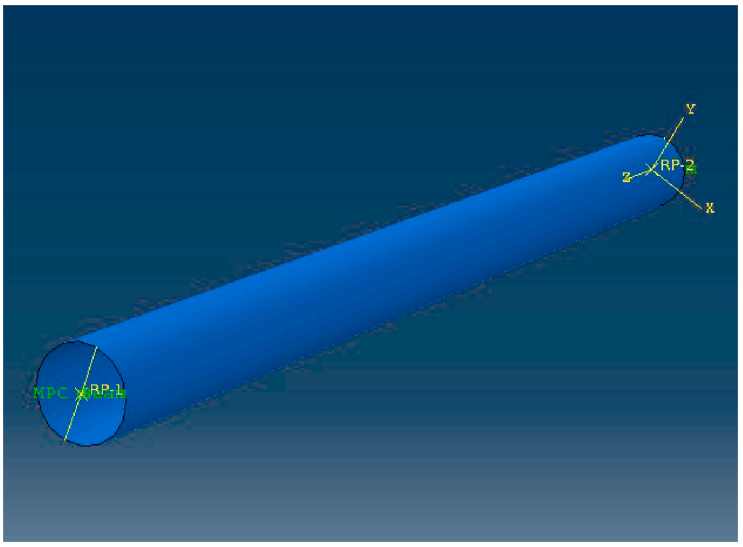

Fig. 10. Pipe model MPC constraint.

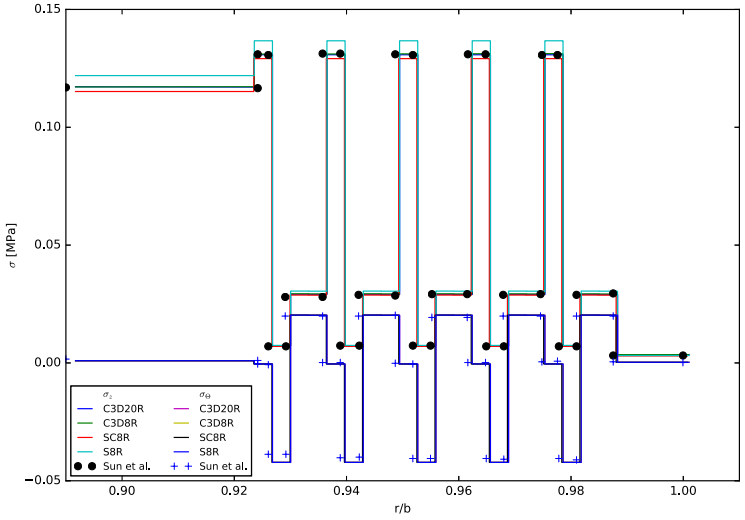

Fig. 11. Stress distributions under axial force.

modelled using linear waves according to the methodology described in section 2, in addition to the parameters in Table 1. The rotations and tension time-traces are extracted from the global models and used as boundary conditions for the finite element continuum shell, composite pipe model. The finite element implicit time domain analysis is performed using the continuum shell elements, *SC8R*. The simulation is five wave periods long with a total time for the simulation of 74.5 s. The hot-spot is identified based on the highest tension and curvature standard deviations. Tensions and curvatures time-traces are the output of the riser analysis, which are applied to the composite pipe model.

A failure criteria is required, in order to quantify the effect of the global methods on the failure of the composite riser at the pipe level. The Tsai-Wu failure criterion is selected, which is a commonly used criterion to predict the first-ply failure and it is recommended as one of the more robust failure theories by the World Wide Failure Exercise. The first-ply is predicted to fail if the left-hand side of equation 16 is equal to, or higher than, unity. Where the terms σ_1, σ_2 and τ_{12} are the fibre longitudinal stress, the stress in the normal to fibre direction and shear stress in the ply; X_t and Y_t are the longitudinal and transverse tensile strengths; while X_c and Y_c are the compressive strengths and; S_{12} is the in-plane shear strength. F_1 is a failure coefficient that is given by equation 17. Composite risers are designed with large safety factors and therefore failure is not expected with the riser properties used in this study. However, the criteria is used here to quantify the effect of both the

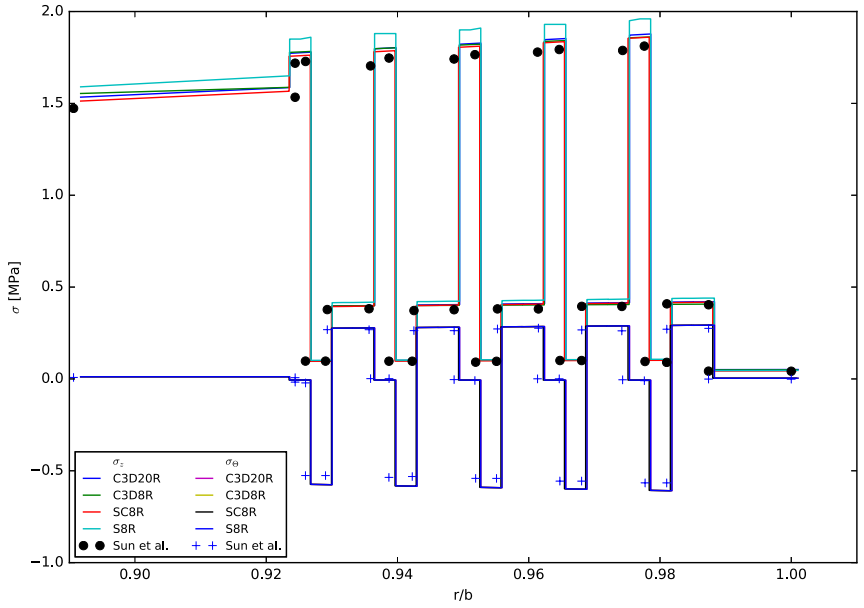

Fig. 12. Stress distributions under bending moment.

Table 7
FEA element type comparison.

Element type	nodes	elements	D.O.F	CPU time[s]
C3D20R	168240	24000	506172	705.27
C3D8R	48098	24000	144876	260.37
SC8R	48098	24000	144876	43.95
S8R	66090	22000	396540	83.85
S4R	22046	22000	132276	27.51

extensible and in-extensible global models on the Tsai-Wu failure index at the hot-spot location.

Table 8
Tsai-Wu failure index.

Global model	Tsai-Wu failure index	
	Unpressurised	Pressurised
RiSim	0.014	0.101
Flexcom	0.016	0.103

the pressure in the riser increases to 200 bar then the percentage difference between RiSim and Flexcom decreases to 2.3% as shown in Table 8. Although the percentage difference is attributed to higher os-

$$\left(\frac{\sigma_1}{X_t X_C}\right)^2+\left(\frac{\sigma_2}{Y_t Y_C}\right)^2+\left(\frac{1}{X_T}-\frac{1}{X_C}\right)\sigma_1+\left(\frac{1}{Y_T}-\frac{1}{Y_C}\right)\sigma_2+\left(\frac{2F_1 2\sigma_1\sigma_2}{\sqrt{X_T X_C Y_T Y_C}}\right)+\left(\frac{\tau_{12}}{S_{12}}\right)^2=1 \tag{16}$$

$$F1=\frac{1}{X_t}-\frac{1}{X_c} \tag{17}$$

The boundary conditions are described in section 2.3. The tension time-traces are extracted from the riser beam model simulation and applied to node RP2 as a point force via the amplitude module in ABAQUS while the rotation angle time-traces are applied to both RP1 and RP2 reference points as boundary conditions.

6.1. Dynamic results

The results shows that the maximum Tsai-Wu failure index is found to be 15% higher for the inextensible formulation in comparison with the extensible simulation, for the unpressurised riser. However, when

cillations observed with the in-extensible formulation as explained in section 3.2.2. The Tsai-Wu failure indices are therefore similar and the formulations don't have a large effect on the composite failure index in strength conditions. The percentage difference is noticed to decrease with higher internal pressure as shown in Table 8. Based on the presented results a reliability analysis or dynamic fatigue simulation is expected to predict marginally higher probabilities of failure if the in-extensible method is used compared to the extensible model. However, these differences are currently captured within the recommended high safety factors that are used in the composite riser design. The finite element analysis running time is 6.8 min to simulate 74.5 s of real time on an *Intel(R) Core(TM) i7-6700 CPU @ 3.*40 GHz with 31 GB RAM computer.

7. Conclusion

As the industry increases the use of composite risers there is a need to review the current techniques used in design. This paper compares models of the global riser and pipe response to determine their appropriateness for composite riser applications. The literature is divided into two main methods for global riser behaviour: extensible and in-extensible beam formulations. In this paper RiSim is developed based on an extensible formulation and compared to an in-extensible FE riser commercial package Flexcom. Both methods predict similar maximum tensions and curvatures with less than 1% difference. However, for the environmental loading conditions listed in Table 3 and sinusoidal top-side excitation following equation 11, the riser tension predicted by the in-extensible formulation experiences spurious high frequency oscillations, although these reduce after the first three wave periods. The source of such oscillations is expected to originate from the in-extensibility condition applied to risers that exhibit lower axial stiffness than flexible steel risers, therefore user care is required during the post-processing stage. The extensible finite difference solution doesn't suffer from spurious oscillations and requires minimal user intervention, and is therefore more suitable for efficient automation and digital-twinning applications, especially those involving supervised learning where these oscillations could affect the machine learning. Composite elements are compared where continuum shell, SC8R, and quadratic shell, S8R, elements are found to be the most suitable to model composite pipe cross-sections. The cross-sectional stresses predicted by the pipe FE model coupled with the in-extensible formulation predicts a Tsai-Wu failure index that is marginally higher than predicted with the extensible formulation. These higher stresses do not have a large effect on the strength response of the composite pipe.

CRediT authorship contribution statement

Hossam Ragheb: Conceptualization, Methodology, Software, Writing - original draft, preparation, Visualization, Investigation. **Adam Sobey:** Supervision, Writing - review & editing.

Declaration of competing interest

The authors declare that they have no known competing financial interests or personal relationships that could have appeared to influence the work reported in this paper.

Acknowledgements

This work was supported by EPSRC Centre of Doctoral Training grant no. EP/L015382/1. We thank wood company for providing academic license of their riser analysis software Flexcom which is used to benchmark the results published in this paper. We would also like to thank Lloyd's Register Foundation, grant no. G0095 for supporting this research.

References

Ablow, C., Schechter, S., 1983. Numerical simulation of undersea cable dynamics. Ocean. Eng. 10 (6), 443–457. https://doi.org/10.1016/0029-8018(83)90046-X.

Bergan, P.G., Mollestad, E., Sandsmark, N., 1985. Nonlinear static and dynamic response analysis for floating offshore structures. Eng. Comput. 2 (1), 13–20. https://doi.org/10.1108/eb023596.

Bernitsas, M.M., Kokarakis, J.E., 1988. Importance of nonlinearities in static riser analysis. Appl. Ocean Res. 10 (1), 2–9. https://doi.org/10.1016/S0141-1187(88)80019-1.

Beyle, A.I., Gustafson, C.G., Kulakov, V.L., Tarnopol'skii, Y.M., 1997. Composite risers for deep-water offshore technology: problems and prospects. 1. Metal-composite riser. Mech. Compos. Mater. 33 (5), 403–414. https://doi.org/10.1007/BF02256894.

Burgess, J., Triantafyllou, M., 1988. The elastic frequencies of cables. J. Sound Vib. 120 (1), 153–165. https://doi.org/10.1016/0022-460X(88)90340-9.

Carr F.B.D.A, Sinclair, M., 2008. Pipeline walking understanding the field layout challenges and analytical solutions developed for the safebuck jip, SPE Projects Facilities and Construction 3. safebuckJIP. URL https://www.onepetro.org/journal-paper/SPE-120022-PA.

Casarella, M., Parsons, M., 1970. Cable systems under hydrodynamic loading. Mar. Technol. Soc. J. 4 (4), 27–44.

Chatjigeorgiou, I.K., 2008. A finite differences formulation for the linear and nonlinear dynamics of 2d catenary risers. Ocean. Eng. 35 (7), 616–636. https://doi.org/10.1016/j.oceaneng.2008.01.006.

Chatjigeorgiou, S.A., Ioannis, K., Mavrakos, 2016. Cable Dynamics for Marine Applications. Springer International Publishing, Cham, pp. 875–906. https://doi.org/10.1007/978-3-319-16649-0_38.

Choc, M.J., Young-IlCasarella, 1972. Configuration of a towline attached to a vehicle moving in a circular path. J. Hydronautics 6. https://doi.org/10.2514/3.62894.

Edmans, B.D., Pham, D.C., Zhang, Z.-Q., Guo, T.F., Sridhar, N., Stewart, G., 2019. An effective multiscale methodology for the analysis of marine flexible risers. J. Mar. Sci. Eng. 7 (10), 340. https://doi.org/10.3390/jmse7100340. URL. https://www.mdpi.com/2077-1312/7/10/340.

Fried, I., 1982. Large deformation static and dynamic finite element analysis of extensible cables. Comput. Struct. 15 (3), 315–319. https://doi.org/10.1016/0045-7949(82)90022-0.

Garrett, D.L., 1982. Dynamic analysis of slender rods. J. Energy Resour. Technol. 104 https://doi.org/10.1115/1.3230419.

Hover, F.S., Grosenbaugh, M.A., Triantafyllou, M.S., 1994. Calculation of dynamic motions and tensions in towed underwater cables. IEEE J. Ocean. Eng. 19 (3), 449–457.

Huang, T., Chucheepsakul, S., 1985. Large displacement analysis of a marine riser. J. Energy Resour. Technol.Trans. ASME 107 (1), 54–59.

Larsen, C.M., 1992. Flexible riser analysis comparison of results from computer programs. Mar. Struct. 5 (2), 103–119. https://doi.org/10.1016/0951-8339(92)90024-J.

Leckie, F.A., Lindberg, G., 1963. The effect of lumped parameters on beam frequencies. Aeronaut. Q. 14 (3), 224–240. https://doi.org/10.1017/S0001925900002791.

McNamara, J.F., O'Brien, P.J., Gilroy, S.G., 1988. Nonlinear analysis of flexible risers using hybrid finite elements. J. Offshore Mech. Arctic Eng. 110 (3), 197–204. https://doi.org/10.1115/1.3257051. https://asmedigitalcollection.asme.org/offshoremechanics/article-pdf/110/3/197/4981764/197/_1.pdf.

Ochoa, O.O., Salama, M.M., 2005. Offshore composites: transition barriers to an enabling technology. Compos. Sci. Technol. 65, 2588–2596. https://doi.org/10.1016/j.compscitech.2005.05.019.

Nordgren, R.P., 1974. On computation of the motion of elastic rods. J. Appl. Mech. 41 https://doi.org/10.1115/1.3423387.

O'Brien, P.J., McNamara, J.F., 1988. Analysis of flexible riser systems subject to three-dimensional seastate loading. Int. Conf. on Behaviour of Offshore Structures (BOSS '88, 1373–1388.

O'Brien, P., McNamara, J., 1989. Significant characteristics of three-dimensional flexible riser analysis. Eng. Struct. 11 (4), 223–233. https://doi.org/10.1016/0141-0296(89)90041-2.

Patel, M., Seyed, F., 1995. Review of flexible riser modelling and analysis techniques. Eng. Struct. 17 (4), 293–304. https://doi.org/10.1016/0141-0296(95)00027-5.

Pham, D.-C., Sridhar, N., Qian, X., Sobey, A.J., Achintha, M., Shenoi, A., 2016. A review on design, manufacture and mechanics of composite risers. Ocean. Eng. 112, 82–96. https://doi.org/10.1016/j.oceaneng.2015.12.004.

Powell, M.J.D., 1964. An efficient method for finding the minimum of a function of several variables without calculating derivatives. Comput. J. 7 (2), 155–162. https://doi.org/10.1093/comjnl/7.2.155 arXiv:http://oup.prod.sis.lan/comjnl/article-pdf/7/2/155/959784/070155.pdf.

Rakshit, S.D.C., Atluri, T., 2008. Viv of a composite riser at moderate Reynolds number using cfd. J. Offshore Mech. Arctic Eng. 130 https://doi.org/10.1115/1.2783849.

Reda, A.M., Forbes, G.L., Al-Mahmoud, F., Howard, I.M., McKee, K.K., Sultan, I.A., 2016. Compression limit state of hvac submarine cables. Appl. Ocean Res. 56, 12–34. https://doi.org/10.1016/j.apor.2016.01.002. URL. http://www.sciencedirect.com/science/article/pii/S0141118716000031.

Reda, A., Sultan, I.A., Howard, I.M., Forbes, G.L., McKee, K.K., 2018. Pipeline walking and anchoring considerations in the presence of riser motion and inclined seabed. Int. J. Pres. Ves. Pip. 162, 71–85. https://doi.org/10.1016/j.ijpvp.2018.01.003. URL. http://www.sciencedirect.com/science/article/pii/S0308016117303824.

Reda, A., McKee, K.K., Howard, I.M., Sultan, I.A., 2019. When is a subsea anchor required for a short pipeline/scr system? Int. J. Pres. Ves. Pip. 171, 278–298. https://doi.org/10.1016/j.ijpvp.2019.02.009. URL. http://www.sciencedirect.com/science/article/pii/S0308016118304204.

Reddy, J.N., 2003. Mechanics of Laminated Composite Plates and Shells, second ed. https://doi.org/10.1201/b12409

Sadowski, A.J., Rotter, J.M., 2013. Solid or shell finite elements to model thick cylindrical tubes and shells under global bending. Int. J. Mech. Sci. 74, 143–153. https://doi.org/10.1016/j.ijmecsci.2013.05.008.

Sun, X.S., Chen, Y., Tan, V.B.C., Jaiman, R.K., Tay, T.E., 2013. Homogenization and stress analysis of multilayered composite offshore production risers. J. Appl. Mech. 81 (3), 031003 https://doi.org/10.1115/1.4024695.

Tarnopol'skii, Y.M., Kulakov, V.L., Mungalov, D.D., 1999. Composites in offshore technology in the next century. Mech. Compos. Mater. 35 (5), 365–372. https://doi.org/10.1007/BF02329321.

Timoshenko, S., Young, D.H., Weaver, W., 1990. Vibration Problems in Engineering 208. https://doi.org/10.1038/208964b0.

Triantafyllou, M.S., 1984. The dynamics of taut inclined cables. Q. J. Mech. Appl. Math. 37 (3), 421–440. https://doi.org/10.1093/qjmam/37.3.421 arXiv:/oup/backfile/content_public/journal/qjmam/37/3/10.1093/qjmam/37.3.421/2/37-3-421.pdf.

Vajravelu, K.V.P.K., 2014. Keller-box Method and its Application. De Gruyter, Berlin, Boston. URL. https://www.degruyter.com/view/product/180086.

Wang, C., Shankar, K., Morozov, E.V., 2015. Tailored local design of deep sea frp composite risers. Adv. Compos. Mater. 24 (4), 375–397. https://doi.org/10.1080/09243046.2014.898438.

Wood, 2018. Flexcom Theory Manual. Woodplc.

Marine Structures 78 (2021) 103015

Contents lists available at ScienceDirect

Marine Structures

journal homepage: www.elsevier.com/locate/marstruc

Extreme response based reliability analysis of composite risers for applications in deepwater

H.A. Ragheb [a,*], M. Goodridge [a], D.C. Pham [b], A.J. Sobey [a,c]

[a] Maritime Engineering Group, University of Southampton, Boldrewood Innovation Campus, Southampton, SO16 7QF, UK
[b] Global Engineering and Materials Inc., 1 Airport Place, Princeton, NJ, 08540, USA
[c] Marine and Maritime Group, Data-centric Engineering, The Alan Turing Institute, The British Library, London, NW1 2DB, UK

ARTICLE INFO

Keywords:
Monte Carlo simulation
Composite risers
Catenary
Durability
Hygrothermal aging

ABSTRACT

As current oil reserves start to deplete, companies are looking to exploit deeper deposits. At these greater depths composite risers, with their high strength-to-weight ratio, reduce the effective tensions and bending moments compared to steel risers. However, there is still limited research into their behaviour, with one key missing element being a comparison with traditional riser designs which accounts for variances in material properties and wave loads. This paper therefore conducts a strength-based reliability analysis of composite catenary risers operating between 1,500 m and 4,000 m. A static global catenary model is combined with Classical Laminate Theory to determine the extreme response and its performance is verified against FEA. This response is evaluated with the Tsai-Wu failure criterion to determine first-ply failure. The effect of laminate moisture absorption on the long-term reliability of submerged composite-based risers is also investigated as it can cause a significant reduction in the strength of composite risers. The reliability analysis is conducted using the Monte Carlo Method, revealing that the composite risers perform well at 4000 m. The degradation in performance from moisture absorption becomes increasingly important at greater depths and needs further investigation for these applications.

1. Requirement for composite risers

The rapid growth in the demand for energy has increased the desire to access new hydrocarbon reserves below the ocean floor. Approximately 12% of global conventional oil reserves lie between 1000 and 4000 m under water. This equates to a total reserve of approximately 300 billion barrels of oil, which could produce 9 million barrels of oil per day by 2035.

Risers are an integral component of this offshore hydrocarbon extraction, allowing oil and gas to be transported from seabed wells to floating platforms for refinement and transfer to shore. Traditionally, these riser elements have been constructed from metal alloys, predominantly steel, which are susceptible to corrosion in the ocean environment, and expensive non-corrosive metal-alloys based on titanium, copper-nickel, duplex and super duplex stainless steel. These conventional materials have had great success in providing safe structures for depths up to 1500 m however, Tarnopol'skii et al. [1] and Ochoa [2] highlight the potential advantages of composite-based risers at greater depths. Composite materials, especially carbon-epoxy, have potential benefits for offshore applications due to a unique combination of their high specific strength, thermal conductivity and low maintenance requirements. Due to these benefits there have been a growing number of investigations into the use of these materials but the lack of research literature and

* Corresponding author.
E-mail address: har1g15@soton.ac.uk (H.A. Ragheb).

https://doi.org/10.1016/j.marstruc.2021.103015
Received 15 May 2020; Received in revised form 4 February 2021; Accepted 19 April 2021
Available online 6 May 2021

current applications has resulted in the use of large safety factors, such as in DNV-RP-F202 DNV [3] which are between 15 and 50. These large safety factors demonstrate that these materials are not well understood for use in these applications, requiring further investigation. One important area highlighted by Pham et al. [4]; is the lack of available studies investigating the reliability of such systems. This is despite the fact that DNV [5] outlines a reliability-based design in their recommendations for composite risers which should meet the target safety levels, outlined in Table 1, which reflect the probability of structural failure due to normal variability in load and resistance. Further motivation comes from Skogdalen and Vinnem [7,8] who describe the risks that can occur in offshore scenarios such as riser breakage which can have major consequences and who advocate a proactive risk-based approach to safety, requiring a greater quantitative understanding of new technologies.

Whilst there is limited published evidence of stochastic analyses for composite risers, steel designs have been utilised for longer and methods are already available to investigate their reliability. Carrillo et al. [9] presents a methodology to analyse the structural reliability of the ultimate limit strength of a steel catenary riser (SCR) under conditions present in the Gulf of Mexico. The results indicate that the lowest probability of failure occurs at the contact point and submarine connection, with annual failure probabilities of 2.958×10^{-5} and 7.318×10^{-5}, with the elements connected with the TLP and Catenary Transition areas experiencing failure rates of 1.731×10^{-14} and 1.133×10^{-11} respectively. Li and Low [10] performed a fatigue reliability analysis for steel risers utilising FORM on a response surface method generated from an Orcaflex model and outlines a number of other studies in this area demonstrating the importance of these studies.

While reliability studies have been conducted on steel catenary risers, application of these to a large-scale composite riser still remains an important challenge, Pham et al. [4]. To help address the gap in the literature this paper performs an analysis of composite risers to determine failure at maximum loads and compares the trends in behaviour to those of steel catenary risers. A static global catenary analysis is performed with the addition of Classical Laminate Theory which is shown to be accurate to FEA within 10% and its performance is empirically adjusted to further reduce this error. A strength-based assessment is selected to provide an initial understanding of risers at larger depths and it is also rare for fatigue failures to occur in composite materials where first-ply failure is a common mode of analysis. In addition, this analysis is extended to investigate the effect of moisture absorption on the composite properties between wet and dry conditions as all current riser analysis addresses only the intact condition. The paper then incorporates the effect of moisture absorption on the composite extreme failure based on the Tsai-Wu failure criterion.

2. Monte Carlo simulation of a riser

The analysis of riser systems has been conducted by various studies using a number of different techniques. DNV [5,6] recommends a global-local procedure, where a global analysis is first conducted to extract effective tensions, bending moments, thermal loads and pressure loads, which act as boundary conditions for the subsequent local analysis. The local analysis then yields the local stresses and strains which are applied to a particular failure criteria to evaluate possible failure mechanisms of the riser elements. Tan et al. [11]; Kang et al. [12] and Zhan [13] all conducted studies utilising static global catenary models to determine equilibrium positions, force extraction or the basis for a further dynamic study. Kang et al. [12] noted that the bending moments generated were larger than those calculated via other methodologies along with some discrepancy in the static position of the riser as compared to other models. However, Bridge [14] concludes that the use of the simple catenary equations is considered a good approximation. In a similar application Da Silva et al. [15] utilised this type of model to optimize a composite laminate structure for a riser system. An analytical catenary solver was used for the static global model due to the faster run times compared to FEA while also providing representative results. The global analysis was used to extract the riser shape and effective axial tensions, based on the weight per unit length, top/departure angle and the operating depth of the riser system. Classical Laminate Theory (CLT) was then utilised to conduct a local analysis of critical sections of the riser and to extract the stresses and strains acting on a segment of the riser. The resulting stresses from the Classical Laminate Theory were then assessed by the Tsai-Wu criterion to determine possible failure. The local model is utilised as the basis for the reliability analysis with the addition of the von Mises failure criterion when metallic risers are considered.

To perform the reliability analysis a Monte Carlo simulation was employed, shown in Fig. 1, to analyse variations in mechanical and manufacturing properties of laminate materials, as well as environmental loads, following a similar procedure to Sobey et al. [16]. The Monte Carlo simulation generates a large number of random values for the stochastic variables (X_i), which are then inserted into the limit state function $G(X)$ to determine if the structure will fail. The method allows for the calculation of the probability of failure over the entire domain of load inputs. In addition to its simplicity and accuracy, the Monte Carlo simulation is also robust in its applicability to various situations. However, in cases of small probabilities of failure, the required number of simulations increases significantly, resulting in additional computational time.

The material properties for the riser are based on Carbon/Epoxy T700/X4201 manufactured by Torayca in Japan with statistical distributions taken from Philippidis et al. [17]. Properties for steel are taken from Xia et al. [18]; which alongside the mechanical

Table 1
Target annual failure rate for composite risers as recommended by DNV [5,6].

Failure Type	Failure Consequence		
	Low Safety Class	*Normal Safety Class*	*High Safety Class*
Ductile	$P_f = 10^{-3}$	$P_f = 10^{-4}$	$P_f = 10^{-5}$
Brittle	$P_f = 10^{-4}$	$P_f = 10^{-5}$	$P_f = 10^{-6}$

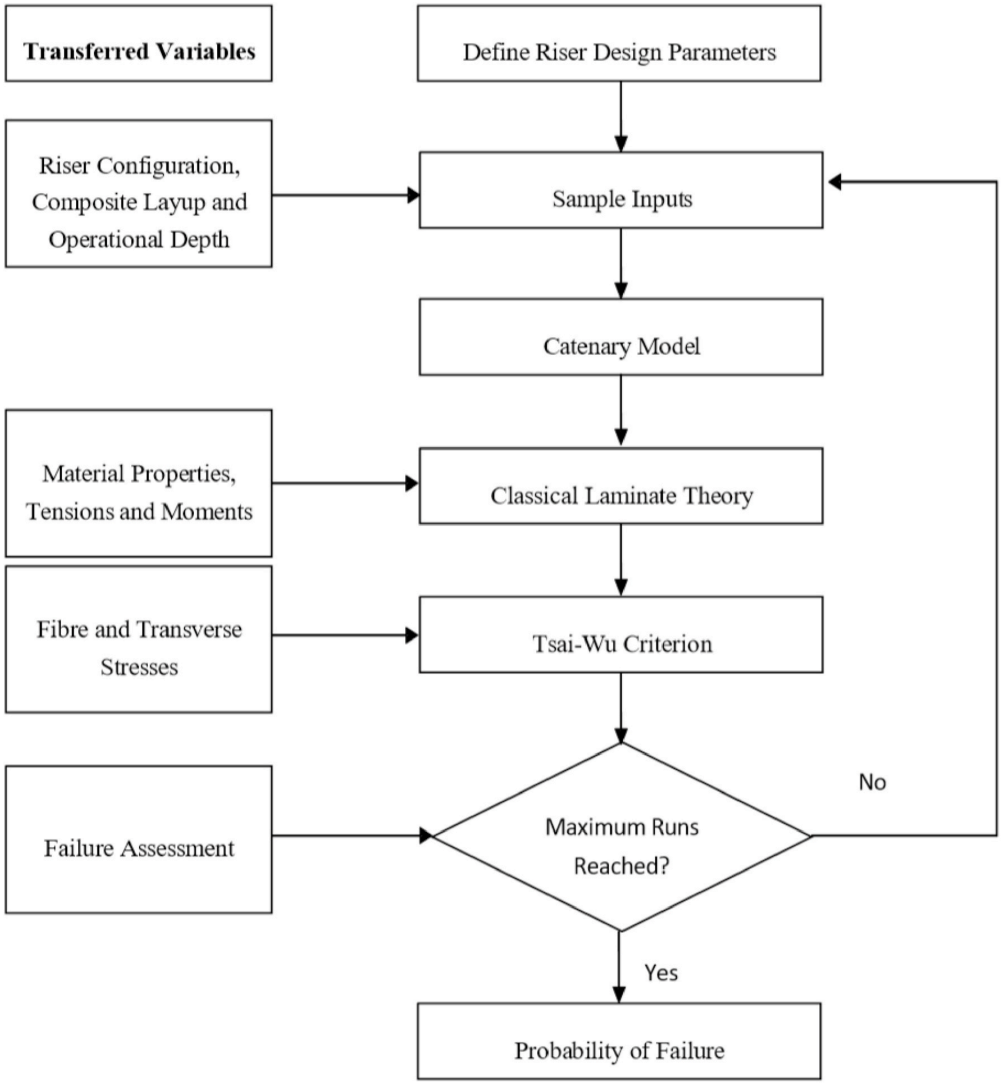

Fig. 1. Monte Carlo simulation methodology.

properties, are given in Table 2, where Xt and Xc are the carbon fibre tensile strength in tension and compression in the fibre direction; similarly Yt and Yc are the strengths in the transverse direction; S is the shear strength; Ex and Ey are the elasticity modulus in the fibre and transverse directions; G is the shear modulus and ν is the Poisson's ratio. It is expected that composite material parameters exhibit co-variation between these properties, however, the available in the literature doesn't account for this co-variation, therefore, and therefore, it is assumed that the material properties are statistically independent.

Two different types of risers, from Tan et al. [11] and from Wei [19]; are assessed with the topology and layup for each riser given in Table 3 and illustrated in Fig. 2. The steel riser was developed to have the same thickness as the larger composite riser found in Wei [19] with a corresponding unit mass of 115 kg/m. The risers were subjected to a horizontal tension of 1.3×10^5 N and were assumed to have an internal fluid density of 700 kg/m^3. The riser designs are selected to determine trends in behaviour, not as direct comparisons between each other.

Table 2
Statistical variations and material properties for carbon/epoxy and steel.

	Composite		Steel		Distribution
	Mean Wei [19]	CoV Philippidis et al. [17]	Mean Xia et al. [18]	CoV Xia et al. [18]	
Xt (MPa)	2450	5%	N/A	N/A	Normal
Xc (MPa)	1570	16%	N/A	N/A	Normal
Yt (MPa)	70	18%	N/A	N/A	Normal
Yc (MPa)	133	16%	N/A	N/A	Normal
S (MPa)	98	11%	N/A	N/A	Normal
Yield Strength (MPa)	N/A	N/A	550	6%	Normal
Ex (GPa)	125	10%	197.5	2%	Normal
Ey (GPa)	9.588	16%	197.5	2%	Normal
G (GPa)	5.4	20%	78	3%	Normal
ν	0.35	11%	0.3	1%	Normal

Table 3
Layup structure & Global properties of each composite pipe under study.

Pipe structure	Steel	Tan et al. [11]	Wei [19]
Number of Laminae	N/A	20-ply	56-ply
Layup	N/A	$[45/-45/15/80]_5$	$[90/15/-15/90/45/-45/45/-45/45/-45]_5 + [45/-45]_3$
Thickness of Steel liner (mm)	18.3	5	7
ID (m)	0.1834	0.2796	0.1836
OD (m)	0.22	0.31667	0.22
Ply Thickness (mm)	N/A	0.675	0.075
Laminate Wall thickness (mm)	N/A	13.5	11.2
Mass in air (kg/m)	91	57	46
Bending Stiffness, EI (MN.m2)	11.9	27.5	8.83
Axial Stiffness, EA (MN)	2319.19	2500.96	1756.65

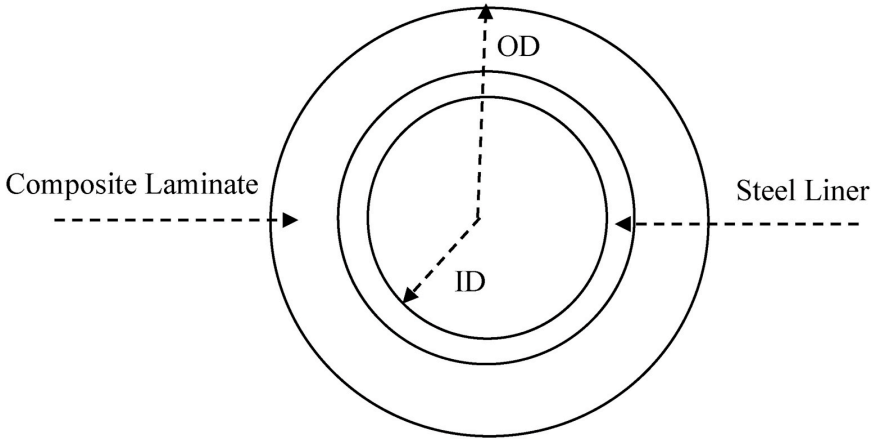

Fig. 2. Composite riser cross-section design.

3. Global response model

The static catenary model is modelled using an analytical approach based on the work of Faltinsen [20]; describing the behaviour of catenary mooring lines and is chosen for computational efficiency.

3.1. Catenary model

The global model used to determine the static equilibrium position of the riser was derived from the steel catenary riser models employed in a number of other analyses including Duan et al. [21]; Bridge [14] and Kang et al. [12]. The catenary model allows a simple representation of the risers including the specification of the geometry of the system as well as the extraction of axial tensions.

While bending stiffness is inherently neglected in this approach, bending moments can be extracted by including material properties and curvature at each point.

The governing mathematical equations for the catenary shape assume neglected bending stiffness, in-extensible cable, infinite axial stiffness, and no hydrodynamic forces. The equation requires the following inputs: w, submerged weight per unit length of the cable; T_H, horizontal tension; ρ_l, density of constituent laminate structure; ρ_i, density of internal fluids; ρ_f, density of external medium; h, operational depth and the geometry of the cylindrical pipe to evaluate the second order differential equation, eq. (1),

$$y''(x) = \frac{1}{\alpha}\sqrt{1 + [y'(x)]^2}; \tag{1}$$

where α is the catenary parameter, $\frac{T_H}{w}$. The boundary conditions are imposed such that eqs. (2)–(4) are valid:

$$y(0) = 0, \tag{2}$$

$$y'(0) = 0, \tag{3}$$

$$\tan\theta_0 = 0; \tag{4}$$

where θ_0, is the angle of the seabed at the touchdown point. Assuming the angle of the seabed is 0 leads to eq. (5),

$$y(x) = \frac{T_H}{w}\left[\cosh\left(\frac{w}{T_H}x\right) - 1\right] - h. \tag{5}$$

which is a catenary curve with a departure point at $y = 0$, sea level and a touchdown point at a depth of h metres below the sea surface.

The length of the catenary section, s, based on the horizontal, x, distance from touch-down point can be determined using eq. (6),

$$s(x) = \frac{T_H}{w}\sinh\left(\frac{w}{T_H}x\right) \tag{6}$$

Forces acting on the riser include tension, both vertical and horizontal, as well as the bending moments, which were estimated using eqs. (7) and (8),

$$T_v(x) = w.s(x), \tag{7}$$

$$T(x) = \sqrt{\left(T_v^2(x) + T_H^2\right)}, \tag{8}$$

where $T_v(x)$ is the distribution of the vertical component of tension along the length of the riser. In addition, the bending moments acting on a segment of the riser can be estimated by multiplying the curvature by the bending stiffness inherent to the material and the geometry, which is shown in eq. (9),

$$M(x) = EI.\kappa(x) = EI\frac{w}{T_H\cos h^2\left(\frac{w}{T_H}x\right)} \tag{9}$$

This model does not consider any environmental factors, and represents the static position as a free hanging chain which excludes sea current and wave effects. These factors were then included via statistical distributions based on the findings of DNV [6]; Chu [22] and Zhan [13] where the forces related to undersea currents are modelled as additions to the constant T_H, while wave and current variability is modelled as additions to the sea depth using the Weibull probability density function shown in equation (10), where the parameters α_H and β are the scale and shape parameters of the Weibull distribution as shown in Table 4. The forces related to current flow were applied using the following simplified assumptions:

1. Tangential current velocity is neglected; this is recommended by DNV [6]; as it is an insignificant consideration for riser applications.
2. Normal current velocity is constant in the Y, vertical direction or depth. This simplifies the application of an ocean current, without losing generality.
3. Acceleration of ocean currents is excluded. It is assumed that the normal velocity of the ocean currents remain constant which eliminates inertial loading effects as predicted by Morison's Formula.

Table 4
Characteristics of ocean current velocity and wave height, DNV [6]] and Chu [22]].

	Distribution	Suggested Parameters
Wave Height	Weibull	$\alpha_H = 0.681$, $\beta = 2.126$
Current Velocity	Weibull	$\alpha_H = 0.3$, $\beta = 2$

$$p(wp) = \frac{\beta}{\alpha H}\left(\frac{wp}{\alpha H}\right)^{\beta-1} exp\left[-\left(\frac{wp}{\alpha H}\right)^{\beta}\right] \tag{10}$$

The Weibull shape parameter β is equal to the slope of the probability plot where β > 1 indicates that the value is close to the mean wave height and slightly positively skewed with a tail to right of the distribution curve, while the scale parameter α_H shrink or squeeze the density function and affect if the function is narrow or wide banded.

Therefore, the force acting on the riser per unit length for constant current is equivalent to the drag term of the Morison formula in eq. (12). Where v_{rel} is the riser velocity relative to the water particle velocity, accounting for wave, v_{wave}, and current velocities, $v_{current}$ as given by eq. (11),

$$v_{rel} = v_{riser} - v_{current} - v_{wave} \tag{11}$$

As this study is based on the static catenary model, the riser velocity, v_{riser} is equal to zero in equation (11). The dynamic effect of the wave and the hang-off excitation is accounted for in the Dynamic Amplification Factor, which is equal to unity for wave conditions that are described in section 3.2 and are the basis of this study.

$$F_n = \frac{1}{2}\rho C_D D v_{rel}|v_{rel}|, \tag{12}$$

where F_n is the force per unit length, ρ is the density of surrounding fluids, C_D is the normal drag coefficient, D is the diameter and v is the current velocity. The C_D for the purpose of this analysis a value of 1.25 was chosen.

3.2. Verification of riser model

The outputs of the developed model using the properties listed in Table 5 are shown in Figs. 4 and 5 in comparison to the FEA model utilised in Zhan [13]. Both models reflect similar results for the static geometric profile and characteristic forces acting on the riser. Maximum tensions and bending moments as well as their distribution along the length of the riser are similar and almost identical between the models. A sensitivity study is carried out using FLEXCOM software to quantify the maximum dynamic amplification factor due to waves and the FPSO motion. A 270 m FPSO is chosen and exposed to a range of sea states with wave periods close to its heave heave natural frequency, of 15.7 s, and water depths, of 1500, 2000, 3000 and 4000 m, to replicate the worst-case scenario. This is performed using the thicker, 56-ply riser configuration proposed for the later studies, documented in Fig. 6, and top-tensions in Table 6. The sensitivity results in Fig. 3 show that the dynamic model using regular waves can be approximated by the simple static approach for regions which are dominant by waves of up to 4 m wave height, at which the dynamic amplification factor is close to unity. This approximation is acceptable for regions, such as Gulf of Guinea, where the short-term environmental conditions matches the criteria of the 4 m maximum wave height. In such cases the variations between the simple static analytical approach and the FEA approach are less than 1%. The effects of wave height are not included in the final model as they are found to increase the computational expense but with a limited increase in accuracy, while current effects are still included.

3.3. Investigation into riser response

A simple comparison between the steel and composite risers, shown in Table 6, gives an indication for the differences between the maximum bending moments that are observed at the touch-down zone and maximum tensions at the hang-off point. Water depths of 1500 m are chosen to represent current deep-water applications with incremental increases to 4000 m, indicating the maximum depth for which future riser applications are likely to be aiming.

Composite catenary risers exhibit greater horizontal displacements than the traditional steel catenary risers with similar operating depths as a result of the lower density and transverse stiffness of composite systems as shown in Fig. 6. This also has the consequence of increasing the necessary length of composite systems compared to steel catenary risers to reach the surface elevation starting from the

Table 5
SCR verification study properties.

Parameter	Value
Outer diameter (m)	0.273
Wall thickness (m)	0.0127
Weight in air (kg/m)	125
Internal fluid density (kg/m^3)	700
Length (m)	2240
Water depth (m)	1000
Hang-off to point of no motion (Horizontal distance)(m)	1500
Modulus of Elasticity (GPa)	207
Boundary condition	Pinned-Pinned
Analysis type	Static

Table 6
Maximum bending moments and tensions related to global models.

Water Depth (m)	Arc-Length (m)	Max. Tension (N)	Max. Bending Moment (Nm)
56-ply composite Wei [19]			
1500	1957	485914	28049
2000	2471	613628	27526
3000	3490	866054	28019
4000	4498	1116779	28049
20-ply composite Tan et al. [11]			
1500	2079	392603.7	66068
2000	2601	491228.6	66893
3000	3625	684859	66922
4000	4642	876417	66068
Steel			
1500	1659	1323057	79672
2000	2160	1723999	80664
3000	3176	2522527	79863
4000	4181	3323526	79672

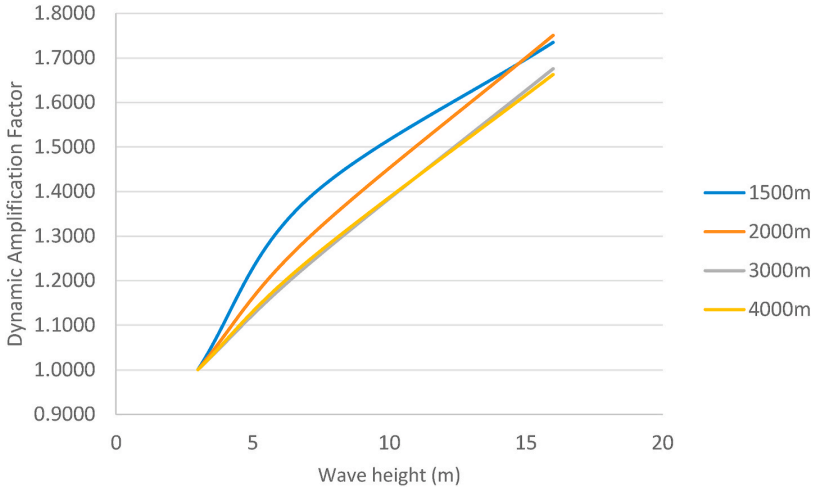

Fig. 3. Amplification factor sensitivity between the static analysis and a dynamic case.

same touch-down point, due to lighter apparent weight of composites. This is most evident for the 20-ply composite system which has the lowest density, and requires a total length of 2079 m to reach its operating depth of 1500 m. It is observed that the maximum bending moments remain constant for those models with the same materials, and is thus independent of operating depth, as opposed to tensions which are weight, and hence depth, dependant. As a result, steel catenary risers incur significantly larger bending moments, which peak at the touchdown point.

4. Pipe model

Global loads are obtained from the catenary equation but because the method is based on a one-dimensional beam formulation, that only represents the centre line of the riser, there is missing information for the remaining two spatial dimensions of the pipe cross-section. Two interface equations are needed to recover this information for the cross-sectional local analysis and to calculate the equivalent in-plane force, N, and the equivalent induced moment, M,. If an infinitesimal section of the composite pipe wall is considered at the maximum curvature location, then the in-plane forces at this location is due to the tension in the beam and the tension induced by the curvature at the location of the outer ply.

The tension, T, and the bending moment, M_{global}, are calculated from the catenary equation. The equivalent in-plane force, N, is the equivalent force that is applied to the laminate x direction and causes the same stress at the outer ply that results from the tension force and bending moment. The calculations are based on equation (13),

$$N = T + Feq_{outerply} \tag{13}$$

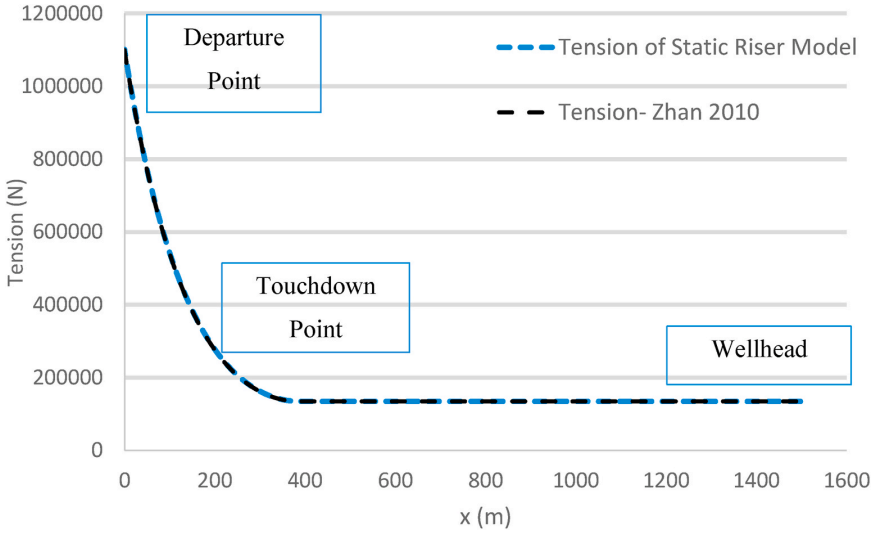

Fig. 4. Tension forces from static global model in comparison to Zhan [13].

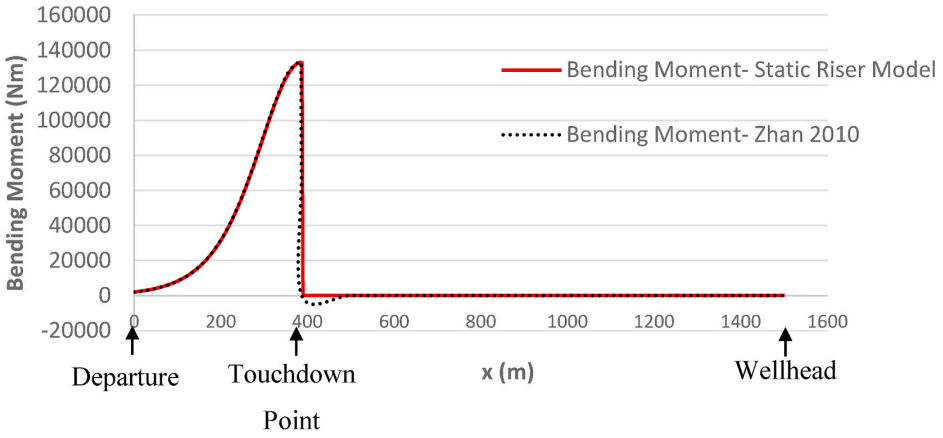

Fig. 5. Bending moments from static global model in comparison to Zhan [13].

which is dependant on $Feq_{outerply}$, the equivalent force at the outer ply, defined in equation (14),

$$Feq_{outerply} = \frac{M_{global} * r_{outerply} * Ac}{I} \tag{14}$$

where r is distance from the pipe neutral axis to the outer ply centre, Ac is the cross-sectional area and I is the second moment of area of the pipe.

The difference between the stress at the outer ply and the mid-plane of the composite laminate generates a rectifying moment about the y axis of the laminate that is located at the neutral axis of the laminate section as shown in Fig. 7. Therefore, the equivalent moment is calculated using equation (15),

$$M = \frac{t^{*}\left(Feq_{outerply} - Feq_{mid-plane}\right)}{2}, \tag{15}$$

where t is the thickness of the riser. The equivalent force at the mid-plane, $Feq_{mid-plane}$, can be found by replacing $r_{outerply}$ with $r_{mid-plane}$ in equation (14). The principal stresses obtained by this analytical method are verified against a finite element model constructed using

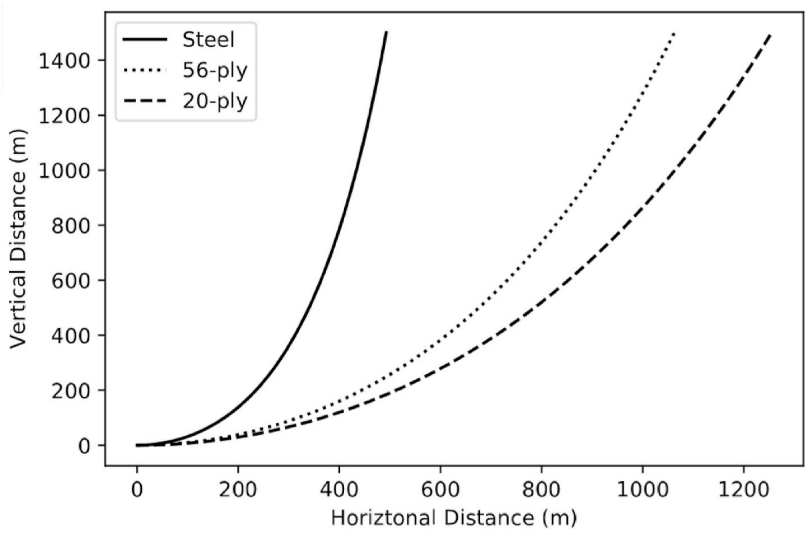

Fig. 6. Comparison of configurations for risers manufactured using different material properties.

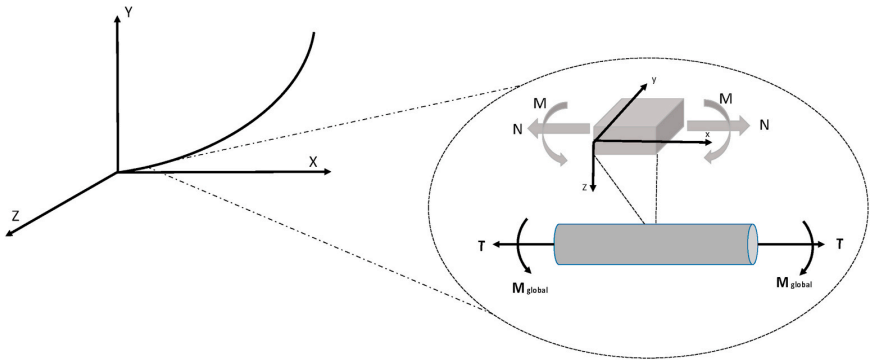

Fig. 7. Schematic of the global loads applied to the local cross-section.

continuum shell elements, where the load from the static model is applied and the end of the pipe are constrained using a multi-point constraint which are tied to a point on the neutral axis. The highest principal component stress at the outer ply is found to be 10% higher than the analytical values, and therefore a multiplier of 1.1 is applied to the analytical model to adjust for this difference.

The pipe analysis is conducted to determine the stresses and strains acting on the laminate structure of the riser. This is performed using Classical Laminate Theory (CLT), defined in equation (16), using the notation from Nijhof [23];

$$\begin{pmatrix} N \\ M \end{pmatrix} = \begin{bmatrix} A & B \\ B & D \end{bmatrix} \begin{Bmatrix} \varepsilon^0 \\ \kappa \end{Bmatrix}; \tag{16}$$

where A is the extension stiffness matrix; B is the bending-extension coupling effects between in plane stresses and curvatures and between bending and twisting moments and in plane strains; D is the stiffness of the laminate in the perpendicular direction under the influence of bending and twisting moments; ε^0 is the vector of strain at a particular point in the laminate; κ is the vector of curvatures induced in the laminate by the external forces; N represents the in-plane forces acting on the segment of the composite pipe and M representing the corresponding induced moments about the laminate mid-plane. The in-plane strain vector $\{\varepsilon\}_k$ for the kth lamina is given by equation (17),

$$\{\varepsilon\}_k = \{\varepsilon^0\} + z_k\{\kappa\} \tag{17}$$

The stress-strain relationship can be determined for the kth lamina by employing equation (18),

$$\{\sigma\}_k = [Q']_k\{\varepsilon^0\} + z_k[Q']\{\kappa\}, \tag{18}$$

where z_k is the distance from the midplane of the laminate in the thickness direction, Q′ is the transformed reduced stiffness matrix for each lamina, dependent on the lamina's angle relative to the principle direction of the laminate, and $\varepsilon = \{\varepsilon_x, \varepsilon_y, \varepsilon_{xy}\}$ is a vector of in-plane strains experienced by the laminate. The stress components of $\{\sigma\}_k$ are evaluated by the Tsai-Wu failure criterion, in equation (19), and is used to determine the reliability,

$$\left(\frac{\sigma_1}{X_T X_C}\right)^2 + \left(\frac{\sigma_2}{Y_T Y_C}\right)^2 + \left(\frac{1}{X_T} - \frac{1}{X_C}\right)\sigma_1 + \left(\frac{1}{Y_T} - \frac{1}{Y_C}\right)\sigma_2 + \left(\frac{2F_1 2\sigma_1\sigma_2}{\sqrt{X_T X_C Y_T Y_C}}\right) + \left(\frac{\tau_{12}}{S_{12}}\right)^2 = 1 \tag{19}$$

The Tsai-Wu criterion is chosen as a good predictor of first-ply failure, and it is assumed that after this initial failure that the riser is unsafe and that the failure will propagate. The left-hand side of the equation is evaluated, at each node along the riser length, and the utilisation factor can take values between 0 and 1, where 1 indicates first ply failure. The highest Tsai-Wu value for each riser is found near the touchdown point (x = 0) or departure point which agrees with the findings of Wang et al. [24] and Buberg [25]; where bending moments and tension forces are maximized respectively. As the operational depth increases the Tsai-Wu value closest to the departure point fails, until by 4000 m, the Tsai-Wu value is lowest at the departure point. This analysis is selected to provide initial guidance on the probability of failure for composite risers, which are unlikely to fail in the same manner as steel, and to ascertain the importance of water saturation. The steel analysis forms a point of reference and in reality extreme bending moments are an unlikely reason for failure in steel catenary risers that are in service because the riser configuration is often designed to avoid low bending radii and that the most likely form of failure is due to fatigue at the touch-down zone.

5. Reliability of risers

An analysis is performed to compare the trends in reliability between conventional steel risers with composite alternatives across different configurations. This analysis is also extended to investigate the change in reliability estimation of FRP composite risers in wet and dry conditions. The number of runs used for each simulation is 10^8 with values below this probability judged to be due to numerical phenomena rather than an accurate estimate of the reliability.

5.1. Sensitivity to dynamic effects

One challenge when combining a dynamic FEA analysis and Monte-Carlo simulation, is the computational expense which makes the approach infeasible. However, a dynamic amplification factor study, shown in Fig. 3, predicts values close to unity for significant wave height conditions that are lower than 4 m. To verify this assumption the following steps are followed and the results compared to the quasi-static approach for dry and wet conditions:

1. A load case matrix is constructed covering 1–6 m wave heights and wave periods ranging between 12 and 22 s. A Flexcom finite element riser model, that is used in the dynamic amplification study in Fig. 3, is utilised to perform the detailed analysis of the load matrix cases. The dynamic amplification factors are estimated for maximum tension and curvature using regular waves. The dynamic amplification factors are estimated as the ratio between the maximum tension or curvature along the riser length divided by the static value for each load case; these values are listed in Tables 9 and 10 in the Appendix.
2. For conservatism, extreme short-term omni-directional wave conditions are assumed. The annual waves distribution is predicted by Weibull distribution in equation (10) and parameters listed in Table 4. This distribution is found to represent the short-term wave height in the Gulf of Guinea region. The maximum short-term significant wave height is found to be 2.67 m, Akinsanya [26]. The environmental directions are assumed to be in the far and near directions for conservatism. In-line waves, currents and offset directions are considered to capture both extreme cases of maximum top-tensions and curvatures.
3. The drag force is calculated using a quasi-static approach by summing the constant velocity current and the maximum wave particle velocities along the riser length.
4. The 2nd Order FPSO response is captured with varying the offset as a function of the wave height as shown in equation (20), the bottom tension is re-calculated for each run with new configurations after adding the offset and the corresponding top tension is estimated. The load case offset, $offset_{LC}$, is given by the following equation (20),

$$offset_{LC} = offset_{max} * \left(\frac{H_{LC}{}^2}{H_{max}{}^2}\right), \tag{20}$$

where the maximum offset, $offset_{max}$, is defined as 0.9% of the depth.
5. The maximum axial force that propagates along the riser, due to the FPSO pitch and heave motions, is approximated using the tension dynamic amplification factor.
6. The maximum curvature that occurs due to the transverse waves propagating along the riser length, due to the FPSO motion, is approximated using the curvature dynamic amplification factor.
7. Two distinctive dynamic amplification factors are used, one for the tension and another for curvature to capture the difference in peak dynamic amplification factor noticed around different wave periods. For environmental conditions that lies between the pre-simulated dynamic amplification factors provided in the Appendix, Tables 9 and 10 a linear interpolation is incorporated.

The reliability analysis results, shown in Fig. 12, are the probability of failures calculated using the quasi-static approach, compared to the detailed dynamic amplification factor predicted by the FEA analysis. A slight increase of the probability of failure is observed, however, the figure shows that the quasi-static approach remains a reasonable approximation for the short-term extreme environmental conditions in the Gulf of Guinea region.

5.2. Steel catenary risers vs composite risers

The reliability of two Steel Catenary Risers, one at 1500 m and another at 4000 m, are analysed and compared to the results of a composite-based riser system to establish a benchmark for comparison. The results show negligible probability of failure and justifies why such risers are in widespread use for offshore hydrocarbon extraction. Further simulations are not performed as the results demonstrate that the probability of failure is low and simulations where failures only occur deep in the tails of the distributions may not be significant from a practical perspective. The reliability of these simulations is similar to the dynamic results from Carrillo et al. [9]; which is assessed to be 1.33×10^{-11} in the catenary transition zone and 1.73×10^{-14} at the connection to the tension leg platform for a riser of unknown length, but who quote a reliability on the order of 10^{-5} at the weakest points near the Touchdown Zone which are not exhibited in this model. The simulation of the Steel Catenary Riser operating in ocean depths of 4000 m reveals a significantly higher top tension much larger than that of the of the Steel Catenary Riser operating at 1500 m. However, the probability of failure for these risers is still lower than composites.

To determine the probability of failure, a convergence study is performed to select the appropriate number of runs required for the Monte-Carlo simulation, illustrated in Figs. 8 and 9. In comparison, Fig. 8 reveals the rate of failures for the 56-ply composite layup operating at 1,500 m. These simulations provide a probability of failure of 4.4×10^{-7} which is higher than the steel catenary riser operating at 1500 m which recorded no failures. However, this is still determined to be a safe value according to the DNV rules, Table 1. This increases to 1.6×10^{-5} for depths of 4000 m which is still safe, but more importantly shows only a small increase in probability of failure but where the rate in change of failure for the steel catenary is unknown as no failures have occurred.

Fig. 9 shows that the probability of failure for the 20-ply riser, [11]; has not converged but reaches a value of 6.0×10^{-8}. However, this can be considered to be a numerical anomaly as they are occurring in the tails in the normal distribution and unlikely to represent real properties as they are unrealistically far from the mean value. Therefore, the simulations are stopped at this point and assumed to be a very low value. This demonstrates a similar probability of failure to that of a steel catenary riser with similar thickness and operating depth. For the 20-ply case the probability of failure increases to 1.2×10^{-7} at 4000 m demonstrating convergence and a similar low probability of failure.

Table 7 compares the different systems with respect to the unit weight and the total weight of the entire riser system. Steel catenary risers show smaller deflections than the composite risers and the low stiffness exhibited by composite materials increases the overall length of the composite system. A larger thickness for the riser might improve the performance of the riser system but will also require higher tension loads and the results in this analysis demonstrate the opposite effect, thin and light risers are less likely to fail. The Marginal Reliability, the improvement in probability of failure for each kilogram of additional material, of Carbon/Epoxy improves reliability by 9.07×10^{-13} and 1.53×10^{-13} for the 56- and 20-ply composite riser respectively and at 4000 m this increased to 1.43×10^{-11} and 1.37×10^{-13}. The probability of failure per kilogram, Pf/kg is a normalized failure probability that is a parameter to allow easier comparison of the cross-sectional design by addition or reduction of riser material to indicate the change in the probability of failure.

Both composite layups fulfil the DNV's lower safety class recommendation, $P_f = 10^{-5}$ DNV [5]; at depths of 1500 m and 4000 m. This builds confidence in the ability of composite risers to be utilised in deep-water conditions and the potential to benefits from lower weight, and therefore reduced installation costs. However, the analysis shows limited benefits, in terms of reliability, over steel under extreme conditions. The steel catenary riser provides a higher level of reliability than the design using a composite material statically. However, the two composite riser and steel catenary riser designs are chosen arbitrarily and the analysis shows that thinner thicknesses of pipe provide a safer design but that the steel benefits from a higher stiffness. This analysis therefore needs to be extended with an analysis performed on optimally designed pipes for each distance, supported by the findings from the parametric study performed in this paper, and a dynamic analysis.

5.3. The impact of moisture absorption of riser reliability

Whilst the results of the previous study indicate the potential for composites for deep-water applications, it is unlikely that these materials will perform for extended periods with the performance of testing in dry conditions. To account for this, the riser properties are degraded to represent the wet state according to experiments from the open literature. Malmstein et al. [27] provide data for glass/epoxy composites in conditions lasting up to 6 weeks in distilled water. The material properties of the degraded material are shown to be more dependent on the composite matrix resin material, so findings related to the degradation percentage of glass provides can be extrapolated to carbon, due to the small quantity of data available in the open literature. The findings of these experiments show that the riser flexural strength is reduced by 50% and the weight is increased by 2%; the flexural modulus is also reduced by 1.6% but this reduction is ignored. The degradation of composites in distilled water is often higher than in salt water and the results are also for flexure, rather than tension, and so this degradation factor is considered as a worst-case scenario. Experiments are also performed on carbon/epoxy specimens by Zafar et al. [28] who found an increase in weight of 2.12% in conditions lasting up to 300 days in salt water. The corresponding loss of tensile strength was 20% and Young's modulus was 10%. These values are therefore included into the model where Zafar et al. [28] represents more realistic values for risers due to the similar materials and

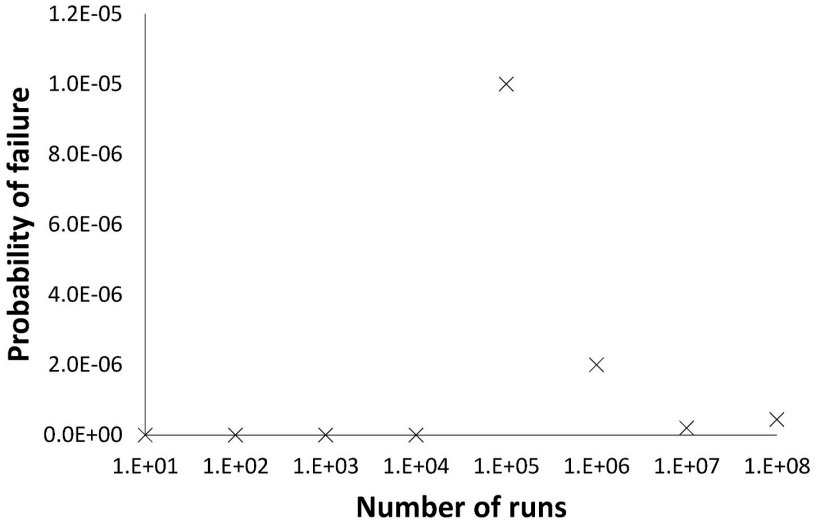

Fig. 8. Probability of failure for the 56-ply composite, Wei [19]; operating at 1500 m.

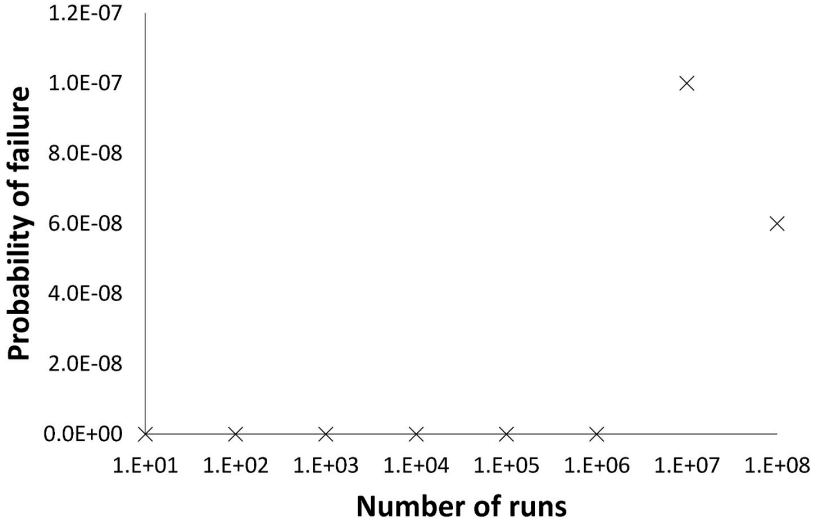

Fig. 9. Probability of failure for the 20-ply composite riser, Tan et al. [11]; operating at 1,500 m.

Table 7
Comparison of weight and probability of failure for steel catenary and composite risers.

	1500 m			4000 m		
	Steel	56-ply	20-ply	Steel	56-ply	20-ply
Submerged weight full of product (N/m)	794	248	189	794	248	189
Arc-Length (**m**)	1659	1957	2079	4181	4498	4642
Total Weight	1.3E+06	4.9E+05	3.9E+05	3.3E+06	1.1E+06	8.8E+05
P_f	<1.0E-8	4.4E-07	6.0E-08	<1.0E-8	1.6E-05	1.2E-07
P_f/kg	<1.0E-13	9.1E-13	1.5E-13	<1.0E-13	1.4E-11	1.4E-13

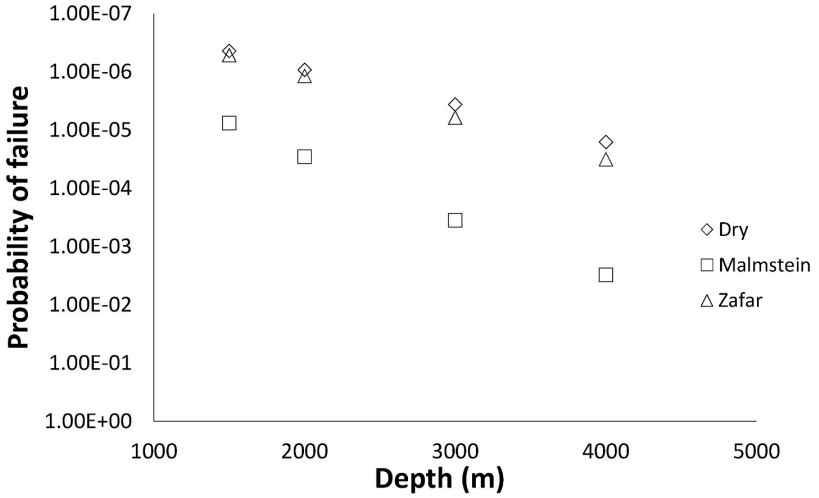

Fig. 10. Probability of failure for the 56-ply composite riser, Wei [19]; after water absorption aging at increasing water depths.

tensile properties alongside experiments conducted in salt water. The reliability analysis for different depths is reported in Fig. 10 where the probability of failure is shown in logarithmic scale, for the 56-ply case, and similarly, Fig. 11, for the 20-ply case. The results are assumed to have converged as the probability of failure for the wet simulations should be higher than those in the dry condition, requiring fewer runs to converge and therefore the same number of simulations are performed.

These results imply that, as expected, there is a negative relationship between water retention and reliability. The reduction in ultimate tensile strength and Young's Modulus combined with the increased weight per unit leads to a combined effect of increasing the tension while reducing the materials resistance to external loadings. This explains why the probability of failure is higher for the moisture absorbed riser systems. Comparing the two types of moisture absorption the Zafar et al. [28] case reports higher probability of failures for all of the risers in comparison to the dry properties; at lower depths this increase is mild however at the larger depths it is more significant. This trend also occurs for the less realistic properties from Malmstein et al. [27] but the probability of failure is higher.

The results for the wet composites, summarised in Table 8, are more indicative of the number of failures to be expected as the system matures over time, and may be used to establish the upper limits for the operating lifetime for FRP riser systems. Even in the

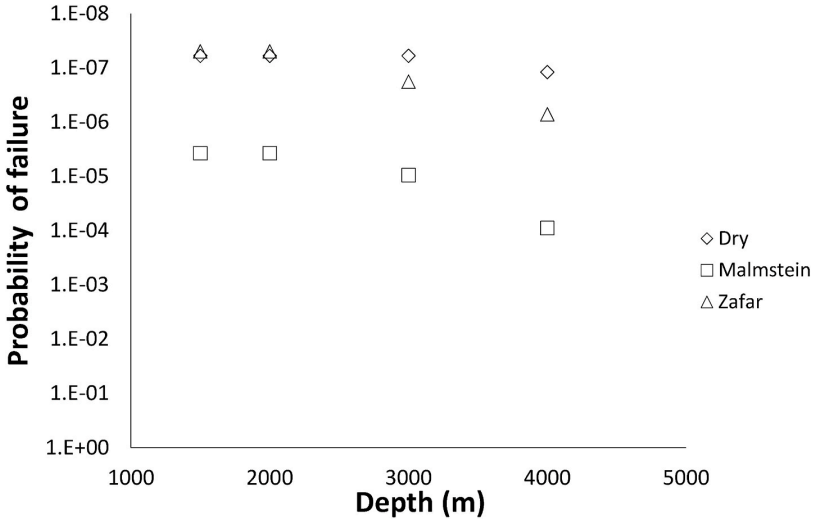

Fig. 11. Probability of failure for the 20-ply composite riser, Tan et al. [11]; after water absorption aging at increasing water depth.

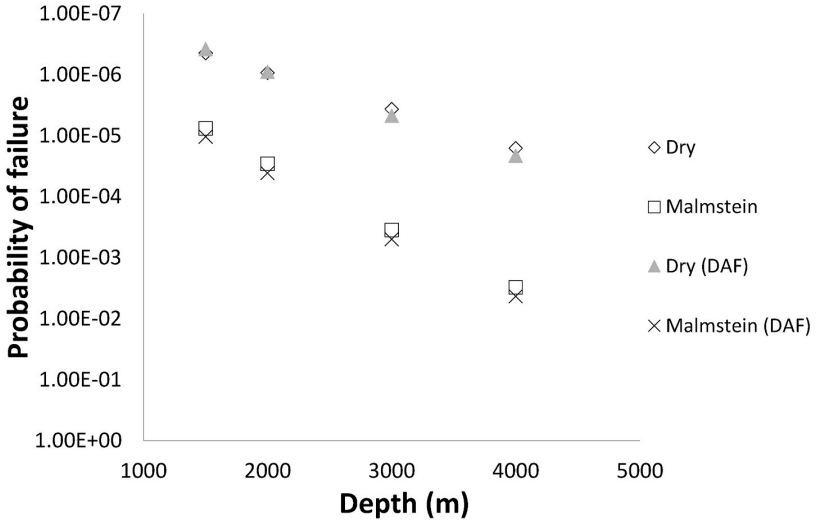

Fig. 12. Probability of failure for the 56-ply composite riser using a quasi-static analysis and dynamic analysis, for dry and after water absorption aging at increasing water depths.

Table 8
Probabilities of failure for composite risers with moisture absorption.

	56-ply			20-ply		
	Dry	Malmstein et al. [27]	Zafar et al. [28]	Dry	Malmstein et al. [27]	Zafar et al. [28]
1500 m						
P_f	4.40E-07	7.56E-06	5.20E-07	6.00E-08	3.74E-06	5.00E-08
Weight (kg)	4.85E+05	4.89E+05	4.89E+05	3.92E+05	3.99E+05	3.99E+05
P_f/kg	9.07E-13	1.55E-11	1.06E-12	1.53E-13	9.37E-12	1.25E-13
2000 m						
P_f	9.30E-07	2.87E-05	1.18E-06	6.00E-08	3.75E-06	5.00E-08
Weight (kg)	6.13E+05	6.18E+05	6.18E+05	4.91E+05	4.99E+05	4.99E+05
P_f/kg	1.52E-12	4.65E-11	1.91E-12	1.22E-13	7.51E-12	1.00E-13
3000 m						
P_f	3.64E-06	3.52E-04	6.08E-06	6.00E-08	9.50E-06	1.80E-07
Weight (kg)	8.65E+05	8.72E+05	8.72E+05	6.84E+05	6.97E+05	6.97E+05
P_f/kg	4.21E-12	4.04E-10	6.97E-12	8.77E-14	1.36E-11	2.58E-13
4000 m						
P_f	1.60E-05	3.05E-03	3.18E-05	1.20E-07	8.95E-05	7.20E-07
Weight (kg)	1.12E+06	1.12E+06	1.12E+06	8.76E+05	8.92E+05	8.93E+05
P_f/kg	1.43E-11	2.71E-09	2.82E-11	1.37E-13	1.00E-10	8.06E-13

worst-case material degradation scenario, the Malmstein et al. [27] aging and the thicker 56-ply case, the probability of failure for the 1,500 m is still 7.56×10^{-6} and is only predicted to pass the lower safety limit at 4,000 m with a probability of failure of 3.05×10^{-3}, which could be reduced with enhanced cross-sectional design.

The increase in probability of failure due to the hygrothermal aging is higher for the thicker composite, where the values increase by a factor of 62–746 over the intact riser for the extreme case of Malmstein et al. [27] and by 1–6 for the more realistic aging case of Zafar et al. [28]; than for the thinner riser, with an increase by a factor of 17–190 for the extreme aging case of Malmstein et al. [27] and 1.18–1.98 for the more realistic aging case of Zafar et al. [28]; where these values are highest at the higher depths. This underscores the need for effective and robust waterproof layering to protect the laminate from direct contact with the surrounding saline environment as suggested by Tan et al. [11] for their composite system. This system will extend the operating lifetime of the pipeline, and potentially reduce maintenance and operational expenses in the long run by reducing moisture contact with the laminate. However, it is unlikely that it will be totally able to remove the moisture from the environment and determining the levels of absorption over time appears to be a critical characteristic in reducing safety factors for composite risers in deep-water conditions, where even the more realistic water uptake estimates give an increase in probability of failure of 6 for the thicker riser and 1.98 for the thinner riser.

6. Conclusions

Composite risers are increasingly being investigated for industrial applications with some current applications already in place. However, there is limited literature documenting the stochastic behaviour of risers made from these materials. Therefore, this paper conducts a strength-based reliability assessment of full-scale carbon/epoxy composite risers in comparison with traditional steel catenary risers. A dynamic amplification factor is derived, and verified, using an FE model to predict a similar probability of failure compared to the quasi-static approach, confirming the suitability of the quasi-static model to predict the failure probability in the Gulf of Guinea region. The results confirm the benefits of FRP composites risers for depths approaching 4,000 m over conventional steel risers, in that they provide a safe but lighter weight system which is therefore cheaper to install; thinner risers are shown to have a lower probability of failure due to the lighter weight and lower tensions. However, the risers are shown to have a higher probability of failure in comparison to the steel equivalents. Additional studies are performed to account for the effect of water absorption on the material degradation and the performance of the composite risers. The results show that the reliability of composite risers is reduced due to moisture absorption and that this becomes more pronounced at depths exceeding 2,000 m.

Declaration of competing interest

The authors declare that they have no known competing financial interests or personal relationships that could have appeared to influence the work reported in this paper.

Acknowledgements

This work was supported by EPSRC Centre of Doctoral Training grant no. EP/L015382/1 and by the Lloyd's Register Foundation.

Appendix

Table 9
Tension Dynamic Amplification Factors (1500/3000/4000 m)

		Wave Period (s)										
		12	13	14	15	16	17	18	19	20	21	22
Maxim	1	1.02/	1.03/	1.04/	1.04/	1.04/	1.04/	1.04/	1.04/	1.04/	1.03/	1.02/
Wave		1.02/	1.03/	1.03/	1.04/	1.04/	1.04/	1.04/	1.04/	1.03/	1.03/	1.02/
Height		1.02/	1.03/	1.03/	1.03/	1.03/	1.03/	1.03/	1.03/	1.03/	1.03/	1.02/
(m)		1.01	1.02	1.03	1.03	1.03	1.03	1.03	1.03	1.03	1.03	1.01
	2	1.04/	1.06/	1.07/	1.08/	1.08/	1.08/	1.08/	1.08/	1.07/	1.07/	1.04/
		1.04/	1.06/	1.07/	1.08/	1.08/	1.08/	1.08/	1.08/	1.07/	1.07/	1.04/
		1.03/	1.05/	1.06/	1.07/	1.07/	1.07/	1.07/	1.07/	1.06/	1.06/	1.03/
		1.03	1.05	1.06	1.06	1.06	1.06	1.06	1.06	1.06	1.05	1.03
	3	1.06/	1.09/	1.11/	1.12/	1.12/	1.13/	1.12/	1.12/	1.12/	1.11/	1.06/
		1.06/	1.09/	1.11/	1.12/	1.12/	1.12/	1.12/	1.12/	1.11/	1.11/	1.06/
		1.05/	1.08/	1.09/	1.11/1.1	1.11/1.1	1.11/1.1	1.1/1.09	1.1/1.09	1.09/	1.09/	1.05/
		1.04	1.07	1.09						1.08	1.08	1.04
	4	1.08/	1.12/	1.15/	1.17/	1.17/	1.18/	1.17/	1.18/	1.17/	1.16/	1.08/
		1.08/	1.12/	1.14/	1.16/	1.17/	1.17/	1.17/	1.17/	1.16/	1.16/	1.08/
		1.07/	1.1/1.09	1.12/	1.14/	1.14/	1.14/	1.14/	1.13/	1.13/	1.12/	1.07/
		1.06		1.11	1.13	1.13	1.13	1.12	1.12	1.11	1.11	1.06
	5	1.1/1.1/	1.15/	1.18/	1.22/	1.22/	1.24/	1.24/	1.24/	1.23/	1.23/	1.1/1.1/
		1.08/	1.15/	1.18/	1.21/	1.22/	1.24/	1.23/	1.23/	1.23/	1.22/	1.08/
		1.07	1.13/	1.16/	1.18/	1.18/	1.18/	1.18/	1.18/	1.17/	1.16/	1.07
			1.12	1.14	1.16	1.16	1.16	1.15	1.15	1.14	1.13	
	6	1.12/	1.18/	1.23/	1.27/	1.29/	1.31/	1.31/	1.32/	1.31/	1.3/	1.12/
		1.12/	1.18/	1.22/	1.27/	1.28/	1.31/	1.3/	1.31/	1.3/	1.29/	1.12/
		1.1/1.09	1.16/	1.19/	1.22/1.2	1.22/	1.23/	1.22/	1.22/	1.22/	1.21/	1.1/1.09
			1.14	1.17		1.19	1.19	1.19	1.18	1.17	1.16	

Table 10
Curvature Dynamic Amplification Factors (1500/3000/4000 m)

		Wave Period (s)										
		12	13	14	15	16	17	18	19	20	21	22
Maxim	1	1.02/	1.03/	1.04/	1.04/	1.04/	1.05/	1.05/	1.05/	1.05/	1.04/	1.02/
Wave		1.02/	1.03/	1.03/	1.04/	1.04/	1.05/	1.05/	1.05/	1.05/	1.05/	1.02/

(*continued on next page*)

Table 10 (*continued*)

		Wave Period (s)										
		12	13	14	15	16	17	18	19	20	21	22
Height (m)		1.01/ 1.01	1.02/ 1.01	1.03/ 1.01	1.03/ 1.02	1.04/ 1.02	1.04/ 1.02	1.04/ 1.02	1.04/ 1.02	1.04/ 1.02	1.04/ 1.02	1.01/ 1.01
	2	1.04/ 1.03/ 1.02/ 1.01	1.06/ 1.05/ 1.04/ 1.02	1.07/ 1.07/ 1.05/ 1.03	1.08/ 1.08/ 1.06/ 1.03	1.09/ 1.09/ 1.07/ 1.04	1.1/ 1.09/ 1.08/ 1.04	1.1/1.1/ 1.08/ 1.04	1.1/1.1/ 1.08/ 1.04	1.1/1.1/ 1.08/ 1.04	1.1/1.1/ 1.08/ 1.04	1.04/ 1.03/ 1.02/ 1.01
	3	1.05/ 1.05/ 1.04/ 1.02	1.08/ 1.08/ 1.06/ 1.03	1.11/ 1.1/ 1.08/ 1.04	1.13/ 1.13/ 1.1/1.05	1.14/ 1.14/ 1.11/ 1.05	1.16/ 1.16/ 1.12/ 1.06	1.16/ 1.16/ 1.12/ 1.06	1.17/ 1.17/ 1.13/ 1.06	1.17/ 1.17/ 1.13/ 1.07	1.17/ 1.17/ 1.13/ 1.07	1.05/ 1.05/ 1.04/ 1.02
	4	1.07/ 1.06/ 1.05/ 1.02	1.11/ 1.1/ 1.08/ 1.04	1.15/ 1.14/ 1.11/ 1.05	1.19/ 1.19/ 1.14/ 1.07	1.21/ 1.21/ 1.16/ 1.07	1.23/ 1.24/ 1.18/ 1.08	1.24/ 1.25/ 1.19/ 1.09	1.25/ 1.26/ 1.2/1.09	1.25/ 1.27/ 1.2/1.09	1.26/ 1.27/ 1.2/1.09	1.07/ 1.06/ 1.05/ 1.02
	5	1.09/ 1.08/ 1.06/ 1.03	1.14/ 1.13/ 1.1/1.05	1.2/ 1.19/ 1.14/ 1.07	1.26/ 1.26/ 1.2/1.09	1.29/ 1.3/ 1.22/1.1	1.33/ 1.35/ 1.26/ 1.11	1.34/ 1.37/ 1.27/ 1.12	1.37/ 1.39/ 1.29/ 1.13	1.37/ 1.4/ 1.29/ 1.13	1.37/ 1.4/ 1.29/ 1.13	1.09/ 1.08/ 1.06/ 1.03
	6	1.1/ 1.09/ 1.07/ 1.03	1.18/ 1.17/ 1.13/ 1.06	1.25/ 1.25/ 1.19/ 1.08	1.35/ 1.36/ 1.26/ 1.11	1.39/ 1.42/ 1.3/1.13	1.46/ 1.5/ 1.36/ 1.15	1.48/ 1.52/ 1.38/ 1.16	1.51/ 1.57/ 1.41/ 1.17	1.51/ 1.57/ 1.41/ 1.17	1.52/ 1.57/ 1.41/ 1.18	1.1/ 1.09/ 1.07/ 1.03

References

[1] Tarnopol'skii YM, Kulakov VL, Mungalov DD. Composites in offshore technology in the next century. Mech Compos Mater 1999;35(5):365–72.
[2] Ochoa OO. Composite riser experience and design guidance, final project report prepared for the minerals management service under the MMS/OTRC cooperative research agreement 1435-01-04-CA-35515, task order 35985. Texas A&M University; 2006. MMS Project Number 490.
[3] Det Norske Veritas. Recommended practice for composite risers. Oslo, Norway: DNV-RP-F202; 2009.
[4] Pham DC, Narayanaswamy S, Qian X, Sobey AJ, Achintha M, Shenoi RA. A review on design, manufacture and mechanics of composite risers. Ocean Eng 2016;112:82–96.
[5] Det Norke Veritas. Recommended practice composite risers. Oslo, Norway: DNV-RP-F202; 2010.
[6] Det Norske Veritas. Environmental conditions and environmental loads. Oslo, Norway: DNV-RP-C205; 2010.
[7] Skogdalen JE, Vinnem JE. Quantitative risk analysis offshore - human organizational factors. Reliab Eng Syst Saf 2011;96:468–79.
[8] Skogdalen JE, Vinnem JE. Quantitative risk analysis of oil and gas drilling, using Deepwater Horizon as case study. Reliab Eng Syst Saf 2012;100:58–66.
[9] Carrillo CC, Cicilia FB, del Angel FC. Structural reliability in catenary upstream pipelines, vol. III. El Portulano De La Ciencia; 2011. p. 907–14.
[10] Li FZ, Low YM. Fatigue reliability analysis of a steel catenary riser at the touchdown point incorporating soil model uncertainties. Appl Ocean Res 2012;38:100–10. https://doi.org/10.1016/j.apor.2012.07.005. Available at:.
[11] Tan L, Chen Y, Jaiman RK. Coupled fluid–structure simulations for evaluating a performance of full-scale deepwater composite riser. Ocean Eng 2015;94:19–35. Available at: http://linkinghub.elsevier.com/retrieve/pii/S0029801814004193.
[12] Kang Z, Zhang L, Zhang X. Analysis on J lay of SCR based on catenary and large deflection beam theory. Ocean Eng 2015;104:276–82. Available at: http://linkinghub.elsevier.com/retrieve/pii/S0029801815001936.
[13] Zhan JP. Review and verification of marine riser analysis programs : global response analysis. Norwegian Univeristy of Science and Technology; 2010.
[14] Bridge C. Effects of seabed interaction on steel catenary. University of Surrey; 2005.
[15] Silva RF Da, et al. Optimization of composite catenary risers. Mar Struct 2013;33:1–20.
[16] Sobey AJ, Blake JIR, Shenoi RA. Monte Carlo reliability analysis of tophat stiffened composite plate structures under out of plane loading. Reliab Eng Syst Saf 2013;110:41–9. https://doi.org/10.1016/j.ress.2012.08.011. Available at:.
[17] Philippidis TP, Lekou DJ, Aggelis DG. Mechanical property distribution of CFRP filament wound composites. Compos Struct 1999;45(1):41–50.
[18] Xia J, Das PK, Karunakaran D. A parametric design study for a semi/SCR system in Northern North Sea. Ocean Eng 2008;35:1686–99.
[19] Wei Z. Mechanical and fatigue test of CFRP risers. National University of Singapore Report; 2015.
[20] Faltinsen O. Sea loads on ships and offshore structures. Cambridge: Cambridge University Press; 1990.
[21] Duan M, Chen J, Li Z. Mechanics of deepwater steel catenary riser. 2011 [Shanghai].
[22] Chu PC. Weibull distribution for the global surface current speeds obtained from satellite altimetry. International Geoscience and Remote Sensing Symposium (IGARSS) 2008;3(1).
[23] Nijhof AHJ. Analysis of laminated composites. In: Shenoi RA, Wellicome JF, editors. Composite materials in maritime structures. Volume 1: fundamental aspects. Cambridge: Cambridge University Press; 1993.
[24] Wang Y, Gao D, Fang J. Static analysis of deep-water marine riser subjected to both axial and lateral forces in its installation. J Nat Gas Sci Eng 2014;19:84–90. https://doi.org/10.1016/j.jngse.2014.04.019. Available at:.
[25] Buberg T. Design and analysis of steel catenary riser systems for deep waters. Norwegian University of Science and Technology; 2014.
[26] Akinsanya A. Swell description for Bonga offshore Nigeria location. Ocean Systems Engineering 2017:345–69.
[27] Malmstein M, Chambers AR, Blake JIR. Hygrothermal ageing of plant oil based marine composites. Composite Strutures 2013;101:138–43.
[28] Zafar A, Bertocco F, Schjodt-Thomsen F, Rauhe JC. Investigation of the long term effects of moisture on carbon fibre and epoxy matrix composites. Compos Sci Technol 2012;72:656–66.

Appendix B - DAF

Table 1: Tension Dynamic Amplification Factors (1500/2000/3000/4000m)

		Wave Period (s)										
		12	13	14	15	16	17	18	19	20	21	22
Maxim	1	1.02/	1.03/	1.04/	1.04/	1.04/	1.04/	1.04/	1.04/	1.04/	1.03/	1.02/
Wave		1.02/	1.03/	1.03/	1.04/	1.04/	1.04/	1.04/	1.04/	1.03/	1.03/	1.02/
Height		1.02/	1.03/	1.03/	1.03/	1.03/	1.03/	1.03/	1.03/	1.03/	1.03/	1.02/
(m)		1.01	1.02	1.03	1.03	1.03	1.03	1.03	1.03	1.03	1.03	1.01
	2	1.04/	1.06/	1.07/	1.08/	1.08/	1.08/	1.08/	1.08/	1.07/	1.07/	1.04/
		1.04/	1.06/	1.07/	1.08/	1.08/	1.08/	1.08/	1.08/	1.07/	1.07/	1.04/
		1.03/	1.05/	1.06/	1.07/	1.07/	1.07/	1.07/	1.07/	1.06/	1.06/	1.03/
		1.03	1.05	1.06	1.06	1.06	1.06	1.06	1.06	1.06	1.05	1.03
	3	1.06/	1.09/	1.11/	1.12/	1.12/	1.13/	1.12/	1.12/	1.12/	1.11/	1.06/
		1.06/	1.09/	1.11/	1.12/	1.12/	1.12/	1.12/	1.12/	1.11/	1.11/	1.06/
		1.05/	1.08/	1.09/	1.11/1.1	1.11/1.1	1.11/1.1	1.1/1.09	1.1/1.09	1.09/	1.09/	1.05/
		1.04	1.07	1.09						1.08	1.08	1.04
	4	1.08/	1.12/	1.15/	1.17/	1.17/	1.18/	1.17/	1.18/	1.17/	1.16/	1.08/
		1.08/	1.12/	1.14/	1.16/	1.17/	1.17/	1.17/	1.17/	1.16/	1.16/	1.08/
		1.07/	1.1/1.09	1.12/	1.14/	1.14/	1.14/	1.14/	1.13/	1.13/	1.12/	1.07/
		1.06		1.11	1.13	1.13	1.13	1.12	1.12	1.11	1.11	1.06
	5	1.1/1.1/	1.15/	1.18/	1.22/	1.22/	1.24/	1.24/	1.24/	1.23/	1.23/	1.1/1.1/
		1.08/	1.15/	1.18/	1.21/	1.22/	1.24/	1.23/	1.23/	1.23/	1.22/	1.08/
		1.07	1.13/	1.16/	1.18/	1.18/	1.18/	1.18/	1.18/	1.17/	1.16/	1.07
			1.12	1.14	1.16	1.16	1.16	1.15	1.15	1.14	1.13	
	6	1.12/	1.18/	1.23/	1.27/	1.29/	1.31/	1.31/	1.32/	1.31/	1.3/	1.12/
		1.12/	1.18/	1.22/	1.27/	1.28/	1.31/	1.3/	1.31/	1.3/	1.29/	1.12/
		1.1/1.09	1.16/	1.19/	1.22/1.2	1.22/	1.23/	1.22/	1.22/	1.22/	1.21/	1.1/1.09
			1.14	1.17		1.19	1.19	1.19	1.18	1.17	1.16	

Table 2: Curvature Dynamic Amplification Factors (1500/2000/3000/4000m)

		Wave Period (s)										
		12	13	14	15	16	17	18	19	20	21	22
Height		1.01/	1.02/	1.03/	1.03/	1.04/	1.04/	1.04/	1.04/	1.04/	1.04/	1.01/
(m)		1.01	1.01	1.01	1.02	1.02	1.02	1.02	1.02	1.02	1.02	1.01
	2	1.04/	1.06/	1.07/	1.08/	1.09/	1.1/	1.1/1.1/	1.1/1.1/	1.1/1.1/	1.1/1.1/	1.04/
		1.03/	1.05/	1.07/	1.08/	1.09/	1.09/	1.08/	1.08/	1.08/	1.08/	1.03/
		1.02/	1.04/	1.05/	1.06/	1.07/	1.08/	1.04	1.04	1.04	1.04	1.02/
		1.01	1.02	1.03	1.03	1.04	1.04					1.01
	3	1.05/	1.08/	1.11/	1.13/	1.14/	1.16/	1.16/	1.17/	1.17/	1.17/	1.05/
		1.05/	1.08/	1.1/	1.13/	1.14/	1.16/	1.16/	1.17/	1.17/	1.17/	1.05/
		1.04/	1.06/	1.08/	1.1/1.05	1.11/	1.12/	1.12/	1.13/	1.13/	1.13/	1.04/
		1.02	1.03	1.04		1.05	1.06	1.06	1.06	1.07	1.07	1.02
	4	1.07/	1.11/	1.15/	1.19/	1.21/	1.23/	1.24/	1.25/	1.25/	1.26/	1.07/
		1.06/	1.1/	1.14/	1.19/	1.21/	1.24/	1.25/	1.26/	1.27/	1.27/	1.06/
		1.05/	1.08/	1.11/	1.14/	1.16/	1.18/	1.19/	1.2/1.09	1.2/1.09	1.2/1.09	1.05/
		1.02	1.04	1.05	1.07	1.07	1.08	1.09				1.02
	5	1.09/	1.14/	1.2/	1.26/	1.29/	1.33/	1.34/	1.37/	1.37/	1.37/	1.09/
		1.08/	1.13/	1.19/	1.26/	1.3/	1.35/	1.37/	1.39/	1.4/	1.4/	1.08/
		1.06/	1.1/1.05	1.14/	1.2/1.09	1.22/1.1	1.26/	1.27/	1.29/	1.29/	1.29/	1.06/
		1.03		1.07			1.11	1.12	1.13	1.13	1.13	1.03
	6	1.1/	1.18/	1.25/	1.35/	1.39/	1.46/	1.48/	1.51/	1.51/	1.52/	1.1/
		1.09/	1.17/	1.25/	1.36/	1.42/	1.5/	1.52/	1.57/	1.57/	1.57/	1.09/
		1.07/	1.13/	1.19/	1.26/	1.3/1.13	1.36/	1.38/	1.41/	1.41/	1.41/	1.07/
		1.03	1.06	1.08	1.11		1.15	1.16	1.17	1.17	1.18	1.03

Appendix C - RVE algorithm

```
def create_rve(fac, elem, voiden, Vf, cvf, Vlratio, Cube,
  frmean, frmin, frmax, vrmin, vrmax,meshfile):
  """
  Returns void center data and radius, voids surface coordinates,
  fibers and matrix physicalgroup, node numbers coordinates.
  Creates a RVE .msh and .vtk models for analysis.
  """
  gmsh.initialize(['-noenv'])
  factory = gmsh.model.occ
  gmsh.option.setNumber("Mesh.Algorithm3D",10)
  #gmsh.option.setNumber("Mesh.RandomFactor", 1.e-6)
  gmsh.option.setNumber("Mesh.Tetrahedra", 1)
  gmsh.option.setNumber("Mesh.Triangles", 1)
  gmsh.option.setNumber("General.Terminal", 1)
  gmsh.option.setNumber("General.Verbosity", 5)
  gmsh.option.setNumber("Mesh.SaveAll", 0)
  gmsh.option.setNumber("Mesh.MshFileVersion", 4.1)
  gmsh.option.setNumber("Mesh.CharacteristicLengthMin", elem * fac)
  gmsh.option.setNumber("Mesh.CharacteristicLengthMax", elem * fac)
  # RVE 1/2 length (Centre axis in the middle of the cube)
  R = Cube
  # Number of spherical voids
  random.seed(10)
  nSvoid = math.floor((voiden * 2 * R * 2 * R * 2 * R) / ((4 / 3) * math.pi *
    vrmax * vrmax * vrmax))
  nFibre = math.floor((Vf * 2 * R * 2 * R * 2 * R) / (math.pi * frmax * frmax * 2
     * R))
  dims = math.floor(math.sqrt(nFibre))
  factory.synchronize()
  box_1 = factory.addBox(-R, -R, -R, 2 * R, 2 * R, 2 * R)
  sbnd = []
  Void_data = {}
  # key: void center coordinates
  # value: void radius
  factory.synchronize()
  spheres = list()
  for s in range(2, nSvoid + 1):
    if s < nSvoid:
      r = vrmin + random.uniform(0.0, vrmax - vrmin)
      x = -R + random.uniform(0.0, 2 * R)
      y = -R + random.uniform(0.0, 2 * R)
      z = -R + random.uniform(0.0, 2 * R)
      sphere = factory.addSphere(x, y, z, r)
      spheres.append(sphere)
      Void_data[(x,y,z)] = r
```

```
    elif s == nSvoid:
      r = vrmin + random.uniform(0.0, vrmax - vrmin)
      x = -R + random.uniform(0.0, 2 * R)
      y = -R + random.uniform(0.0, 2 * R)
      z = -R + random.uniform(0.0, 2 * R)
      sphere = factory.addSphere(x, y, z, r)
      factory.dilate([(3, sphere)], x, y, z, Vlratio, 1, 0.5)
      spheres.append(sphere)
  factory.synchronize()
  #count = 0
  for sphere in spheres:
    sphere_bnd = gmsh.model.getBoundary([(3,sphere)],False,False,False)
    sbnd.append(gmsh.model.addPhysicalGroup(2,[sphere_bnd[0][1]]))
    #gmsh.model.setPhysicalName(3, sbnd[count], "void"+str(count))
    #count +=1
  entities = gmsh.model.getEntities()
  sph = []
  for entity in entities:
    if gmsh.model.getType(entity[0],entity[1]) == 'Sphere' and entity[0]==2:
      sph.append(entity[1])
  voidsph = gmsh.model.addPhysicalGroup(2,sph)
  gmsh.model.setPhysicalName(2,voidsph,"voids")
  factory.synchronize()
  #phy_gp = gmsh.model.addPhysicalGroup(3, [sphere])
  difference = factory.cut([(3, box_1)], [(3, tag) for tag in spheres],
    removeObject=True, removeTool=True)
  # get the tag :
  difference = difference[0][0][1]
  dx = (2 * R) / dims
  #count = 0
  # parameters for  cylinder axis
  dxF, dyF, dzF = 0, 0, 2 * R

  cylinders = list()
  Fibers_data = {}
  for i in range(0, dims):
    for j in range(0, dims):
      # Fibre diameter
      Fr = random.uniform(frmin, frmax)
      # Center of grid box in the RVE
      cgx = (-R + 0.5 * dx) + j * dx
      cgy = (-R + 0.5 * dx) + i * dx
      # Center of cylinder base
      xF = (cgx - 0.5 * dx + Fr) + random.uniform(0.0, dx - 2 * Fr)
      yF = (cgy - 0.5 * dx + Fr) + random.uniform(0.0, dx - 2 * Fr)
      zF = -R
      Fibers_data[(xF,yF)] = Fr
      cylinder = factory.addCylinder(xF, yF, zF, dxF, dyF, dzF, Fr)
      cylinders.append(cylinder)
  factory.synchronize()
  phy_cylinders = list()
  for cyl in cylinders:
    phy_cyl = gmsh.model.addPhysicalGroup(3, [cyl])
    phy_cylinders.append(phy_cyl)
  #cylinders_cp = factory.copy(cylinders)
  phy_fibres = gmsh.model.addPhysicalGroup(3, cylinders)
  gmsh.model.setPhysicalName(3, phy_fibres, "Fibres")
```

```
100   allvol = [cylinders[i] for i in range(len(cylinders))]
101   matrix = factory.cut([(3, difference)], [(3, t) for t in cylinders],
        removeObject=True, removeTool=False)
102   factory.synchronize()
103   matrix = matrix[0][0][1]
104
105   box_bnd = gmsh.model.getBoundary([(3,matrix)],False,False,False)
106   Bnd = [gmsh.model.addPhysicalGroup(2,box_bnd[i]) for i in range(len(box_bnd))]
107   allvol.append(matrix)
108   phy_matrix = gmsh.model.addPhysicalGroup(3, [matrix])
109   gmsh.model.setPhysicalName(3, phy_matrix, "Matrix")
110   factory.synchronize()
111  RVE = gmsh.model.addPhysicalGroup(3,allvol)
112   gmsh.model.setPhysicalName(3, RVE, "RVE")
113   factory.synchronize()
114  # Create Mesh
115   gmsh.model.mesh.generate(3)
116   gmsh.model.mesh.removeDuplicateNodes()
117   gmsh.model.mesh.renumberNodes()
118   gmsh.model.mesh.renumberElements()
119   gmsh.model.mesh.optimize("Netgen")
120   gmsh.write(meshfile+".msh")
121   gmsh.write(meshfile+".vtk")
122  # Return voids coordinates
123   entities = gmsh.model.getEntities()
124   void_mesh = {}
125   for entity in entities:
126     if gmsh.model.getType(entity[0],entity[1]) == 'Sphere' and entity[0]==2:
127       N_sp,Cor_sp,Cor_para = gmsh.model.mesh.getNodes(entity[0],entity[1],
        includeBoundary=True,returnParametricCoord=False)
128       void_mesh[entity[1]] = N_sp,Cor_sp
129     # Key: PhysicalGroup no
130     # Value: fibres and matrix node number, coordinates
131   Fiber_mesh = {}
132   Matrix_mesh = {}
133   for group in gmsh.model.getPhysicalGroups(-1):
134     if gmsh.model.getPhysicalName(group[0], group[1]) == 'Fibres':
135       Fnodes, Fcor = gmsh.model.mesh.getNodesForPhysicalGroup(group[0],group[1])
136       FGno = group[1]
137       Fiber_mesh[FGno] = Fnodes, Fcor
138     if gmsh.model.getPhysicalName(group[0], group[1]) == 'Matrix':
139       Mnodes, Mcor = gmsh.model.mesh.getNodesForPhysicalGroup(group[0],group[1])
140       MGno = group[1]
141       Matrix_mesh[MGno] = Mnodes, Mcor
142   gmsh.finalize()
143   return Void_data, void_mesh, Fiber_mesh, Matrix_mesh, Fibers_data
```

Appendix D - Multi-scale algorithm

```
"""

CRIMMO

Composite Riser Multi-scale Modelling


The code is a framework to perform  multi-scale modelling of composite risers,

coupled with RiSim. the non-linear time-domain riser simulation code.

abaqus cae -noGUI CRIMMO.py

"""

__author__ = "Hossam Ragheb"

__data__ = "29/01/2020"

__copyright__ = "Copyright 2020, The CRIMMO Project"

__credits__ = ["Hossam Ragheb"]

__license__ = "GPL"

#-----------------------------------------------------------------------------

#                                    IMPORTS

#-----------------------------------------------------------------------------

from part import *

import amplitude

from material import *

from section import *

from assembly import *

```

```
from step import *

from interaction import *

from load import *

from mesh import *

from job import *

from sketch import *

from visualization import *

from connectorBehavior import *

import regionToolset

from abaqusConstants import *

from driverUtils import executeOnCaeStartup

from caeModules import *

from odbAccess import *

from sys import argv, exit

import glob

import os

import io

import csv

import numpy as np

import pickle

session.viewports['Viewport: 1'].setValues(displayedObject=None)

showODB = False


def rightTrim(input,suffix):

if (input.find(suffix) == -1):

input = input + suffix

return input


def getMaxStrain(odbName,elsetName):

```

```
""" Print max principle strain location and value given odbName and elset (
    optional)"""

elset = elemset = None

region = "over the entire model"

""" Open the output database """

odb = openOdb(odbName)

assembly = odb.rootAssembly

""" Check to see if the element set exists

in the assembly

"""

if elsetName:

try:

elemset = assembly.elementSets[elsetName]

region = " in the element set : " + elsetName;

except KeyError:

print('An assembly level elset named %s does'\

'not exist in the output database %s' \

% (elsetName, odbName))

odb.close()

exit(0)

""" initialize maximum values """

maxStrain = -1.0E-20

maxElem = 0

maxStep = "_None_"

maxFrame = -1

Strain = 'LE'

isStrainPresent = 0


for step in odb.steps.values():

print('Processing Step:', step.name)
```

```
154
155 for frame in step.frames:
156
157 allFields = frame.fieldOutputs
158
159 if (allFields.has_key(Strain)):
160
161 isStrainPresent = 1
162
163 strainSet = allFields[Strain]
164
165 if elemset:
166
167 strainSet = strainSet.getSubset(region=elemset)
168
169 for strainValue in strainSet.values:
170
171 #print(strainValue.maxPrincipal)
172
173 if strainValue.elementLabel > 1000 and strainValue.elementLabel < 6200:
174
175 if (strainValue.maxPrincipal > maxStrain):
176
177 maxStrain = strainValue.maxPrincipal
178
179 maxElem = strainValue.elementLabel
180
181 maxStep = step.name
182
183 maxFrame = frame.incrementNumber
184
185 if(isStrainPresent):
186
187 print('Maximum principal strain %s is %f in element %d'%(
188
189 region, maxStrain, maxElem))
190
191 print ('Location: frame # %d step: %s '%(maxFrame,maxStep))
192
193 else:
194
195 print ('Strain output is not available in' \
196
197 'the output database : %s\n' %(odb.name))
198
199 """ Close the output database before exiting the program """
200
201 odb.close()
202
203 return maxStrain,maxElem
204
205 #--------------------------------------------------------------------------
206
207 #                                    INPUTS
208
209 #--------------------------------------------------------------------------
210
```

```
211 # Model material name
212
213 def CRIMMO(serial,depth,L,TensionAmp,Rot1Amp,Rot2Amp):
214
215 showODB = False
216
217 material = 'IM7-8552'
218
219 name = 'CFRP'
220
221 LCname = material + '_' + name
222
223 #serial = 1
224
225 g = 9.81
226
227 rho_w = 1025.
228
229 #depth = 30.
230
231 # Modelled section length
232
233 #L = 10. # [m]
234
235 # Internal diameter
236
237 ID = 0.28 # [m]
238
239 # Outer diameter
240
241 OD = 0.31432#0.32067 # [m]
242
243 # Liner thickness
244
245 tlin = 0.005 #[m]
246
247 # Outer sheath
248
249 tsh = 0.002 # [m]
250
251 # Composite laminate layer thickness
252
253 tcomp = 0.01016
254
255 # Lay-up sequence from inner to outer
256
257 complayup = [0,90,45,-45,0,90,45,-45,0,90,45,-45,0,90,45,-45,0,90,45,-45]
258
259 # Density
260
261 den = 2293 # kg/m3
262
263 # Young's modulus along fiber direction
264
265 E11 = 171e09 # [Pa]
266
267 # Young's modulus along transverse direction
```

```
268
269 E22 = 9.08e09 # [Pa]
270
271 # E33 = E22 for isotropic lamina
272
273 E33 = 9.08e09 # [Pa]
274
275 # Poisson's ratio
276
277 v12 = 0.32
278
279 # Poisson's ratio (v13 = v12 for transverse isotropic lamina)
280
281 v13 = 0.32
282
283 # Poisson't ratio
284
285 v23 = 0.5
286
287 # In plane shear modulus 1-2 plane
288
289 G12 = 5.29e09 # [Pa]
290
291 # Transverse shear modulus 2-3 plane
292
293 # G23 = E22/2(1+v23) for transver isotropic lamina
294
295 G23 = E22/(2*(1+v23)) # [Pa]
296
297 # In plane shear modulus 1-3 plane (g13=g12 for transverse isotropic lamina)
298
299 G13 = 5.29e09 # [Pa]
300
301 # Longitudinal tensile strength
302
303 XT = 2326e06 # [Pa]
304
305 # Longitudinal compressive strength
306
307 XC = 1200e06 # [Pa]
308
309 # Transverse tensile strength
310
311 YT = 63.0e06 # [Pa]
312
313 # Transverse comporessive strength
314
315 YC = 199.0e06 # [Pa]
316
317 # In-plane shear strength
318
319 SL = 92.0e06 # [Pa]
320
321 # Transver shear strength
322
323 ST = 101.2e06 # [Pa]
324
```

```
325 # Fracture plane angle for pure compressioni (default=53deg)
326
327 a0 = 53.0 # [deg]
328
329 # Misalignment angle at fialure for pure compression
330
331 Phi0 = 2.544 # [deg]
332
333 # Longitudinal shear friction coefficient
334
335 etaL = 0.082
336
337 # Transverse shear frictioni coefficient
338
339 etaT = 0.29
340
341 # Interlaminar fracture toughness
342
343 GIC = 0.27e03 #[j/m2]
344
345 GIIC = 0.78e03 #[j/m2]
346
347 GICft = 97.8e03 #[j/m2]
348
349 GICfc = 106e03 #[j/m2]
350
351 GICmt = 0.25e03 #[j/m2]
352
353 #Element Type
354
355 Eltype = 'S8R'
356
357 circRes = 10
358
359 Tension_stat = TensionAmp[0][1] #[N] wall tension
360
361 Pext = depth * rho_w * g
362
363 #Pin = 500.0e05
364
365 Pin = 100.0e6
366
367 instemp = 4.0
368
369 Optemp = 180.0
370
371 cP1 = (0.0, 0.0, 0.0)
372
373 cP2 = (0.0, 0.0, L)
374
375 #------------------------ Create the Pipe model-----------------------------------
376
377 mdb.models.changeKey(fromName='Model-1', toName=LCname)
378
379 CFRPModel = mdb.models[LCname]
380
381 #------------------------Create the Part-----------------------------------
```

```
382
383 # Sketch the pipe cross section using circular tool
384
385 CFRPProfileSketch = CFRPModel.ConstrainedSketch(name='CFRP CS Profile',\
386
387 sheetSize=OD*5)
388
389 CFRPProfileSketch.CircleByCenterPerimeter(center=(0.0,0.0), \
390
391 point1=(0.0,0.5*OD))
392
393 # Create 3D deformable part named "CFRP" by extruding the sketch
394
395 CFRPPart = CFRPModel.Part(name='CFRP', dimensionality=THREE_D,\
396
397 type=DEFORMABLE_BODY)
398
399 if Eltype == 'S8R':
400
401 CFRPPart.BaseShellExtrude(sketch=CFRPProfileSketch, depth = L)
402
403 #-------------------------Create Material-----------------------------------------
404
405 # Create material i.e IM7-8552 or T300/934..etc
406
407 CFRPMaterial = CFRPModel.Material(name=material)
408
409 CFRPMaterial.Density(table=((den, ), ))
410
411 CFRPMaterial.Elastic(type=ENGINEERING_CONSTANTS, table=((E11, E22, E33, v12, \
412
413 v13, v23, G12, G13, G23), ))
414
415 #-------------------------Create Composite Section-------------------------------
416
417 compositeLayup = CFRPPart.CompositeLayup(name='CompositeLayer', \
418
419 description='', elementType=SHELL, offsetType=MIDDLE_SURFACE, symmetric=FALSE,\
420
421 thicknessAssignment=FROM_SECTION)
422
423 compositeLayup.Section(preIntegrate=OFF, integrationRule=SIMPSON,
424
425 thicknessType=UNIFORM, poissonDefinition=DEFAULT, temperature=GRADIENT,
426
427 useDensity=OFF)
428
429 faces1 = CFRPPart.faces.findAt(((0.5*OD,0.0,0.0),))
430
431 normalAxisRegion = regionToolset.Region(side1Faces=faces1)
432
433 edge1 = CFRPPart.edges.findAt(((0.5*OD,0.0,0.0),))
434
435 PrimaryAxisRegion=regionToolset.Region(edges=edge1)
436
437 compositeLayup.orientation.setValues(orientationType=DISCRETE)
438
```

```
compositeLayup.ReferenceOrientation(orientationType=DISCRETE, localCsys=None,

additionalRotationType=ROTATION_NONE, angle=0.0,

additionalRotationField='', axis=AXIS_3, stackDirection=STACK_3,

normalAxisDefinition=SURFACE, normalAxisRegion=normalAxisRegion,

normalAxisDirection=AXIS_3, flipNormalDirection=False,

primaryAxisDefinition=EDGE, primaryAxisRegion=PrimaryAxisRegion,

primaryAxisDirection=AXIS_1, flipPrimaryDirection=False)

layup = []

if tlin != 0:

layup.append(0)

layup = layup + complayup

if tsh != 0:

layup.append(0)

#CFRPRegion = (CFRPPart.cells,)

faces = CFRPPart.faces.findAt(((0.5*OD,0.0,0.0),))

CFRPRegion = regionToolset.Region(faces=faces)

for i, ang in enumerate(layup):

compositeLayup.CompositePly(suppressed=False, plyName='Ply'+str(ang)

+'-'+str(i), region=CFRPRegion,material=material,

thicknessType=SPECIFY_THICKNESS, thickness=tcomp/len(complayup),

orientationType=SPECIFY_ORIENT, orientationValue=ang,

additionalRotationType=ROTATION_NONE, additionalRotationField='',

axis=AXIS_3, angle=0.0, numIntPoints=3)


#------------------------------Create the assembly-------------------------------

# Create part instance

CFRPAssembly = CFRPModel.rootAssembly

CFRPInstance = CFRPAssembly.Instance(name='CFRP Instance', part=CFRPPart, \

dependent=ON)

```

```
#-------------------------Create Step-------------------------------------------

CFRPModel.StaticStep(name='Step 1', previous='Initial',

description='Step 1: Apply Static Wall tension, External Pressure', nlgeom=ON)

CFRPModel.StaticStep(name='Step 2', previous='Step 1',

description='Step 2: Apply internal pressure and temperature ', nlgeom=ON)

CFRPModel.ImplicitDynamicsStep(name='Step 3', previous='Step 2',

description='Step 3: Apply dynamic tension, rotations', \

timePeriod=TensionAmp[-1][0], maxNumInc=100000, \

initialInc=TensionAmp[0][0], minInc=1e-8, nlgeom=ON)


CFRPModel.TabularAmplitude(name='Wall_tens_top', data=TensionAmp,smooth=
    SOLVER_DEFAULT, timeSpan=STEP)

CFRPModel.TabularAmplitude(name='Rot_top', data=Rot2Amp,smooth=SOLVER_DEFAULT,
    timeSpan=STEP)

CFRPModel.TabularAmplitude(name='Rot_bot', data=Rot1Amp,smooth=SOLVER_DEFAULT,
    timeSpan=STEP)

#-------------------------Create field output request---------------------------

CFRPModel.fieldOutputRequests.changeKey(fromName='F-Output-1',

toName='Selected Field Outputs')

CFRPModel.fieldOutputRequests['Selected Field Outputs'].setValues(

variables=('S', 'E', 'PEMAG', 'U', 'RF', 'CF', 'UVARM'))

#-------------------------Create History Output request-------------------------

CFRPModel.historyOutputRequests.changeKey(fromName='H-Output-1',

toName='Default History Outputs')

CFRPModel.historyOutputRequests['Default History Outputs'].setValues(

variables=PRESELECT)

#-------------------------Create Reference Point--------------------------------

CFRPAssembly.ReferencePoint(point = cP1) # RP1

CFRPAssembly.ReferencePoint(point = cP2) # RP2

#-------------------------Create Multipoint constraint--------------------------

r1 = CFRPAssembly.referencePoints
```

```
550
551 ref_top = (r1[4],)
552
553 Ref_top = regionToolset.Region(referencePoints=ref_top)
554
555 edge_top = CFRPAssembly.instances[name+' Instance'].edges.findAt(((\
556
557 0.5*OD,0.0,L),))
558
559 Edg_top = regionToolset.Region(edges=edge_top)
560
561 CFRPModel.MultipointConstraint(name='Const_top',
562
563 controlPoint=Ref_top, surface=Edg_top, mpcType=BEAM_MPC,
564
565 userMode=DOF_MODE_MPC, userType=0, csys=None)
566
567
568 ref_bot = (r1[3],)
569
570 Ref_bot = regionToolset.Region(referencePoints=ref_bot)
571
572 edge_bot = CFRPAssembly.instances[name+' Instance'].edges.findAt(((\
573
574 0.5*OD,0.0,0.0),))
575
576 Edg_bot = regionToolset.Region(edges=edge_bot)
577
578 CFRPModel.MultipointConstraint(name='Const_up',
579
580 controlPoint=Ref_bot, surface=Edg_bot, mpcType=BEAM_MPC,
581
582 userMode=DOF_MODE_MPC, userType=0, csys=None)
583
584 #-------------------------------Create Mesh-------------------------------------
585
586 elementType = ElemType(elemCode=Eltype, elemLibrary=STANDARD)
587
588 CFRPCells = CFRPPart.cells
589
590 selectedCFRPcells = CFRPCells.findAt(((0.5*OD, 0.0, 0.0),))
591
592 CFRPmeshRegion = (selectedCFRPcells,)
593
594 CFRPPart.setElementType(regions=CFRPmeshRegion, elemTypes=(elementType,))
595
596 CFRPPart.seedPart(size=OD/circRes, deviationFactor=0.1)
597
598 CFRPPart.generateMesh()
599
600 #-------------------------------Create Boundary Conditions-----------------------
601
602 CFRPModel.DisplacementBC(name='BC_top',\
603
604 createStepName='Initial', region=Ref_top, u1=0.0, u2=0.0, u3=UNSET,\
605
606 ur1=UNSET, ur2=0.0, ur3=0.0, amplitude=UNSET, fixed=OFF,\
```

```
607
608 distributionType=UNIFORM, fieldName='', localCsys=None)
609
610 CFRPModel.DisplacementBC(name='BC_bot',\
611
612 createStepName='Initial', region=Ref_bot, u1=0.0, u2=0.0, u3=0.0,\
613
614 ur1=UNSET, ur2=0.0, ur3=0.0, amplitude=UNSET, fixed=OFF,\
615
616 distributionType=UNIFORM, fieldName='', localCsys=None)
617
618 #------------------------------Create Tension Load-----------------------------------
619
620 # Step 1 load
621
622 # Wall tension
623
624 CFRPModel.ConcentratedForce(name='Tension_top',\
625
626 createStepName='Step 1', region=Ref_top, cf3=Tension_stat,\
627
628 distributionType=UNIFORM, field='', localCsys=None)
629
630 CFRPModel.loads['Tension_top'].deactivate('Step 3')
631
632 #------------------------------Create external pressure Load-----------------------
633
634 # Step 1 load
635
636 # External Pressure
637
638 regi = regionToolset.Region(side1Faces=CFRPAssembly.instances[name+' Instance'].
    faces.findAt(((0.5*OD,0.0,0.0),)))
639
640 CFRPModel.Pressure(name='External_Pressure', createStepName='Step 1',region =regi
     , distributionType=UNIFORM, field='', magnitude=Pext)
641
642 #------------------------------Create internal pressure Load-----------------------
643
644 # Step 2 load
645
646 # Internal Pressure
647
648 CFRPModel.Pressure(name='Internal_Pressure', createStepName='Step 2', \
649
650 region =regi , distributionType=UNIFORM, field='', magnitude=-Pin)
651
652 #------------------------------Create temperature load-----------------------------
653
654 # Step 2 load
655
656 # initial temperature
657
658 regitemp = regionToolset.Region(faces=CFRPAssembly.instances[name+' Instance'].
    faces.findAt(((0.5*OD,0.0,0.0),)))
659
```

```
CFRPModel.Temperature(name='Operating Temperature',createStepName='Step 2',
    region=regitemp, distributionType=UNIFORM,crossSectionDistribution=
    CONSTANT_THROUGH_THICKNESS, magnitudes=(Optemp, ))

#CFRPModel.TemperatureBC(name='InitTemp',createStepName='Initial', region=regitem
    , distributionType=UNIFORM,fieldName='', magnitude=4.0, amplitude=UNSET)

#-------------------------------Dynamic step-----------------------------------------

CFRPModel.ConcentratedForce(name='dynTension_top',\

createStepName='Step 3', region=Ref_top, cf3=1.0, \

distributionType=UNIFORM, field='', localCsys=None,amplitude= 'Wall_tens_top')

CFRPModel.boundaryConditions['BC_bot'].setValuesInStep(

stepName='Step 3', ur1=1.0, amplitude='Rot_bot')

CFRPModel.boundaryConditions['BC_top'].setValuesInStep(

stepName='Step 3', ur1=-1.0, amplitude='Rot_top')

#-------------------------------Create Job-------------------------------------------

jobname = LCname+'_'+str(serial)

mdb.Job(name=jobname, model=LCname, description='Job simulates composite pipe',
    type=ANALYSIS,

atTime=None, waitMinutes=0, waitHours=0, queue=None, memory=90,

memoryUnits=PERCENTAGE, getMemoryFromAnalysis=True,

explicitPrecision=SINGLE, nodalOutputPrecision=SINGLE, echoPrint=OFF,

modelPrint=OFF, contactPrint=OFF, historyPrint=OFF, userSubroutine='',

scratch='', resultsFormat=ODB, multiprocessingMode=DEFAULT, numCpus=8,

numDomains=8, numGPUs=0)

#parallelizationMethodExplicit=DOMAIN, multiprocessingMode=DEFAULT,

#          numDomains=1

#-------------------------------Run Job----------------------------------------------

mdb.jobs[jobname].submit(consistencyChecking=OFF)


#Do not return control till job is finished running

mdb.jobs[jobname].waitForCompletion()

#End of job run

```

```
713 #----------------------------Create Visualization-----------------------------------
714
715 CFRP_viewport = session.Viewport(name='CFRP Results Viewport')
716
717 CFRP_Odb_Path = jobname+'.odb'
718
719 #----------------------------Post-processing-----------------------------------
720
721 elsetName = None
722
723 A,B = getMaxStrain(CFRP_Odb_Path,elsetName)
724
725 with open(jobname+".csv",'w') as f:
726
727 f.write(str(A)+","+str(B))
728
729 if showODB==True:
730
731 odb_obj = session.openOdb(name=CFRP_Odb_Path)
732
733 CFRP_viewport.setValues(displayedObject=odb_obj)
734
735 CFRP_viewport.odbDisplay.display.setValues(plotState=(DEFORMED,))
736
737 def Get_BC(Tensions,angles,Select,run,span=3):
738
739 TenAmp = Tensions[run,np.argmax(Tensions[run,:np.argmin(Tensions[run,:,Select]),
      Select])-100:np.argmax(Tensions[run,:np.argmin(Tensions[run,:,Select]),Select
      ])+100,Select+span]
740
741 Rot1 = angles[run,np.argmax(Tensions[run,:np.argmin(Tensions[run,:,Select]),
      Select])-100:np.argmax(Tensions[run,:np.argmin(Tensions[run,:,Select]),Select
      ])+100,Select-span]
742
743 Rot2 = angles[run,np.argmax(Tensions[run,:np.argmin(Tensions[run,:,Select]),
      Select])-100:np.argmax(Tensions[run,:np.argmin(Tensions[run,:,Select]),Select
      ])+100,Select+span]
744
745 time = np.linspace(0,TenAmp.shape[0]*0.185,TenAmp.shape[0])
746
747
748 TensionAmp = tuple((time[i],TenAmp[i]) for i in range(len(TenAmp)))
749
750 Rot1Amp = tuple((time[i],Rot1[i]) for i in range(len(Rot1)))
751
752 Rot2Amp = tuple((time[i],Rot2[i]) for i in range(len(Rot2)))
753
754 return TensionAmp, Rot1Amp, Rot2Amp
755
756 def get_para(ext="*.ri"):
757
758 """
759
760 Returns Analysis parameters given input file extension.
761
762
763 ext : string
```

```
764
765 input file extension
766
767
768 Returns
769
770 _______
771
772 S      :float
773
774 Cable length.
775
776 ds     :float
777
778 Element length.
779
780 Ns     :integer
781
782 Number of nodes.
783
784 nospp :integer
785
786 Number of time steps per wave period.
787
788 nop    :integer
789
790 Number of wave periods.
791
792 Nt     :integer
793
794 Number of time steps.
795
796 Tp     :float
797
798 Wave period [s]
799
800 dt     :float
801
802 Time step [s]
803
804 """
805
806 file = glob.glob(ext)
807
808 inputfile = open(file[0],'r').readlines()
809
810 S = float(inputfile[8].split(",")[0])
811
812 ds = float(inputfile[8].split(",")[1])
813
814 Ns = int(1+S/ds)
815
816 nospp = int(inputfile[13].split(",")[2])
817
818 nop = int(inputfile[13].split(",")[3])
819
820 Nt = nospp*nop
```

```
821
822 Tp =float(inputfile[13].split(",")[1])
823
824 dt = float(inputfile[13].split(",")[6][:-1])
825
826 return S, ds, Ns, nospp, nop, Nt, Tp, dt, file
827
828 def get_dynamic(file,Ns,dt):
829
830 """
831
832 Reads the dynamic solution
833
834
835 file     : ndarray, shape(no of files ".ri")
836
837 List of files that are analysed in the folder.
838
839 basefile: string
840
841 name of the static file wihtout the extension.
842
843 """
844
845 Folder = [f[:-3] for f in file]
846
847 #Time step of each simulation
848
849 Nt1 = [len(glob.glob(f+"/*.dat"))-3 for f in Folder]
850
851 Nt = np.max(Nt1)
852
853 Xd = np.zeros((len(Folder),Nt,Ns))
854
855 Yd = np.zeros((len(Folder),Nt,Ns))
856
857 Td = np.zeros((len(Folder),Nt,Ns))#tension
858
859 Snd = np.zeros((len(Folder),Nt,Ns))#shear force in the normal direction
860
861 Thetasd = np.zeros((len(Folder),Nt,Ns))#angle?
862
863 Gbd = np.zeros((len(Folder),Nt,Ns))#curvature
864
865 sd = np.zeros((Ns))
866
867 u = np.zeros((len(Folder),Nt,Ns))#transverse velocity
868
869 v = np.zeros((len(Folder),Nt,Ns))#normal velocity
870
871 time_stamp = np.zeros((len(Folder),Nt))
872
873 stdev = np.zeros((len(Folder),Td.shape[-1]))
874
875 stdevcurv = np.zeros((len(Folder),Td.shape[-1]))
876
877 hotspot = np.zeros(len(Folder))
```

```
878
879 for j in range(len(Folder)):
880
881 for i in range(0,Nt1[j]):
882
883 time_stamp[j,i] = dt*float(i)
884
885 with FortranFile(str(Folder[j])+'/Dynamic_step-'+str(i+1)+'.dat','r') as g:
886
887 Resultsd = g.read_reals(float).reshape((9,Ns))
888
889 sd[:] = Resultsd[0]
890
891 Xd[j,i,:] = Resultsd[1]
892
893 Yd[j,i,:] = Resultsd[2]
894
895 Td[j,i,:] = Resultsd[3]
896
897 Snd[j,i,:] = Resultsd[4]
898
899 Thetasd[j,i,:] = Resultsd[5]
900
901 Gbd[j,i,:] = Resultsd[6]
902
903 u[j,i,:] = Resultsd[7]
904
905 v[j,i,:] = Resultsd[8]
906
907 for k in range(Td.shape[-1]):
908
909 stdev[j,k] = np.std(Td[j,2::,k])
910
911 stdevcurv[j,k] = np.std(Gbd[j,2::,k])
912
913 hotspot[j] = np.argmax(stdevcurv[j]*stdev[j])
914
915 return sd, Xd, Yd, Td, Snd, Thetasd, Gbd, u, v, stdev, hotspot,Folder, Nt
916
917 if __name__ == '__main__':
918
919 # S, ds, Ns, nospp, nop, Nt, Tp, dt, file = get_para()
920
921 # sd, Xd, Yt, Tensions, Snd, angles, Gbd, u, v, stdev, hotspot,Folder, Nt =
      get_dynamic(file,Ns,dt)
922
923 dt = 0.185
924
925 ds = 3.
926
927 # hotspot = np.load("hotspot2.npy",allow_pickle=True)
928
929 # Folder = np.load("Folder2.npy",allow_pickle=True)
930
931 # Tensions = np.load("TdF2.npy",allow_pickle=True)
932
933 # angles = np.load("ThetasdF2.npy",allow_pickle=True)
```

```
934
935 # Nt = np.load("Nt2.npy",allow_pickle=True)
936
937 # Yt = np.load("YdF2.npy",allow_pickle=True)
938
939 # SelK = int(max(set(list(hotspot)), key = list(hotspot).count))
940
941 # SelT = len(Tensions[0,0,:])-3
942
943 # Sel = [SelK,SelT]
944
945 #Element length 3 m, simulate pipe with 12 m length to reduce far-field boundary
    coundtions erros. two element right and left of the hotspot
946
947 run = 0
948
949 titl = {0:"TDZ",1:"HO"}
950
951 dep = {0:400,1:15}
952
953 for i in range(73):
954
955 for k in range(2):
956
957 Tfile = "IM7-8552_CFRP_"+str(i)+"_"+titl[k]+"_T1.csv"
958
959 R1file = "IM7-8552_CFRP_"+str(i)+"_"+titl[k]+"_R1.csv"
960
961 R2file = "IM7-8552_CFRP_"+str(i)+"_"+titl[k]+"_R2.csv"
962
963 TensionAmp = np.loadtxt(Tfile)
964
965 Rot1Amp = np.loadtxt(R1file)
966
967 Rot2Amp = np.loadtxt(R2file)
968
969 #depth = np.round(Yt[run,0,-1] - Yt[run,0,Sel[k]])
970
971 depth = dep[k]
972
973 L = ds * 4
974
975 subtitle = Tfile[:-7]
976
977 CRIMMO(subtitle,depth,L,TensionAmp,Rot1Amp,Rot2Amp)
978
979 run = run + 1
```